UNIVERSITY OF
BIRMINGHAM

Nanofabrication via Laser Interference Lithography and Integration of Various Optical Systems for Remote Sensing Applications

By

Muhammad Waqas Khalid

A thesis submitted to

The University of Birmingham

For the degree of

DOCTOR OF PHILOSOPHY

School of Engineering
The University of Birmingham

(04/02/2019)

Abstract

Nanophotonic devices help to manipulate light at nanometric scale through various optical phenomena in near infrared and visible regions of the electromagnetic spectrum. This research aims to present the fabrication, modelling, optical characterisation and real life applications of optical devices based on materials such as ink, soft polymer, gelatine, leuco dye and liquid crystals. Laser interference-based ablation is utilised to generate phase conjugate nanostructures on ink, gelatine based edible nanostructures for food decoration purposes, and flexible polymeric nanostructures on polydimethylsiloxane substrate to demonstrate their use for remote sensing applications. Replication of Cornercube Retroreflector array and diffusing surface is conducted in this research to construct flexible force and temperature sensors.

CCRs are mainly exploited in this research due to their retroreflection property. Reflected light from CCRs is sent back towards the source through total internal reflection and is independent of the incident angle. A silver coated CCR is used to fabricate a 2D conjugate periodic gratings structure on ink coated glass substrate through Denisyuk reflection holography. Diffractive gratings (super prism) fabricated from simple mirror-based interference reflection have less features to manipulate as compared to the conjugate diffractive gratings made by using interference obtained from CCRs. Nanometric holographic CCR showed somewhat similar optical properties as shown by master centimetric CCR *e.g.* phase conjugation. Predictions through computational modelling were also in good agreement with the experimental (optical characterisation) results.

CCR array structures are most commonly encountered in everyday life activities such as traffic signals, vehicle safety systems and nightwear clothing. The use of brittle optical devices is limited due to their rigidity. In this research, PDMS was used to replicate rigid CCRs array structures into a flexible form. Polymeric CCRs array was examined and compared to the

stencil by utilising optical microscopy. Optical characterisations were performed under various mechanical and thermal stress levels. Optical properties dependent on structure's dimension were tuned based on the external stimuli such as force. It is concluded in this study that polymeric optical structures have a potential to be employed in numerous sensing applications for stretch, temperature, pH, and humidity.

Combination of CCRs and thermochromatic materials can yield remote temperature sensors based on active components. This research also demonstrates two different systems including liquid crystals and leuco dyes to record temperature changes within a region of interest. Glass based CCRs were coated with leuco dye and liquid crystals and were treated at various known temperatures under continuous monochromatic light illumination. Reflected power from thermochromatic CCR was tuned based on supplied temperature and was found to be dependent on the colour scheme. These novel systems may help to monitor environmental conditions such as temperature changes within hazardous areas, where human access is restricted.

Finally, edible, flexible and multi-layered materials were engineered with photonic structures to examine the flexibility of Nd:YAG laser ablation in Denisyuk reflection mode. Fabricated structures were examined by scanning electron microscopy and optically characterised with monochromatic and broadband light sources. Various shapes of nanostructures were achieved by utilising provided parameters for fabrication. It is hence concluded that laser interference-based ablation is simple, fast, cost-effective and flexible technique to copy reflective objects in nanometric scale.

Dedicated to my Family and Teachers

Acknowledgement

I wish to express my sincere gratitude to my supervisors Dr Haider Butt and Dr Carl Anthony for their guidance, ideas, support and encouragement throughout my doctoral research. I am extremely grateful to Dr Haider Butt for inspiring me through his innovative ideas and his noteworthy passion towards research. I have greatly benefitted from his knowledge and am very thankful to him for his patience and kindness during this research study. I feel fortunate to be supervised by such a great personality.

I am thankful to Dr Rajib Ahmed for his help with numerical modelling according to my experimental parameters input and all my colleagues, especially Tawfiq Alqureshi, Ijaz Rashid, Catherine Whitehouse, Bader Alqattan, Yousef Alqureshi, and Mohamed Elsherif for their useful discussions and motivations.

I am also grateful to Dr Ali K. Yetisen, Mushfiqur Rahman, Dr Umair Hassan and Dr Ali Raza for their kind help and valuable suggestions during my PhD research.

I would also like to thank all my teachers, since my childhood who enabled me to procced step by step during my studies and have helped me in successfully conducting this research.

Finally, I would like to give my sincere thanks to my parents, my aunty and all my family and friends for their prayers, support and encouragement during my research study.

List of Publications

[1] **Khalid, M.W.,** et al., Holographic Writing of Ink-Based Phase Conjugate Nanostructures via Laser Ablation. Scientific Reports, 2017. **7**(1): p. 10603.

[2] **Khalid, M.W.,** et al., Flexible cornercube retroreflector array for temperature and strain sensing. RSC advances, 2018. 8(14): p. 7588-7598.

[3] **Khalid, M.W.,** et al., Remote Thermal Sensing by Integration of Corner-Cube Optics and Thermochromic Materials. Advanced Optical Materials, 2019. **7**(2): p. 1801013.

Abbreviations

Bright Field	BF	Light Emitting Diode	LED
Back Scattered Electron	BSE	Milli Joule	mJ
Cornercube Retroreflector	CCR	Neodymium-doped Yttrium Aluminium Garnet	Nd:YAG
Dynamic Cornercube Retroreflector	DCCR	Nanosecond	Ns
Dark Field	DF	Optical Phase Conjugation	OPC
Detection Limit	DoL	Optical Microscopy	OM
Electromagnetic Radiations	EMRs	One/Two/Three dimensional	1/2/3D
Electron Beam Lithography	EBL	Phase Conjugate Mirror	PCM
Electromagnetic Spectrum	EMS	Polydimethylsiloxane	PDMS
Electron Beam Lithography	EBL	Poly-methyl methacrylate	PMMA
Energy Dispersive X-Ray	EDX	Phase Conjugated Wave	PCW
Fast Fourier Transform	FFT	Plane Mirror	PM
Finite Element Method	FEM	Position	Pos
Focussed Ion Beam	FIB	Refractive Index	RI
Femtosecond	Fs	Silver	Ag
Gold	Au	Secondary Electrons	SE
Light Amplification by Simulated Emission of Radiation	LASER	Scanning Electron Microscopy	SEM
Liquid Crystal Display	LCD	Total Internal Reflection Ultraviolet	TIR Ultraviolet

Nomenclature

A	Amplitude	T_c	Critical Temperature
B	Magnetic Field	v	Velocity
C	Speed of light	d_0	Original Gratings Period
D	Spacing	ΔS	Change of Sensitivity
E	Electric Field	Λ	Grating's spacing
E	Energy	É	Young's Modulus
F	Force	ε	Strain
H	Height	ε^*	conjugate/reversal of polarization
I	Intensity	$\hbar$	Reduced Planck's Constant
J	Electric Current Density	η	Index of Refraction
K	Wave number	σ	Stress
l	Length	ω	Angular frequency
M	Phase modulation of reflection	Θ	Angle
P	Pitch	ϕ	Phase
R	Reflection	Λ	Wavelength
$\bar{S}$	Pointing vector	ρ	Density
T	Transmission	μ_o	Free space permeability
t	Time	ε_o	Free Space Permativity

Table of Contents

List of Figures

List of Tables

Chapter 1 Introduction

1.1 Overview

The Electromagnetic spectrum (EMS) is composed of wavelengths ranging from gamma rays of few picometers to radio waves of some kilometres. The term light or optical radiations refers to a small portion of EMS with a wavelength range between 390 nm and 750 nm, often denoted by the colours visible to human eye. Optics is a branch of science which deals with the study of light behaviour, properties and light matter interaction such as, refraction, reflection, absorption, diffraction, and transmission. Optics involves very basic phenomenon of visualisation to the very complex mechanisms of utilising optical elements to facilitate sectors including biosciences, astronomy, geology, information technology, imaging, microscopy and several others. Historically, the term optics is rooted from the term ‘‘appearance’’ called by the Greeks and this began with the development of lenses, centuries ago [1]. Early modern Europeans were the pioneers of diffraction optics, which further acted as a pivotal moment around which the construction and development of modern optical devices was based.

Denis Gabor developed the theory of holography in 1947, which evoked scientists all over the world. Despite of equipment limitations, scientists elaborated Gabor’s work and explored their understanding about this process and its potential for the next generation of researchers in the field. The emergence of laser in 1960s enabled first practical optical holographic image. Since then, holograms have been in focus for a great amount of research and development [1]. A hologram is a physical structure, which under light illumination can reconstruct the wavefront by means of diffraction [2, 3]. Several methods exist which are well known for the construction of physical structures with dimensions comparable to the wavelength within visible and near infrared region of EMS. There are many different techniques for holography such as e-beam

lithography, focussed ion beam milling, direct laser writing and surface embossing. All these techniques come along with their relevant advantages and disadvantages. FIB milling and e-beam lithography are required connection with advanced expensive equipment such as scanning electron microscopy and FIB and are expertise dependent more over the eroding process is slower and have low through put. Nanofabrication through direct laser writing is limited due to the dependence of dimensions of fabricated structures on the spot size of incident laser beam. Surface embossing is currently the most productive method to be used for nanofabrication but still it has the drawbacks such as the dimensions of replicated nanostructures are limited to the dimensions of the stencil. Moreover, the material choice is limited for these methods.

In this research work laser interference-based lithography is optimised to create nanostructures within various materials including conductive and nonconductive thin films. Laser interference beam lithography is simple to operate, no extensive laser tuning is required and provides many different parameters to control the sizes and dimensions of 1D/2D nanostructures. Fabrication process is completed within few minutes. Size of the grooved structures is comparable to the wavelength of laser beam so the beam spot limitation can be overthrown.

Optical structures interact with incident light through various phenomenon depending upon their dimensions, shapes and cross-sectional area to produce corresponding visible pattern at far fields.

Any changes in dimensions or other properties of physical structures under illumination based on external stimuli such as, thermal effect, natural or mechanical forces, chemical changes and other environmental conditions may lead to a change in their optical response, which can then be analysed to measure and quantify the variation/transformation in these environmental factors. In this research, a simple, cost effective and productive method is adopted to observe

nanostructures on variety of substrates including rigid, flexible, conductive, nonconductive and edible characteristics. Moreover, fabricated nanostructures were optically characterised to elaborate their potential applications in remote sensing.

CCR is perhaps one of the smartest optical devices ever constructed, by employing three reflective surfaces, which intersect perpendicularly to each other to receive reflected light from the device without any angle of reflection [4]. Incident light at the cornercube is reflected once from each three surfaces and then propagates towards the source, regardless the incident angle, through the total internal reflection mechanism as shown in figure 1.1 [4, 5].

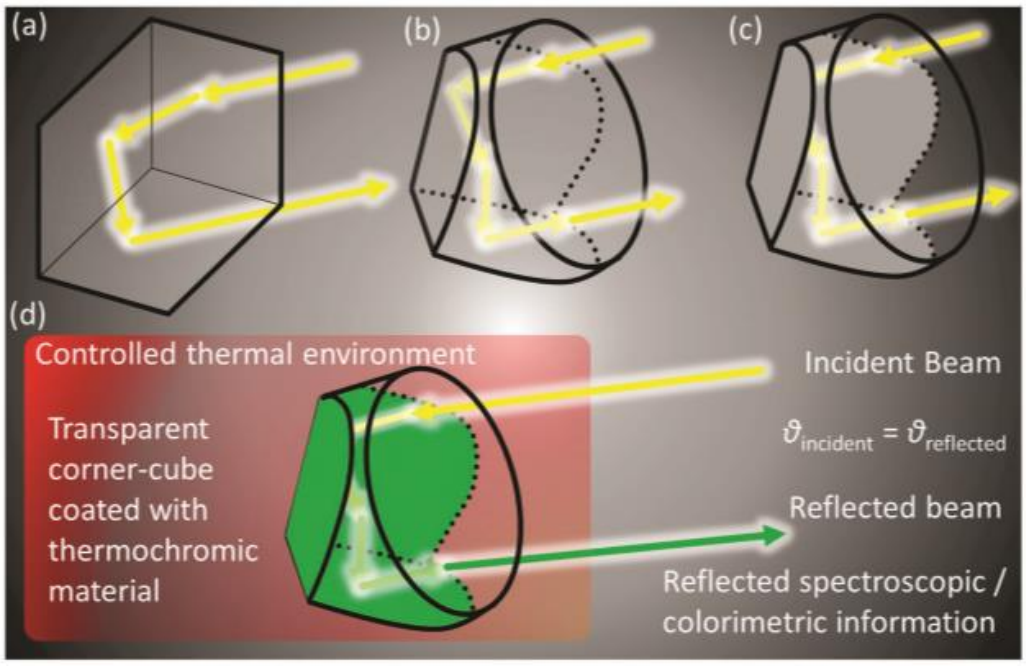

Figure 1. 1: Schematics of CCR and temperature sensing: a) hollow corner-cube retroreflector, b) uncoated solid TIR corner-cube retroreflector, c) back coated solid corner-cube retroreflector, d) a TIR–CCR coated with the thermochromic material used to obtain colorimetric modulation at various thermal conditions.

Interference pattern originated from the CCR was utilised to selectively ablate the light absorbing material (black ink) coated on silica glass in order to fabricate optical elements in

the form of diffractive gratings during this research work. The fabricated optical structures that are more compact on illumination show somehow similar optical properties as the parent recorded interference pattern. Optical phase conjugation, diffraction, beam splitting, and phase conjugate periodic structures are demonstrated in detail. It is anticipated that the holographic structures may help to improve the application of ordinary diffraction gratings such as remote sensing, data storage, and narrow band colour filters.

Rigid cornercube array are easily available reflectors in the market, which are mostly used in wearable devices, traffic signals and vehicle lights [6]. Their replication into a flexible substrate may enhance their usability in advance optical instruments. In this research study, flexible cornercube arrays are generated within a soft polymer (PDMS) *via* embossing. Optical response is then tuned based on external stimuli i.e. temperature and force. Optical characterisation of constructed polymeric structures were performed under continuous external load suspension and various temperature values turn by turn to demonstrate their feasibility as remote temperature and strain sensors.

Thermochromatic materials, as their name suggests can undergo a change in colour and in turn vary their optical properties when subjected to different temperatures [7, 8]. A combination of these kinds of materials with CCRs could allow for quantitatively mapping surfaces or environmental thermal conditions. Simple, cost effective and compact remote temperature sensors are created by coating liquid crystal and leuco dye separately on CCRs. Both systems produced interesting results (with an average relative error of 2%) during heating and cooling events and showed potential that they could be improved further for the existing heat sensing devices. It is revealed that temperature sensors based on liquid crystals are more thermally sensitive than those with lueco dye.

Although the replication process is simple and have low cost, there are some issues, which have to be addressed before proceeding for the mass production technique at an industrial level. Firstly, the replication process is slower as compared to the laser ablation through interference pattern. Another issue that lies with the use of replication process is the variability in the size of the structures within the stencil as the size of master surface remains constant. Hence, a cost effective, fast, productive, simple and flexible method is proposed to fabricate optical structures of various sizes within soft polymers, edible materials, and rigid glass coated with different light absorbing materials (conductive, nonconductive and combination of both conductive and nonconductive) in this study. All structures are optically characterised along with their diffraction efficiency calculations to obtain interesting results. Polymeric structures are utilised for stress/strain sensing applications. Whereas, edible materials based on optical structures are shown to be used for food decoration purposes. It is also proposed that structuring the multilayer of conductive and nonconductive coating may help to produce electronic devices within few minutes via laser interference-based lithography.

Polymeric optical structures such as diffraction gratings or diffusers can change their dimensions during the application of external forces, which in turn changes their optical response i.e. diffraction pattern or diffusion angles. This change in optical response could then be correlated with the applied force and utilised to quantify the strain caused within the region of interest. In this research, diffraction gratings and diffusing surfaces from master surfaces are replicated within PDMS blocks in order to generate lightweight, low cost and cheap sensors for strain sensing application. Calculated Young's Modulus is found in good agreement to the Young's Modulus of PDMS i.e. 360-870 kpa [9, 10].

1.2 Aims and objectives

The main aim of this research was to fabricate cost effective, compact nanophotonic devices by optimising fast, simple, flexible and productive fabrication methods. This research work undertakes a brief study of printable holographic optical structures in the form of difractive gratings (often called superprism) engineered on rigid glass, soft polymers, edible gelatine, permanent ink, and gold *via* selective laser ablation; polymeric cornercube array and optical diffusers *via* PDMS replication and integration of cornercube optics with thermochromatic materials to demonstrates their applications in real life. The fabricated nanophotonic devices made with easily available materials and through simple fabrication procedures, find potential use in diffraction optics, miniature optical communication devices and remote sensing applications. The strategic approach includes performing an extensive literature review and adopting research work in the relevant field, i.e. prediction through computational modelling, selection of a suitable fabrication method, cornercube optics, microscopic analysis, optical characterisation, and further exploration of potential applications. Several laser safety and chemical hazardous courses are undertaken, additional trainings such as, electron microscopy, optical microscopy, Nd:YAG laser and of other relevant equipment are also carried out to get a full command along with being able to safely conduct experimental work in the relevant laboratories.

In order to satisfy the aim of this project, the following objectives were developed to guide this study:

i. Extensive review of recent researches, photonic devices, and optical phenomena
ii. Review of available methods of fabrication to fabricate desired optical device
iii. Apparatus calibrations for various optical characterisation
iv. Computational modelling/simulation to further understand and explore experimental results.

v. Qualitative and quantitative analysis of the achieved results in order to successfully utilise fabricated optical devices for various applications.

1.3 Layout of research thesis

The structure of this PhD thesis is organised by dividing the content into seven chapters to describe in detail the research performed on understanding optical structures. Layout of the thesis is as follows:

Chapter 1 contains the overview of research, the aims and objectives and layout of the thesis. **Chapter 2** presents the background and literature review of optics and photonics phenomena along with the materials and methods used for sample fabrication and optical characterisation. Literature for the specific devices is detailed in the relevant chapters.

Chapter 3 is reproduced from "Khalid, M.W., et al., Holographic Writing of Ink-Based Phase Conjugate Nanostructures via Laser Ablation. Scientific reports, 2017. **7**(1): p. 10603." and introduces the ink-based phase-conjugated nanostructures fabricated *via* reflection holography along with optical phase conjugation. Diffraction of light through phase conjugate nanostructures is shown through image projection under broadband and monochromatic light illumination. Scanning electron microscopy is employed to characterise surface morphologies of phase conjugate nanostructures. Effect of parameters variation such as working distance, supplied energy, exposure angle and height on surface morphologies of fabricated structures as well as on resulting diffraction patterns are discussed in detail. Novelty and possible applications are also demonstrated. Phase-conjugated nanostructure fabrication, sample preparation and conjugated nanostructure recording theory are also presented. Optical properties and computational modelling of 1D and 2D conjugated nanostructures are also reported in this chapter.

Chapter 4 is reproduced from "Khalid, M.W., et al., Flexible corner cube retroreflector array for temperature and strain sensing. RSC advances, 2018. **8**(14): p. 7588-7598." and is composed of the research carried out on polymeric CCR array replicated within a PDMS block through embossing. Fabricated CCR array is utilised for remote sensing application. Optical response is tuned based on applied stress as load suspension and temperature variation. Numerical simulations (COMSOL) were also performed in this study to predict the optical response and were validated by the experimental results. Feasibility of the fabricated sensor to function in transmission as well as in reflection mode is also demonstrated.

Chapter 5 is reproduced from "Khalid, M.W., et al., Remote Thermal Sensing by Integration of Corner-Cube Optics and Thermochromic Materials. Advanced Optical Materials, 2019. **7**(2): p. 1801013." and describes the utilisation of a combination of CCRs with thermochromatic materials to construct a compact optical sensor, which could be used to measure and quantify the environmental/atmospheric temperature. The motivation of this project is taken from the visualisation of pigment colours through naked eye and structural colour from a morpho-butterfly or peacock feathers under broadband light illumination. CCR is chosen for this project as it reflects light towards the source through total internal reflection mechanism without any angle of reflection. Leuco dye and liquid crystal are coated on two different CCRs and optically characterised through monochromatic and broadband light sources. Both optical sensors show satisfactory results to be used as temperature sensing devices operating within the hazardous or human restricted areas.

Chapter 6 includes the optimisation of Nd:YAG laser in Densyuk reflection mode to engineer periodic structures on various substrates including, edible gelatine, soft polymers, and rigid glass substrates. Conductive gold coating, nonconductive ink coating and combination of both types of coating are also selectively ablated by directing interference pattern to their surface. Flexible periodic grating designed on a soft polymer are used as stress sensing application.

Whereas, gratings made on edible materials are shown to be used as food decoration purposes. It is also proposed that the ablation of conductive/nonconductive materials tinted on each other may help to produce mass electronic devices within few minutes through this fast, simple and cost-effective fabrication technique (laser interference-based lithography).

Chapter 7 contains the main key findings of this study while concluding the work showing the main outcome of this PhD research along with providing further recommendations for future research.

References (i)

1. Hoad, T.F., *The concise Oxford dictionary of English etymology*. 1993: Oxford University Press Oxford.
2. Vasconcellos, F.d.C., et al., *Printable surface holograms via laser ablation.* ACS Photonics, 2014. **1**(6): p. 489-495.
3. Smalley, D., et al., *Anisotropic leaky-mode modulator for holographic video displays.* Nature, 2013. **498**(7454): p. 313.
4. Hsu, V., J. Kahn, and K. Pister, *MEMS cornercube retroreflectors for free-space optical communications.* University of California Publication, 1999: p. 1-53.
5. Newman, W.I., *Continuum Mechanics in the Earth Sciences*. 2012: Cambridge University Press.
6. Barrett, H.H. and S.F. Jacobs, *Retroreflective arrays as approximate phase conjugators.* Optics letters, 1979. **4**(6): p. 190-192.
7. Panák, O., M. Držková, and M. Kaplanová, *Insight into the evaluation of colour changes of leuco dye based thermochromic systems as a function of temperature.* Dyes and Pigments, 2015. **120**: p. 279-287.
8. White, M.A. and M. LeBlanc, *Thermochromism in commercial products.* Journal of chemical education, 1999. **76**(9): p. 1201.
9. Kulangara, K. and K.W. Leong, *Substrate topography shapes cell function.* Soft Matter, 2009. **5**(21): p. 4072-4076.
10. Park, J.Y., et al., *Increased poly (dimethylsiloxane) stiffness improves viability and morphology of mouse fibroblast cells.* BioChip Journal, 2010. **4**(3): p. 230-236.

Chapter 2 Theoretical Background and Methodologies

2.1 Overview

This chapter contains theoretical background and an overview of basic optical phenomena. Section 2.2 briefly discusses the EMS. Basics of light interactions with matter are covered in section 2.3. Basic principles of lasers and microscopy are demonstrated in sections 2.4 and 2.5, respectively. Thermochromatic, and other optical materials are detailed along with their mechanical properties in section 2.6 and 2.7. Classification of holography, holographic recording of optical structures, laser ablation, phase conjugation as real time holography, optical elements and displays are listed in sections 2.8 to 2.12, respectively. Simulation and computational modelling theory are detailed in section 2.13.

2.2 Electromagnetic spectrum

EMS is the foundation of the information age and of our modern world. Electromagnetic radiations (EMRs) ranging from gamma rays to radio waves are produced by oscillation of charged particles, consist of electric and magnetic fields and travel as waves [1]. The difference between both kind of waves is the medium required to travel for ocean waves, whereas EMRs can travel through the vacuum with the speed of light [2]. EM waves have crests and troughs, and the distance between two adjacent troughs or crests is called wavelength. Within the EMS, the wavelengths range from kilometres (radio waves) to picometers (gamma rays) range [3]. The number of crests that pass through a fixed point within a second is known as frequency (SI unit is Hz) of the wave. Radio waves have lower frequencies and are less energetic than that of shorter wavelengths and higher frequencies [4]. Human eyes are capable of interpreting only the radiation within the wavelength range of 390- 750 nm which is the visible region of the EMS as shown in figure 2.1 [5]. Materials have specific colours because a portion of the EMS

is reflected, and the rest is absorbed by the materials. The reflected portion of the visible light waves is translated to our brain through the eyes as specific colour code. Pigmented colours come from the chemical/biological composition of the objects (e.g. ink colours), whereas, structural colours are yielded from the structural arrangements (e.g. colours from peacock feather) [6-8].

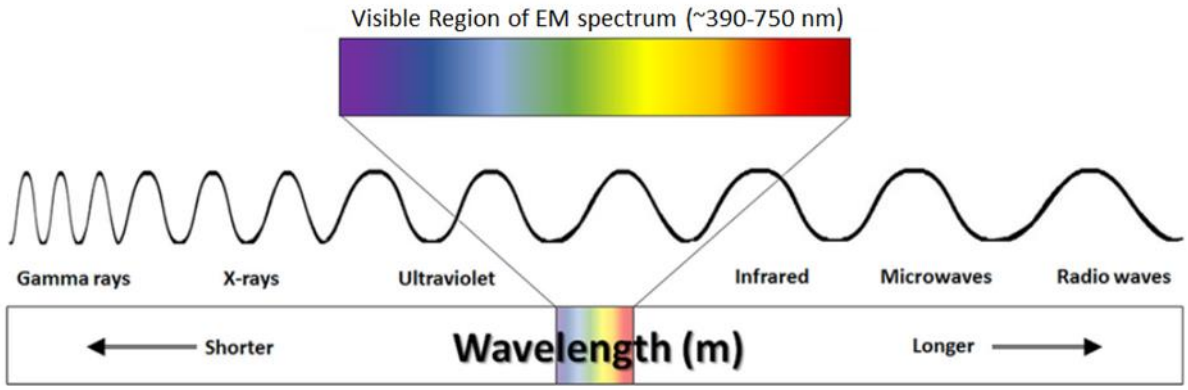

Figure 2. 1: Electromagnetic spectrum emphasizing visible light [9].

Maxwell was able to unify the field of electromagnetism into a set of four differential equations which are known as Maxwell's equations of electromagnetism. These partial differential equations are used to describe light propagation within arbitrary medium and generation from current flow or charge.

$$\nabla \cdot E = \frac{\rho}{\varepsilon_\circ} \tag{2.1}$$

$$\nabla \cdot B = 0 \tag{2.2}$$

$$\nabla \times E = -\frac{\partial B}{\partial t} \tag{2.3}$$

$$\nabla \times B = \mu_\circ (J + \varepsilon_\circ \frac{\partial E}{\partial t}) \tag{2.4}$$

Here $\boldsymbol{E}$ represents the electric field with SI unit volt/m, $\boldsymbol{B}$ is the magnetic field with SI unit Wb/m^2, $\boldsymbol{J}$ is the electric current density with SI unit Amp/m^2, $\boldsymbol{\rho}$ is electric charge density with

SI unit coul/m^3, ε_o is free space permittivity and μ_o is the free space permeability. Equation 2.1 explains that electric charge produces an electric field regardless of its shape or size. Equation 2.2 explains the continuity of magnetic field lines, whereas equations 2.3 and 2.4 correlate electric and magnetic field and their corresponding influences on each other. Also, $\boldsymbol{D} = \varepsilon\mathbf{E}$ and $\boldsymbol{B} = \boldsymbol{\mu}\mathbf{H}$ are called constitutive equations which define the interaction between the medium and electromagnetic field. Here, $\mu = \mu_o \mu_r$ and $\varepsilon = \varepsilon_o \varepsilon_r$ where μ_r is relative permeability and ε_r relative permittivity.

Table 2. 1: Physical significance of Maxwell's equations [10]

Faraday's law	$\nabla \times E = -\frac{\partial B}{\partial t}$	The voltage induced in a close loop is proportional to the rate of change of the magnetic flux through that loop
Ampere's law	$\nabla \times H = J + \frac{\partial D}{\partial t}$	The magnetic field induced around a close loop is proportional to the electric current plus displacement current in that loop
Gauss's law of electricity	$\nabla \cdot D = \rho$	The electric flux leaving a volume is proportional to the charge inside
Gauss's law of magnetism	$\nabla \cdot B = 0$	Total magnetic flux through a closed loop is zero

In time domain, an electromagnetic wave is considered as travelling through source free, linear and isotropic, instantaneous and homogenous medium. In free space *i.e.* containing no charge

and no current, $\boldsymbol{\rho} = 0$ and $\boldsymbol{J} = 0$, [11] application of curl operation on both sides of equation 2.3 as follow:

$$\nabla^2 E = \mu_\circ \mathcal{E}_\circ \frac{\partial^2 E}{\partial t^2} \tag{2.5}$$

As $\frac{1}{\sqrt{\mu_\circ \mathcal{E}_\circ}}$ = c

$$\nabla^2 E = \frac{1}{c^2}\frac{\partial^2 E}{\partial t^2} \tag{2.6}$$

Similarly, by modifying equation 2.4,

$$\nabla^2 B = \frac{1}{c^2}\frac{\partial^2 B}{\partial t^2} \tag{2.7}$$

Equations 2.6 and 2.7 are called wave equations for the wave propagating at speed of light. The simplest solutions to the differential equation 2.6 and 2.7 are sinusoidal wave function. Consider a linearly polarized plane wave travelling in x direction at the speed of light. Electric and magnetic fields are associated with y and z directions respectively. They can be defined as a function of x and t.

$$E(x,t) = E(x,t)j \tag{2.8}$$

$$B(x,t) = B(x,t)k \tag{2.9}$$

Sinusoidal wave functions are the simple solution of partial differential equations:

$$E(x,t) = E_{max}\cos{(kx - \omega t)} \tag{2.10}$$

$$B(x,t) = B_{max}\cos{(kx - \omega t)} \tag{2.11}$$

In the above equation, k is the wavenumber defined as $k = 2\pi/\lambda$, ω is angular frequency, λ is the wavelength. ω/k is equivalent to c (speed of light).

Substituting partial derivatives of $\boldsymbol{E}$ and $\boldsymbol{B}$ into Faraday's law:

$$\frac{\partial E}{\partial x} = -kE \sin(kx - \omega t) \tag{2.12}$$

$$\frac{\partial B}{\partial t} = \omega \sin(kx - \omega t) \tag{2.13}$$

As $$\frac{E}{B} = \frac{\omega}{K} = c$$

From the above equations, the ratio of E and B is equal to the speed of light c (*i.e.* $3 \times 10^8\ m/s$). Pointing vector $\boldsymbol{S}$ is the rate of energy transfer to a unit area of a surface perpendicular to the direction of EM wave propagation and is equal to the cross product of the corresponding electric and magnetic fields divided by the permeability of free space (W/m^2). Intensity of the EM wave can be correlated to the pointing vector as:

$$I = S_{ave} = \frac{{E_{max}}^2}{2\mu_o c} = \frac{{B_{max}}^2}{2\mu_o c} \tag{2.14}$$

Here *I*, being the intensity, which is directly proportional to the average of pointing vector S_{ave}.

2.3 Basic phenomena of light matter interaction

Newton observed that colours are not inherent in objects. Rather, the surface of objects reflects some wavelength of incident light and absorb the rest. Reflected wavelength determines the colour of the object. Thus, the surface of a red object is reflecting the wavelength which is translated as red colour to us and absorbs all the rest. If the object absorbs all the incident light, then it will appear black and if reflects all the light falling on it then will appear white. Red, green and blue are known as additive primary colours, which can combine in balanced amount to produce all other colours including white. Pink colour is produced by mixing up red and violet colours existing on the opposite edges of the visible spectrum. There are two types of photoreceptors in human eyes named as rods and cones.

Rods are active mostly in dim light and transmit black and white information to the brain whereas cones are active in higher levels of intensity. Cones have three different shaped cells each of which is sensitive to short, medium or long wavelengths of the visible spectrum of light. These then in combination send information through nerve cells to brain which further interprets and creates familiar sensation of colour. Visible light belongs to the nonionizing radiation family when incident on a target material and usually undergoes through one of the following interaction mechanisms [12].

2.3.1 Optical reflection

In general, when light bounces from a target surface the phenomenon is called optical reflection as shown in figure 2.2. Law of reflection states that angle of incidence with the surface normal is equal to the angle of reflection [13]. When light is reflected from a smooth and shiny surface like a mirror, the reflection is classified as a specular reflection and if the light is reflected in all directions from a rough surface and could not return all wave-front to one point, this type of reflection is known as diffused reflection [14, 15].

Devices made by joining three mutually perpendicular surfaces as one unit similar to the shape of a corner cube can be used to reflect light directly towards the source i.e. independent from the incidence angle or angle of reflection through total internal reflection mechanism [16]. These types of optical devices are known as retroreflectors and are favourable choices to be used for remote sensing applications. Certain colour dyes reflect more light than other colour dyes e.g. white colour dye reflects most of the light incident on it than any other colour dye. White coloured clothing is most commonly used in summer as white colour reflect most of the incident light bombarded from the sun [17].

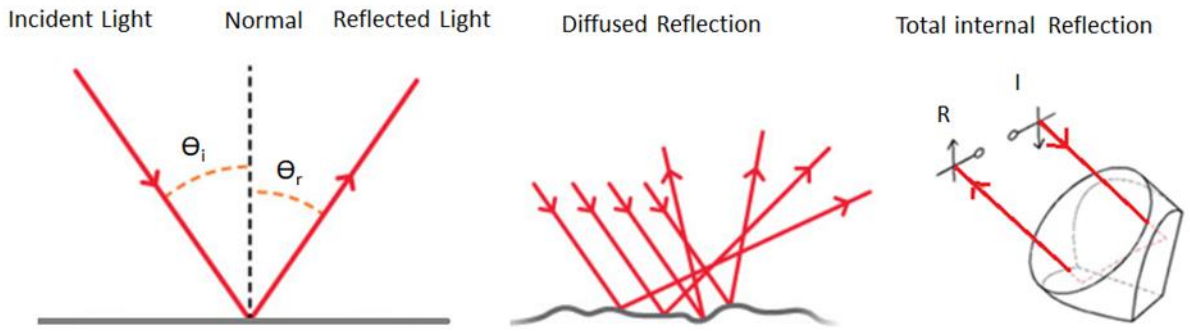

Figure 2. 2: optical reflection from smooth surface, diffused reflection from nonlinear surface and total internal reflection from Cornercube [15].

2.3.2 Optical transmission and absorption

When light falls on a transparent or semi-transparent surface, a beam or a portion of light passes through that object in the same direction as that of the incident beam without undergoing any interactions within the volume of the object. This phenomenon is known as optical transmission [18]. Whereas some part of the or all of the incident beam is absorbed by the atoms or molecules within the volume of object if it matches with target material's energy states , in the case of opaque or semi-transparent objects [19, 20]. The process of the absorbed energy being converted to heat energy is called optical absorption as shown in figure 2.3 [21]. Darker coloured clothing is preferred in the winter as it is able to absorb more incident radiation and help keep the body warm.

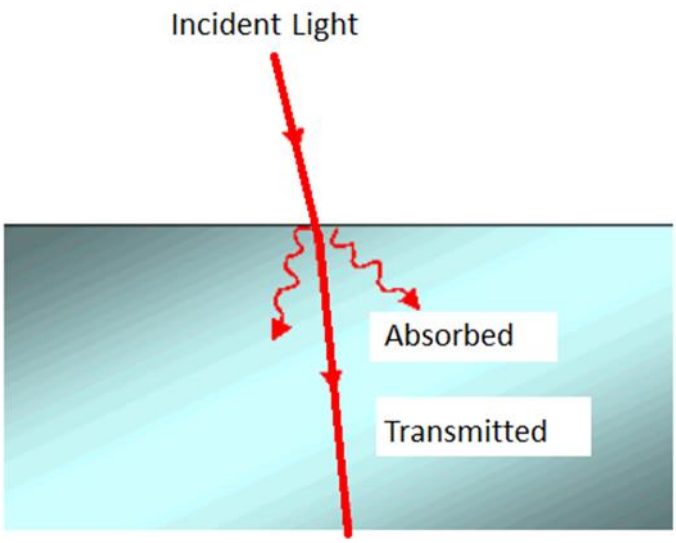

Figure 2. 3: Light absorption and transmission [22].

2.3.3 Light refraction

When light propagates through the interface of two different media, it bends towards or away from the norm i.e. changes its speed due to density difference between two media, this is known as refraction as shown in figure 2.4 [23, 24]. The speed of light ''c'' in vacuum is constant i.e. $3x10^8 m/s$, however light propagates slower through a denser medium [25]. Index of refraction is defined as the ratio of velocity of light of a given wavelength in vacuum to the velocity of light in a substance.

$$\eta = \frac{c}{v} \tag{2.15}$$

Here η is called the index of refraction, c is the speed of light in vacuum and v is the speed of light in any other medium. Index of refraction is also inversely proportional to the wavelength of the light. According to Snell's law:

$$n_i sin\Theta_i = n_R sin\Theta_R \tag{2.16}$$

$$\frac{n_i}{n_R} = \frac{sin\Theta_R}{sin\Theta_i} = \frac{\lambda_R}{\lambda_i} \tag{2.17}$$

Here Θ_i is the incident angle and Θ_R is the refracted angle respectively from the norm. n_i is the refractive index of incident medium through which light is entering the interface of the refracted medium with a refractive index n_R. $\lambda_i$is the wavelength of light in the incident medium and λ_R is the wavelength of light in the refracted medium.

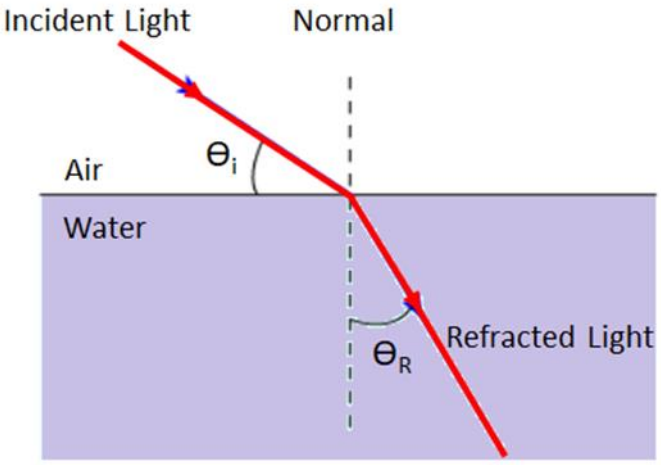

Figure 2. 4: optical refraction of incident light from air (medium 1) to water (medium 2) [26].

2.3.4 Optical diffraction

Bending of light through the corners of a fringe or obstacle to illuminate the shadow region of that obstacle is known as optical diffraction. When incident light of certain wavelength propagates through the aperture or periodic gratings with the comparable size to its wavelength then the interference of light occurs [27]. When two or more waves, interfere with each other in such a way that their crests superimpose on each other they undergo constructive interference; crests not aligned with each other experience destructive interference [28]. In the case of visible light, at the image screen, this combination of constructive and destructive

interference is observed in the form of intensity based well-ordered diffraction pattern as shown in figure 2.5 [29, 30]. The phenomenon is explained by Bragg's law:

$$2dsin\Theta = n\lambda \qquad (2.18)$$

Here n represents the order of diffraction, d is aperture's spacing, λ is the wavelength of incident light and Θ defines the angle of diffraction.

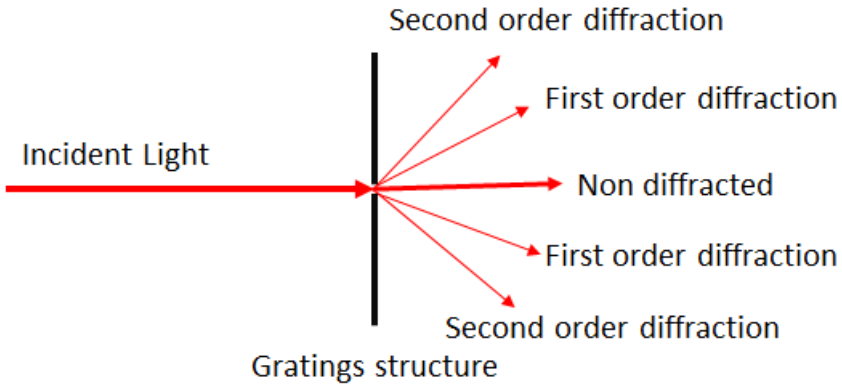

Figure 2. 5: diffraction of light at wide angles during light transmission through a single slit.

2.3.5 Optical scattering and diffusion

Scattering is a process in which a well-collimated incident beam of light is dispersed randomly through the nonuniform structures within the medium as shown in figure 2.6. There can be one or more scattering centers within the medium through which incident light scatters through. The single scattering point often yields a random dispersion of light [31]. Whereas, multiple scattering centers give uniform scattering when averaged and can be modelled to use with diffusion theory [32]. Ordered diffusion is utilised to soften the sharp incident light and disperse along large angles for various optical application [32-35]. When the light propagates through a transparent solid and is scattered by smaller structures compared to the radiation's wavelength then the scattering process is called Rayleigh scattering. The intensity of scattered light I, by a

small sphere of size x, from a light beam of wavelength λ of original intensity I_0 is given by [36],

$$I = I_0 \frac{1+cos^2\theta}{2y^2}\left(\frac{2\pi}{\lambda}\right)^4\left(\frac{n^2-1}{n^2+2}\right)^2\left(\frac{x}{2}\right)^6 \quad (2.19)$$

Here y is the distance from the scattering object and θ is the scattering angle. An average of all angles yields Raleigh scattering cross section. Scattering of light also depends strongly upon its wavelength *i.e.* (λ^{-4}) [37].

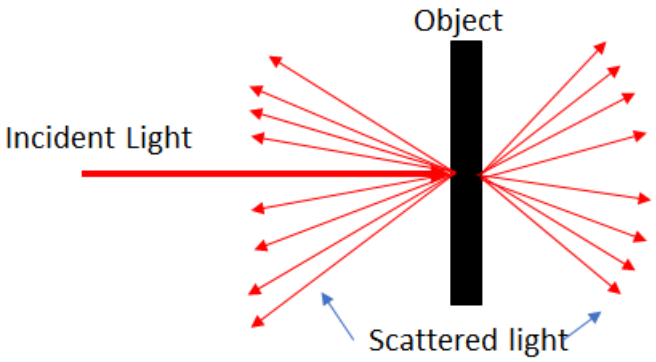

Figure 2. 6: light scattering from an object.

2.4 Basic principles of laser

White light (broadband) is composed of rainbow colours i.e. red, orange, yellow, green, blue, indigo and violet. It can be broken down into its constituents by optical mechanisms of diffraction/refraction. Light of a single wavelength i.e. one colour is called monochromatic light. A laser is an abbreviation of ‘’Light Amplification through Stimulated Emission of Radiation’’. A laser is a source which generates monochromatic light through a mechanism of light amplification via stimulated emission of electromagnetic radiations. In the 1960s the first laser was made operational by Theodore H Maiman since then the laser is being used in optical sensors, holography, material processing, non-destructive testing, spectroscopic

measurements, communications, advanced machining, chemical processing, medical procedures and much more [38-41]. Laser light sources are different from other light sources because they can produce monochromatic, directional and coherent beams of light which can be accurately pointed at a small area (nanometric scale). Laser sources can yield a continuous wave of monochromatic light as well as intense light pulses depending upon the demand [42, 43]. The functioning of a laser is based on stimulated emission, population inversion and optical resonators [44, 45].

Electrons within an atom can acquire certain energy levels [46]. Absorption of a photon (energy) by an electron (atom) occupying ground state can jump into any higher excited state depending upon the absorbed energy by an incident photon [47]. After staying in an excited state for a short period of time (~10^{-8}s), the electron will spontaneously return to the ground state by emitting a photon of energy equivalent to the energy difference between the excited and the ground state [48-50]. This process is known as spontaneous emission and will not contribute to the optical amplification. According to the uncertainty principle, the phase and direction of emitted photons will be random [51-54].

$$\Delta E = E_2 - E_1 = \hbar\omega \tag{2.20}$$

$\hbar$ is the reduced Planck's constant and ω is the angular frequency. ΔE is the energy of an emitted photon. When an excited electron is perturbed with the electric field of a photon of frequency ω, it may decay to the ground state by emitting another photon of same frequency and phase as that of an incident photon maintaining the coherency. Light amplification will occur in this case and the emission is known as stimulated emission. The number of atoms in an excited state should be higher than the number of atoms in the ground state. Otherwise, the system can attain the saturation effect which will stop any further amplification [55-57]. To avoid this saturation effect, instead of two levels system a three level or four level systems are

employed. Lasing material which is pumped by an external source (laser diode, electrical current, flash lamp) to start the amplification process can be in a gaseous or solid state.

Table 2. 2: Demonstrating the specifications operating principles and utilisation of various laser types. [58-63].

Laser type	Wavelength	Pump source	Application
Nd:YAG laser	1064 nm, 532 nm	Flash lamp	Ablation, high power laser
Ruby laser	694.3 nm	Flash lamp	Tattoo removal, ablation
Helium neon laser	632.8	Electrical discharge	Holography, barcode scanning
CO_2 laser	10.6 micrometre	Electrical discharge	Mechanical cutting, direct laser writing
Free electron laser	100 nm- few mm	Electron beam	Medical applications

2.5 Optical and electron microscopy (SEM)

Optical elements are used to magnify objects under observation. Light microscopes are based on a simple optical mechanism in which light is collected from the illuminated object through an object lens to focus on a set of lenses which further magnify and yield an inverted virtual image. Maximum useful magnification obtained by optical microscopy is approximately 1000 times [64, 65]. Conventional bulbs used in OM's emit larger wavelengths and are unable to achieve higher resolutions than 1000 times ($\lambda/2$ limit is reached). For higher resolutions, the

wavelength of incident radiation must be decreased [66]. In scanning electron microscopy, electrons are usually accelerated to higher velocities i.e. higher energies; wavelengths associated with these particles range from 0.027-0.0009 nm [67]. There are many possible interactions between the highly energetic electron beam and the atoms in the specimen. Compton scattering is being the most favored interaction mechanism. Some electrons may transmit through the specimen without having any interactions at all with the target material depending upon the atomic number(Z) and the thickness of the specimen. SEM can provide information on surface topography, crystal structure, chemical composition and electrical behavior of the top 1 mic of the sample under observation. Additional features can be attached to the SEM to get observations under various conditions [68-70].

Electrons gun used in most SEMs consist of a tungsten filament which is heated over $2500°C$ by passing current through it to produce thermal emission of electrons. Electrons can be energized up to $40\ keV$ [71, 72]. This electron beam is then condensed with two or three condensers to convert it into a fine probe, which is scanned on a selective area. The electrons penetrate the specimen in a tear-drop shape volume, whose overall dimensions are determined by the energy of the electron beam, the atomic number of the specimen and the angle at which the electron beam hits the specimen. Penetration power of the electron beam is directly proportional to the energy of the electron beam.

Electrons from the primary beam hit the surface of the specimen and transfer a portion of its energy to the atomic electrons (secondary electrons). If the energy gained by the electron is higher than its shell binding energy, the electron separates from the nuclear field and is considered a free electron. The emitted electrons (secondary electrons) are collected by a secondary electron detector (semiconductors, e.g. Si) which help develop images. Secondary electrons are the basic source of information about the specimens [73, 74].

Electrons from the incident field strike the electrons of the surface atoms of the specimen and are scattered through a large angle. The angle depends on the loss of energy during the interaction (energy transfer). The scattered electrons are then collected by Backscatter detector to deliver the required information through further processing.

Electrons are emitted from a shell after receiving enough energy to leave its shell. K-shell has the highest probability due to its highest cross-section leaving behind a vacancy (hole). The vacancy is filled by an electron from a higher shell i.e. L, M or higher. When an electron from a higher shell jumps down to a lower shell, X-rays are emitted which consists of energy equivalent to the energy difference between two participant shells. These X-rays are used in SEM to perform energy dispersive X-ray analysis, providing information about the chemical composition of the sample [68, 69].

Samples can undergo a charge build-up while being analysed under SEM, e.g ink coated on glass. To overcome this charging effect, a thin layer (10-40 nm) of conducting materials e.g. carbon or gold is deposited on the sample [75].

2.6 Thermochromatic materials

Thermochromatic materials change their colours and optical properties when exposed to different temperatures. Liquid crystals possess the properties of both liquids and crystalline solids i.e. they have flow characteristics as well as structural arrangements. In addition, they exhibit dynamic optical properties. Thermochromatic liquid crystals tune their colour codes at specific temperatures within activation range by selectively reflecting wavelengths of incident broadband light [76]. Molecules in thermochromatic liquid crystals are arranged in regular discreet orders i.e. they have both positional and orientational order [77]. Thermotropic liquid crystals structures can be categorised as smectic and nematic. Nematic liquid crystals have orientational order (the long axes of the molecules are parallel to one another), but do not have

positional order (seemingly random position). Smectic liquid crystals have both orientational order and positional order; the molecules are arranged in discrete molecular layers. The following Figure 2.7 shows the molecular structure of nematic and smectic liquid crystals. The molecules are orientated along the vector ***n***, which are known as 'director' [78-80].

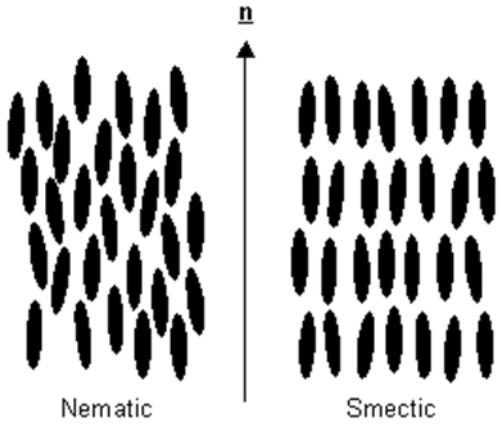

Figure 2. 7: Molecular orientation of nematic and smectic liquid crystals [81].

Nematic liquid crystals are twisted and are highly optically active or non-twisted structural arrangement can be obtained. The twisted nematic structures can perturb the plane of polarized light. Nematic liquid crystals which are optically more active can be further divided into two categories; cholesteric liquid crystals are composed of cholesterol and sterol-based compounds whereas chiral nematic liquid crystals are made from nonsterol-based compounds [81]. Figure2.8 shows the hierarchical classification of liquid crystals.

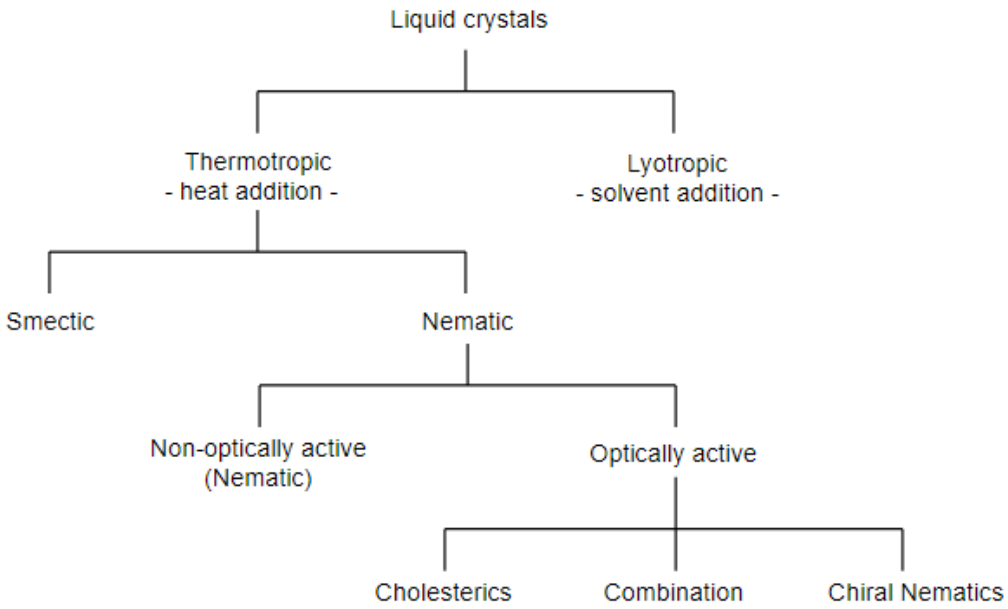

Figure 2. 8: Hierarchical classification of liquid crystals [81].

The molecular structure of chiral nematic liquid crystals consists of twisted thin layers of constituents stacked on top of one another extended in all directions.

Desirable textures are Focal Conic (axes of helical molecules should align parallel to the surface of the substrate) and Planar textures (axes of helical molecules should align perpendicular to the surface of the substrate) [81]. Optical properties of thermochromatic liquid crystals tuned based on temperature variation include birefringence, optical activity, circular dichroism, and diffraction [81, 82].

From the principle of Bragg's scattering, the molecular (constituent) spacing is responsible for observed thermochromatic effect within thermochromatic liquid crystal when altered due to a change in temperature. Bragg's diffraction equation is given as follows [81]:

$$n\lambda = 2d \sin \phi \qquad (2.21)$$

When the pitch length is comparable to the wavelength of incident light within the visible range, specific colours are yielded that vary with thermal condition [81]. Temperature changes

within the activation temperature limits, the orientation of the directional vector in molecular layers changes, which, alters the pitch length and hence the reflected wavelength [83]. Figure 2.9 shows the phase changes and associated colour changing properties of a nematic liquid crystal. Nematic liquid crystals commonly exhibit smectic mesophases at lower temperatures [81].

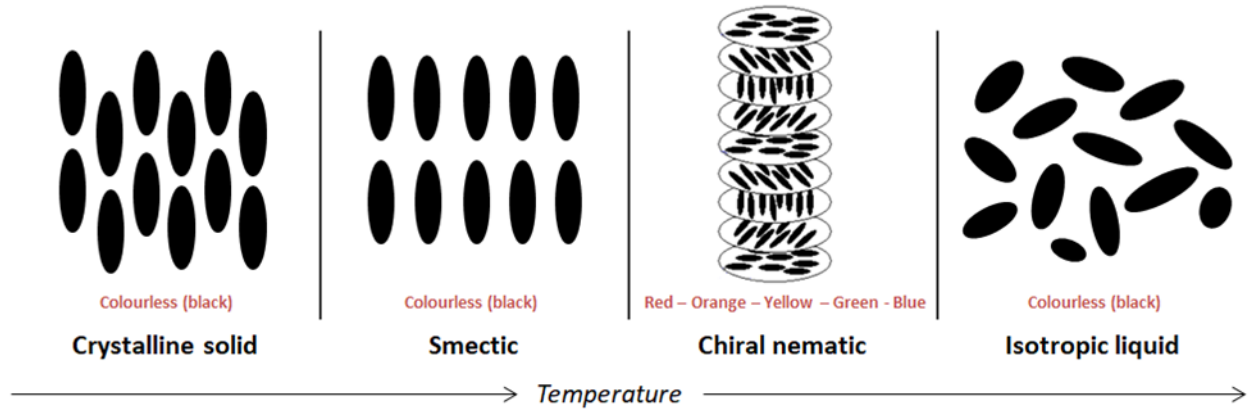

Figure 2. 9: colour changing properties and associated phases of a nematic liquid crystal [81].

Thermochromism is also achieved by using organic dyes. Leuco dye is a dye which can switch in between two chemical forms one of which is colorless [84]. The leuco dye system normally require three components to perform a reversible thermochromatic effect; organic dyes, colour developers, and solvents [85]. Operation procedures of these systems are about temperature-sensitive pH transitions which cause colour transition within leuco dyes [86, 87]. The colour developers are mostly weak acid alkyl-p-hydroxybenzoates, bisphenol A, 1,2,3-triazoles, or 4-hydroxycoumarin, which dissociates incompletely within solution by releasing only a few of their hydrogen atoms causing a reversible colour change. It is the pronation and subsequent ring opening of the lactones by the weak acid colour developer that causes reversible colour transition of the leuco dye as shown in figure 2.9A [80].

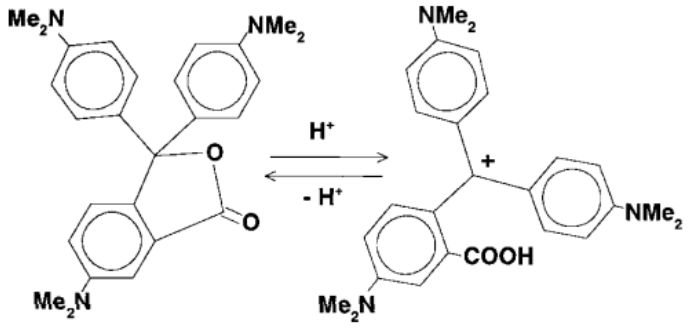

Figure 2.9A: Crystal violet lactone changes from colourless to coloured when combined with a weak acid [80].

The co-solvents are typically alcohol, ester or amide, whose melting point controls the colour change at specific temperatures [85, 88]. The co-solvents are typically alcohol, ester or amide, whose melting point controls the colour change at specific temperatures. The leuco dye system contains, leuco dye, colour developer and solvent as a combination. At lower temperatures, the solvent is in a solid state in contact with a leuco dye and weak acid, yielding coloured compound. As the temperature rises above the melting point of co-solvent, the colour producing components come apart and the compound appears colourless [89]. Microencapsulation is also utilised to encapsulate a combination of different dyes to generate a range of colour at various temperatures and to protect leuco dyes from harsh environment [85].

2.7 Light absorbing materials, replication and mechanical properties

Light absorbing materials absorb incident light and convert it into thermal energy. Examples include ink pigments, metallic films, dyes, etc. Semi-transparent and opaque materials/optical devices are most commonly used materials as light absorbers to deduct energy from incident light and convert it into heat. When laser beams of sufficiently higher energies are directed towards the localised area the energy is absorbed within the molecules of the target material

for a short period. The energy is released as heat and can vaporise the material at the focused area. This process is known as laser ablation [90]. Materials which have the ability to replicate the surface nanostructures successfully without any major changes in the dimension of the original structures from the stencil are known as replication materials e.g. gelatines and polymers. The process is known as surface stamping or embossing [91]. Stress is the minimum force required to create strain within a region of interest. Stress at micro or macro levels could be applied due to different forces such as mechanical, thermal, chemical or ph changes which can create a reversible/irreversible change in the dimensions. The strain is known as the degree of change in the dimensions of a given specimen under applied stress e.g. if a force is applied to create change in length then the strain will be the ratio of change in length and original length [92-95]. Mathematically,

$$\sigma = \frac{F}{A} \tag{2.22}$$

$$\varepsilon = \frac{\Delta L}{L} \tag{2.23}$$

Here σ represents stress, F is applied force on area unit area $A$and ε is strain created within the specimen. Young's modulus is defined as the ratio of stress to strain and is mathematically given bellow:

$$\acute{E} = \frac{\sigma}{\varepsilon} \tag{2.24}$$

Where É is the ratio of applied stress and corresponding strain and is called Young's modulus. Materials behave to the applied stress according to their mechanical properties such as elasticity i.e. whether they are brittle (glass) or ductile (polymers).

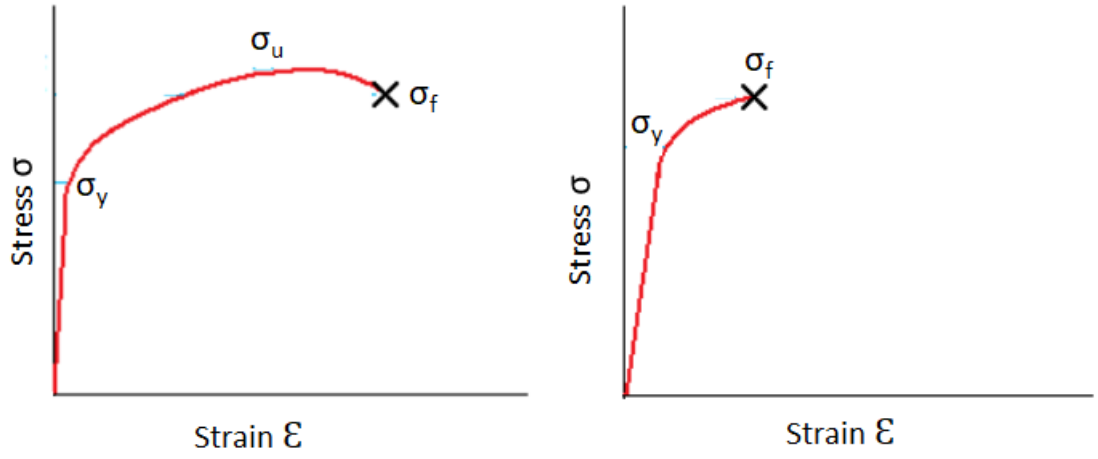

Figure 2. 10: showing ductile and brittle behaviour under stress application [96].

In fig. 2.10 σ_y is yield stress, σ_u ultimate stress and σ_f fracture stress. Both kinds of materials do not show any strain before the applied forces cross the threshold. However above the corresponding threshold stress, ductile materials show both elastic and plastic deformation whereas brittle materials do not experience considerable deformation and break down (mechanical failure) suddenly as soon as elastic deformation starts [95, 97].

2.8 Classification of holographic lithography

Amplitude holograms are recorded by the light interference between reflected beam from the object and a reference beam within varied absorption coefficient of recording media. While the phase holograms are recorded when thickness variation of recording media occurs. In volumetric holograms the diffraction pattern is recorded inside the volume rather than on surface [98].

Laser interference based lithography in Denisyuk reflection holography mode is convenient to use, simple and more productive laser ablation technique as it does not require extensive laser tuning of laser beams or attachment with expensive equipment. This technique requires an

extended laser beam which passes through the semi-transparent recording media kept on axis and records information from the object to be copied in the wave front. Interference occurs between the antiparallel waves propagating in opposite direction of recording media to create standing wave effects. Copied information is then recorded within the light absorbing material in the form of periodic gratings by means of ablation. Recorded hologram has no physical resemblance with the original object but carries the optical properties of the object [99]. Interference pattern originated by the simple mirror yields simple diffraction gratings and hence simple diffraction pattern whereas, interference caused by phase conjugate mirror will yield the phase conjugate structures which on illumination with monochromatic light yield phase conjugate diffraction pattern on image screen [100]. whole event is then replayed by illuminating the recorded hologram with reading beam and virtual image is viewed by the observer on the image screen kept on the other side of the hologram. Reflection holography are used to generate various nanophotonic devices due to their lower dispersion and supress conjugate images.

Whereas, in transmission holography both waves interfere from the same side of the object to produce standing wave. Object and laser waves are off axis of the recording medium. Virtual image of the copied object is then viewed from the same side of the observer and reading wave under illumination. Transmission holography is often used to recorded holograms on the opaque photosensitive materials and have applications in identity cards and currency notes etc. Due to of axis geometry the transmission holograms can separate conjugate images but cannot supress them completely. Higher light dispersion of transmission holograms as compared to reflection holograms limits their use.

2.9 Holographic recording via laser interference-based lithography

Holograms made via laser beam interference-based ablation use two coherent beams to record a hologram within a substrate [100]. One beam scatters/reflects from the object to be copied and travels towards the recording medium while the second beam is a reference beam which interferes with the first beam and creates an interference pattern at the recording media. The recorded holograms are in the form of periodic gratings depending upon constructive/destructive interference pattern and have no physical resemblance with the original object [99, 101]. When these holographic gratings are illuminated with the monochromatic or broadband light sources often called reading beam, then copied object is displayed at the far field (image screen) depending upon the dimensions of the recorded gratings. The word hologram is referred to both physical structures as well as to the resulting diffraction pattern. The holography is the process of coding and decoding information where the whole recorded event can be replayed by simply shining any small part the recorded film with a light source [102]. Consider a holographic plane $x - y$ of the hologram Ħ; the respective reference wave can be expressed as

$$A_a(x, y) = A_{a1}\cos\left[2\pi\omega t + \phi(x, y)\right] \tag{2.25}$$

Here A_{a1} is the amplitude of reference beam, ϕ is the phase term as function of position with respect to holographic plane. The reflected wave from an object S is defined as,

$$A_s(x, y) = A_{as}\cos\left[2\pi\omega t + \phi_s(x, y)\right] \tag{2.26}$$

The reflected wave will store information about the object S, encoded in spatial variation of a wavefront. Holographic laser writing process involves superimposition of $A_a(x, y)$ and $A_s(x, y)$ to irradiate photosensitive material. Hence, the reconstructing wave and resulting irradiance could be mathematically defined as,

$$A_R(x, y) = A_{aR}\cos\left[2\pi\omega t + \phi(x, y)\right] \tag{2.27}$$

$$I(x,y) = |(A_R + A_s)^2|_T = \frac{A^2{}_{aR} + A^2{}_{as}}{2 + A_{aR}A_{as}\cos(\phi - \phi_a)} \quad (2.28)$$

Information about the object is given in the above equation where both phase and amplitude modulated from the position dependency for $\phi_s(x,y)$ and $A_{as}(x,y)$. Amplitude of transmission profile during wavefront reconstruction is considered to be proportional to irradiance, $I(x,y)$. The final resulting wave is directly proportional to the product of irradiance and reconstructing wave,

$$A_F(x,y) = \frac{A_{aR}(A^2{}_{a1} + A^2{}_{as})cos[2\pi\omega t + \phi(x,y)] + A_{aR}A_{as}A_{a1}\cos[2\pi\omega t + 2\phi - \phi_a]}{2}$$

$$+ \frac{A_{aR}A_{as}A_{a1}\cos[2\pi\omega t + \phi_a]}{2} \quad (2.29)$$

Here the first term represents the modulated amplitude of the reconstructed beam. Any part of the recorded hologram in the form of diffraction gratings can replay the whole event. Zero-order of the diffraction order represented by first term carries no information about the object phase. Next two diffracted orders represented by second and third terms yielded from summation and difference carry both phase and amplitude information of the object [101].

2.10 Laser ablation in Densyuk reflection holographic mode

When two coherent laser beams interfere with each other in space, they can add up or cancel out depending on whether they interfere constructively or destructively. If the crests of both beams are superimposed on each other, the interference is called constructive interference otherwise they will undergo destructive interference. A standing resultant wave is obtained which can carry sufficiently high enough energy to ablate the target material placed on the path of its propagation. The interference pattern can then be recorded within the target substrate. The region exposed to the constructive interference part of the wave (crest) will be ablated whereas the region which comes across the destructive part of the wave (trough) will stay intact,

resulting in a well-ordered diffraction pattern recorded within the substrate. The recording medium used can be in the form of absorbing inks, dyes, polymers or films based on metallic nanoparticles e.g. gold. Energy transferred by the standing wave to the light absorbing materials results in localised heat generation which vaporises the material instantly. Materials exposed to the nanosecond laser pulses of high energy can be melted and vaporised without an interference pattern [28]. Selection of ablation pattern is dependent on the incident laser beam energy, the distance between the recording media and the object, exposure angles and, the wavelength of the incident laser [28, 99].

Laser ablation as being the backbone of many research and developments in the fields like metallurgy and material science, laser-based holographic techniques, and medical procedures. Nanosecond pulsed laser ablation is of great importance for material processing including metals and non-metals (bulk and thin film) due to cost effectiveness, efficient pulsed laser sources [103, 104]. The process of material removal from the target due to the highly intense ns laser beam is considered as vaporization/phase explosion and can be considered a thermal process [104]. A pulse duration of ns laser is higher than phonon-electron relaxation time in the target material which is of the order of picosecond in gold [105]. Intense standing waves caused by interference of incident and reflected ns beams interact within the light absorbing material by transferring its energy to the atoms/electrons of the target material. The localised surface under focus may be heated above the critical temperature i.e. well above the boiling temperature e.g. gold has critical temperature 6977 °C and boiling temperature 2700 °C [105]. The material is melted and vaporised as a function of heat and pressure.

In the event of sufficient laser fluence, the surface temperature of the target material may reach 80% of critical temperature i.e. for gold 5581°C causing a transition in optical and electrical properties of the material, hence light absorption falls [106]. However, upon additional absorption of energy from laser beam, the localised temperature approaches 90% of critical

temperature resulting into formation of more bubbles, yielding into the ejection of material as liquid droplets and vapor by explosive boiling, or phase explosion [107].

Laser ablation through reflection holography has been extensively used to fabricate phase conjugate diffraction gratings, diffusers and lenses [108]. laser ablation is a thermal process through which material is selectively evaporated from the surface of the stencil by rapid deposition of energy carried by laser beam. Laser ablation process is similar to the photolithography however photolithography needs lower fluence than laser ablation to overcome threshold energy for ablation [106, 109].

Laser interference-based lithography is influenced by laser characteristics, object to be copied, exposure angle, exposure distance, recording media and sample location from focal plane. Nanofabrication through laser ablation is still under continues research through different parameters manipulation and for patterning many different materials include ink, gold, gelatine and soft polymers. Laser ablation-based holography utilises the interference of two or more coherent beams to record holograms in light sensitive media. Surface stamping is perhaps the most commonly used technique to transfer nanostructures from the stencil to the target surface include gelatines and soft polymers [110, 111]. Photopolymers and photoresists have been used to record holograms in classical holography, however process is costly and time consuming. FIB milling and e-beam lithography are also used to prepare master surfaces which are further used for surface stamping [112, 113]. Both methods need expensive equipment, expertise dependent, time consuming and have low throughput [114, 115]. To overcome these challenges laser ablation-based lithography has been employed to create nanostructures with in conductive, nonconductive, soft polymers, gelatines and ink dyes. Pulsed laser of sufficient high energy (100-300 mJ/cm^2) is required to ablate the target material is used to structure a wide range of materials with different optical properties. dimensions of fabricated structures are comparable to the wavelength of the light used. Sizes of the structures may vary from half

of the wavelength of the light used to the five times of the wavelength. depending on adjustments of provided parameters (exposure angles and working distance).

Consider an arbitrary wave with amplitude (A), wavelength λ and angular frequency V, propagating in x-direction,

$$E_i = Acos2\pi(Vt - \frac{x}{\lambda}) \quad (2.30)$$

Reflected wave from the object will be,

$$E_r = Acos2\pi(Vt + \frac{x}{\lambda}) \quad (2.31)$$

Standing wave caused by interference of both waves

$$E_i + E_r = Acos2\pi(Vt - \frac{x}{\lambda}) + Acos2\pi(Vt + \frac{x}{\lambda}) \quad (2.32)$$

$$= \left|2Acos2\pi\frac{x}{\lambda}\right| cos2\pi Vt \quad (2.33)$$

Total interference occurs between two or more waves due to overlapping in the optical paths [102]. Net electric field at a point r is the sum of all electric fields involve at time t,

$$E(r,t) = E_1(r,t) + E_2(r,t) + \cdots + E_n(r,t) \quad (2.34)$$

I being the interference intensity is the absolute square of net electric field,

$$I = \sum_{i=1\ldots n}|E_i(r,t)|^2 \quad (2.35)$$

Between minimum and maximum electric field values the intensity distribution shows the net electric field variation from point to point. Maximum intensity occurs during constructive interference whereas minimum intensity is shown during the event of destructive interference. This periodic intensity distribution is directed to the light absorbing media to be structured. Electric field vector of multibeams laser light is given by,

$$E_m = E_m u_m \exp\left[i(K_m r - \omega t + \varphi_m)\right] \quad (2.36)$$

Here, E_m is Amplitude, u_m unit polarisation vector and φ_m is phase of the mth wave. Total intensity distribution is given by,

$$I = \sum_n E_n^2 + 2\sum_{n<m}^{N} E_{nm}^2 u_{nm}^2 \cos\left[k_{nm} r + \varphi_{nm}\right] \quad (2.37)$$

Here $E_{nm}^2 = |E_n E_m|$, $K_{nm} = K_n - K_m$, $\varphi_{nm} = \varphi_n - \varphi_m$ and $u_{nm} = |u_n u_m|$. Periodicity of the recorded gratings depends upon phase, amplitude, wave vector and polarisation difference between waves [116].

2.11 Phase conjugation as real time holography

Optical Phase Conjugation (OPC) is a complex phenomenon of a photorefractive medium in which a Phase Conjugated Wave (PCW) is generated [117]. The PCW is the reverse phase of an electromagnetic field at every point as compared to incident light [118]. It has applications in optical tomography, interferometry, near-field microscopy, wavefront correction, imaging, and biochemical sensing [118-121]. The PCW can be generated via three major mechanisms. The first method involves four-wave mixing process; the second technique is based on various backward simulated (Brillouin, Raman, Rayleigh-wing or Kerr) scattering processes; and the third method is pivoting on single/multi-photon pumped backwards stimulated emission process (lasing). There is a common physical mechanism among all three techniques which plays the same vital role in generating backwards phase conjugate beam which is based on optical nonlinearity [122-126].

To discuss the formal analogy between conventional holography and four-wave mixing, consider the process of hologram recording and reconstruction by interference between a reference beam A_r and reflected beam from the object A_o. The resulting transmission function is then given by [127],

$$T \propto (A_o + A_r)+(A_o^* + A_r^*)=|A_o|^2+|A_r|^2+ A_o A_r^*+ A_o^* A_r \quad (2.38)$$

A_r (x,y) and A_o (x,y) denote the complex amplitudes of the reflected and reflected from the object fields, respectively, in the hologram plane $z = 0$. Recorded hologram is then illuminated with a reading beam A_R imposing from the opposite direction of reference beam Ar *i.e.* $A_R = A_r^*$. Thus, the diffraction field A_d which is recorded at image screen opposite to the reading beam A_R is given,

$$A_d = T A_R = (|A_o|^2+|A_r|^2+ A_o A_r^*+ A_o^* A_r)A_r^* \quad (2.39)$$

$$=(|A_o|^2+|A_r|^2) A_r^*+(A_r^*)^2 A_o+|A_r|^2 A_o^* \quad (2.40)$$

In equation first term on the right side is proportional to the incident field $A_R = A_r^*$. The second term $(A_r^*)^2 A_o$ in a thick hologram will have a phase factor $exp\ [-i(2k_r - k_o).r]$ and is thus phase mismatched, *i.e.* will not radiate. The third term, at $z < 0$ is related to a time-reversed phase conjugate hologram of the object field A_o.

To establish the formal analogy between phase conjugation and holography can be established by exploring the possibility of application of four-wave mixing to conventional holography. In conventional holography, spatial filtering, convolution and correlation in the focal plane of suitably placed lenses [127-129]. It can be extended to the same line of reasoning by nonlinear experiments in which the holographic films are replaced by nonlinear optical media to find possibility of many useful applications.

2.12 Optical structures and displays

Surfaces which can manipulate incident light by changing the plane of polarised light, diffraction, scattering, reflecting or absorbing are called optical elements. Optical structures are often in nanometric scale i.e. comparable to the wavelength of the visible region of EMS. These structures could be diffraction gratings, diffusing surfaces, micro-lenses,

retroreflectors/reflectors, or polariser etc. Holographic structures are fabricated/copied from the original optical elements onto a substrate via replication or laser ablation. On illumination, the optical response from these holographic structures can be displayed at the image screen in the form of a diffraction pattern, diffusion field or any other shape depending on the structure. Due to their compactness and cost-effectiveness, holographic optical structures are being used in many optical applications as they can replace the master surface and can help develop more advanced novel optical devices. Some methods which have potential to perform nanofabrication include e-beam lithography (focussed beam of electrons is used to draw customised patterns onto an electron sensitive film) [130, 131], and ion beam lithography (scanning of a beam of ions to create desirable nanopatterns onto a surface) [132, 133]. Both methods require expertise, and expensive equipment and are also time-consuming hence cannot be used for mass production [115, 134, 135]. Direct laser writing function is the continuous focus of a highly energetic beam of the laser on a target substrate to generate optical structures via direct ablation of the material. Size of the fabricated structures is limited to the spot size. Surface imprinting or embossing is a technique to replicate nanostructures from any stencil in contact with the replication material such as polymers. The technique is limited to ductile materials as replication cannot be performed on brittle materials. Dimensions of the replicated structures stay permanent and are comparable to the master surface. Laser interference-based ablation in Denisyuk reflection mode is also used to engineer nanopatterns in light absorbing films coated on various substrates. This technique provides many parameters which can be adjusted to control the size of optical structures, flexibility in the choice of material, are easy to operate without exhausted laser alignment. The technique is also speed and cost-productive.

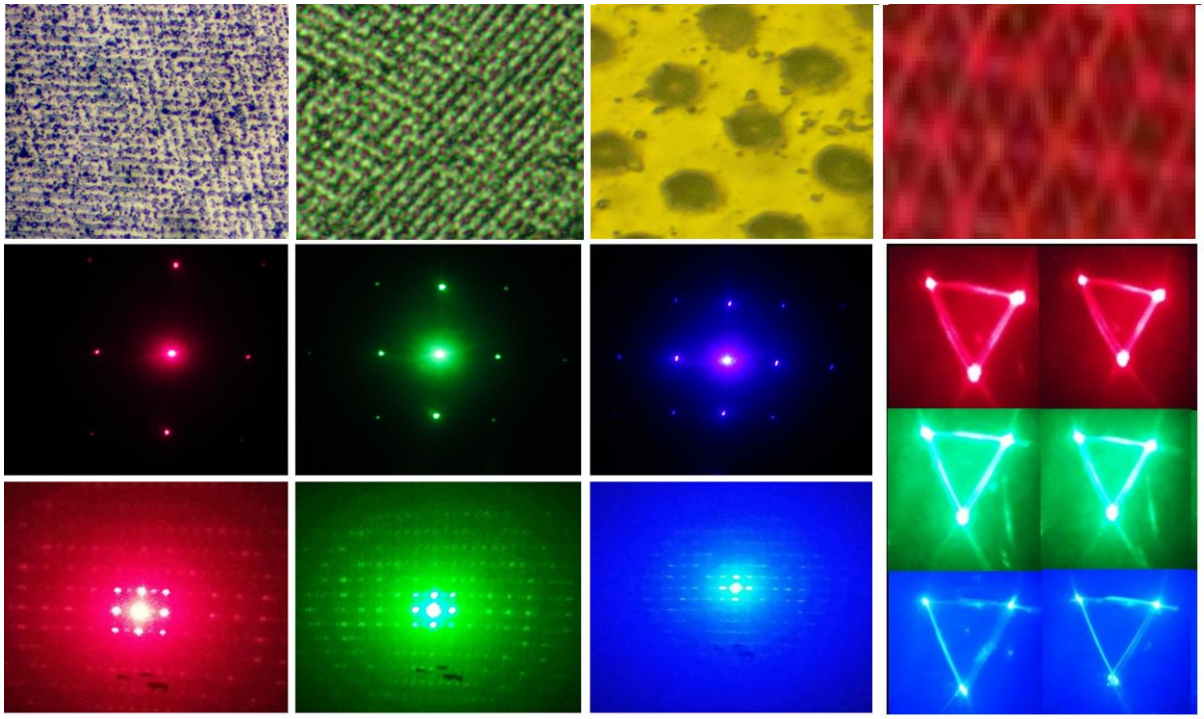

Figure 2. 11: Various optical structures and their resulting pattern under illumination.

The word hologram refers to both physical structures and the resulting diffraction pattern. Holographic displays functioning in a reflection mode are more useful in various applications such as remote sensing, where flexible holographic structures fabricated within the sensitive medium are stacked within distant objects or human restricted areas to monitor environmental conditions via tuned optical response in the form of reflected pattern based on external stimuli. However, holograms functioning within transmission mode are also important for applications such as data storage, displays, communications and decoration.

2.13 Computational and numerical modelling

Different numerical methods are used to solve problems related to electromagnetic radiation propagation, sound waves, fluid dynamics and heat-transfer. The solution of numerical methods are based on partial-derivatives of Maxwell equations [136]. Most popular numerical methods to solve electromagnetic problems are [137]:

1. Finite Element Method (FEM)
2. Finite Difference Time Domain Method (FDTD)
3. Finite Difference Method (FDM)
4. Finite Volume Method (FVM)
5. Method of Lines (MoL)
6. Plane Wave Expansion Method (PWEM)
7. FMM (Fast Multipole Method)

FEM is a numerical method to approximate numerical solutions based on boundary value problems. FEM also is known as a finite element analysis (FEA), where a large problem is divided into small problems to get an approximate solution. The approximate solution is based on a combination of the elementary functions known as basic functions. FEM is based on one/two/three-dimensional (1/2/3D) meshing elements. FEM is considered as a boundary value problem based on a mathematical model (e.g. differential equations) to deceive physical behaviour in a certain domain (e.g. waveguide) [136].

FDTD is a differential method based on time-dependent Maxwell equation to get the solution of a numerical problem. FDTD is based on grids or Yee cells and the partial derivative of Maxwell equations and is used to discretise the grids into the time and space-domain. During FDTD simulations, electric-field components are discretized in space-domains and then followed by magnetic field components discretized in time-domain. FDTD simulations are limited with thinner and longer structures [138].

FDM is a numerical method which is based on a simulation domain and differential equations. The derivative approximation is based on the discretization of finite difference equations.

Numerically approximate solutions are based on discretization errors. Step size and discretization equations are the main criteria of simulation quality and duration. Generally, larger steps reduce simulation period however produce simulation instability and reduce data quality [139].

FVM is based on algebraic equations and solution approximations found through the evaluation of differential equations. The meshed geometry is used to calculate discretise volume while the divergence theorem is used to convert volume integrals into surface integrals. FVM is widely applied in fluid dynamics [140].

MoL is an initial value problem based on volume discretization with at least one domain. During simulation, only spatial derivatives discretise and time variables remain continuous [141]. Solution approximations are based on independent variable approximation through one or more differential equations. Finite difference, finite elements, or Fourier series approximation can be used to approximate solution of MoL [142].

PWE is computational technique to solve Maxwell's equations by formulating a characterictic vector (eigenvalue) problem from the equation. PW are solutions to homogeneous Helmholtz equation, which represent EM field in the periodic medium [143]. PWE provide precise solutions and is well established technique to the modal solution problem. Appearance of spurious modes and large problem scaled make this technique time consuming and complex in terms of memory requirement as compared to FDTD and FEM which are model transients and simpler [144].

FMM is most popular numerical technique in computational electromagnetics based on integral-equation group whereas FDTD and FEM are the mostly used for partial differential equation group. FMM relies on the application of discrete form of integral equations (on the surfaces of the geometries) [145]. FMM is based on the iterative solution of linear system and

provides an accurate calculation of the matrix vector multiplications as required by solver. It improves memory requirement and processing time and enables to solve larger problems [145].

Through computation modelling, the most suitable method selected will need to be considered using the advantages and disadvantages of all available methods.

Numerical techniques for electromagnetics are generally characterised into two categories: partial differential equation and integral equation techniques. FDTD and FEM are the most popular and well-established techniques for partial differential equation [146]. FEM is capable to handle complex geometries as compared to FDTD. FEM is more suitable method to describe complex geometries and to interpret the maps of the fields, whereas FDTD is utilised in the case of large number of wavelengths, non-regular and non-Cartesian mesh refinement [147]. FDM is older method and is faster than FEM but has limited features and provides less accuracy, whereas FEM provides higher order of accuracy and is more demanding on the mesh quality. FVM and FDM provide discreet solution whereas FEM provides continues solutions.

FEM is fast in terms of modelling different designs and materials through software, can solve the problems with higher degree of accuracy, useful for time/frequency dependent simulations and provides boundary conditions (point forces, distributed forces, thermal effects) utilisation to define the model needs to respond. Therefore, FEM was used to perform computational modelling of diffraction optical structures. COMSOL Multiphysics software is a commercially available software based on FEM has been used for optical modelling. It is a user-friendly, simple, easy-going graphical tool to model optical structures, small scale diffractive optical devices. It consists of features such as 2D/3D modelling, user-defined variable, material selection, customized or variable grid/mesh size, time/frequency domain accurate results analysis with smaller time periods.

FEM was used to perform computational modelling of diffraction optical structures. COMSOL Multiphysics software is a commercially available software based on FEM has been used for optical modelling. It is a user-friendly, simple, easy-going graphical tool to model optical structures. FVM and FDM provide discrete solutions, while FEM provides a continuous solution (up to a point). It consists of features such as 2D/3D modelling, user-defined variable, material selection, customized or variable grid/mesh size, time/frequency domain accurate results analysis with smaller time periods. The approximate solution in FEM is based on the combination of elementary functions, which are known as shape or basic function.

The approximate solution in FEM is achieved by the combination of shape or basic functions (elementary function). Mathematical problem (differential equations) describes a boundary value problem, which is related to physical behaviour (EM field) in a certain domain *D* (e.g. a photonic crystal, a waveguide) [136].

$$\Delta U = N \qquad \text{in} \qquad D$$

$$U|_{\partial D} = U_o$$

Here, Δ is differential operator, N is known function and U is unknown function. In 2D FEM, triangular finite element are simplest elements and are proposed for continuous problems as other elements can be produced from triangular elements. Basis function for triangular meshing will be $e_i(x_i , y_j)=1$ if $i \neq j$ and $e_i(x_i , y_j)=0$ if $i=j$.

Grid size is defined in pre-processing stage. 2D/3D geometry is created by CAD, geometry is simplified to reduce complexity during meshing by eliminating unimportant features. Geometric parameters/structures can also be exported from external source. Characteristics of the material are defined. Meshes are introduced to CAD geometry in order to produce smaller segments. Processing time and order of accuracy depends on mesh orientation and size.

Processing speed can be improved by introducing larger mesh sizes at the compensation of accuracy. Loads and constraints are applied by defining boundary conditions. A field quantity is incorporated, which can interpolate over entire meshed structure by integrating elements together in order to form individual polynomial for every single meshing element and to share degree of freedom to neighbouring nodes. Each node forms a set of algebraic equations instead of algebraic equation for whole geometry. for linear systems, Ac=b, where A and b are stiffness matrix and constant. Solution of linear system gives unknown variable at nodes, $c=bA^{-1}$. Post processing stage provides results which can be viewed and analysed. In the case of unsatisfied results mesh formation is performed and the process is repeated until the desired results.

References (ii)

1. Bushberg, J.T. and J.M. Boone, *The essential physics of medical imaging*. 2011: Lippincott Williams & Wilkins.
2. Poletti, F., et al., *Towards high-capacity fibre-optic communications at the speed of light in vacuum.* Nature Photonics, 2013. **7**(4): p. 279.
3. Brongersma, M.L., J.W. Hartman, and H.A. Atwater, *Electromagnetic energy transfer and switching in nanoparticle chain arrays below the diffraction limit.* Physical Review B, 2000. **62**(24): p. R16356.
4. Budden, K.G., *The propagation of radio waves: the theory of radio waves of low power in the ionosphere and magnetosphere*. 1988: Cambridge University Press.
5. Asahi, R., et al., *Visible-light photocatalysis in nitrogen-doped titanium oxides.* science, 2001. **293**(5528): p. 269-271.
6. Ma, S.-H., et al., *Aqueous pigmented inks for ink jet printers*. 1992, Google Patents.
7. Vukusic, P., J. Sambles, and C. Lawrence, *Structural colour: colour mixing in wing scales of a butterfly.* Nature, 2000. **404**(6777): p. 457.
8. Giannakis, S., et al., *Solar disinfection is an augmentable, in situ-generated photo-Fenton reaction—Part 2: A review of the applications for drinking water and wastewater disinfection.* Applied Catalysis B: Environmental, 2016. **198**: p. 431-446.
9. Giannakis, S., et al., *Solar disinfection is an augmentable, in situ-generated photo-Fenton reaction—part 1: a review of the mechanisms and the fundamental aspects of the process.* Applied Catalysis B: Environmental, 2016. **199**: p. 199-223.
10. Ranada, A.F., *Knotted solutions of the Maxwell equations in vacuum.* Journal of Physics A: Mathematical and General, 1990. **23**(16): p. L815.
11. Yee, K., *Numerical solution of initial boundary value problems involving Maxwell's equations in isotropic media.* IEEE Transactions on antennas and propagation, 1966. **14**(3): p. 302-307.

12. Hori, M., et al., *Lethal effects of short-wavelength visible light on insects.* Scientific reports, 2014. **4**: p. 7383.
13. Tomlin, S., *Optical reflection and transmission formulae for thin films.* Journal of Physics D: applied Physics, 1968. **1**(12): p. 1667.
14. Torrance, K.E. and E.M. Sparrow, *Theory for off-specular reflection from roughened surfaces.* Josa, 1967. **57**(9): p. 1105-1114.
15. Sillion, F. and C. Puech. *A general two-pass method integrating specular and diffuse reflection*. in *ACM SIGGRAPH Computer Graphics*. 1989. ACM.
16. Scholl, M.S., *Ray trace through a corner-cube retroreflector with complex reflection coefficients.* JOSA A, 1995. **12**(7): p. 1589-1592.
17. Matsuoka, L.Y., et al., *Clothing prevents ultraviolet-B radiation-dependent photosynthesis of vitamin D3.* The Journal of Clinical Endocrinology & Metabolism, 1992. **75**(4): p. 1099-1103.
18. Marcuse, D., *Light transmission optics.* 1972.
19. Aydin, K., et al., *Broadband polarization-independent resonant light absorption using ultrathin plasmonic super absorbers.* Nature communications, 2011. **2**: p. 517.
20. Huang, K. and A. Rhys, *Theory of light absorption and non-radiative transitions in F-centres*, in *Selected Papers Of Kun Huang: (With Commentary)*. 2000, World Scientific. p. 74-92.
21. Dyer, P. and J. Sidhu, *Excimer laser ablation and thermal coupling efficiency to polymer films.* Journal of applied physics, 1985. **57**(4): p. 1420-1422.
22. Henderson, G.R. and D.A. Grafton, *Method and apparatus for measuring light reflectance absorption and or transmission*. 1975, Google Patents.
23. Xu, Q., et al., *Experimental demonstration of guiding and confining light in nanometer-size low-refractive-index material.* Optics letters, 2004. **29**(14): p. 1626-1628.
24. Aieta, F., et al., *Out-of-plane reflection and refraction of light by anisotropic optical antenna metasurfaces with phase discontinuities.* Nano letters, 2012. **12**(3): p. 1702-1706.
25. Hau, L.V., et al., *Light speed reduction to 17 metres per second in an ultracold atomic gas.* Nature, 1999. **397**(6720): p. 594.
26. Yu, N., et al., *Light propagation with phase discontinuities: generalized laws of reflection and refraction.* science, 2011. **334**(6054): p. 333-337.
27. Klein, W. and B.D. Cook, *Unified approach to ultrasonic light diffraction.* IEEE Transactions on sonics and ultrasonics, 1967. **14**(3): p. 123-134.
28. Yetisen, A.K., et al., *Light-directed writing of chemically tunable narrow-band holographic sensors.* Advanced Optical Materials, 2014. **2**(3): p. 250-254.
29. Stover, J.C., *Optical scattering: measurement and analysis*. Vol. 2. 1995: SPIE optical engineering press Bellingham.
30. Harvey, J.E., A. Krywonos, and J.C. Stover. *Unified scatter model for rough surfaces at large incident and scatter angles*. in *Advanced Characterization Techniques for Optics, Semiconductors, and Nanotechnologies III*. 2007. International Society for Optics and Photonics.
31. Tuchin, V.V. and V. Tuchin, *Tissue optics: light scattering methods and instruments for medical diagnosis.* 2007.
32. Alqurashi, T., et al., *Nanosecond pulsed laser texturing of optical diffusers.* AIP Advances, 2017. **7**(2): p. 025313.
33. Bohren, C.F. and D.R. Huffman, *Absorption and scattering of light by small particles*. 2008: John Wiley & Sons.
34. Prum, R.O., et al., *Coherent light scattering by blue feather barbs.* Nature, 1998. **396**(6706): p. 28.
35. Colton, D. and R. Kress, *Inverse acoustic and electromagnetic scattering theory*. Vol. 93. 2012: Springer Science & Business Media.
36. Seinfeld, J.H. and S.N. Pandis, *Atmospheric chemistry and physics: from air pollution to climate change*. 2016: John Wiley & Sons.
37. Roqué, J., et al., *Copper and silver nanocrystals in lustre lead glazes: Development and optical properties.* Journal of the European Ceramic Society, 2006. **26**(16): p. 3813-3824.
38. Eckhardt, S., et al., *Nanobio silver: its interactions with peptides and bacteria, and its uses in medicine.* Chemical reviews, 2013. **113**(7): p. 4708-4754.

39. Gibson, I. and D. Shi, *Material properties and fabrication parameters in selective laser sintering process.* Rapid prototyping journal, 1997. **3**(4): p. 129-136.
40. Mori, K., et al., *A new non-contacting non-destructive testing method for defect detection in concrete.* NDT & E International, 2002. **35**(6): p. 399-406.
41. Sasaki, I., T. Hirayama, and T. Hatsuda. *Vehicle information networking based on inter-vehicle communication by laser beam injection and retro-reflection techniques*. in *Proceedings of VNIS'94-1994 Vehicle Navigation and Information Systems Conference*. 1994. IEEE.
42. Vogel, A. and V. Venugopalan, *Mechanisms of pulsed laser ablation of biological tissues.* Chemical reviews, 2003. **103**(2): p. 577-644.
43. Jia, F., *High power continues wave laser diode array end pumped Nd: YAG/LBO red lasers operated at 669 nm and 659 nm.* Laser physics, 2010. **20**(7): p. 1559-1563.
44. Svelto, O. and D.C. Hanna, *Principles of lasers*. Vol. 4. 1998: Springer.
45. Koechner, W., *Solid-state laser engineering*. Vol. 1. 2013: Springer.
46. Wannier, G.H., *The structure of electronic excitation levels in insulating crystals.* Physical Review, 1937. **52**(3): p. 191.
47. Chen, J.C., *Theory of Subexcitation Electron Scattering by Molecules. II. Excitation and De-Excitation of Molecular Vibration.* The Journal of Chemical Physics, 1964. **40**(12): p. 3513-3520.
48. Elsayed-Ali, H., et al., *Time-resolved observation of electron-phonon relaxation in copper.* Physical Review Letters, 1987. **58**(12): p. 1212.
49. Firsov, O., *A qualitative interpretation of the mean electron excitation energy in atomic collisions.* Zhur. Eksptl'. i Teoret. Fiz., 1959. **36**.
50. Hazi, A., T. Rescigno, and A. Orel, *Theoretical study of the deexcitation of KrF and XeF excimers by low-energy electrons.* Applied Physics Letters, 1979. **35**(7): p. 477-479.
51. Rybicki, G.B. and A.P. Lightman, *Radiative processes in astrophysics*. 2008: John Wiley & Sons.
52. Heisenberg, W., *The physical principles of the quantum theory*. 1949: Courier Corporation.
53. Dudarev, S., et al., *Electron-energy-loss spectra and the structural stability of nickel oxide: An LSDA+ U study.* Physical Review B, 1998. **57**(3): p. 1505.
54. Hofstadter, D.R., *Energy levels and wave functions of Bloch electrons in rational and irrational magnetic fields.* Physical review B, 1976. **14**(6): p. 2239.
55. Close, D.H., *Strong-field saturation effects in laser media.* Physical Review, 1967. **153**(2): p. 360.
56. Klimov, V., et al., *Optical gain and stimulated emission in nanocrystal quantum dots.* Science, 2000. **290**(5490): p. 314-317.
57. Huang, X., et al., *Plasmonic photothermal therapy (PPTT) using gold nanoparticles.* Lasers in medical science, 2008. **23**(3): p. 217.
58. Anderson, R.R., et al., *Selective photothermolysis of cutaneous pigmentation by q-switched Nd: YAG laser pulses at 1064, 532. and 355 nm.* Journal of Investigative Dermatology, 1989. **93**(1): p. 28-32.
59. Gilling, P.J., et al., *Combination holmium and Nd: YAG laser ablation of the prostate: initial clinical experience.* Journal of endourology, 1995. **9**(2): p. 151-153.
60. Grossman, M.C., et al., *Damage to hair follicles by normal-mode ruby laser pulses.* Journal of the American Academy of Dermatology, 1996. **35**(6): p. 889-894.
61. Passarella, S., et al., *Increase of proton electrochemical potential and ATP synthesis in rat liver mitochondria irradiated in vitro by helium-neon laser.* FEBS letters, 1984. **175**(1): p. 95-99.
62. Walsh Jr, J.T., et al., *Pulsed CO2 laser tissue ablation: effect of tissue type and pulse duration on thermal damage.* Lasers in surgery and medicine, 1988. **8**(2): p. 108-118.
63. Sprangle, P., V. Granatstein, and R. Smith, *Free electron lasers and stimulated scattering from relativistic electron beams.* Infrared and millimeter waves., 1979. **1**: p. 279-327.
64. Payne, D., *Use and limitations of light microscopy for diagnosing malaria at the primary health care level.* Bulletin of the World Health Organization, 1988. **66**(5): p. 621.

65. Watt, I.M., *The principles and practice of electron microscopy*. 1997: Cambridge University Press.
66. Van Putten, E., et al., *Scattering lens resolves sub-100 nm structures with visible light.* Physical review letters, 2011. **106**(19): p. 193905.
67. Redwood, P.S., et al., *Characterization of humic substances by environmental scanning electron microscopy.* Environmental science & technology, 2005. **39**(7): p. 1962-1966.
68. Flegler, S.L., J.W. Heckman Jr, and K.L. Klomparens, *Scanning and transmission electron microscopy: an introduction.* Oxford University Press(UK), 1993, 1993: p. 225.
69. Goldstein, J.I., et al., *Scanning electron microscopy and X-ray microanalysis*. 2017: Springer.
70. Seiler, H., *Secondary electron emission in the scanning electron microscope.* Journal of Applied Physics, 1983. **54**(11): p. R1-R18.
71. Stokes, D., *Principles and practice of variable pressure/environmental scanning electron microscopy (VP-ESEM)*. 2008: John Wiley & Sons.
72. Goldstein, J., *Practical scanning electron microscopy: electron and ion microprobe analysis*. 2012: Springer Science & Business Media.
73. Everhart, T.E. and R. Thornley, *Wide-band detector for micro-microampere low-energy electron currents.* Journal of scientific instruments, 1960. **37**(7): p. 246.
74. Tasneem, K., et al. *Effects of Aggregate Mineralogy on the Thermal Expansion Behavior of Concrete*. in *T&DI Congress 2014: Planes, Trains, and Automobiles*. 2014.
75. Suzuki, E., *High-resolution scanning electron microscopy of immunogold-labelled cells by the use of thin plasma coating of osmium.* Journal of microscopy, 2002. **208**(3): p. 153-157.
76. Smith, C., D. Sabatino, and T. Praisner, *Temperature sensing with thermochromic liquid crystals.* Experiments in fluids, 2001. **30**(2): p. 190-201.
77. Bahadur, B., *Liquid crystals: applications and uses*. Vol. 1. 1990: World scientific.
78. Nehring, J. and A. Saupe, *On the schlieren texture in nematic and smectic liquid crystals.* Journal of the Chemical Society, Faraday Transactions 2: Molecular and Chemical Physics, 1972. **68**: p. 1-15.
79. Als-Nielsen, J., F. Christensen, and P.S. Pershan, *Smectic-A order at the surface of a nematic liquid crystal: synchrotron x-ray diffraction.* Physical Review Letters, 1982. **48**(16): p. 1107.
80. Oswald, P. and P. Pieranski, *Nematic and cholesteric liquid crystals: concepts and physical properties illustrated by experiments*. 2005: CRC press.
81. https://www.doitpoms.ac.uk/tlplib/anisotropy/liquidcrystals.php, U.o.C.L.c.A.a.
82. Schattschneider, P., et al., *Detection of magnetic circular dichroism using a transmission electron microscope.* Nature, 2006. **441**(7092): p. 486.
83. Tropea, C. and A.L. Yarin, *Springer handbook of experimental fluid mechanics*. 2007: Springer Science & Business Media.
84. Panák, O., M. Držková, and M. Kaplanová, *Insight into the evaluation of colour changes of leuco dye based thermochromic systems as a function of temperature.* Dyes and Pigments, 2015. **120**: p. 279-287.
85. White, M.A. and M. LeBlanc, *Thermochromism in commercial products.* Journal of chemical education, 1999. **76**(9): p. 1201.
86. Muthyala, R., *Chemistry and applications of leuco dyes*. 2006: Springer Science & Business Media.
87. Shen, T., et al., *Photosensitized reduction of benzil by heteroatom-containing anthracene dyes.* Journal of Photochemistry and Photobiology A: Chemistry, 1989. **47**(2): p. 203-212.
88. Bamfield, P., *Chromic phenomena: technological applications of colour chemistry*. 2010: Royal Society of Chemistry.
89. 20/11/17), T.H.T.t.A.a.h.w.t.c.h.-i.-w.t.A.
90. Morales, A.M. and C.M. Lieber, *A laser ablation method for the synthesis of crystalline semiconductor nanowires.* Science, 1998. **279**(5348): p. 208-211.
91. Kim, K., et al., *Rapid replication of polymeric and metallic high aspect ratio microstructures using PDMS and LIGA technology.* Microsystem Technologies, 2002. **9**(1-2): p. 5-10.
92. Popovics, S., *A numerical approach to the complete stress-strain curve of concrete.* Cement and concrete research, 1973. **3**(5): p. 583-599.

93. Sasaki, N. and S. Odajima, *Stress-strain curve and Young's modulus of a collagen molecule as determined by the X-ray diffraction technique.* Journal of biomechanics, 1996. **29**(5): p. 655-658.
94. Duncan, J.M. and C.-Y. Chang, *Nonlinear analysis of stress and strain in soils.* Journal of Soil Mechanics & Foundations Div, 1970.
95. Dowling, N.E., *Mechanical behavior of materials: engineering methods for deformation, fracture, and fatigue*. 2012: Pearson.
96. 91. Brittle and Ductile Materials, h.w.e.c.l.m.s.h., 31.07.2018.
97. Siegel, R.W. and G.E. Fougere, *Mechanical properties of nanophase metals.* Nanostructured Materials, 1995. **6**(1-4): p. 205-216.
98. Orlov, S.S., *Volume holographic data storage.* Communications of the ACM, 2000. **43**(11): p. 47-47.
99. Vasconcellos, F.d.C., et al., *Printable surface holograms via laser ablation.* Acs Photonics, 2014. **1**(6): p. 489-495.
100. Khalid, M.W., et al., *Holographic Writing of Ink-Based Phase Conjugate Nanostructures via Laser Ablation.* Scientific reports, 2017. **7**(1): p. 10603.
101. Syms, R.R.A., *Practical volume holography*. 1990: Clarendon Press.
102. Ahmed, R., et al., *Printable ink lenses, diffusers, and 2D gratings.* Nanoscale, 2017. **9**(1): p. 266-276.
103. Kelly, R. and A. Miotello, *Contribution of vaporization and boiling to thermal-spike sputtering by ions or laser pulses.* Physical Review E, 1999. **60**(3): p. 2616.
104. Miotello, A. and R. Kelly, *Critical assessment of thermal models for laser sputtering at high fluences.* Applied Physics Letters, 1995. **67**(24): p. 3535-3537.
105. Buffat, P. and J.P. Borel, *Size effect on the melting temperature of gold particles.* Physical review A, 1976. **13**(6): p. 2287.
106. Porneala, C. and D.A. Willis, *Effect of the dielectric transition on laser-induced phase explosion in metals.* International journal of heat and mass transfer, 2006. **49**(11-12): p. 1928-1936.
107. Yetisen, A.K., et al., *Reusable, robust, and accurate laser-generated photonic nanosensor.* Nano letters, 2014. **14**(6): p. 3587-3593.
108. Ko, S.H., et al., *Nanosecond laser ablation of gold nanoparticle films.* Applied physics letters, 2006. **89**(14): p. 141126.
109. Cabalin, L. and J. Laserna, *Experimental determination of laser induced breakdown thresholds of metals under nanosecond Q-switched laser operation.* Spectrochimica Acta Part B: Atomic Spectroscopy, 1998. **53**(5): p. 723-730.
110. Choi, W.M. and O.O. Park, *A soft-imprint technique for direct fabrication of submicron scale patterns using a surface-modified PDMS mold.* Microelectronic Engineering, 2003. **70**(1): p. 131-136.
111. Bodas, D. and C. Khan-Malek, *Direct patterning of quantum dots on structured PDMS surface.* Sensors and Actuators B: Chemical, 2007. **128**(1): p. 168-172.
112. Altissimo, M., *E-beam lithography for micro-/nanofabrication.* Biomicrofluidics, 2010. **4**(2): p. 026503.
113. Matsui, S., et al., *Lithographic approach for 100 nm fabrication by focused ion beam.* Journal of Vacuum Science & Technology B: Microelectronics Processing and Phenomena, 1986. **4**(4): p. 845-849.
114. Heaney, P.J., et al., *Focused ion beam milling: A method of site-specific sample extraction for microanalysis of Earth and planetary materials.* American Mineralogist, 2001. **86**(9): p. 1094-1099.
115. McCord, M.A. and M.J. Rooks, *Electron beam lithography.* Handbook of microlithography, micromachining, and microfabrication, 1997. **1**: p. 139-249.
116. Lu, C. and R. Lipson, *Interference lithography: a powerful tool for fabricating periodic structures.* Laser & Photonics Reviews, 2010. **4**(4): p. 568-580.
117. Feinberg, J. and K.R. MacDonald, *Phase-conjugate mirrors and resonators with photorefractive materials*, in *Photorefractive Materials and their applications II*. 1989, Springer. p. 151-203.

118. Bozhevolnyi, S.I., E.A. Bozhevolnaya, and S. Berntsen, *Theoretical model for phase conjugation of optical near fields.* JOSA A, 1995. **12**(12): p. 2645-2654.
119. Yaqoob, Z., et al., *Optical phase conjugation for turbidity suppression in biological samples.* Nature photonics, 2008. **2**(2): p. 110.
120. Yoder, P., *Study of light deviation errors in triple mirrors and tetrahedral prisms.* JOSA, 1958. **48**(7): p. 496-499.
121. Chipman, R.A., et al., *Wavefront correcting properties of corner-cube arrays.* Applied optics, 1988. **27**(15): p. 3203-3209.
122. Yariv, A., *Phase conjugate optics and real-time holography [invited paper].* IEEE Journal of Quantum Electronics, 1978. **14**(9): p. 650-660.
123. He, G.S., *Optical phase conjugation: principles, techniques, and applications.* Progress in Quantum Electronics, 2002. **26**(3): p. 131-191.
124. Yust, B.G., D.K. Sardar, and A. Tsin. *Phase conjugating nanomirrors: utilizing optical phase conjugation for imaging*. in *SPIE BiOS*. 2011. International Society for Optics and Photonics.
125. Arnoldus, H.F. and T.F. George, *Observation of atomic relaxation near an interface through detection of emitted fluorescence*. 1989, DTIC Document.
126. Shkunov, V.V. and B.I. Zeldovich, *Optical phase conjugation.* Scientific American, 1985. **253**: p. 54-59.
127. Yariv, A., *Four wave nonlinear optical mixing as real time holography.* Optics Communications, 1978. **25**(1): p. 23-25.
128. Yariv, A., *Phase conjugate optics and real-time holography.* IEEE Journal of Quantum Electronics, 1978. **14**(9): p. 650-660.
129. Günter, P., *Holography, coherent light amplification and optical phase conjugation with photorefractive materials.* Physics Reports, 1982. **93**(4): p. 199-299.
130. Fujita, T., H. Nishihara, and J. Koyama, *Blazed gratings and Fresnel lenses fabricated by electron-beam lithography.* Optics letters, 1982. **7**(12): p. 578-580.
131. Quate, C.F., *Scanning probes as a lithography tool for nanostructures.* Surface Science, 1997. **386**(1-3): p. 259-264.
132. Harvey, T.R., et al., *Efficient diffractive phase optics for electrons.* New Journal of Physics, 2014. **16**(9): p. 093039.
133. Dhawan, A., et al., *Focused ion beam fabrication of metallic nanostructures on end faces of optical fibers for chemical sensing applications.* Journal of Vacuum Science & Technology B: Microelectronics and Nanometer Structures Processing, Measurement, and Phenomena, 2008. **26**(6): p. 2168-2173.
134. Qin, D., Y. Xia, and G.M. Whitesides, *Soft lithography for micro-and nanoscale patterning.* Nature protocols, 2010. **5**(3): p. 491.
135. Zhao, X.-M., Y. Xia, and G.M. Whitesides, *Soft lithographic methods for nano-fabrication.* Journal of Materials Chemistry, 1997. **7**(7): p. 1069-1074.
136. Di Pasquale, F., *Electromagnetic Fields and Propagation, Scuola Superiore Sant'Anna, Pisa, 2013*.
137. Pintus, P., et al., *Analysis and design of microring-based switching elements in a silicon photonic integrated transponder aggregator.* Journal of Lightwave Technology, 2013. **31**(24): p. 3943-3955.
138. 99. Olivier de Weck, F.E.M., http://web.mit.edu/16.810/www/16.810_L4_CAE.pdf on 21 October, 2017.
139. Finite-difference time-domain method, h.e.w.o.w.F.-d.t.-d.m., on 21 October, 2017.
140. Finite volume method, h.e.w.o.w.F.v.m., on 20 March, 2018.
141. Method of lines, h.e.w.o.w.M.o.l., on 20 March, 2018.
142. Meyer, G.H., The Time-discrete Method of Lines for Options and Bonds: A PDE Approach. 2015: World Scientific.
143. https://www.ece.nus.edu.sg/stfpage/eleadj/planewave.htm. Accessed on 24.08.2019
144. https://empossible.net/wp-content/uploads/2019/08/Lecture-19-Plane-Wave-Expansion-Method.pdf. Accessed on 24.08.2019

145. Ergül, Ö.S., *Fast multipole method for the solution of electromagnetic scattering problems*. 2003, bilkent university.

146. Harrington, R.F., *Field computation by moment methods*. 1993: Wiley-IEEE Press.

147. Grosges, T., A. Vial, and D. Barchiesi, *Models of near-field spectroscopic studies: comparison between finite-element and finite-difference methods.* Optics Express, 2005. **13**(21): p. 8483-8497.

Chapter 3 Ink-Based Phase Conjugate Nanostructures

3.1 Overview

This chapter discusses ink-based phase-conjugated nanostructures fabricated via CCR integrated nanosecond pulsed laser. Nanofabrication through retroreflection based lithography result into interesting novel features in terms of surface morphologies and optical properties. Fabricated nanostructures are recorded in the form of phase conjugated diffractive gratings rather than ordinary gratings. Introduction and conjugated nanostructure recording theory are discussed in section 3.2. Sample preparation and phase-conjugated nanostructure fabrication are presented in section 3.3. Optical properties and computation modelling of 1D and 2D conjugated nanostructures are reported in sections 3.4-3.7. Diffraction intensity comparison of ordinary gratings made with simple metallic mirror and phase conjugate gratings made with CCR are presented in 3.8. The chapter is summarized in section 3.9.

This chapter is reproduced from ‘’**Khalid, M.W.,** et al., Holographic Writing of Ink-Based Phase Conjugate Nanostructures via Laser Ablation. Scientific Reports, 2017. **7**(1): p. 10603.’’

3.2 Introduction

An ideal phase conjugate mirror (PCM) reflects a light wave in which the wave vector and the amplitude are reversed and are complex conjugated to the incident wave to create PCW [1, 2]. A CCR also produces phase conjugated reflected light through total internal reflection (TIR) based on three-mirror reflection effect [3]. However, the use of three dimensional or volumetric PCM/CCRs is limited due to fabrication complexity, time-consumption and higher costs. Recently, flat optical devices have been produced on functionalized substrates using low-cost single pulse holography [4-6]. Additionally, optical phase-conjugated flat CCR array

holograms have been created in functionalized gelatine substrates through holographic Denisyuk reflection mode recording [3, 7-9]. Phase conjugate nanostructures can be produced in the form of periodic gratings recorded in light absorbing medium by the interference pattern formed when a plane electromagnetic wave is reflected from a phase-conjugate mirror or CCR rather than from an ordinary mirror [10]. Single pulse Denisyuk reflection holography is a low cost, fast, and simple technique to fabricate nanostructures which on light illumination can diffract light ion phase conjugation manners [3, 11]. Phase conjugate holograms recorded in the form of phase conjugate gratings have applications in optical tomography, interferometry, near field microscopy, wavefront correction, imaging and biochemical sensing [1, 12-17]. Figure 3.1d-f shows SEM, OM images of phase conjugate diffractive gratings and diffraction field, respectively.

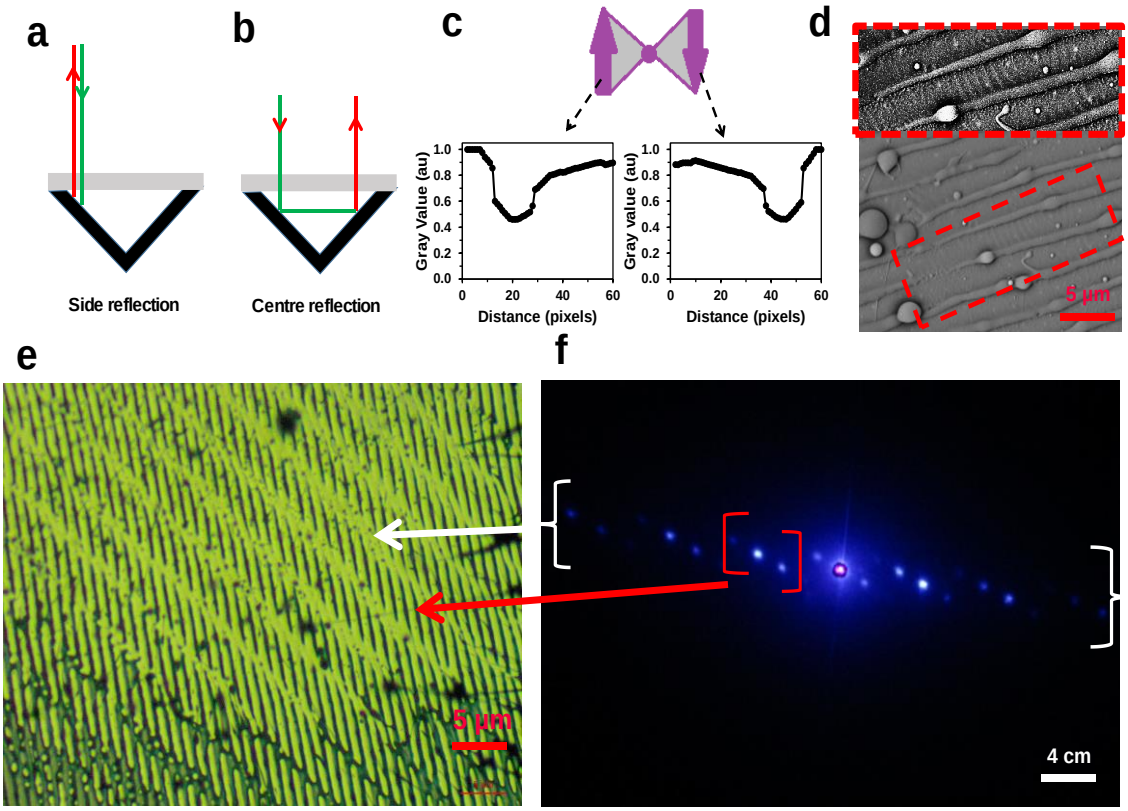

Figure 3. 1: (a,b) Light illumination at side and center of the CCR. (c) Optical phase conjugation. (d) SEM image of the conjugated patterns. (e,f) Light diffraction property of the conjugated structures through violet light illumination.

Fabrication of phase conjugate nanostructures demonstrated in this chapter is performed through a more productive, cost effective as it does not require to be attached with expensive equipment and convenient to use technique called Denisyuk reflection image writing [18, 19]. Nanofabrication by integrating CCR and Nd: YAG laser is novel technique and reported first time ever. A single pulsed nanosecond laser is used to record phase-conjugate holograms on ink coated glass substrates. In this process, an incident laser beam propagates through the light absorbing media impinges the CCR surface and retroreflected to interfere with the incident beam. Now the standing wave have enough energy to ablate the material depending upon the interference pattern caused by both waves. Conjugated periodicity depends on the intensity distribution of an interference pattern and the optical properties of light absorbing material (i.e.

absorption, refractive index). Resulting conjugated patterns are also affected by the tilt angle of the recording media, working distance, height, and the localized energy distribution from the laser source. 1D/2D phase conjugate nanostructures can be produced in holographic films through optimized parameters. In the reading step, A single beam of monochromatic or broadband light illuminates the recorded structures. The diffraction field caused by reading event shows phase conjugation properties.

3.2.1 Conjugate nanostructure recording theory

Phase conjugate nanostructures were copied in the form of periodic gratings on an ink coated glass substrate via interference-based laser ablation. The recording process involved light inference through a cornercube retroreflector in a light-sensitive ink-based holographic recording medium. A cornercube retroreflector having three mutually perpendicular mirror surfaces that reflect light toward the source through total internal reflection. The incident light is reflected three times to create a retroreflection [20]. However, not all light entering the cornercube is reflected three times and become a part of retroreflection. Light entering at the centre of the cornercube has more probability to be retroreflected than entering at the sides (Figure 3.2a-b) [3]. The retroreflected light is phase conjugated to the incident light. The incident light is transmitted (plane-to-plane of CCR) and interferes with the reflected phase conjugated light to produces phase conjugated nanostructures at the ink substrate through laser ablation. Consider an arbitrary incident plane wave under paraxial the approximation is:

$$E_i(r,t) = \varepsilon A(i) e^{[i.(k_i.r-\omega t)]} \tag{3.1}$$

Here *A(i)* is a amplitude function, k_i is a wave vector, and ε is a unit polarization vector so that $\varepsilon.\varepsilon^*$. The light reflected from a CCR can be approximated with ideal PCM if (a) the physical

dimension of the CCR is large enough, and (b) the centre of the CCR coincides with optical axis. Therefore, reflected wave from a CCR is:

$$E_{CCR}(r,t) = R\varepsilon^{*}A^{*}(i)\mathrm{e}^{[i.(-k_i.r-\omega t)]} \tag{3.2}$$

Here R indicates amplitude reflectivity of a CCR, $-k_i$ reverse direction of the reflected wave, ε^{*}, and $A^{*}(i)$ indicates conjugate/reversal of polarization and amplitude vectors [21, 22]. The recorded phase-conjugated nanostructure due to the resulting complex interference between the incident and transmitted or reflected PCW is:

$$E\ (r,t) = E_i(r,t) + E_{CCR}(r,t) = [\varepsilon A(i)\mathrm{e}^{i.(k_i.r)} + R\varepsilon^{*}A^{*}(i)\mathrm{e}^{i.(-k_i.r)}]e^{-i\omega t} \tag{3.3}$$

Consider the time-averaged electric energy density of the total field at a typical point in the space $z > 0$. $\langle E\rangle = (1/16\pi)E.E^{*}$ [23], which is independent of time. By substituting into this expression from 3.3 and using $\varepsilon.\varepsilon^{*}=1$ we readily find that:

$$\langle E(r)\rangle = (1/16\pi)\{(1+|R|^2)|A(i)|^2 + [\varepsilon^2 R^{*}A(i)^2 e^{(2ik_i.r)} + CC]\} \tag{3.4}$$

where CC denotes complex conjugate. Using trigonometry identity and $R = |R|e^{i\phi}$, $A(i) = |A(i)|e^{i\alpha}$, $\varepsilon^2 = |\varepsilon^2|e^{i\delta}$, the interference field is [21]:

$$I = \langle E(r)\rangle = \frac{|A(i)|^2}{16\pi}[1+|k|^2 + 2|k||\varepsilon^2| \times \cos(2k_i.r + 2\alpha - \varphi + \gamma)] \tag{3.5}$$

For maximum light interference, $\cos(2k_i.r + 2\alpha - \varphi + \gamma) = 1$ and

$$I_{\max.} = \frac{|A(i)|^2}{16\pi}[1+|k|^2 + 2|k||\varepsilon^2|] \tag{3.6}$$

For minimum light interference, $\cos(2k_i.r + 2\alpha - \varphi + \gamma) = -1$ and

$$I_{\min.} = \frac{|A(i)|^2}{16\pi}[1 + |k|^2 - 2|k||\varepsilon^2|] \tag{3.7}$$

For simplicity, the interference between the incident and retroreflected light is taken into account. Interference due to transmitted light from plane-to-plane of CCR is not considered. However, phase-conjugated nanostructures fabrication through a CCR is a complex multibeam interference phenomenon i.e. interference between the incident beam, reflected beams from different planes (without three times reflection), and the retroreflected beam.

3.3 Experimental setup and procedures

3.3.1 Sample preparation

The sample preparation is done using the following stages: (a) a glass plate is cleaned with acetone, and then dried for 1 min, (b) black permanent ink is then diluted in ethanol (1:1, v/v), (c) the ink-ethanol solution is poured on to the glass plate, which spins at 400 rpm for 60 s, followed by 900 rpm for 20 s, and (d) the ink-coated glass sample is then exposed to the laser pulse for recording nanostructures (as shown in Figure 3.2a). The recording process is completed in a few seconds. The transmission spectrum of the coated black ink indicated broadband absorption in the visible range as shown in figure 3.2b.

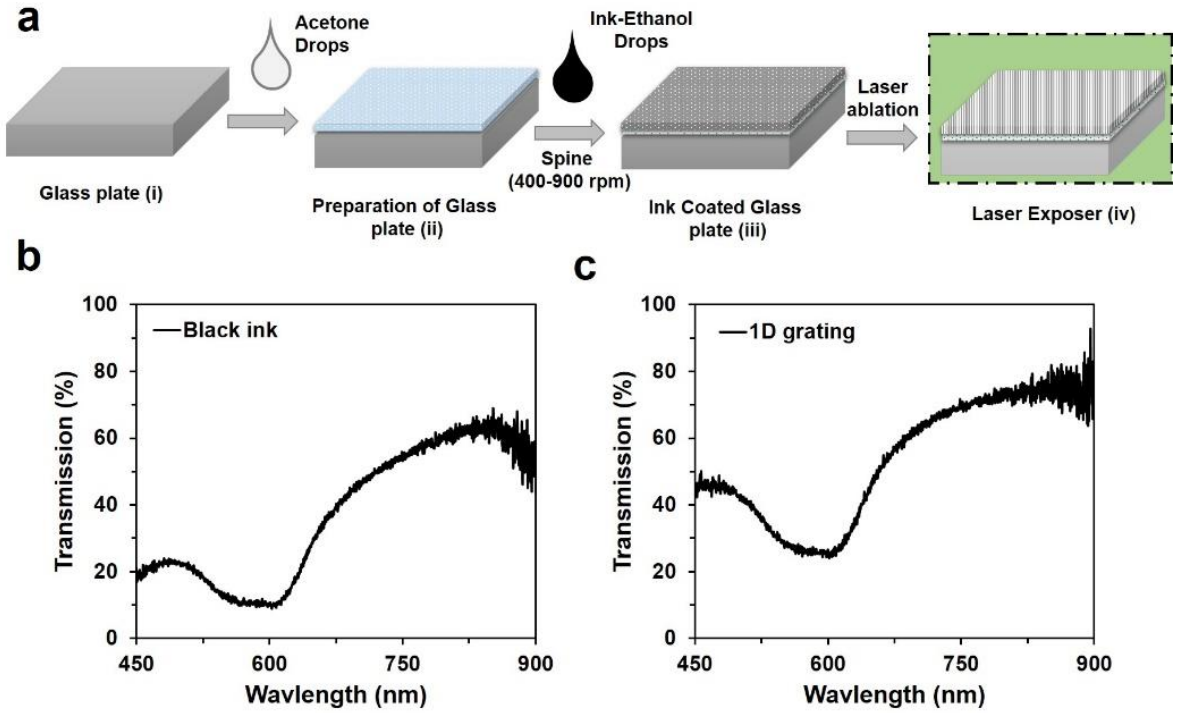

Figure 3. 2**:** (a) Sample preparation. (b,c) Transmission property of black ink and 1D grating.

3.3.2 Phase conjugate nanostructure recording

The optical recording of the phase conjugated nanostructure is based on a single pulse nanosecond laser and in-line Denisyuk reflection holography (Figure 3.3a). A 1064 nm beam from a Nd:YAG laser (pulse duration=3.5 ns, 300 mJ) is passed through the optical filters, a beam expander and a series of dichroic mirrors setup before exposing the recording medium. At the exposure stage, a recording medium (black ink coated on a glass slide) and an object (single CCR) are placed parallel to each other. The expanded laser beam passes perpendicular to the exposure stage and is reflected back from the CCR. The laser beam enters the CCR from the surface plane, which is reflected once from all three surfaces of the CCR and finally phase conjugates with respect to the incident beam. Both the incident and reflected beams propagate in the opposite direction. The resulting standing wave propagates toward the substrate, ablating the thin ink film and produces periodic gratings. A standing wave is produced as a result of

interference between the incident and the reflected wave which allows the formation of ablated and non-ablated regions on the recording medium as shown in Figure 3.1a.

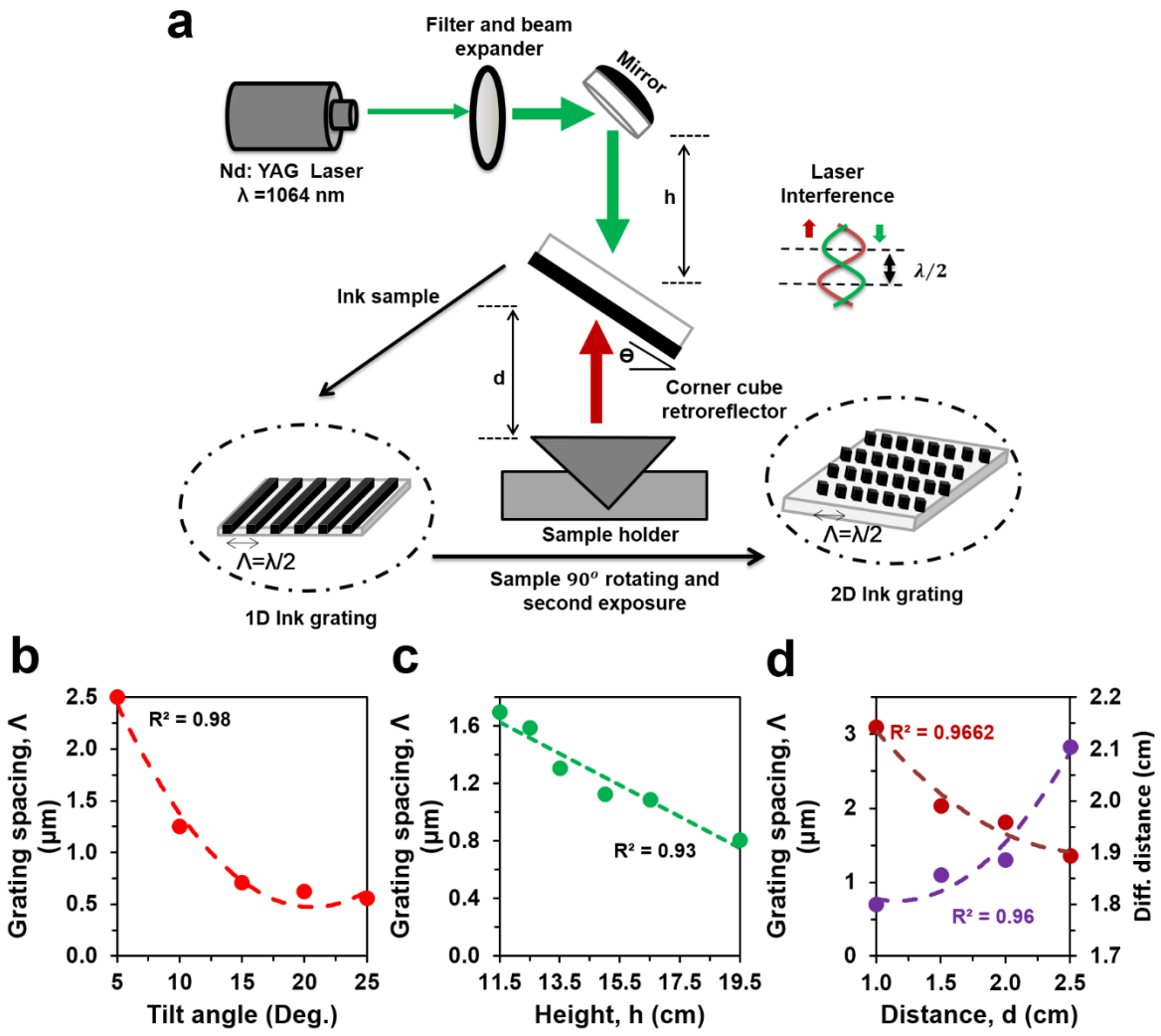

Figure 3. 3: Holographic fabrication of phase conjugate nanostructures using Denisyuk reflection mode recording on ink coated glass substrate. (a) Schematic of the experimental setup to fabricate conjugate nanopatterns. (b) Grating spacing as a function of tilt angle (θ°), i.e. the angle between the ink coated glass substrate and the surface plane of CCR. (c) Grating spacing as a function of height (h), i.e. the distance between the laser tip and the surface plane of CCR. (d) The grating spacing of the structures and separation between the diffraction spots of resulted diffraction pattern as a function of working distance (d), i.e. distance between the ink-coated glass substrate and CCR.

3.4 1D Ink-based conjugate nanostructures

Phase conjugate 1D nanostructures are fabricated on an ink coated glass substrate through in-line Denisyuk reflection holography. Figure 3.3a shows the experimental diagram to produce ink-based conjugate nanostructures. 1D/2D phase conjugate nanostructures are based on one or two pulses of a laser beam at specific exposure angles. The fabricated nanostructures are uniform to produce conjugate patterns (Figure 3.1c). The characteristics of ink-based nanostructure patterns depend on the laser wavelength, energy, and geometrical parameters. Ink-coated glass substrate is adjusted in a flexible sample holder (able to move along x, y and z-axes) above the retroreflector to vary the tilt angle (θ) of the substrate from 0° to 25°; the distance (d) (distance with respect to the surface plane of the retroreflector) from 1.0 cm to 2.5 cm; the height (h) (distance between Nd:YAG laser tip to the surface plane) from 11.5 cm to 19.5 cm. The Nd: YAG laser energy (E) is varied from 90 mJ to 360 mJ. During the nanostructure recording, only one parameter is changed while others are kept constant. Figure 3.3b-d depicts the spacing of fine diffraction conjugate grating structures as a function of θ, h, and d.

Surface morphologies are varied by adjusting provided parameters during fabrication however, phase conjugation property persist in all the fabricated structures. Periodicity of the adjacent fringes considerably changed by optimising tilt angle and working distance. Reduction rate in the grating spacing slower down as we get closer to the half the wavelength limit of laser light used for fabrication. The grating spacing is decreased from 2.50 μm to 0.555 μm while increasing tilt angle of the glass substrate from the surface plane (θ=5°,10°, 15°, 20°, 25°) and keeping other parameters constant (E=300 mJ, h=11.5 cm and d=1.5 cm). Similarly, as the h and d increased, the grating spacing decreased (Figure 3.3c, d). To observe the influence of h variation on grating spacing, all other parameters are kept constant (E=300 mJ, d=1.5 cm, and

θ=15°); for d variation, h was fixed (h=11.5 cm, E=300 mJ, and θ=15°). Additionally, the resolution of diffraction i.e. the distance between the diffraction orders increased with decreasing d.

3.5 Optical characteristics of 1D conjugate structures

The recorded patterns in the ink-based 1D conjugate nanostructure were analysed through optical and electron microscopy. The light entering from the side of the CCR does not show three mirror retroreflection effects and act like a normal mirror. The only light beam entering at the active regions of CCR undergoes three mirror reflection and produces retroreflection properties. Therefore, the recorded nanostructures with sidewall reflection were analogous to plane mirror reflection based holographic recording. The resulting recorded nanostructures (diffraction gratings) were based on two-beam interference strategy. Figure 3.4a-d shows optical and scanning electron microscope images of the recorded diffraction gratings at the sidewall laser illumination regions of the CCR with different tilt angle variations (θ = 6° and 10°). The computed Fast Fourier Transform (FFT) of the recorded nanostructures allowed visualizing 1D diffraction patterns (Figure 3.4e, f). As the tilt angle increased, the diffraction distance also increased due to the decrease in grating spacing. Lowering the tilt angle increased the ablation depth (Figure 3. 4g). However, light entering at the active regions of the CCR showed retroreflection. Light entered from one plane of CCR to another at 45° before leaving the last plane and returning towards the source. Therefore, light entering at the active regions of the CCR produces multibeam interference to create conjugate diffraction gratings. Figure 3.4h, I show optical microscopic images of the conjugate nanostructures. The conjugate were formed due to multiple inference waves between the incident and phase conjugate waves from different CCR planes. The large grating structure was due to the light interference between the incident light and reflected phase conjugate light and have a 180° interference angle. However,

internally tilted smaller grating structures were due to the light interference between incident light and reflected light passing from one plane to the other and have an interference angle of 45° (Figure 3. 4h). The electron microscope image of the conjugated nanostructure also had larger and internal smaller multigrating structures (Figure 3. 1d-f).

The FFT simulation of the recorded conjugated nanostructures was predicted from the far-field diffraction patterns (Figure 3. 4j, k). The simulated FFT patterns showed tilted multi-order diffraction patterns when the illumination angle was varied. Furthermore, the far-field diffraction patterns of the fabricated planar and conjugated nanostructure were captured through the image screen experiment (Figure 3. 4l-n). The monochromatic (red, green, and blue) light was normally illuminated at the recorded nanostructures.

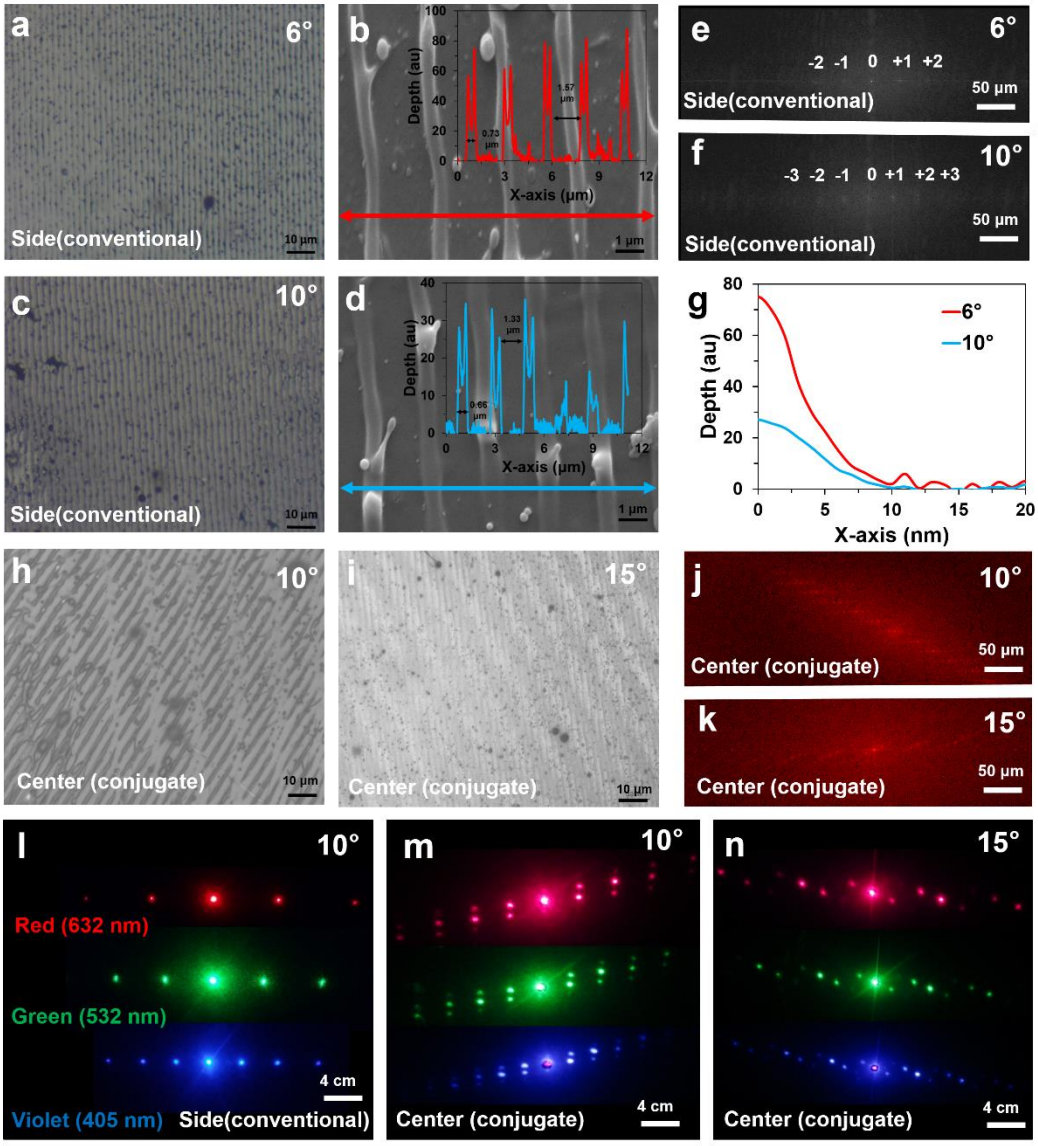

Figure 3. 4: Surface morphology and response to monochromatic light illumination of the simple and conjugated nanopatterns. (a-d) Optical and electron microscope images of the conventional gratings recorded at 6° and 10° tilt angles. (e, f) FFT of the planar patterns with 6° and 10° tilt angles. Scale bars = 50 µm. (g) Depth of the normal fabricated patterns at 6° and 10° tilted sample. (h, i) 2D phase conjugate nanostructures recorded by tilting sample at 10° and 15°. (j, k) FFT of the conjugated patterns with 10° and 15° sample tilt angles. Scale bars = 50 µm. (l-n) Projected conventional, and conjugated diffraction patterns through red (λ=650 nm), green (λ=532 nm), violet (λ=450 nm) light in normal transmission. Scale bars = 4.0 cm.

Well-ordered symmetric diffraction patterns were observed in the experiment. The diffraction patterns of the conjugated structures were different compared to the simple structures. The first order diffraction distances along vertical and horizontal directions were measured from the non-diffracted zero-order. As the tilt angle increased, the horizontal diffraction distance increased exponentially with red, green, and violet light at normal illumination (Figure 3. 5a, b). Similarly, vertical diffraction distances generally increased with variation in tilt angle. However, maximum diffraction distances were observed with red light illumination at tilted angles. Violet light showed minimum diffraction distance compared to the green light at tilted illumination angles. Therefore, the diffraction property of the conjugate nanostructure followed Bragg's law equation 2.18. The far-field diffraction pattern with tilt angle variation (5-20°) was captured with normal red-light illumination. Green and violet diffraction patterns were also captured as the tilt angle was varied (Appendix-A, Figure S3.3,3.4). Red light (reading beam) which has largest wavelength among green and violet, diffracted at highest angle as compared to green and violet. Distinct multi-ordered diffraction patterns were observed due to conjugated nanostructures with tilted angle variations. Diffraction patterns were also analysed through variations of working distance, d (Figure 3. 5c-d). The rotation angles of the vertically oriented orders from the normal (y-axis) were plotted in degrees as a function of d (variation from 1.0 cm to 2.5 cm with 0.5 cm increment). As d increased, the rotation angles increased sinusoidally. The horizontal diffraction distances were also plotted as a function of d. Red and blue light also showed maximum and minimum horizontal diffraction distances and increased sinusoidally as d increased. The far-field diffraction patterns were also captured with red light normal illumination at d variation. Further conjugate diffraction patterns as a function of h and E variation were also captured through monochromatic (red, green, and violet) light illumination (Figure 3. 5g-h).

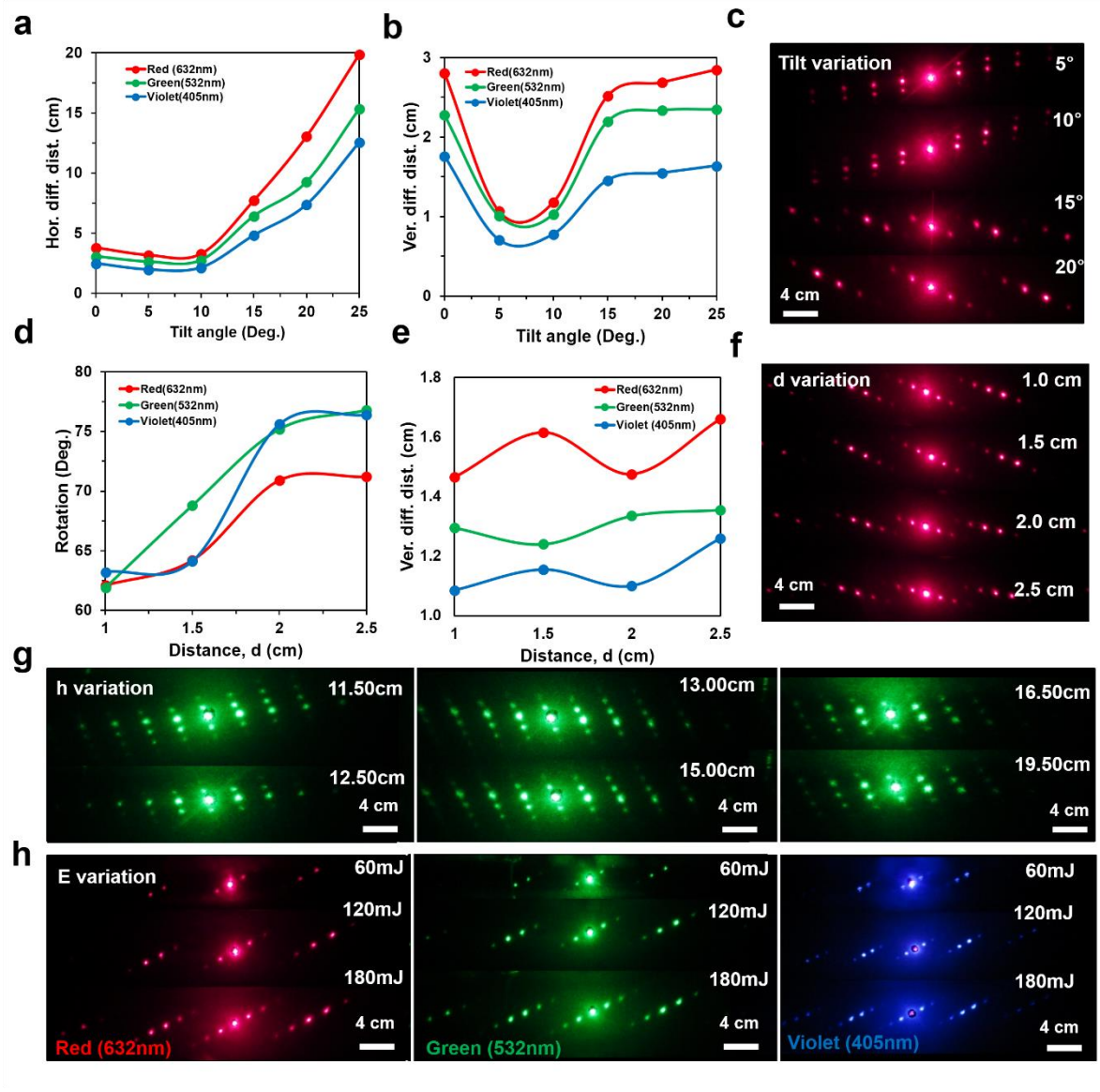

Figure 3. 5: Optical characterization of 1D phase conjugate diffraction patterns with respect to variations in optimized parameters. (a-b) Horizontal and vertical diffraction distance as a function of tilt angle (θ) variation. (c) Far-field diffraction patterns through tilt angle variation at normal red light illumination. Scale bar = 4.0 cm. (d-e) The rotation angle and horizontal diffraction distance as a function of distance (d) variation. (f) Far-field diffraction patterns through distance (d) variation at red light normal illumination. Scale bar = 4.0 cm. (g-h) Far-field diffraction patterns through height (h), energy (E) variation using red, green, and violet light normal illumination. Scale bar = 4.0 cm.

3.6 1D phase conjugated diffraction

Far-field optical experiments were performed with 1D conjugated nanostructures through a screen set up for image projection (Figure 3. 6a). The monochromatic light was illuminated normally to a conjugate nanostructure fixed in a sample holder, which was positioned through a 2D $x-y$ rotational stage. A white screen was placed behind the sample holder and a digital camera was used to capture the far-field patterns. Figure 3. 6b-d shows the captured images of the conjugate diffraction patterns with red (λ=650 nm), green (λ=532 nm) and violet (λ=440 nm) lights at 15° tilt angle. It is obvious from all three different coloured conjugate patterns that the same order numbers along each side of the central spot are analogous in shape, but in reverse intensity order i.e. they have inversion symmetry. If a vector (**R**) is associated with the first order on the left-hand side of the zero-order specular reflection spot, then the first order on the right-hand side will be a vector ($-\mathbf{R}$) i.e. the same magnitude but in an antiparallel orientation. This conjugate diffraction property is also applicable to the second and higher orders. Phase conjugation between same order number is obvious by measuring the patterns obtained with respect to the intensity of the spots. The intensity plots profiles in the insets were produced on the left (dotted line) and right sides (solid line) of the first order diffraction patterns. Both plots had similar trends but were oriented along the opposite direction, which indicated their mutual phase conjugation or inversion symmetry. The phase-conjugation patterns were analysed through conjugated structure recorded at 20° tilt angle (Figure 3. 6e, f). Phase conjugation patterns in a vertical direction are shown with arrows and order numbers. The conjugated diffraction order is always opposite to each other or inversely symmetric. 1D phase conjugate diffraction properties were analysed with 15° and 20° tilted conjugate nanostructures. However, phase conjugated diffraction properties were also valid with other tilt angles (0-25°), E and structural parameter variation (h and d) (Appendix-A, Figure S3.3-3.6).

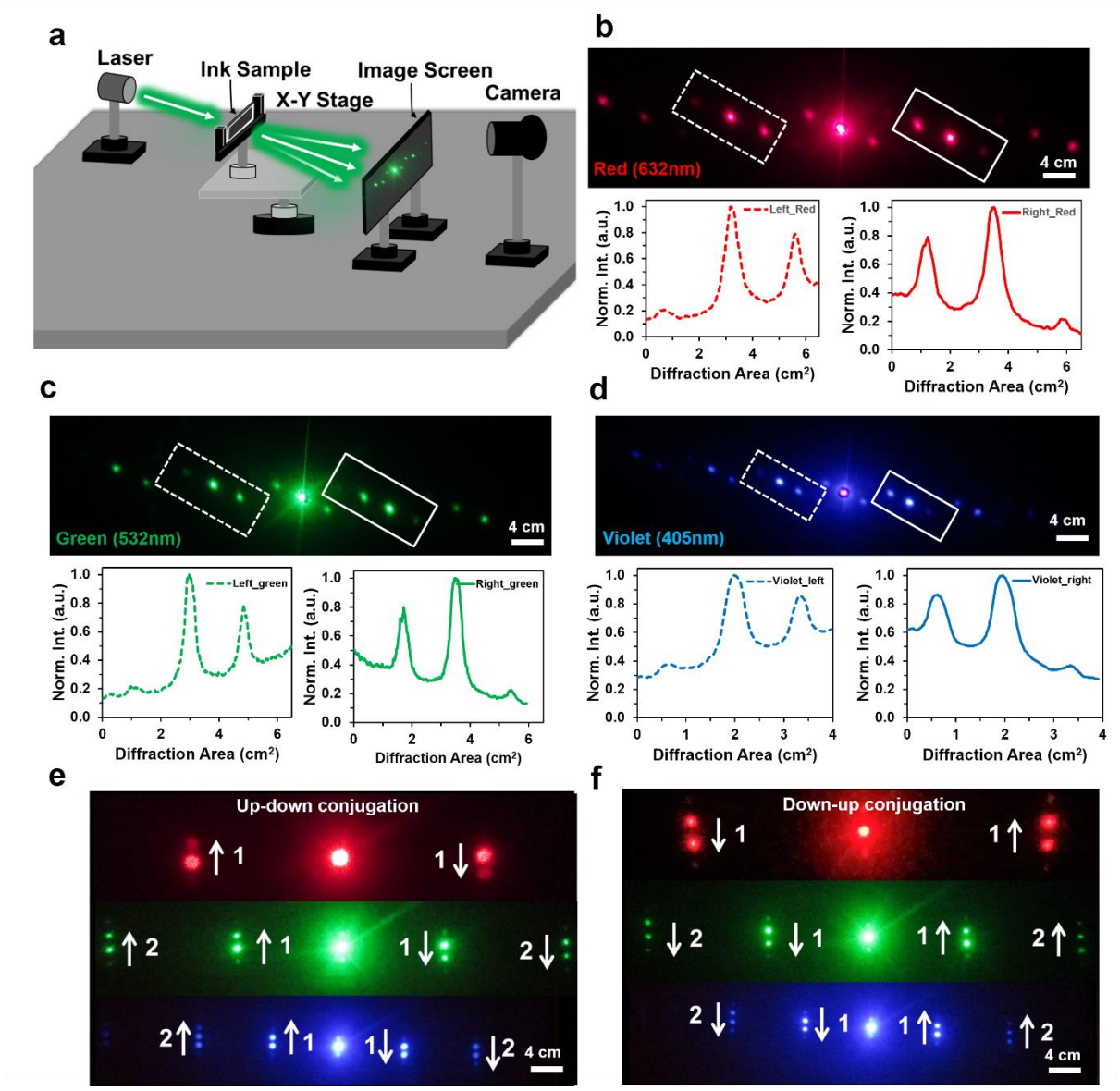

Figure 3. 6: 1D phase conjugate diffraction patterns through monochromatic (red, green, and violet) light normal illumination. (a) Schematic of the far-field image diffraction setup. (b-d) Far-field conjugate diffraction patterns (15° tilted structure) and relevant plot profiles showing phase conjugation (inversion symmetry) between first orders of red, green and violet diffraction patterns. Scale bars = 4.0 cm. (e, f) Far-field conjugate diffraction patterns (10° tilted structure) in vertical direction with monochromatic light normal illumination. Arrows indicate conjugation between the diffracted orders and associated numbers (1 or 2). Scale bars = 4.0 cm.

During reading beam illumination all the structures under continues light illumination diffracted light in phase conjugation manners. Phase conjugation property of the conjugate

nanostructures is consistent and is independent of parameters variation. However, resolution of the conjugate diffraction pattern is improved by customising provided parameters. Highest resolution is obtained at smaller working distance values and increased exposure angles.

3.7 2D conjugated nanostructures

2D conjugated nanostructures were fabricated by a two pulses laser exposure to the ink-based recording medium using the setup shown in Figure 3. 3a. After the first exposure, the sample was rotated to a predefined angle and subsequently exposed to a second laser pulse. Multiple pulses of different laser energies and precise exposure angles are required to create a customized complex nanophotonic structure. Square and rectangular conjugated nanostructures were fabricated with 90° and 30° rotation of the samples before the second exposure. Figure 3. 7a, b shows the optical microscopic images of the recorded ink-based 2D conjugated nanostructures. The internal microstructures with the squared shape (90°) and rectangular (30°) patterns were observed from the microscopic images. The simulated FFT of the recorded conjugate structures allowed predicting the far-field 2D square and rectangular patterns (insets in Figure 3. 7a,b) [24]. Characteristics of the 2D phase conjugated structures were studied with light transmission measurements through an optical microscope. The light transmission through the 2D rectangular (30°) structure was higher than a 2D triangular (90°) structure (Figure 3. 7c). However, the transmission property of the 2D structure was similar to black ink and 1D grating (Figure 3.2b, c). The monochromatic (red, green, and violet) and broadband light normally illuminated the conjugate structures to produce far-field diffraction patterns (Figure 3. 7d). 2D diffraction patterns were observed with predefined recording angles. Diffraction spots obtained from the 90° square shaped grating were well defined and also positioned at 90° with respect to each other resulting in a square-shaped 2D diffraction pattern for each colour. Diffraction spots were arranged in a rectangular pattern but were not

distinguishable by orders in the rectangular 2D conjugate diffraction pattern obtained from 30° rectangular gratings.

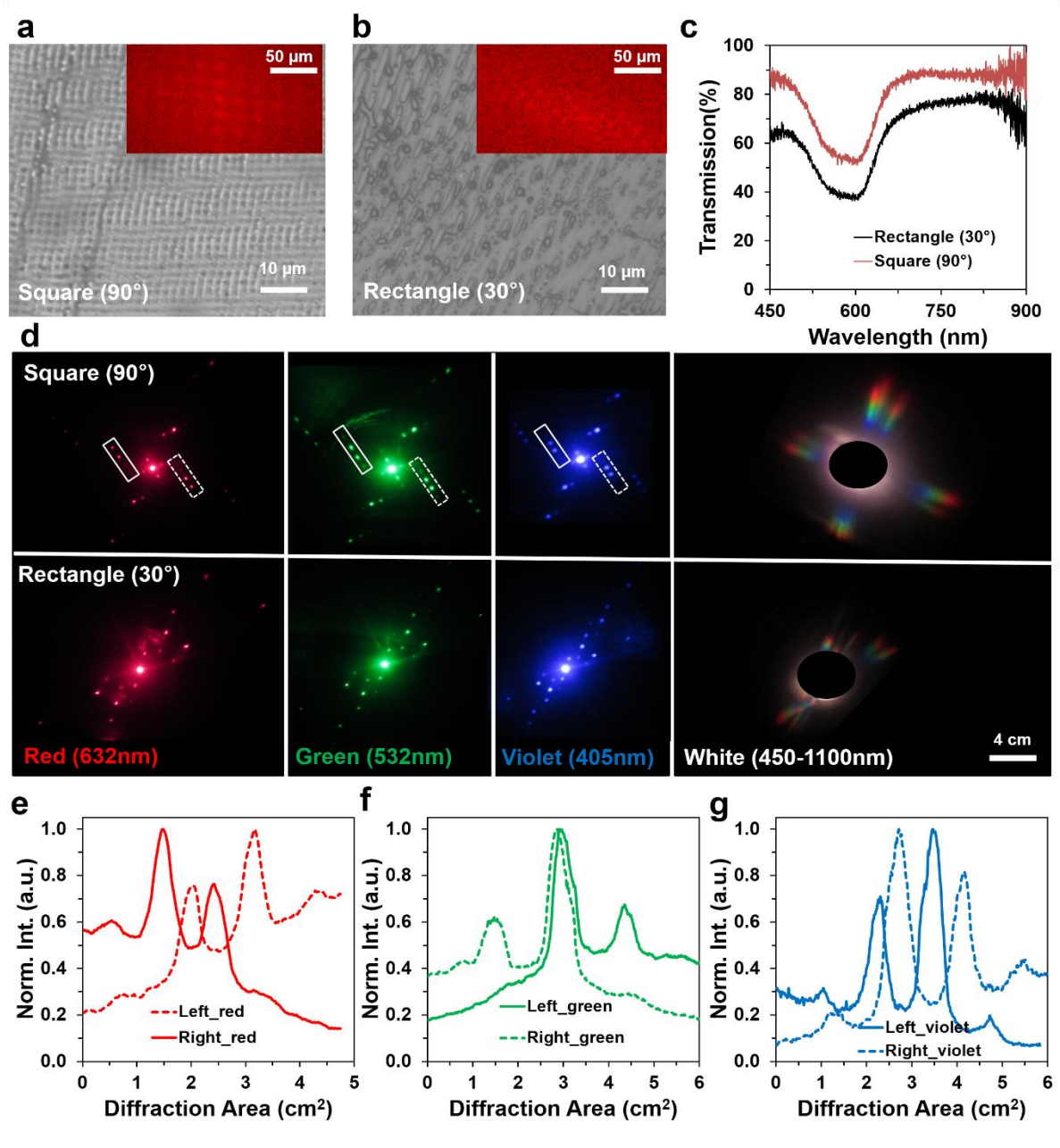

Figure 3. 7: Ink-based 2D conjugated nanostructure fabrication using Denisyuk reflection holography. (a,b) Optical microscopic images of 2D conjugated nanostructures. Insets show FFT patterns. Scale bars = 10 μm. Inset scale bars = 50 μm. (c) Optical transmission property of the 2D square (90°), and rectangular (30°) conjugated structures. (d) Far-field diffraction patterns with monochromatic (red, green, and violet) and broadband light normal illumination. Scale bar = 4.0 cm. (e-g) Left and right side conjugated wavefronts (1st order) through monochromatic light normal illumination.

Square (90°) and rectangular (30°) far-field rainbow patterns were observed for broadband light illumination. Violet light diffracted at the lowest angle, green at intermediate and red at the highest angle as predicted from Bragg's law (Figure 3. 7d). The 2D phase conjugated diffraction property was also observed. Figure 3. 7e-g shows profiles for 2D phase conjugation between the first orders on the left and right side of the central spot of squared diffraction patterns for red, green, and violet colours, respectively. Plots showed symmetrical phase inversion property at the left and right diffraction orders. Phase conjugation remained in 2D structures as well regardless the exposure angle.

3.8 Diffraction efficiency

A simple, and fast technique is utilised by integrating CCR with Nd: YAG pulsed laser to obtain phase conjugated nanostructures. Fabrication of nanostructures using a cornercube retroreflector is efficient and robust, showing selective laser ablation though laser interference lithography on ink-coated glass substrates. Optical properties of the recorded 1D/2D ink-based nanostructures showed multiple highly-intense diffraction orders and more efficient optical phase conjugation. Light diffraction properties of the different orders from the non-diffracted zero-order were symmetric and displayed an efficient inversion of the wavefronts through monochromatic and broadband light at normal illumination. The diffracted light intensity from the conjugated ink-based nanostructures also showed an approximately two-fold increase in efficiency (at red light normal illumination) compared to conventional diffractive gratings. Figure 3. 8a-f shows microscopic images of the ink-based conventional and conjugated nanostructures, its simulated FFT patterns, and far-field diffraction patterns through monochromatic light (red, green, and violet) at normal illumination. The diffracted light plots along the horizontal direction had similar optical properties (Appendix-A, Figure S3.6). However, diffracted light intensities were compared between the conventional and conjugate orders (Figure 3. 8g-i). Phase conjugate nanostructures had higher efficiency of light diffraction

than conventional gratings; red as 2:1, green as 2:1.2, and violet as 2:1.5. These nanostructures were fabricated by infrared laser beam (λ=1064 nm) so the gratings diffracted red light more efficiently than green and blue lights. Measured horizontal distance between the first order and the central diffraction spot was for violet (min.) ~8.9 mm, green ~13 mm, and red (max.) ~18 mm during light transmission through conjugated nanostructures. Similarly, vertical mutual distance between the spots of first order was violet ~1.7 mm (min.), green ~2.1 mm, and red ~2.5 mm (max.) light transmission through conjugate gratings, respectively, which showed longer wavelength diffraction at higher angles. Therefore, maximum light diffraction from the ink-based conjugated nanopatterns may have possible applications in printable diffraction gratings and micro optical devices.

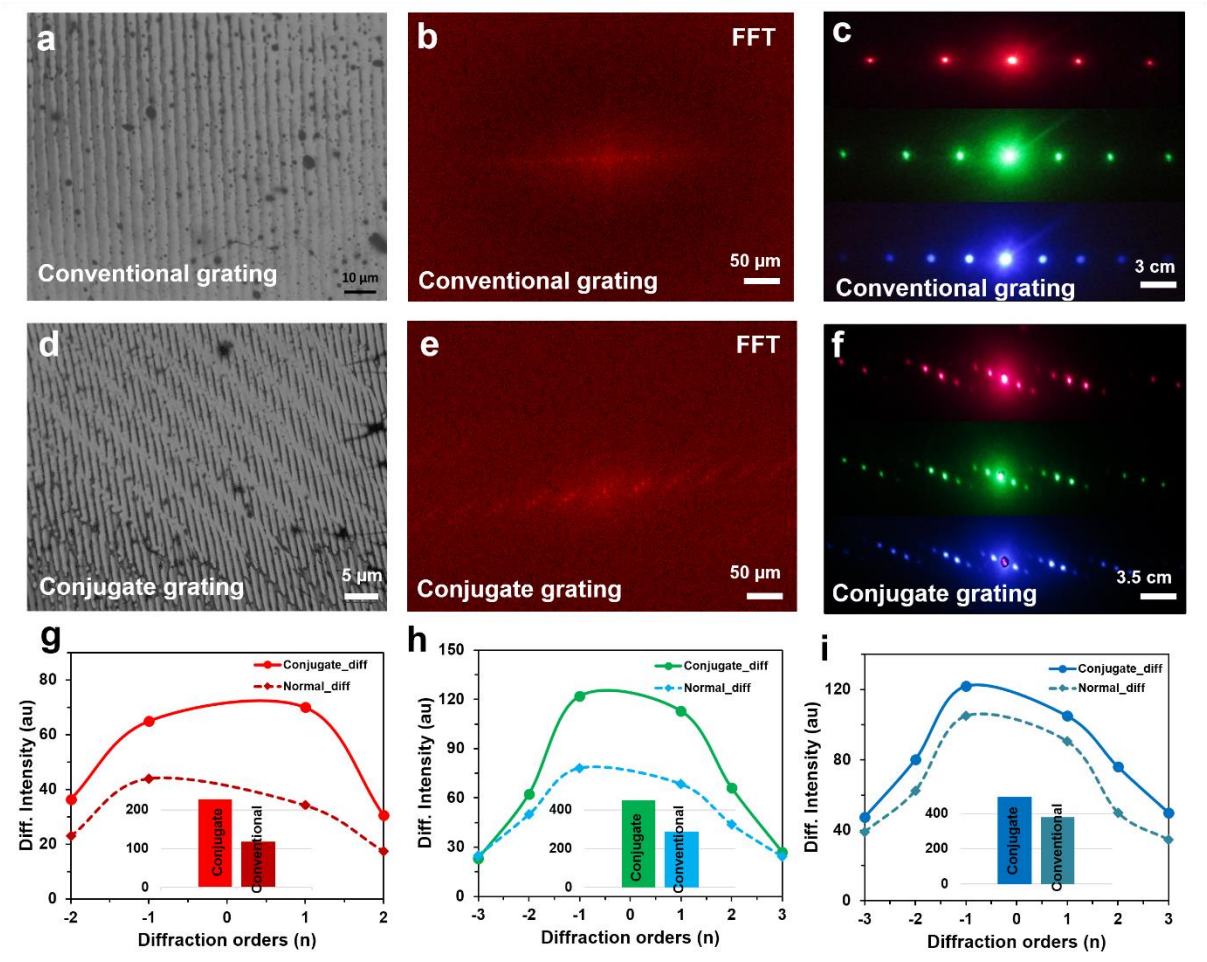

Figure 3. 8: Comparison between ink-based conventional and phase conjugate nanostructures in terms of light diffraction. (a-c) Optical microscopic image of conventional ink-based nanostructure, FFT simulation, and light diffraction with monochromatic beam at normal illumination. Scale bars = 10 μm, 50 μm, and 3.0 cm, respectively. (d-f) Optical microscopic image of conjugated ink-based nanostructure, FFT simulation, and light diffraction with monochromatic light at normal illumination. Scale bars = 5 μm, 50 μm, and 3.5 cm, respectively. (g-i) Optical light diffraction of the conventional and conjugated nanostructures through red, green, and violet light at normal illumination.

3.9 Discussion and summary

Ink based phase conjugate nanostructures were fabricated by integrating a CCR and nanosecond laser in Denisyuk reflection holography mode. Recorded ink-based nanostructures in the form of periodic gratings diffracted light in phase conjugation manners similar to the function of a CCR. Permanent ink was coated on silica glass, which is easily available, non-

toxic and cost effective rather than metallic coatings which need extended facilities like sputtering etc. to prepare holographic film. For broadband light illumination phase conjugate nanostructures provided wavelength selective diffraction based on illumination angles. Nanofabrication through laser interference-based lithography in Denisyuk reflection mode is a simple and cost-effective process which does not require connections with expensive equipment as compared to e-beam lithography or FIB milling which are required to be connected with expensive SEM etc. for operations. 1D/2D phase conjugate nanostructures have been produced in ink-substrates through optimized parameters. The projection experiments through an image screen setup allowed displaying phase-conjugated diffraction patterns at the far-field. The diffracted wavefronts showed symmetrically and phase-inversion from non-diffracted light. Conjugated surface patterns showed a two-fold increase in diffraction intensity at monochromatic red-light normal illumination compared to simple gratings. Phase conjugation diffraction property remained consistently in all fabricated nanostructures regardless the parameters variations used to change the size and surface morphologies as shown in figure 3.9 (a-f).

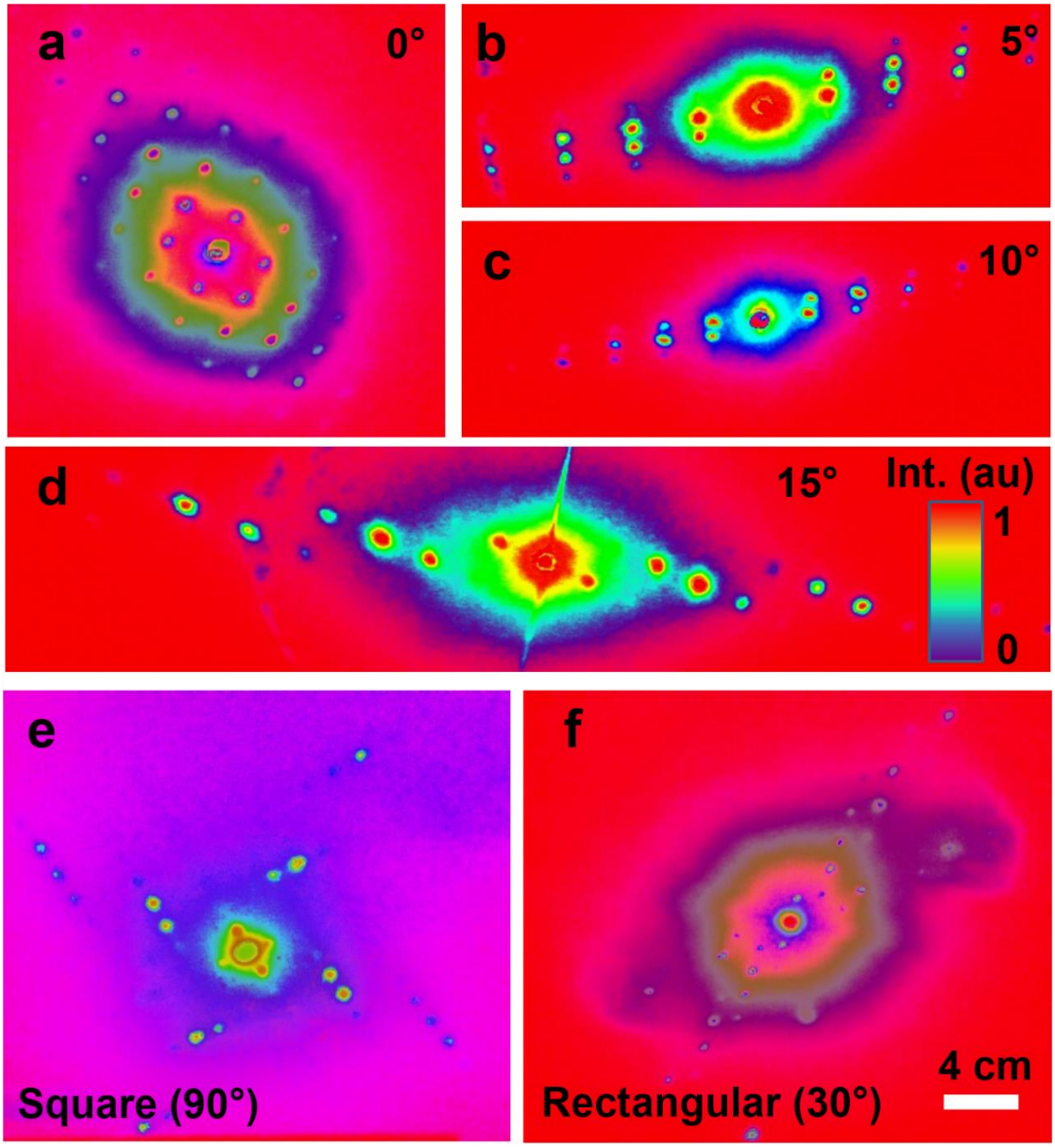

Figure 3. 9: Thermal images of the ink-based 1/2D conjugated diffraction patterns. (a-d) Thermal 1D diffraction patterns with tilt angle (θ) variation. (e.f) Thermal images of 2D square (90°) and rectangle (30°) diffraction patterns. Scale bar = 4.0 cm.

Multiple interference patterns were produced to fabricate 2D phase conjugate nanostructures by directing the incident beam toward the centre of CCR, where the incident beam split into smaller fragments. Each fragment retroreflected toward the source, along the opposite direction with respect to the incident beam, resulting in multiple interference patterns. Only

retroreflected standing waves contributed to the fabrication of the conjugate nanostructures, which had high-energy intensity to ablate the ink recording medium. Exposure parameters were varied to examine their influence on the characteristics of the recorded holograms in the form of periodic gratings and resulting images of the diffraction patterns in the far field. Optical phase conjugation was observed for both 1D and 2D ink-based nanostructures. The diffracted light intensity from the conjugated nanostructures were symmetrical. The phase-conjugated diffraction plots showed inverse symmetry between same order numbers on the left and right side with respect to non-diffracted zero-order. Thermal images of the 1D/2D diffraction patterns also showed symmetrical inversion properties of the light intensities (Figure 3. 9). Optical performance of the gratings were compared for the conventional diffraction spots and the phase conjugate diffracted spots. It is anticipated Ink-based holographic nanofabrication may have improved applications in printable low-cost optical devices include diffraction gratings, tunable wavelength-selective filters, diffusers, and lenses. A single-step laser pulse ablation is a facile, reliable and efficient technique in terms of cost and device production time to record holographic patterns on various light absorbing materials including transparent/opaque polymers and dyes. Ink-based conjugate diffraction patterns having unique morphology with multiple features is a step forward in holography and can be utilized to create numerous novel applications in encrypted data storage, identification (business cards), biosensing, and security labels.

References (iii)

1. Yariv, A., *Phase conjugate optics and real-time holography.* IEEE Journal of Quantum Electronics, 1978. **14**(9): p. 650-660.
2. He, G.S., *Optical phase conjugation: principles, techniques, and applications.* Progress in Quantum Electronics, 2002. **26**(3): p. 131-191.
3. Ahmed, R., et al., *Color-selective holographic retroreflector array for sensing applications.* Light: Science & Applications, 2017. **6**(2): p. e16214.

4. Ahmed, R., et al., *Printable ink lenses, diffusers, and 2D gratings.* Nanoscale, 2017. **9**(1): p. 266-276.
5. AlQattan, B., et al., *Holographic direct pulsed laser writing of two-dimensional nanostructures.* RSC advances, 2016. **6**(112): p. 111269-111275.
6. Alqurashi, T., et al., *Nanosecond pulsed laser texturing of optical diffusers.* AIP Advances, 2017. **7**(2): p. 025313.
7. Ahmed, R., et al., *Phase-conjugated directional diffraction from a retroreflector array hologram.* RSC Advances, 2017. **7**(41): p. 25657-25664.
8. Vasconcellos, F.d.C., et al., *Printable surface holograms via laser ablation.* Acs Photonics, 2014. **1**(6): p. 489-495.
9. Zhao, Q., et al., *Printable ink holograms.* Applied Physics Letters, 2015. **107**(4): p. 041115.
10. Khalid, M.W., et al., *Holographic Writing of Ink-Based Phase Conjugate Nanostructures via Laser Ablation.* Scientific reports, 2017. **7**(1): p. 10603.
11. Yetisen, A.K., et al., *Mechanism of multiple grating formation in high-energy recording of holographic sensors.* Applied Physics Letters, 2014. **105**(26): p. 261106.
12. Brignon, A. and J.-P. Huignard, *Phase conjugate laser optics.* 2004.
13. Bozhevolnyi, S.I., E.A. Bozhevolnaya, and S. Berntsen, *Theoretical model for phase conjugation of optical near fields.* JOSA A, 1995. **12**(12): p. 2645-2654.
14. Yaqoob, Z., et al., *Optical phase conjugation for turbidity suppression in biological samples.* Nature photonics, 2008. **2**(2): p. 110.
15. Yoder, P., *Study of light deviation errors in triple mirrors and tetrahedral prisms.* JOSA, 1958. **48**(7): p. 496-499.
16. Günter, P., *Holography, coherent light amplification and optical phase conjugation with photorefractive materials.* Physics Reports, 1982. **93**(4): p. 199-299.
17. Marrakchi, A., J. Huignard, and J. Herriau, *Application of phase conjugation in Bi12Si O20 crystals to mode pattern visualisation of diffuse vibrating structures.* Optics Communications, 1980. **34**(1): p. 15-18.
18. Butt, H., et al., *Visible diffraction from graphene and its application in holograms.* Advanced Optical Materials, 2013. **1**(11): p. 869-874.
19. Jiang, N., et al., *Laser Interference Lithography for the Nanofabrication of Stimuli-Responsive Bragg Stacks.* Advanced Functional Materials, 2018. **28**(24): p. 1702715.
20. Chipman, R.A., et al., *Wavefront correcting properties of corner-cube arrays.* Applied optics, 1988. **27**(15): p. 3203-3209.
21. Wolf, E., et al., *Interference pattern produced on reflection at a phase-conjugate mirror. I: Theory.* JOSA B, 1987. **4**(8): p. 1260-1265.
22. Jacobs, A.A., et al., *Interference pattern produced on reflection at a phase-conjugate mirror. II: Experiment.* JOSA B, 1987. **4**(8): p. 1266-1268.
23. Born, M. and E. Wolf, *Principles of optics: electromagnetic theory of propagation, interference and diffraction of light*. 2013: Elsevier.
24. Butt, H., et al., *Carbon nanotube biconvex microcavities.* Applied Physics Letters, 2015. **106**(12): p. 121108.

Chapter 4 Flexible Cornercube Retroreflector Array

4.1 Overview

In this chapter, flat, thinner, and flexible CCR array based on stamping/embossing process is presented. A replicated copy of polymeric CCR array on a flexible surface showed far-field diffraction property. This chapter introduced polymeric CCR array fabrication through PDMS replication, and some possible applications in section 4.2. Sample preparation, CCR array replication, and FEM modelling are presented in sections 4.3. Optical properties of dynamic CCR array is reported in section in section 4.4. Optical characterization and stress/strain modelling property of CCR array is presented in section 4.5. Finally, chapter is summarized and discussed in section 4.6.

This chapter is produced from '' **Khalid, M.W.,** et al., Flexible cornercube retroreflector array for temperature and strain sensing. RSC advances, 2018. 8(14): p. 7588-7598.''

4.2 Introduction

An alternative to conventional planar, rigid and brittle electronic devices are soft polymeric and more flexible optical devices [1]. Temperature sensors such as Classic mercury glass thermometer, infrared Pyrometer, Electronic thermometer (made of thermocouple, thermistor, RTD etc.) have active components and require a power supply to function; they have limitations such as high cost and manufacturing complexity, and they are prone to electromagnetic (EM) and thermal noise interference [2]. Sensing platforms based on optical components to detect and monitor environmental factors such as humidity, pressure, shear, and torsion have applications in robotics, wearable devices, medical diagnostics, and healthcare monitoring [3-8]. Fiber optics sensors have been utilized in temperature and strain quantification due to certain advantages such as lower costs, compactedness, flexibility, low

noise/interference, high sensitivity and reliability [9-11]. However, these optical devices cannot be used to measure temperature and strain simultaneously and have often construction complexity. Therefore, the development of simple, cost-effective, and robust optical sensing technologies is highly desirable for remote sensing applications.

A CCR array is composed of a number of retroreflectors arranged in series. Each CCR in the array consists of three mutually perpendicular intersecting surfaces that produces unique retro-reflected light under light illumination [12-14]. the retroreflection property of a CCR array are based on reflection from each mirrored surface [14, 15]. Directional properties of a CCR array help reflect light back to the source and is independent of the illumination angle which makes it a perfect choice to be used in remote sensing applications [16]. Directional property of CCR array have also applications in imaging, navigation, displays, sensors, optical communication, and low-powered sensor networks [17-22]. Although CCR array made by joining perfect CCRs are always desired to produce retroreflection light [23], however imperfect CCR array also have practical applications in traffic signals or car lights [20, 24]. Imperfect CCR array produces quasi-retroreflected light formed through intentionally introduced artefacts or structural imperfections during their fabrication process [23]. CCR array fabrication is based on a range of methods including microelectromechanical methods, nanoimprinting, lithography, and direct laser writing [25-27]. Mask-based direct etching methods, diamond micromachining, and laser ablation techniques have been used to fabricate CCR array structures [26, 28, 29]. Fabrication techniques are limited due to being expensive, expertise-dependent, requiring advanced equipment, complex and time-consuming processes. Faster and lower cost holography techniques have been used recently to fabricate CCR array and miniature diffractive optical devices (lens, diffusers, and gratings) [14, 20, 30].

A method to rapidly produce optical sensors composed of a CCR array structured in polymer polydimethylsiloxane (PDMS), through replication process is demonstrated. This fabrication

is robust, flexible, low cost, simple, immune to EM and thermal noise interference and is passive (i.e. no power supply needed). PDMS based sensors can be useful in harsh environments due to their stable chemical properties [31-33]. Transmission of light of the desired wavelength could be achieved by an appropriate concentration of a doping dye; PDMS is a non-toxic and inert silicon-based organic polymer capable of replicating 3D structures in microscale [34], and has been a popular choice for soft lithography due to its robust nature, low cost and ease of fabrication to replicate microscale structures [28]. Compared to a traditional etching and bonding approach, PDMS microfabrication is rapid and simple. PDMS has a refractive index of ~ 1.4 and is transparent in the visible range (400 - 800 nm) [35], and inert properties make PDMS suitable for prototyping and testing [36].

Monochromatic light illumination of the polymerised CCR array yields a far-field triangle response on the image screen. Any perturbation (expansion or compression), either due to mechanical stress or thermal effect, alters the internal angle size of the fabricated flexible CCR array and therefore optical response (retroreflection or far-field triangular structure) changes accordingly. The retroreflected light from the flexible CCR array is tuned based on external stimuli such as temperate or strain caused by weight suspension and inward/outward bending. Change in the dimensions of structures (compression or expansion) due to environmental factors will changes the profile of light transmitted/reflected through/from an elastomeric CCR array, which can be used to measure and quantify the change in those environmental conditions.

4.3 Experiments and results

4.3.1 Sample preparation and CCRs replication

Mechanical stamping/embossing process is used to fabricate flexible CCR arrays (Figure 4.1a). PDMS monomer and curing agent (10:1, v/v) are mixed to prepare the PDMS polymer solution.

The mixture process was run for 20 mins by a magnetic stirrer and followed by ultrasonic cleaning to remove air bubbles from the mixture. CCR arrays were placed in a Petri dish and fixed with the rotary stage of a spinner. The PDMS precursor mixture was poured into the dish and rotated through 400, 600, and 800 rpm for the uniform distribution on the top of CCR mould. Different levels of chemical mixtures were poured into the Petri dish and rotation speed was increased to make thicker to thinner samples (Figure 4.1b).

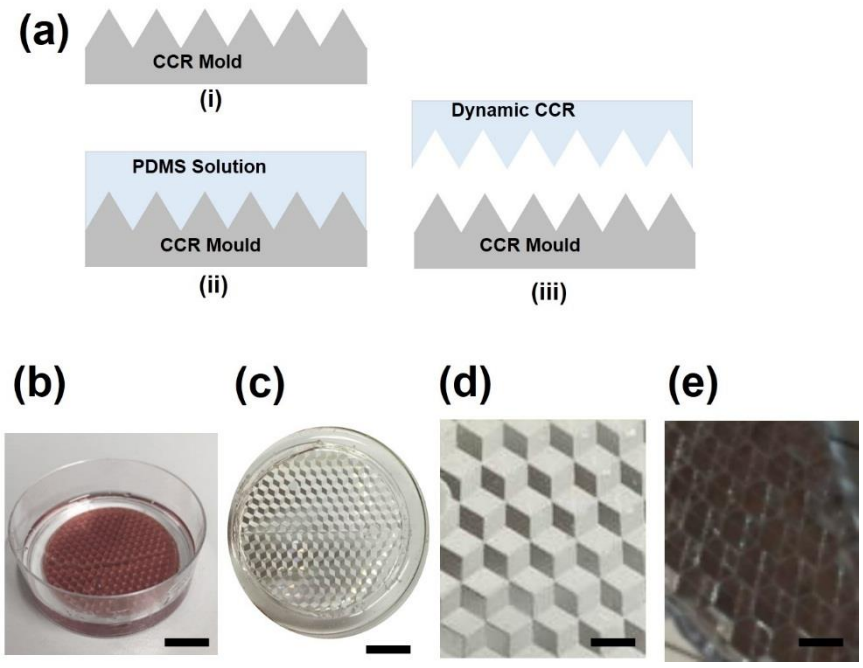

Figure 4. 1: Dynamic CCR array fabrication. Schematic diagram (a-c) of sample fabrication via PDMS replication method. Scale bar =1.5cm. (d,e) Replicated flexible CCR array, magnified version of without and with Au coated samples. Scale bars =1.5, and 0.2cm.

Samples were kept at 50 °C for 3 hours to cure the mixture. The fabricated PDMS replica was peeled off from the original CCR array mould. Replicated structures were immediately ready for optical sensing in transmission mode (Figure 4.1c). The fabricated flexible CCR array consisted of internal three mirror surfaces (Figure 4.1c). For further examinations of the CCR array and checking the feasibility in reflection mode, a 20 nm thick layer of gold coating was sputtered on the surface to increase the reflectivity. The fabricated coated samples consisted of

micro cubic-corner retroreflector (MCCR) array structures, where three mirror-reflection planes were in hexagonal patterns (Figure 4.1d).

4.3.2 FEM modelling

COMSOL Multiphysics software based on FEM was used to model the flexible CCR array. Optical retroreflection/directional properties from the flexible CCR array were modelled through broadband light illuminated to the Au material based triangular grating surface at normal, and tilted angles (10°, 20°, 30°, and 40°). Temperature and strain effects on the flexible CCR array was simulated through 10%, 20%, and 30% expansion of rectangular structure. The reflected light from the triangular grating was measured from the hemispherical surface surrounded by air medium. User define customised physics-controlled mesh (mesh size was one fourth of wavelength) was utilised to for modelling. Customised mesh containing more mesh elements around the spherical domain. For further reduction of element number a swept mesh is applied which considerably minimises the size of the model and complexity of simulation. Customising the meshing also helps to reduce memory requirement by controlling quality of elements by creating efficient and accurate simulation environment. The continuity and scattering boundary conditions were considered at triangular grating and hemispherical surface during FEM simulation. Sub-meshing (one-fourth of incident light) and mesh convergence test was performed during simulation for the result accuracy. Triangular meshing elements were considered at the simulation domain. The maximum degree of freedom used was 137870. The completed mesh consisted of 701 boundary elements and 19605 domain elements. The solution time was 30 seconds and 30 minutes during 2D and 3D simulation respectively. Therefore, the 2D simulation was performed to reduce additional computational time and complexity. The CCR array structure viewed as a triangular grating structure (side view). Therefore, compression or expansion of the flexible CCR array was considered as the variation of triangular grating structures.

4.4 Optical properties of flexible CCRs array

The optical property of flexible CCR arrays is based on the total internal reflection (TIR) effect [14]. The incident light is reflected three times from each mirror plane once and becomes a retroreflected beam. The retroreflected light is phase conjugated to the incident light. Figure 4.2 shows the optical reflection property of a plane mirror, a rigid CCR array, and flexible CCR array. All three optical devices change the direction of the normal component of the reflected light, however, a plane mirror does not change the amplitude and phase component of the reflected light (Eq. 2). As incident angle changes the reflection angle also changes, obeying Snell's law. However, the CCR array changes both amplitude and phase components of the of the light incident on it (Eq. 3). The incident light is retroreflected from the CCR array and is independent of illumination angle. The flexible CCR array changes the internal angles and dimensions of the three-mirror surface due to applied stress.

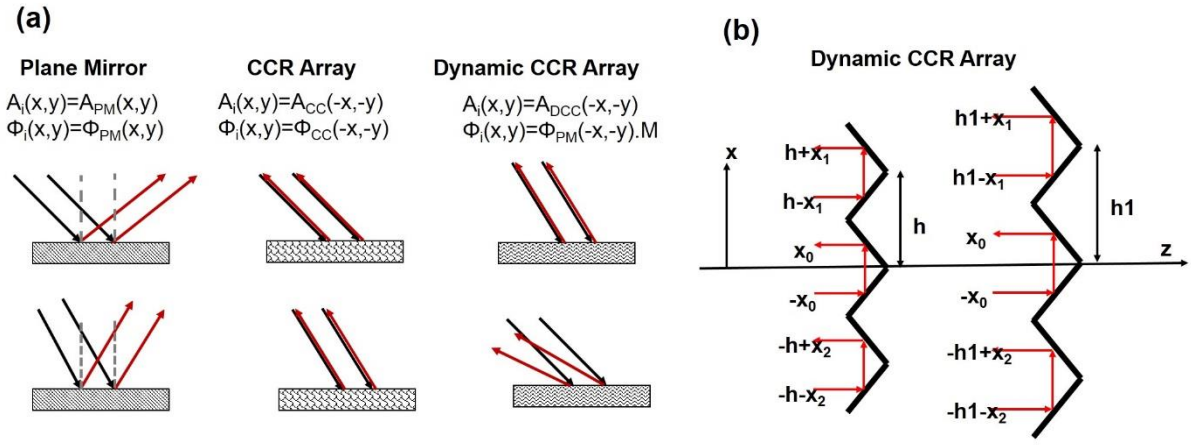

Figure 4. 2: (a-b) Reflection and retroreflection property of plane mirror, CCR array, and dynamic CCR array.

The retroreflection property works up to certain illumination angle; light scatters at larger angles and is unable to fulfil three mirrors based retroreflection (Eq. 4, Figure S2). Directional reflection property of a flexible CCR array can be expressed based on wavefront analysis.

Consider a plane wave propagating along z-axis (Eq 4. 1) under paraxial approximation (K_z= K = $2\pi/\lambda$):

$$E_i(x,y,z) = A(x,y)e^{(i\phi(x,y)-ikz)} \tag{4.1}$$

The reflected light from the plane mirror is:

$$E_{PM}(x,y,z) = A(x,y)e^{(i\phi(x,y)+ikz)} \tag{4.2}$$

The reflected light from phase conjugate mirror is:

$$E_{PCM}(x,y,z) = A(x,y)e^{-i\Phi(x,y)+ikz} \tag{4.3}$$

The reflected light from CCR array is:

$$E_{CCR}(x,y,z) = \sum_{m,n} A(2mh-x,2nh-y)e^{(i\phi(2mh-x,2nh-y)+ikz)} a_{CC}(x,y)rect(\frac{x-mh}{h},\frac{y-nh}{h}) \tag{4.4}$$

E_{PCM} (eq.4.3) can be considered as E_{CCR} (eq. 4.4) if following conditions are satisfied [20]:

(i) If amplitude in each CCR remains constant,

$$A(x,y)rec(\frac{x-mh}{h},\frac{y-nh}{h}) \approx A(mx,ny)rect(\frac{x-mh}{h},\frac{y-nh}{h})$$

(ii) And if in each CCR phase remains in linear relationship,

$$\phi(x,y)rec(\frac{x-mh}{h},\frac{y-nh}{h}) \approx \phi(k_{x,m,n}x+k_{y,m,n}y)rect(\frac{x-mh}{h},\frac{y-nh}{h})$$

therefore equation 4.4 can be written as,

$$E_{CCR}(x,y,z)=\sum_{m,n} A(mh,nh)exp(2i(mhk_{x,m,n}+nhk_{y,m,n}y)+ikz)exp(-i(mk_{x,m,n}+np_{y,m,n})$$

$$a_{ccr}rect\frac{x-mh}{h},\frac{y-nh}{h}) \tag{4.5}$$

Here, *exp (2i(*$mhk_{x,m,n}+nhk_{y,m,n}$*))* and *exp(-i(*$mk_{x,m,n}x+nk_{y,m,n}y$*))* represent the phase conjugation and phase mismatch between the segments. Figure 4.2 (a, b) illustrates amplitude and phase reversal of the reflected wave from plane mirror, CCR array, and Dynamic CCR array.

Thus, the reflected light from a flexible CCR array can be written as:

$$E_{DCCR}(x,y,z) = \sum_{m,n} A(2mh-x,2nh-y)e^{(i\phi(2mh-x,2nh-y)M+ikz)}a_{CC}(x,y)rect(\frac{x-mh}{h},\frac{y-nh}{h}) \quad (4.6)$$

where $A(x,y)$, $\phi(x, y)$ and $rect(x, y)$ represent amplitude, phase and rectangular functions, respectively. m and n are optical field segments of the reflected light by each single CCR. M represents the optical phase modulation of reflection due to size change of the flexible CCR array. $a_{cc}(x,y)$ is a scalar quantity defined as the aperture function of the reflected beam amplitude. *rect* (x,y) represents a rectangular function and defined as 1, where abs$(x,y)<1/2$ and 0 otherwise [20].

4.5 Dynamic modelling and optical characterization

Optical characterization of the flexible CCR was performed using monochromatic light illumination and a far-field experimental setup (Figure 4.3a). Upon illumination with a monochromatic light source, the flexible CCR array produced a triangular shape on the image screen in both transmissions and reflection mode. The spot size of the incident laser beam was larger than the dimensions of a single cornercube structure. The incident light transmitted through each plane once and some part of the incident light was reflected and propagated along plane-to-plane of the cornercube. All these segments of light interfere and produce a triangular shape at the far field. In the transmission mode, a sample holder was used to keep the sample fixed and the sample was illuminated in the normal direction with the monochromatic light source.

In the reflection mode, monochromatic light was illuminated at 30° tilt angle (Appendix-B, Figure S4.1). The reflected/transmitted light produced a far-field triangular interference pattern on the image screen, which was captured using a digital camera. External weight was added to the sample holder to physically expand the elastomer CCR array sample. Figure 4.3b and c show the strain sensing response of the flexible CCR as a function of external load. The size of the interference triangle increased as the weight increased during transmission/reflection mode. Reflected or transmitted light through/from the flexible CCR array depended on internal angle variation. Therefore, minimum or maximum reflection distance between two interference points of the triangular structure changed due to physical expansion or compression of the flexible CCR array structure. During reflection/transmission mode, minimum reflection distances were measured with lower weights and normal green (532 nm) light illumination.

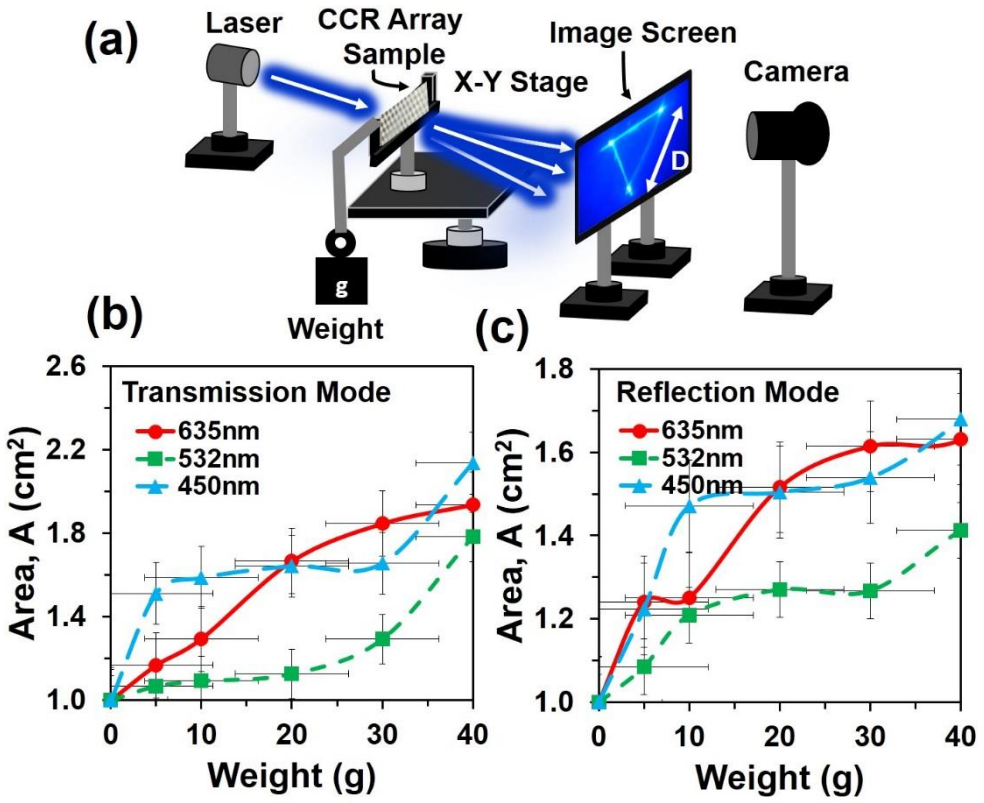

Figure 4. 3: (a) Schematic far-field experiment setup for optical characterization during transmission mode. (b, c) Reflection area of transmitted and reflected triangle as a function of weight suspension.

The angle between the CCR structures increased as the CCR array expanded due to high strain or temperature variation. Figure 4.4a, and b show a 3D simulation diagram and associated mesh diagram with the variation of triangular grating structures.

Figure 4.5a shows a hemispherical block diagram for FEM simulation of the flexible CCR array. The CCR array structure viewed as a triangular grating structure (side view). Therefore, compression or expansion of the flexible CCR array was considered as the variation of triangular grating structures. Figure 4.5b shows reflected light intensity as a function of the arc length of the incident laser wavelength. The reflected light intensity also increased as the wavelength increased. Therefore, minimum and maximum light reflections were observed with violet (450 nm) and red (635 nm) light under normal illumination respectively.

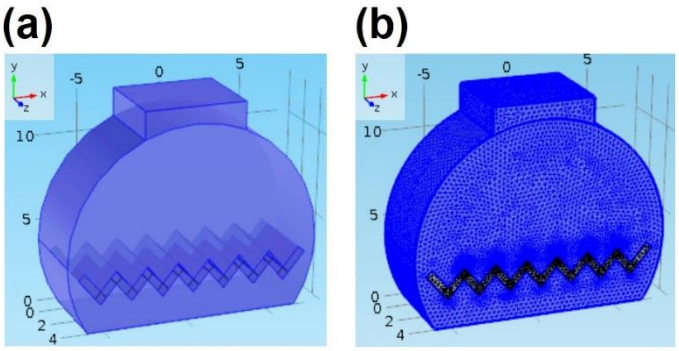

Figure 4. 4: (a-b) 3D simulation and mesh diagram.

Further simulations were also carried out with the expansion of cornercube structures and associated light reflection properties. Figure 4.5c shows reflected light intensity as a function of arc length due to the triangular mesh geometry variation by 10%, 20% and 30% (having 90° triangular angle). Fixed wavelength (635 nm) was considered during triangular structural variation due to strain. However, similar simulation results were also observed with violet (450 nm) and green (532 nm) light illumination with triangular structural variation (FigureS4,5). Figure 4.5d-f shows the electric field intensity distribution due to incident wavelength

variation. Maximum and minimum light reflection from the triangular grating structures were observed due to red (635 nm) and violet (450 nm) light illumination. The retroreflection property was valid for every illumination wavelength. Similarly, Figure 4.5g-i shows electric field intensity distribution due to triangular structure variation with fixed incident wavelength (635 nm). Maximum and minimum light reflection from the triangular structures were observed at the maximum (30%) and minimum (10%) from normal illumination. Comparable light reflection field intensity distribution was also observed with green and violet light normal illumination (Appendix-B, Figure S4.2, 4.3). Maximum light reflected towards the source was reduced compared to a fixed CCR size. However, retroreflection property was also valid with CCR array size variation and at fixed illumination wavelength.

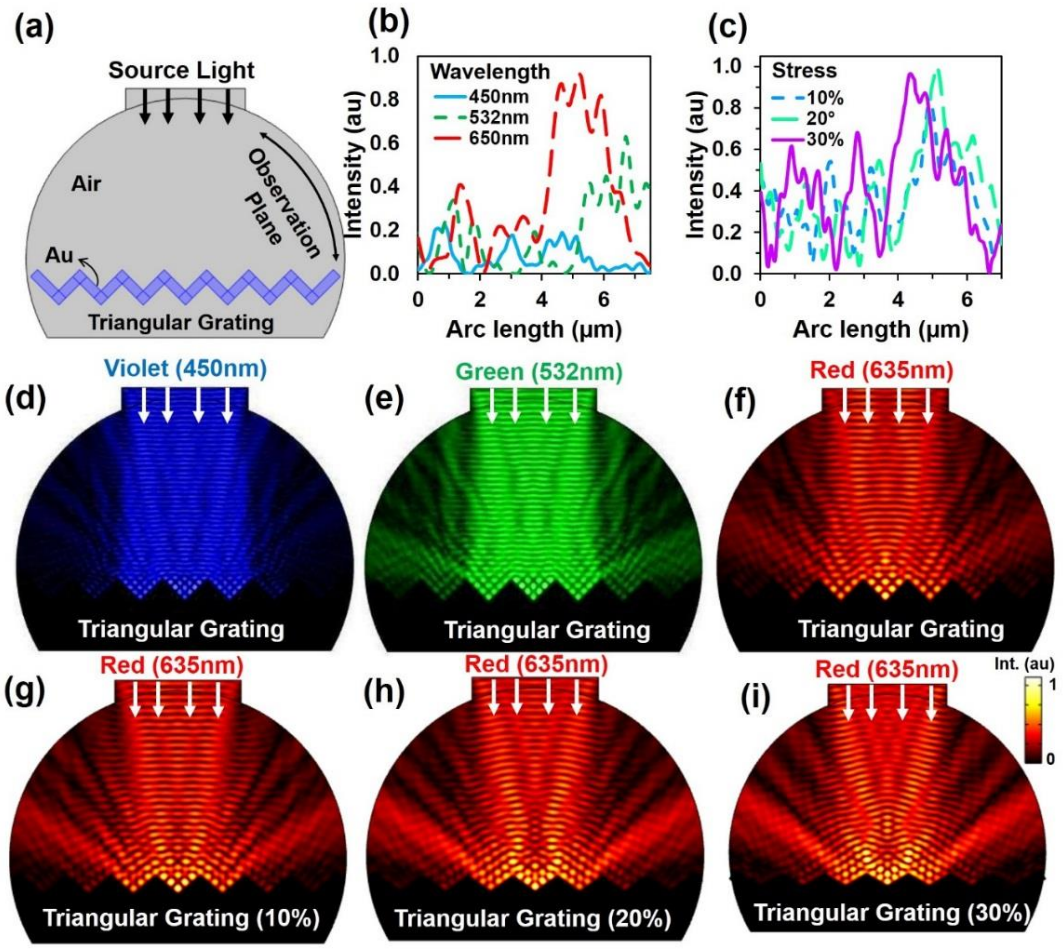

Figure 4. 5: Computation modeling of light reflection from triangular grating structure with normal light illumination. (a) Schematic diagram of FEM simulation. (b) Reflected light intensity with monochromatic normal light illumination. (c) Reflected light intensity with stress variation. (d-i) Electric field distribution with monochromatic light illumination and stress variation.

Further simulations were conducted to observe light retroreflection with the fixed and triangular grating structural variation at tilted red (635 nm) light illumination. Figure 4.6a shows reflected light intensity with illumination angle variation. Generally, the lower reflection was observed at lower tilted angles. However, light reflection had fewer influxes with the triangular grating structure due to direction property of CCR structure. Figure 4.6b-d shows the electric field intensity distribution with 10°, 20°, and 30° tilt illumination. Directional reflection intensity towards the source increased with tilted illumination. Figure 4.6e-h shows

light retroreflection, reflection property with a fixed tilt angle of 10° and 10%, 20% and 30% expansion of triangular structure from the normal. The reflected light intensity increased as the structure expanded. Therefore, the maximum (90%) and minimum (20%) light reflection was observed at 30% and 10% expansion of triangular structure respectively. Figure 4.6f-h shows retroreflection, reflection electric field light distribution with (10% to 30%) and fixed angle (10°) illumination. Maximum reflection field intensity distribution was observed at 30% of triangular structure expansion. Figure 4.6i-l shows light reflection property with tilt angle (20°, 30°, 40°) variation and 10%, 20% and 30% triangular structure expansion from the normal. As tilt angle and triangular structure expansion increased, reflected light intensity also increased. Maximum (90%) and minimum (30%) light reflection from the triangular structure was observed at the maximum and minimum tilted angle of triangular structure expansion from the normal. Figure 4.6i-l shows the electric field intensity distribution with tilted illumination and triangular structure expansion. Maximum light reflection distribution was observed with a maximum tilted angle (40°) and triangular structure expansion (30%) from the normal. The light reflection was also observed with triangular structure variation, green and violet light at tilt angle variation are shown in Appendix-B, Figure S4.4-4.7. In all the electric field intensity distributions, maximum light reflected towards the source and showed retroreflection property and its validity with structural variation.

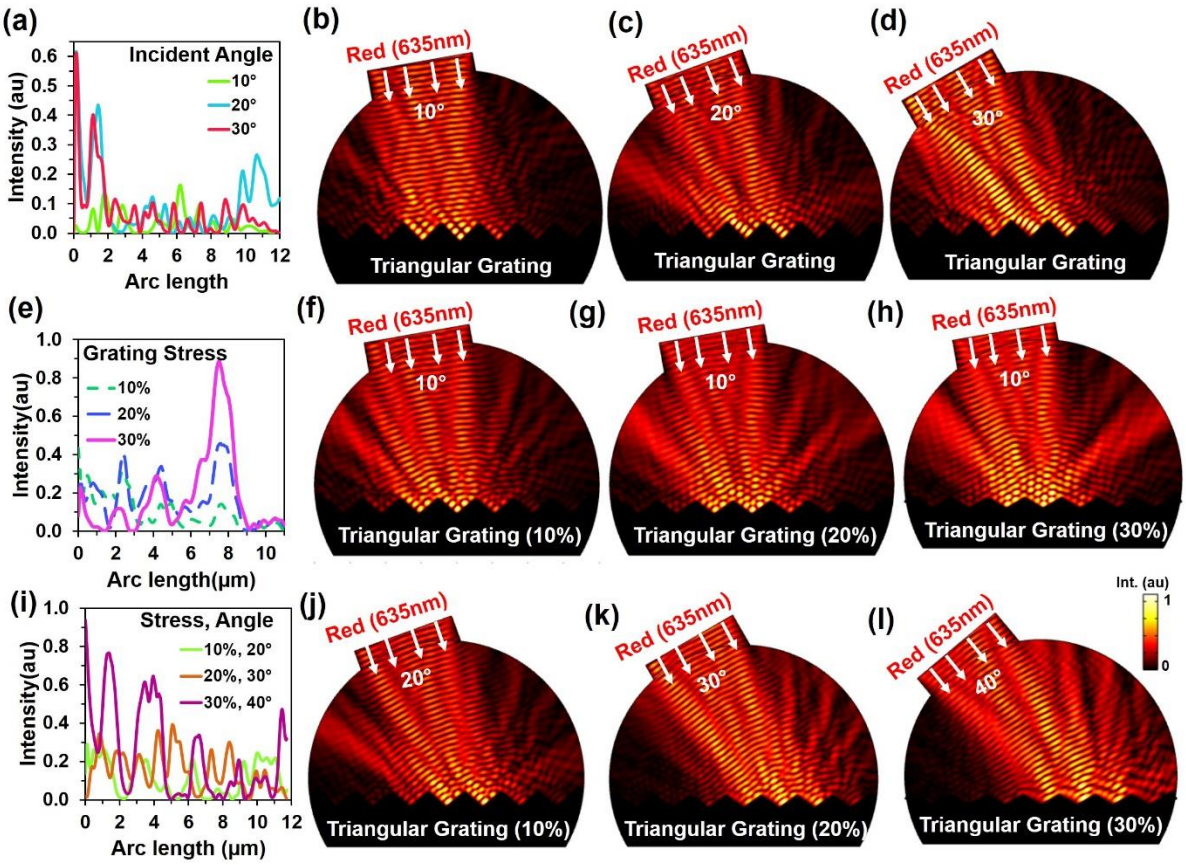

Figure 4. 6: Computation modelling of light reflection from triangular grating structure with tilted light illumination. (a-d) Reflected light intensity and electric field distribution and with tilted illumination (10, 20, and 30°) and fixed triangular grating structure. (e-h) Reflected light intensity and electric field distribution and with fixed tilted illumination (10°) and triangular grating structure expansion (10, 20, and 30%) from normal. (i-l) Reflected light intensity and electric field distribution with tilted illumination (20, 30, and 40°) and triangular structure expansion (10, 20, and 30%) from normal.

Light retroreflection from the triangular structure was predicted by computational modelling. Optical experiments were performed to observe the flexible CCR's response to the triangular structure variation based on external stimuli. Retroreflection property of the fabricated flexible CCR structure was observed through the reflection measurements. One of the important attributes of the CCR array is its directional property, i.e. incident light is reflected towards the source at any illumination angle. The flexible CCR structure strongly followed this directional

property. Retroreflective light was measured through an established optical setup to observe the directional property of the flexible CCR array and tune its optical property with external stimuli (Figure 4.7a).

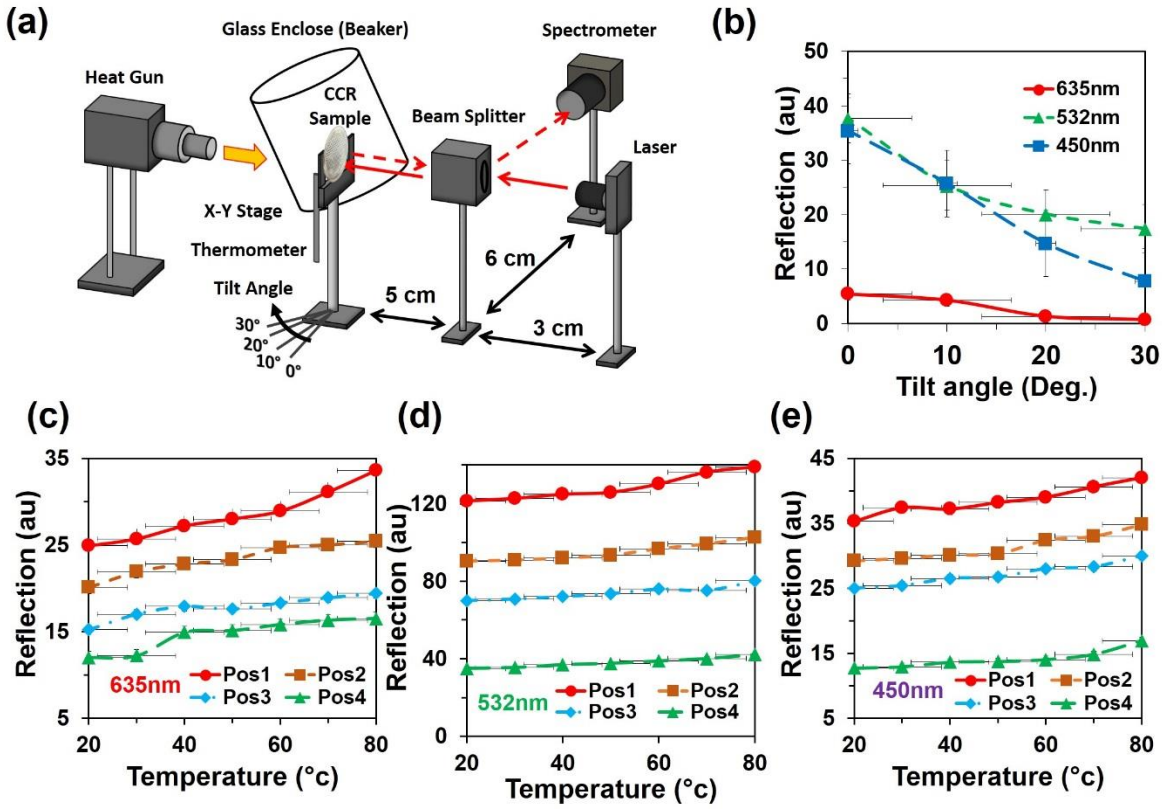

Figure 4. 7: Directional reflection of flexible CCR array with temperature variation. (a) Schematic experiment diagram for selective directional reflection measurement with temperature and angle variation. (b) Directional reflection of flexible CCR array as a function of tilted angle variation with red, green, and violet light normal illumination. (c-e) Directional reflection of flexible CCR array as a function of temperature variation with red, green, and violet light normal illumination at four different positions (pos1, pos2, pos3, and pos4).

The light was illuminated using a laser source and passed through the input port of a polarization-independent beam splitter. A spectrophotometer used to measure the intensity of the reflected light from the Au coated flexible CCR sample. Constant heat flux was supplied from a hot air blower (heat gun) to observe the temperature-dependent expansion of the flexible

CCR array structure and the associated reflected light intensity variation. A glass enclosure was used to ensure uniform temperature distribution and to reduce vibrational effects from the flow of heat. A mercury thermometer was used to measure the temperature of the enclosure. The distance between the sample and the beam can be adjusted as the experiment was set up on a rail system. An $x - y$ positioning stage held the flexible CCR sample, therefore the laser focus position could be chosen and was able to rotate at predefined angles to observe angle-dependent directional reflection. Heating the sample expanded the cornercube structures, which in turn enlarged the size of the reflected triangle and affected the optical response of the CCR array. A direct relationship was observed between the temperatures and reflected optical power for PDMS based CCR arrays.

The optical response was recorded on a far-field screen (a triangle) using various light sources (635 nm, 532 nm, and 450 nm) illuminated on the sample without a weight suspension. Weight was suspended from the free side of the sample and increased from $10\ g$ to $40\ g$ for the next trial. Increasing the weight elongated the cornercube array via mechanical strain force. Increasing weight increments increased the degree of expansion of the cornercube structure in the array, which affected the size of the transmitted triangle on the far screen and recorded with a digital camera. A direct relationship between increasing load and magnitude of the transmitted power (area of transmitted/reflected triangle) was measured consistently. In general, a $0.02\ N$ increment of applied inward force increased the area of the transmitted triangle by $0.2\ cm^2$. However, the strain produced by a specific force depended upon the thickness of the fabricated PDMS block (sample). The sample was also coated with a gold layer and kept at an angle of 120° to the light source and far-field screen to obtain data in reflection mode. Figure 4.7b shows directional reflection intensity as a function of tilt angle.

Directional reflected light intensity was measured with normal (red, green, and violet) light illumination at room temperature. Maximum and minimum light intensities were recorded with green and red light illumination. Directional reflected light intensity was measured at 4 different locations at different temperatures (Figure 4.7c-d); reflected light intensity increased with increasing temperature. Maximum and minimum directional reflections were observed with green and red light illumination respectively, with high and minimum temperature. Therefore directional reflection amount was tunable through temperature variation.

An angular directional reflection experiment was performed to measure the optical response of the flexible CCR array with temperature and tilt angle variation. Figure 4.8a-c shows directional reflection from the flexible CCR with a temperature range of 25-75 °C and tilt angle variation of 0°-30° with red (635 nm), green (532 nm) and violet (450 nm) light illumination. Maximum directional reflection was found at 0° and minimum reflection at 30°. Moreover, green and red light reflected the maximum and minimum amount of light. Figure 4.8d-f shows reflected light intensity as a function of temperature. The maximum intensity was at a smaller tilt angle (< 10°) for red, green, and violet light illumination.

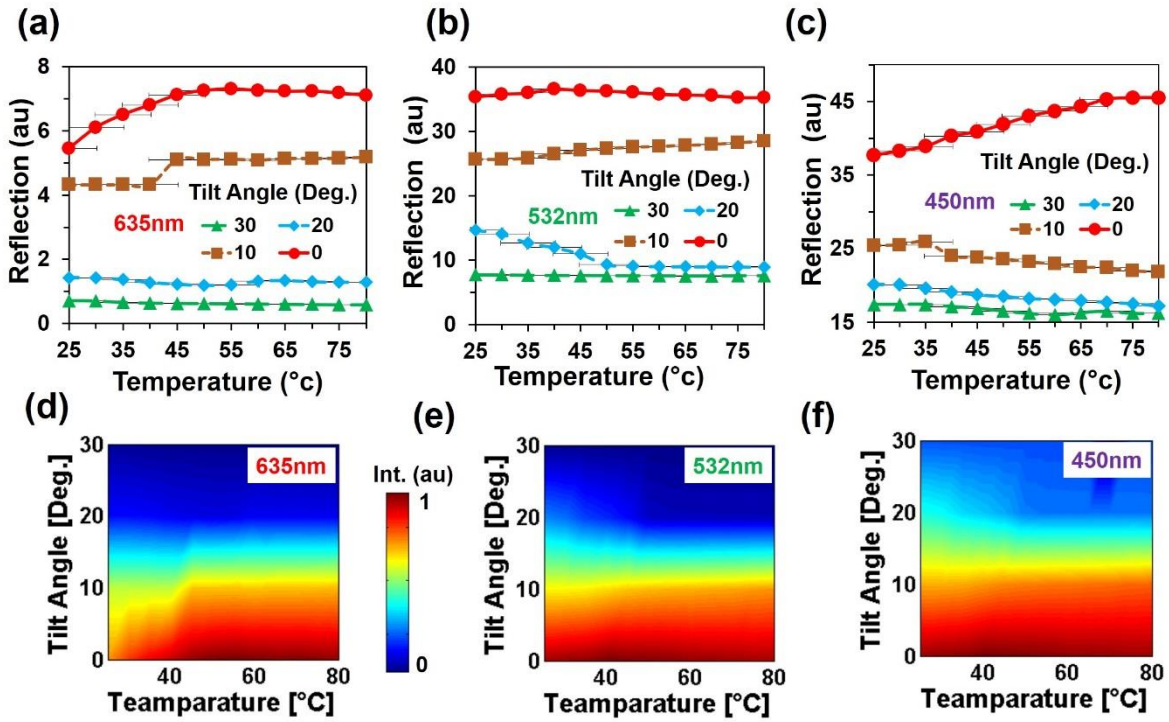

Figure 4. 8: Directional reflection of flexible CCR array with temperature and tilt angle variation. (a-c) Directional reflection of flexible CCR array as a function of temperature and tilted angle variation with red, green, and violet light normal illumination. (d-f) Directional reflected light intensity as a function of temperature variation with red, green, and violet light normal illumination.

Optical experiments were also performed to measure the optical response of the flexible CCR array due to inward and outward bending force in transmission and reflection modes (Figure 6). The optical response of the sample subjected to the applied force (compression or expansion) was captured from the image screen. The triangular profile stayed the same until a threshold value for perturbation was reached. Above this threshold force, optical response suddenly increased. The intensity *I*, of a laser at a point was defined as the energy per second per unit of area arriving at that point normal to the propagation direction ($I = Power/Area = P/A$). For a triangle with the base length *b* and height *h*, intensity can be expressed as $I = 2P/bh$. Change in the transmitted/reflected light intensity, I_c can be empirically correlated with the

strain as $I_c(\mathcal{E}) = I_o$, *if* $\mathcal{E} <$ *threshold* or otherwise, $I_c(\mathcal{E}) = \mathcal{E} \times I_o -$ *threshold*, where Ɛ is strain (degree of change in expansion due to applied force divided by initial structure without any force application), I_c is the change in intensity after force application and I_o is the initial intensity of light when no force is applied.

Figure 4.9a, b shows the area of reflection triangle as a function of inward force during transmission and reflection modes. As the inwards force increased, the area of the transmitted/reflected triangle increased with (red, green and violet) illumination in reflection and transmission mode. Figure 4.9b shows the area of reflected triangle increased by 0.9 cm2 (90%) as a result of 0.08 N applied inward force. During inward bending, the internal CCR structure and associated angle of planes reduced. As a result, the far-field reflected light produced a larger reflection triangle with increased inward force [20]. Figure 4.9c shows the far-field reflection triangle with an increased inward force which was captured using an image screen setup. Similarly, Figure 4.9d, e shows the area of the reflection triangle as a function of outward force during transmission and reflection modes. As the outward force increased, the area of reflected profile decreased with red, green and violet light illumination in reflection and transmission modes. During outward bending, the internal CCR structure and associated angle of planes increased. Figure 4.9f shows far-field reflection triangle with an increased outward force which reduced in size as a result. The area of the reflected triangle decreased up to 50% of the original area (i.e. no stress) due to 0.08 N of the outward applied force.

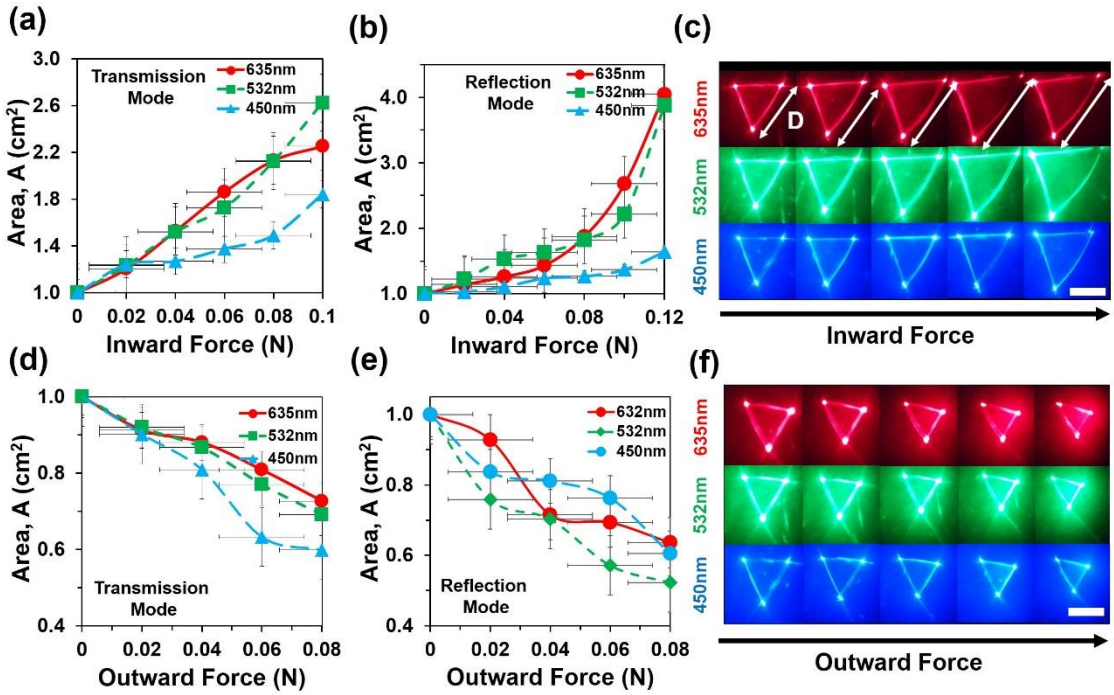

Figure 4. 9: Force sensing of flexible CCR array with inward and outward bending during transmission and reflection mode. (a, b) Reflection area of far-field reflection triangle as a function of inward force with red, green, and violet light illumination. (c) Far-field reflection triangle due to increased inward force. Scale bar = 0.5cm. (d, e) Reflection area of far-field reflection triangle as a function of inward force with red, green, and violet light illumination. (f) Far-field reflection triangle due to increased inward force. Scale bar = 0.5cm.

The directional retroflexion response of the flexible CCR array, when subjected to external stimuli, can be applied in temperature and strain sensors. The amount of retroreflected light changed with the variation of temperature and strain. The reflected far-field triangular structure also increased/decreased based on temperature and strain variation. Optical response of the flexible CCR array worked in both reflection and transmission modes. The amount of retroreflected light also depended on the tilt angle. Therefore, the retroreflected light (area of triangle) can be considered as a function of temperature and strain variation:

$$k\Delta S(T,F,\theta) = \left.\frac{\Delta R}{\Delta T}\right|_{F,\theta=const.} or \left.\frac{\Delta R}{\Delta F}\right|_{T,\theta=const.} \quad (4.5)$$

where *k* is a proportional constant and related with environmental conditions (relative humidity, temperature), ΔR, ΔT, and ΔF are changes in retroreflection, temperature, and force related to strain. $\Delta S(T,F,\theta)$ is the change of sensitivity as a function of temperature, force related with strain or weight suspension and tilt angle of the flexible CCR sample. Therefore, sensitivity, S can be measured as a ratio of changes in retroreflected light or distance of far-field triangular pattern (*d*) and small change of temperature or strain variation (in the form of inward/outward force or weight suspension) during reflection or transmission mode (Eq. 5). At fixed illumination and without any load suspension or strain force, temperature sensitivity can be measured as S_T = 0.265 AU/°C (from the tangent of temperature response curve, Figure 4d). Similarly, at fixed illumination and room temperature, strain sensitivity can be measured as S_S = 31.1267 cm^2/N (from the tangent of inward force, red (635 nm) illumination for response curve, Figure 6b).

4.6 Discussion and summary

Optical properties of the fabricated flexible CCR array were characterized through reflection, transmission, far-field experiments as well as numerical modelling. Soft flexible CCR array showed total internal reflection based on the three mirror retroreflection. The incident light reflected towards the source with a different tilt illumination and showed directional reflection. In general, the retroreflected power decreased considerably from 10° tilt angle with increased temperature. The flexibility and directional reflection of the fabricated CCR array structure were observed during strain and temperature variation. The amount of retroreflection varied with temperature, strain variation and provided selective directional reflection. As the structure of the CCR array changed due to temperature or strain variation, the angle in the CCR structure

increased/decreased; the thickness of PDMS block changed which increased/decreased the size of the reflected/transmitted triangle and also changed the magnitude of retroreflection intensity. A direct relationship between temperature, strain, and the retroreflected optical power of CCR array can be observed. In general, the reflected power of PDMS CCR increased with increasing temperature for all selected positions and monochromatic light illumination.

A gradual decrease in directional retroreflection occurred when the sample was tilted at larger angles. At the normal angle (0° illumination), maximum reflection power was detected as all retroreflections were directed to the source which was redirected by the beam splitter to the optical spectrometer. Part of the incident light is unable to reach inside the cornercube due to the three mirrored triangular mesh and the increased tilt angle. It is scattered out by bulk PDMS block and redirected away from the beam splitter. Therefore retroreflection was not detected by the optical power meter. Moreover, the cross-sectional area of the cornercube array towards the incident ray may directly influence the retroreflected beam. The highest cross-sectional area was achieved without tilting the sample and resulted in the highest amount retroreflection. Laser illumination on different sample positions resulted in a different amount of retroreflection. Therefore, the choice for first illumination point in each experiment was the position where the maximum reflection was found. The distance between the flexible CCR array, beam splitter, spectrometer, and laser source did not affect the retroreflection, given the focus point was fixed at a constant position. The lowest detectable signals also called DOL (temperature/force as weight suspension) can be calculated from the intercept between the regression lines of the standard errors (Appendix-B, Figure S4.8). For red (635nm) light illumination, the DOL values for temperature and weight variation are approximated at 30 °C and 5 gm. However, DOL values are influenced by incident light wavelengths, materials, and structural properties of the replicated CCR structure and metal-coating thickness.

For temperature or strain sensing, the aperture size was an important factor which had to be positioned in a way that all the retroreflected light from the flexible CCR array reached the spectrometer. Light power will be only detected by the photometer if it passes through the aperture and reaches the detector. By increasing the temperature, the flexible CCR array expanded, the magnitude of reflected triangular profile became bigger than the size of the aperture which resulted into decreased power detected by the photometer (some light may scatter away in the surroundings) as detection power of the photometer was limited to the aperture size caped on it. In general, the detected power of PDMS CCR array due to thermal expansion increased with increasing temperature. During sensor sensitivity measurement, the constant tilt angle (normal illumination) were considered for measurement simplicity. Moreover, external stimuli (humidity, temperature, strain force, and tilted illumination) may change the flexible CCR response in a complex way and reduce the sensor's optical response and sensitivity. The directional reflection intensity and sensitivity of the proposed PDMS based CCR array sensor is low due to non-uniform gold coating. However, the reflection intensity and sensitivity can be improved/enhanced by uniform selective coating as well as controlling the thickness of both PDMS replica and metal-coating.

The directional retroreflection of the PDMS based flexible CCR array was demonstrated. The retroreflection property of a flexible CCR array was tuned through external stimuli (temperature and strain due to inward/outward force from weight suspension). Compared to a conventional CCR array, the selective directional reflection was achieved using a flexible CCR array. Moreover, conventional CCR arrays are limited due to fixed retroreflection, however, flexible CCRs allow tuning of retroreflection and are passive (no electronics required). Moreover, flexible CCR arrays based in temperature and strain sensors described in this work were low cost, flexible and easy to fabricate. The sensitivity of a polymer-based, flexible CCR array sensor could be customized with other copolymers or the PDMS CCR array could be

coated with silver or gold nanoparticles to tune its optical-mechanical properties. Reflected optical power was independent of the positioning and movement of the laser source. The direct relationship between the force and magnitude of the transmitted/reflected triangle was demonstrated in the flexible CCR array using a strain sensor. In addition, temperature and reflected power optical values were in good agreement to prove the flexible CCR array could act as a temperature sensor. Sensors based on soft, flexible CCR arrays may have application in remote sensing as strain and temperature sensors where manual sensing is not possible. It is anticipated that polymerised CCR array based optical devices may have applications in space science, where light waves can travel without being lost as heat to enable astronauts in space to measure the temperature and deformation of devices/parts of the spacecraft by having a flexible CCR array installed on the surface and directing a laser at it. Another application may be in nuclear power stations and nuclear-related research where human operators measure temperature or nuclear expansion at a safe distance to ensure their safety and well-being from radiation and other environmental hazards.

References (iv)

1. Do, T.N. and Y. Visell, *Stretchable, Twisted Conductive Microtubules for Wearable Computing, Robotics, Electronics, and Healthcare.* Scientific Reports, 2017. **7**.
2. Ahuja, D. and D. Parande, *Optical sensors and their applications.* Journal of Scientific Research and Reviews, 2012. **1**(5): p. 060-068.
3. Yeo, J.C. and C.T. Lim, *Emerging flexible and wearable physical sensing platforms for healthcare and biomedical applications.* Microsystems & Nanoengineering, 2016. **2**.
4. Morin, S.A., et al., *Camouflage and display for soft machines.* Science, 2012. **337**(6096): p. 828-832.
5. Xu, S., et al., *Soft microfluidic assemblies of sensors, circuits, and radios for the skin.* Science, 2014. **344**(6179): p. 70-74.
6. Gong, S., et al., *A wearable and highly sensitive pressure sensor with ultrathin gold nanowires.* Nature communications, 2014. **5**: p. 3132.
7. Kaltenbrunner, M., et al., *An ultra-lightweight design for imperceptible plastic electronics.* Nature, 2013. **499**(7459): p. 458.

8. Araci, I.E., et al., *An implantable microfluidic device for self-monitoring of intraocular pressure.* Nature medicine, 2014. **20**(9): p. 1074.
9. Ding, W., et al., *High-temperature fiber-optic Fabry-Perot interferometric sensors.* Review of Scientific Instruments, 2015. **86**(5): p. 055001.
10. Liu, S., et al., *High-sensitivity strain sensor based on in-fiber rectangular air bubble.* Scientific reports, 2015. **5**: p. 7624.
11. Liu, Y., D. Wang, and W. Chen, *Crescent shaped Fabry-Perot fiber cavity for ultra-sensitive strain measurement.* Scientific reports, 2016. **6**.
12. Hansen, J.P. and S. Madhu, *Angle scintillations in the laser return from a retroreflector.* Applied optics, 1972. **11**(2): p. 233-238.
13. Park, B., T. Eom, and M. Chung, *Polarization properties of cube-corner retroreflectors and their effects on signal strength and nonlinearity in heterodyne interferometers.* Applied optics, 1996. **35**(22): p. 4372-4380.
14. Khalid, M.W., et al., *Holographic Writing of Ink-Based Phase Conjugate Nanostructures via Laser Ablation.* Scientific reports, 2017. **7**(1): p. 10603.
15. Chipman, R.A., et al., *Wavefront correcting properties of corner-cube arrays.* Applied optics, 1988. **27**(15): p. 3203-3209.
16. Arbabi, A., et al., *Planar metasurface retroreflector.* Nature Photonics, 2017. **11**: p. 415-420.
17. Bozhevolnyi, S.I., E.A. Bozhevolnaya, and S. Berntsen, *Theoretical model for phase conjugation of optical near fields.* JOSA A, 1995. **12**(12): p. 2645-2654.
18. Baharav, Y., et al., *Wave-front sensing by pseudo-phase-conjugate interferometry.* Applied optics, 1995. **34**(1): p. 108-113.
19. Zhou, L., J.M. Kahn, and K.S. Pister, *Corner-cube retroreflectors based on structure-assisted assembly for free-space optical communication.* Journal of Microelectromechanical Systems, 2003. **12**(3): p. 233-242.
20. Ahmed, R., et al., *Phase-conjugated directional diffraction from a retroreflector array hologram.* RSC Advances, 2017. **7**(41): p. 25657-25664.
21. Wang, S., et al., *Detection and monitoring of microparticles under skin by optical coherence tomography as an approach to continuous glucose sensing using implanted retroreflectors.* IEEE sensors journal, 2013. **13**(11): p. 4534-4541.
22. Bergen, M.H., et al., *Retroreflective imaging system for optical labeling and detection of microorganisms.* Applied optics, 2014. **53**(17): p. 3647-3655.
23. Park, S.-W., et al., *Quasi-retroreflection from corner cubes with refractive free-form surfaces.* Applied optics, 2014. **53**(28): p. 6605-6611.
24. Kim, H., S.-W. Min, and B. Lee, *Geometrical optics analysis of the structural imperfection of retroreflection corner cubes with a nonlinear conjugate gradient method.* Applied optics, 2008. **47**(34): p. 6453-6469.
25. Shaar, N.S., G. Barbastathis, and C. Livermore, *Integrated folding, alignment, and latching for reconfigurable origami microelectromechanical systems.* Journal of Microelectromechanical Systems, 2015. **24**(4): p. 1043-1051.
26. Lou, Y., et al., *Analysis and fabrication of corner cube array based on laser direct writing technology.* Applied optics, 2010. **49**(29): p. 5567-5574.
27. Sherlock, T., et al., *Suspended, micron-scale corner cube retroreflectors as ultra-bright optical labels.* Journal of Vacuum Science & Technology B, Nanotechnology and Microelectronics: Materials, Processing, Measurement, and Phenomena, 2011. **29**(6): p. 06FA01.
28. Yuan, J., et al., *Design and fabrication of micro-cube-corner array retro-reflectors.* Optics communications, 2002. **209**(1): p. 75-83.
29. Jolic, K., M. Ghantasala, and E.C. Harvey, *Excimer laser machining of corner cube structures.* Journal of Micromechanics and Microengineering, 2003. **14**(3): p. 388.
30. Ahmed, R., et al., *Printable ink lenses, diffusers, and 2D gratings.* Nanoscale, 2017. **9**(1): p. 266-276.
31. Lee, L.-H., *Adhesives, sealants, and coatings for space and harsh environments*, in *Adhesives, Sealants, and Coatings for Space and Harsh Environments*. 1988, Springer. p. 5-29.

32. Chung, G.-S., *Characteristics of SiCN microstructures for harsh environment and high-power MEMS applications.* Microelectronics Journal, 2007. **38**(8-9): p. 888-893.
33. Kim, K.N., et al., *Highly stretchable 2D fabrics for wearable triboelectric nanogenerator under harsh environments.* ACS nano, 2015. **9**(6): p. 6394-6400.
34. Hassanin, H., A. Mohammadkhani, and K. Jiang, *Fabrication of hybrid nanostructured arrays using a PDMS/PDMS replication process.* Lab on a Chip, 2012. **12**(20): p. 4160-4167.
35. Hoshino, K. and I. Shimoyama, *Analysis of elastic micro optical components under large deformation.* Journal of Micromechanics and Microengineering, 2002. **13**(1): p. 149.
36. Jo, B.-H., et al., *Three-dimensional micro-channel fabrication in polydimethylsiloxane (PDMS) elastomer.* Journal of microelectromechanical systems, 2000. **9**(1): p. 76-81.

Chapter 5 Remote Thermal Sensing by Integration of Corner-Cube Optics and Thermochromic Materials

5.1 Overview

CCRs with thermochromatic materials and hydro-chromic paints are investigated to define their potential application as remote temperature sensors and moisture level detectors in this chapter. Section 5.2 illustrates the basic properties of CCRs, monochromatic and broadband light interaction with various colours, and thermochromic properties of liquid crystals and leuco dyes. Schematics of the remote temperature sensing setup, phase inversion property of CCRs and influence of distance variation between laser light sources to the target CCR are presented in sections 5.3. Experimental results from ink pigments, acceptance angle, leuco dye, liquid crystals and hydro-chromic paint along with computational modelling are shown in 5.3 subsections. Section 5.4 provides a discussion and summary of the conducted experiments.

This chapter is reproduced from ‘’**Khalid, M.W.,** Whitehouse, C., Ahmed, R., Hassan, M.U. and Butt, H., 2018. Remote Thermal Sensing by Integration of Corner-Cube Optics and Thermochromic Materials. *Advanced Optical Materials*, p.1801013.’’

5.2 Introduction

Temperature is one of the most commonly monitored parameters within industry [1, 2]. Remote temperature monitoring is typically performed through an electronic wireless sensor over radio wave transmission or through wired sensors that transmit data over cables directly to the readout and control system [2, 3]. These devices have active components requiring a power supply to function. Many have limitations, including a poor communication range, high manufacturing costs, a slow response time, and are prone to electromagnetic interference and thermal noise [4]. Remote sensing becomes extremely important in areas that are either difficult

to access or due to the environmental conditions, such as high temperatures, radioactivity, pressure, toxicity, or other stringent constraints, allow the operator to supervise a system placed in a hazardous environment at a safe distance [5]. Since these stringent conditions pose limitations on certain sensing methodology, optical sensing and probing offer a promising alternative monitoring methodology [6].

Thermochromatic materials based fibre optics temperature sensing are being utilised by many researchers and are being explored for their feasibility as a cost-effective, simple, higher sensitivity and real-time sensing response [7, 8]. Commonly used fiber optic temperature sensors are mainly classified into two types interferometric and non-interferometric. However, these devices are applicable only to human accessible areas as they are operated manually. Another issue with POF based sensor is the presence of active components in them such as thin semiconductor ships. Temperature sensing systems based on purely optical elements to measure the temperature of distant objects or human restricted areas are in high demand [9, 10]. In general, thermochromatic materials-based temperature sensors provide a visual indication of temperature through colour coding. The base is coated with several different liquid crystals which change colour at their activation temperatures. These types of sensors are most commonly used for room temperature monitoring etc [11].

Sensors involving thermochromatic materials have been in use for various applications where the monotonic relationship between temperature and colour enables accurate mapping of temperature distribution within the region of interest [9, 11, 12]. These materials allow the broadband spectrum of a certain wavelength to pass through them at a specific temperature and absorb or reflect the rest. The transmitted/reflected wavelength that can be detected is processed with processing devices/optical detectors to correlate temperature with the wavelength (colour code). Combination of thermochromatic materials with luminophore or inclusion in electrical devices are also proposed, however, these devices may not be eligible to

map temperature distribution across the human restricted environments e.g. high radioactive sites or other chemical hazardous areas. Hence a device is proposed which is based on thermochromatic material coated on a CCR [13-15].

The incident monochromatic beam is reflected once from each of the three mirror surfaces and returns towards the source. The reflected laser beam is phase conjugated to the original incident beam. An arbitrary incident plane wave under paraxial approximation is:

$$E_i(r,t) = \varepsilon A(i)\mathrm{e}^{[i.(k_i.r)-\omega t]} \tag{5.1}$$

where A_i is an amplitude function, k_i is a wave vector, and ε is a unit polarization vector so that $\varepsilon.\varepsilon^* = 1$. The light reflected from a CCR can be approximated with ideal PCM if (a) the physical dimension of the CCR is large enough, and (b) the centre of the CCR coincide with optical axis. Therefore, reflected wave from a CCR is:

$$E_{CCR}(r,t) = R\varepsilon^* A^*(i)\mathrm{e}^{[i.(-k_i.r-\omega t)]} \tag{5.2}$$

where R indicates amplitude reflectivity of a CCR, $-k_i$ shows reverse direction of the reflected wave, ε^* , and A_i^* indicates conjugate/reversal of polarization and amplitude vectors.

It is the Bragg's scattering which determines the characteristic spectrum of colours when the light of a specific wavelength interacts with thermochromatic materials undergoing a colour transition due to temperature changes. Mathematically, Bragg's diffraction equation can be expressed as follows [16, 17]:

$$\lambda = \mathrm{P}\,\eta\sin\phi \tag{5.3}$$

Here, λ is the wavelength of the incident light, P indicates the pitch of optically active molecule under illumination, η denotes mean refractive index, and ϕ is the exposure angle or angle of incidence. It is observed from equation 5.3 that helicoidal pitch determines the ability of the thermochromatic material to selectively reflect the wavelength of incident light i.e. when incident light (broadband 400-700 nm) is comparable to the pitch length then a range of colours

are produced depending upon their associated wavelength [17]. Temperature change under normal illumination changes the pitch length and changes the orientation of the direction vector, hence the reflection percentage of the incident light can be selectively tuned. Any applied stress can also change the pitch length by changing the orientation of the direction vector which can lead to ambiguity in temperature sensing data [18].

5.3 Experiments and results

Optical characterization of a CCR coated with various coatings of different coloured ink dyes, and thermochromatic materials were performed using a simple set up shown in Figure 5.1 (a).

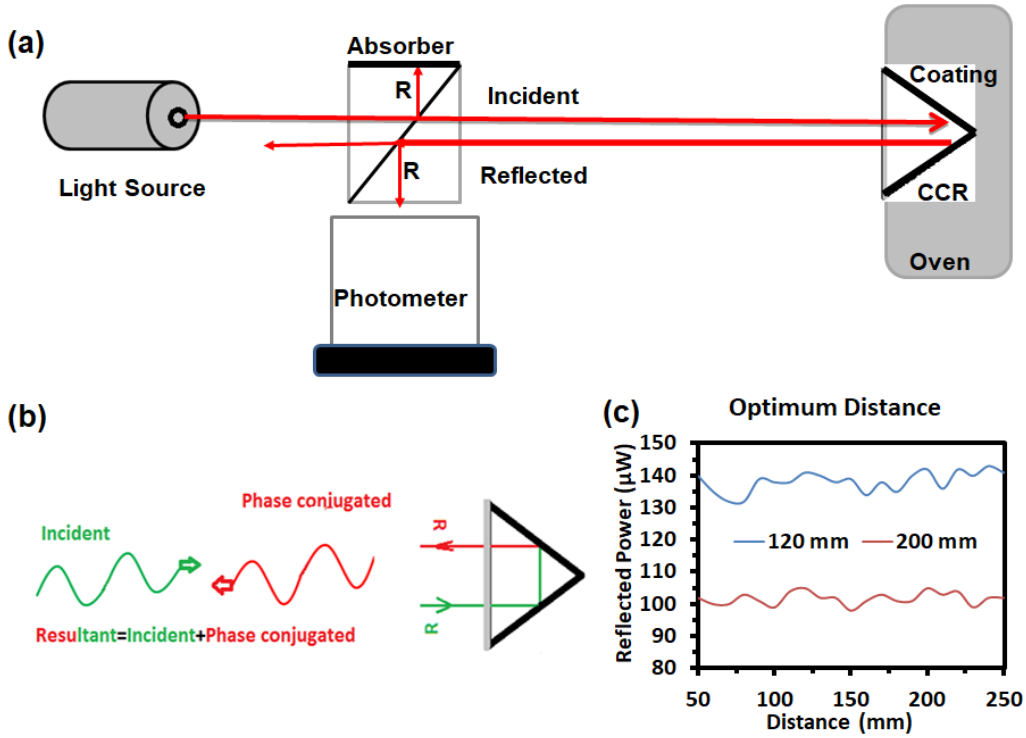

Figure 5. 1: (a) schematic of experimental setup showing the beam propagation from laser source towards CCR after passing through the beam splitter, reflected beam from CCR is directed towards the power meter. (b) showing Phase conjugation property of CCR. (c) is the plot depicting recorded reflected power against distance between laser source (red, 635 nm) to the CCR.

Monochromatic light of variable wavelengths at various temperatures are directed at the CCR and the resulting reflected power is recorded with a power meter. Reflected power was significantly influenced by the colour coating on the CCR walls. A CCR having three mutually perpendicular surfaces, which on illumination directed the reflected light of the same wavelength as of incident light influenced by external stimuli i.e. colour in the target, which was changing due to thermochromatic effects. A power meter was placed to detect the reflected power which was further correlated with the temperature and colour codes. A basic concept of colour visualisation was used to plan the experiment i.e. the observed colour is reflected by the object under observation. If the broadband light is directed at a red table, only the red light/wavelength will be reflected, and the rest is absorbed. Similarly, if the red laser is pointed at the red colour, most of the red light is reflected; if violet light is shined on the red colour most of the light is absorbed i.e. reflected power will be reduced for the second case.

Using the experimental set-up shown in Figure 5.1 (a), monochromatic light sources include; red (635nm), green (532nm) and violet (405nm). The beam-splitter was used to direct the reflected optical response from the coated CCRs with various colours sequentially. Several different coatings were applied under various wavelength illumination; reflective coating, black ink, red ink, green ink, blue ink, yellow ink and white ink, and controlled measurements were taken by illuminating an uncoated CCR. The coatings were spray painted to achieve even and smooth layers of coverage adhered to the glass. The optical response i.e. retroreflection from the CCR was measured using a power meter. From figure 5.1 (c) it can be seen that the distance variation between the laser source and the CCR does not affect the reflected power at the fixed focus point of the CCR.

5.3.1 Characterisation and calibration of CCR and pigmented colours

The optical characterisation of CCR without any coating and simple dye colours were done in order to generally assess its response to incident light. The uncoated CCR yielded the highest reflected power for monochromatic light sources, red (635 nm), green (532 nm) and violet (405 nm) through total internal reflection (TIR). Applied coating reduced the reflected power significantly due to light intensity losses as absorption and scattering at the interface of the CCR [19-21]. Under normal red (635 nm) illumination at various coloured coatings, the red reflective coating produced the highest reflected power; followed by white, red, yellow, green and blue coloured coating respectively as shown in figure 5.2 (b).

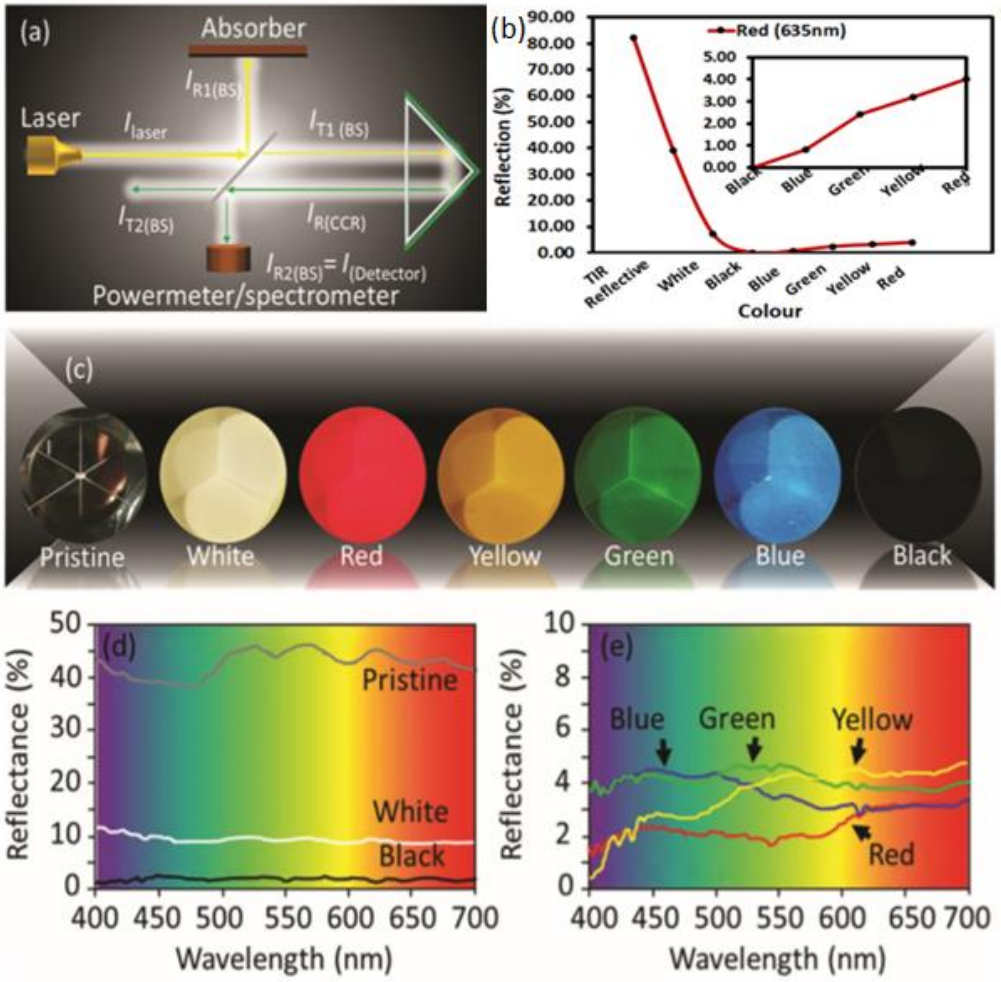

Figure 5. 2: Experimental setup used for normal spray painted CCRs and their reflectance behaviour. a) Schematic of the experiment: R (reflectance) and T (transmittance) show the path taken by the laser beam. b) monochromatic red light (635nm) reflected from uncoated CCR, highly reflective material coating and then from white, black, blue, green, yellow as well as red ink coated CCRs. c) Trialled backing colors applied to the rear of the CCR for the preliminary experiment. From left to right: reflective, white, red, yellow, green, blue, and black, respectively. d) Spectral reflectance curves obtained from pristine (not coated), and black and white coated CCRs, the CCR was illuminated by a broadband white light beam. e) Spectral reflectance curves obtained from coated CCR in blue, green, yellow, and red colors, the CCR was subject to broadband white light.

The black coloured coating reflected no light i.e. all the incident light was absorbed by the black ink. Change in the distance between the laser source and the CCR had a negligible effect

on the measured power. Broadband illumination at various coloured coating showed consistency as predicted and obtained from the monochromatic red light. The wavelength of incident broadband light which also determines the colour of the light showed higher reflection when illuminated at a similar colour as can be seen in figure 5.2 (d-e). The uncoated TIR corner-cube produced the highest reflectance across the entire visible spectral range (Figure 5.2d-e). The reflection percentage was low (<10%) for various coloured coating, and lower than expected for the reflective coating (<40%). This is most likely due to the method of application and nature of the spray paints used to coat the CCR (with losses occurring due to absorption or scattering of incident light at the interface of CCR/coated layer). Poor surface application and use of non-glossy paints create a roughened surface that is only partially reflective; a higher proportion of energy is scattered and absorbed than reflected towards the source.

The red (635nm) laser beam produced the highest reflected power when incident on the red coating colour. Broadband contains all wavelengths of visible light, with each colour having a different wavelength. Under white light, a red object appears red because it absorbs all other wavelengths of white light and reflects only the red portion of the EMS. It follows that a blue object illuminated with a red laser beam should, ideally, appear black. However, colours are not discrete entities; the pigments that form a colour, such as a paint or dye will reflect a range of wavelengths within the EMS. This would suggest the highest reflected power from the red laser beam would be measured when incident on a red or yellow backing and lowest when incident on a blue backing as this is furthest removed from the red portion of the EMS.

5.3.2 Acceptance angle

The acceptance angle of the uncoated CCR was measured using monochromatic red (635nm) light through the same experimental set-up to the one detailed in Figure 5.1 (a). The incident beam was varied between 0 and 90° by changing the combinations of yaw and pitch of the CCR. The resultant percentage reflection could then be measured and plotted as shown in Figure 5.3 (a).

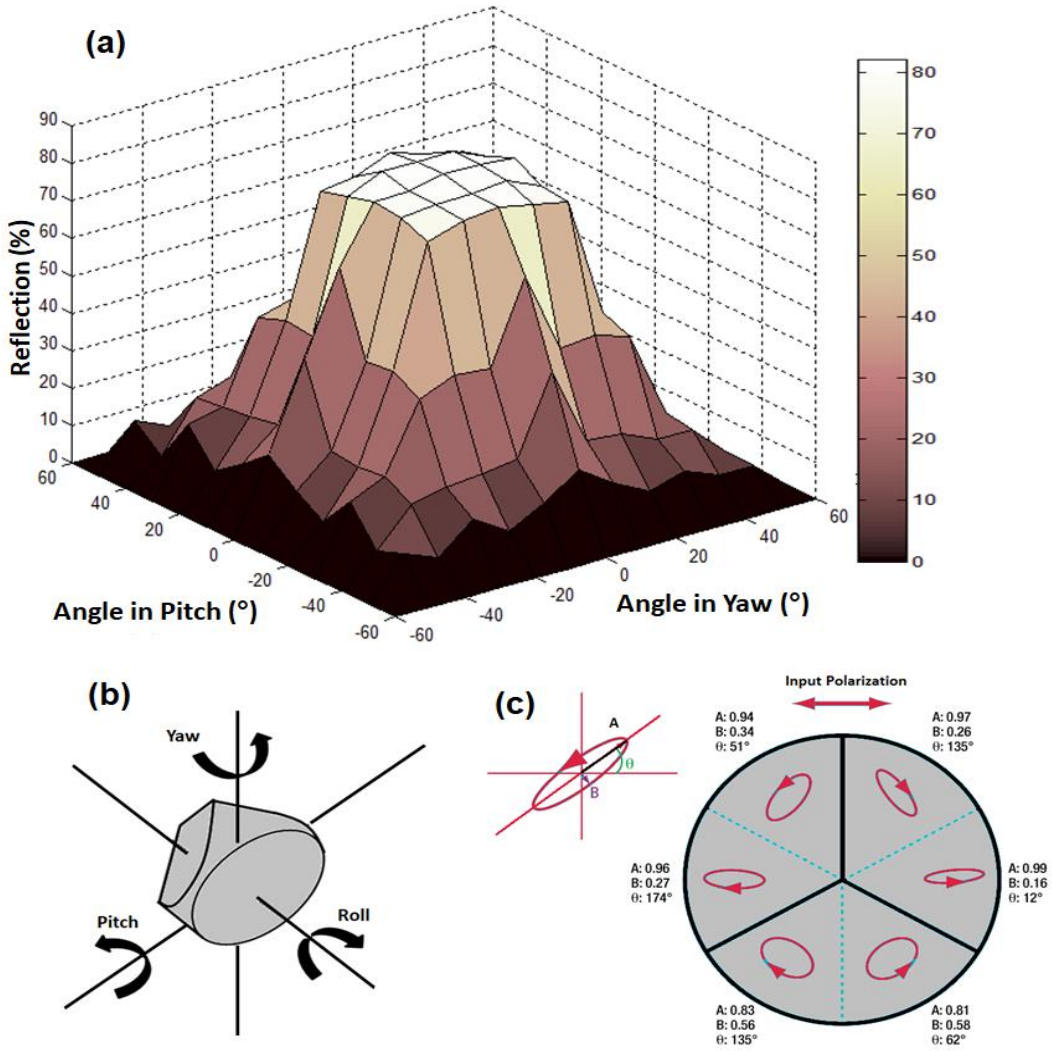

Figure 5. 3: Acceptance angle calculations (a) plot of resultant percentage reflection. (b) details the CCR coordinate system, whereas, figure 5.3 (c) explains the output polarisation of horizontally polarised incident light incident within a perfect CCR [21, 22].

The greatest retro-reflection occurred when the incident light beam was between 0 - 20° in combinations of yaw and pitch. Beyond 20°, a remarkable decrease in reflected power suggested the limiting angle of TIR had been exceeded. Beyond 60°, the CCR did not retro-reflect any incident light. The acceptance angle appeared to be independent of the size of the CCR. Acceptance angles depend upon the refractive indices of coated materials on CCR walls and the wavelength of incident light. The refractive index for violet light (1.530) is slightly larger than the red light (1.512) in crown glass i.e. index of refraction is inversely proportional to the wavelength of light. So, theoretically acceptance angle and percentage reflection is slightly increased during violet light illumination at CCR [23-25].

5.3.3 Leuco dye

Using the similar experimental setup as shown in figure 5.1a, the reflected optical power from a solid glass CCR coated with the leuco dye was measured in different thermal conditions (Figure 5.4).

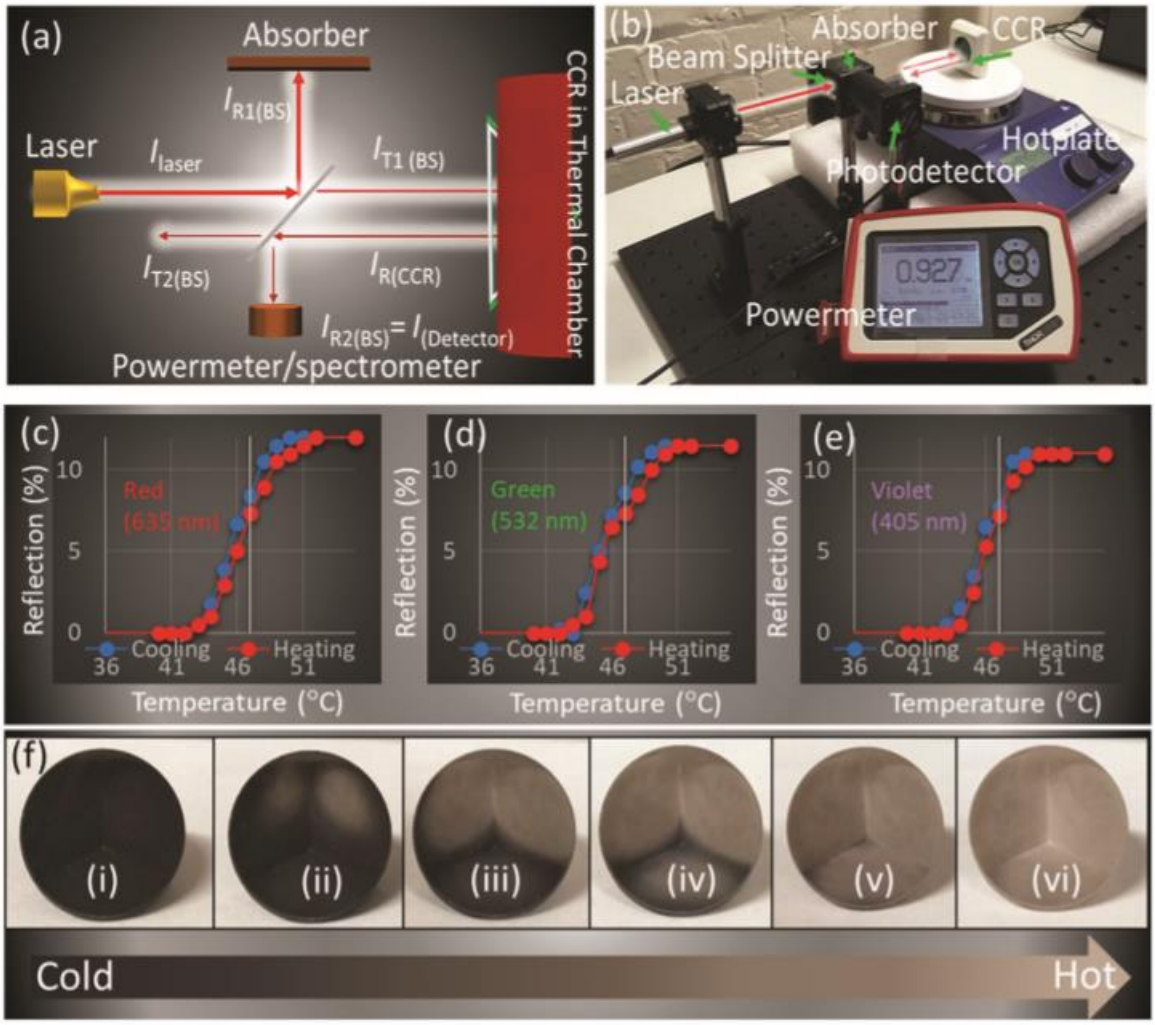

Figure 5. 4: Experimental setup/method of controlling the surface temperature of the coated CCR and thermal response of the coated CCR. a,b) Schematic/ray diagram of the optical and heating setup. c–e) Percentage reflectance values against temperature for a CCR coated in leuco dye as measured with red, green, and violet lasers. f) Color changing transition of the leuco dye from cool (dark) to hot (colorless), from (i) to (vi), respectively.

The measurements were performed for heating and cooling between 35 and 55 °C; the surface temperature of the CCR was controlled by transferring heat from a hot plate through a thermally conductive potting compound that encapsulated the CCR. The potting compound had a thermal conductivity of 1.26 W m^{-1} K^{-1} and operational temperature range of −40 to 130 °C. Each retro-reflected power measurement was taken after ensuring the entirety of the potting

compound had reached thermal equilibrium with the hot plate. Measurements were carried out using red, green and violet laser light sources. The experiment was repeated for three times. The leuco dye had an activation temperature (TA) of 47 °C, at which point it changed from black to colorless. There was a negligible difference in percentage reflectance values from the use of a red, green and violet laser. The reflectance values were also independent of the distance between the laser source and the CCR. Below the value of 43 °C, the dye remained black as all incident laser light colors were absorbed by the dye and therefore the recorded percentage reflection values were 0%. The dye began to lose color beyond the value of 43 °C and so the recorded percentage reflection values increased in accordance with the increase in reflected laser light. The dye transitioned from black to colorless across the temperature range of 43–50 °C, peaking at a percentage reflection value of ≈11.5% for all three laser light sources. Heating beyond 50 °C did not change the percentage reflection values further, indicating that the dye had completed its transition. At 55 °C, the hot plate was turned off, and the percentage reflectance values during cooling were measured. Reflectance values across the entire temperature range were higher for the cooling cycle as compared with the heating cycle, leading to a hysteresis. The presence of the hysteresis loop between the heating and cooling curves is mainly due to the thermal mass of the CCR, which can be minimized by improving the heatsink efficiency of the system. Although the response time of both, the sensing layer is less than 20 ms, the sensor showed a stable change after a few seconds. The CCR in the present study are made of borosilicate glass, notice that the thermal conductivity of glass is less than 1 W cm^{-1} K^{-1}, whereas that for metals, the value is two to three orders of magnitude larger (for Au: ≈300 and Cu: ≈400 W cm^{-1} K^{-1}). Therefore, the response of such sensors is a function of thermal mass (/conductivity), and efficiency can be increased by increasing the conductivity as well as reducing the overall size of the sensor. The peak percentage reflectance values of ≈11.5% were lower than expected for this experiment. It was assumed when under heat, the

dye would appear completely colorless and so allow the CCR to carry out the better internal reflection. Instead, the dye appeared a mottled grey, only partially reflecting the incident laser beams. A later investigation into the appearance of the dye at high temperatures as a function of its thickness revealed only the thinly applied dye (one to two coats) disappeared completely. It may be possible, therefore, to "boost" the percentage reflection values by applying the leuco dye sparingly to the rear of the CCR. Also, the TIR is limited because of the higher refractive index of the dye as compared to air. Therefore, the interface between the CCR surface and dye require a larger incident angle for a better TIR. In order to validate the results, the CCR was heated to a certain temperature (between 42 and 52 °C) and the percentage reflection value measured using the red, green, and violet laser. This was then compared to the results obtained in Figure 5.4c–e, from which a temperature could be predicted. The average relative error between the true and predicted residual temperature was ≈1.7%.

5.3.4 Liquid crystal

The retro-reflected power from a CCR with three coats of liquid crystals coatings was measured during heating and cooling. All coats performed under identical conditions using an airbrush at a maximum pressure of 20 PSI. After drying the liquid crystal ink, a black paint backing was applied via an aerosol. The CCR was heated between the temperatures of 20–35 °C, whereas, the liquid crystal had a bandwidth of 24 to 29 °C, over which it changed from red (at lower temperatures) to yellow and green (at mid-temperature range) and then blue (at higher temperatures). Outside of this temperature range, the liquid crystals generally appeared transparent. The blue phase generally appears in the temperature range between isotropic liquid and chiral nematic phases. Change in the temperature changes the arrangement of the LC molecules, hence changing interspacing between LC layers. This in turn changes the wavelength of light that is reflected back due to constructive interference. This phase can be exploited to measure very narrow temperature range but can also be designed to encompass

thermal large ranges. The broad colorimetric modulation in the coated material within a narrow temperature range can be exploited to attain an enhanced sensitivity within the desired range.

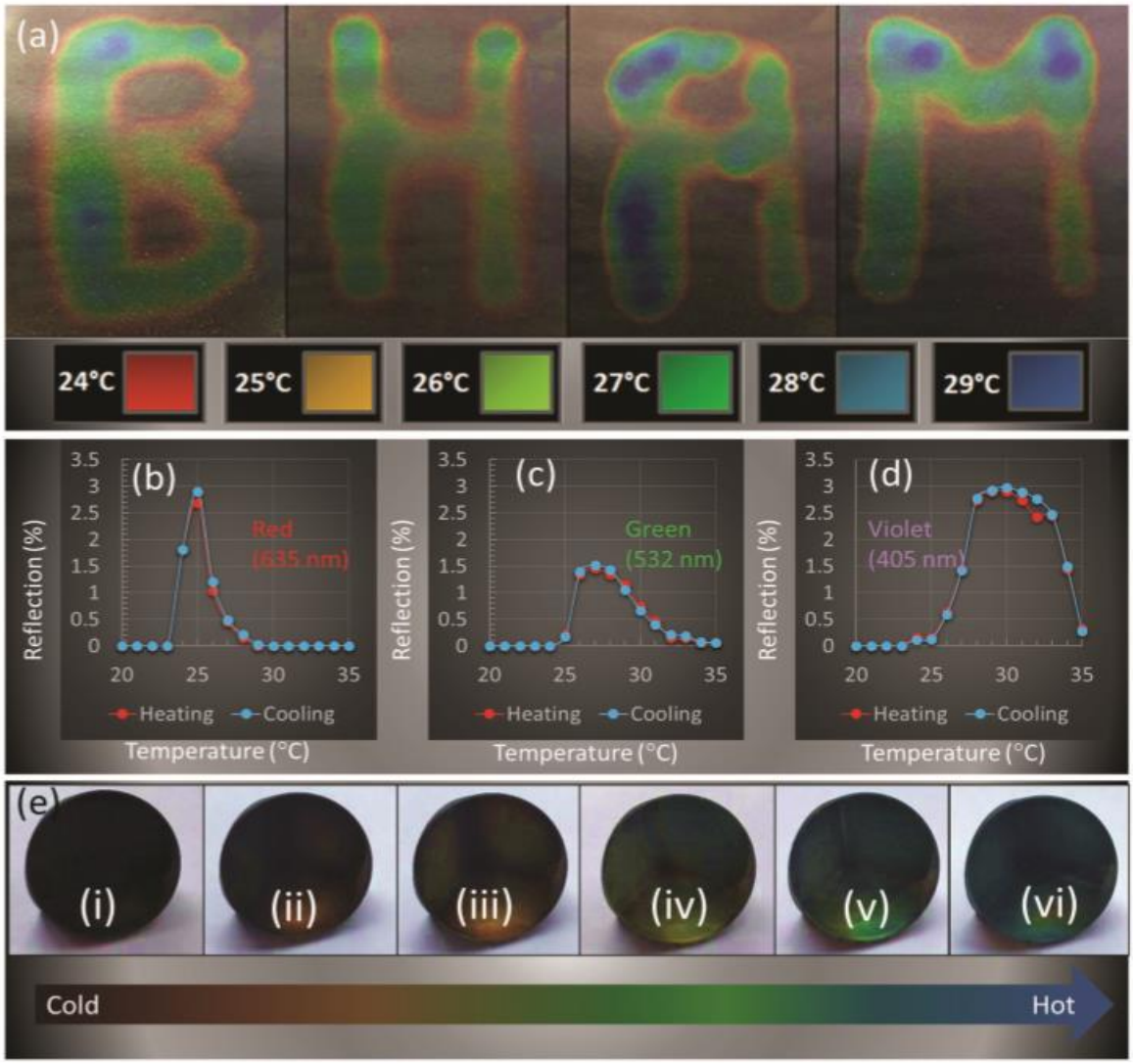

Figure 5. 5: Color spectrum displayed by the liquid crystal. a) The liquid crystal appears red at lower temperatures, changing to yellow, green then blue at higher temperatures. The liquid crystal was deposited on top of a black backing to absorb incident light not reflected by the liquid crystal layer. b) Percentage reflectance values against temperature for a CCR coated in liquid crystal ink as measured with a red, green and violet laser light source. The red line represents heating, while the blue line represents cooling. c) Color changing transition of the liquid crystal ink from cold (red) to hot (blue), from (i) to (vi) respectively.

BHAM (abbreviated Birmingham) is written with the liquid crystal ink to display the thermal response of liquid crystals when heated (Figure 5.5a). The hottest spot turned dark blue, while in the nonuniformly heated specimen (heated via a hair dryer) revealed the black backing outside the operating range. Measurements from the CCR sensor were carried out using a red (635 nm), green (532 nm), and violet (405 nm) lasers, each having a maximum power of ≈4.5 mW. The experiment to take one reading was carried out a for three times The peak percentage reflectance values occurred when the laser light source of a given wavelength fell on the same color (reflecting the peak maximum at the same wavelength) that is the red laser (635 nm) produced the highest percentage reflectance values when incident on a red coloring between 24 and 25 °C (Figure 5.5b–d). The cooling curve is represented by the dashed line and closely follows that of the heating curve. The thermal hysteresis loop in the case of liquid crystal coated CCRs was negligible as compared to leuco dye, indicating better thermal conduction properties. Photographic recording of the heating CCR showed the subsequent change in color of the liquid crystal ink from a deep red to blue (Figure 5.5e). Beyond 29 °C, the liquid crystal did not immediately turn transparent. Instead, it retained a dark blue coloring from 29–32 °C and gradually turned transparent (and hence revealed the black backing) thereafter. This retention of color extended the band over which the green and violet laser experienced retro-reflection. To validate the experiment, the CCR sensor was heated to a certain temperature within the range of 23 and 35 °C and percentage reflection values measured using a red, green and violet laser. Using Figure 5.5b–d, the predicted temperature was calculated by taking a mean of the predicted temperatures for each laser color. The CCR was allowed to cool between each run. Using all the three laser curves, enabled to predict the temperature within 1% of error.

5.3.5 Hydro-chromic paint

Hydrochromic paints undergo through a reversible change in colour from milky white to transparent when treated with water. These materials are most commonly used to hide secret colours, texts as well as in hundreds of other applications. Hydrochromic inks are non-toxic, easily available in market and environment friendly, thus so could be feasibly utilised for any novel application. In this research, a combination of a CCR with hydrochromic paint sprayed on its walls was used to construct a remote sensor for moister level supervision in hazardous areas, where human access is restricted. Using the same idea as for leuco dye and liquid crystals, hydrochromic paint is coated on CCR and optically characterized with various light sources including broadband and monochromatic light sources under various moister conditions. Initially, coated CCR with hydrochromic paint which was white, nearly opaque was immersed in water to transform in transparent form. After that, the system was monitored while undergoing a reversible transformation attaining its actual color i.e. white. Reflected power from the hydrochromic system was recorded and plotted as shown in figure (5.6c).

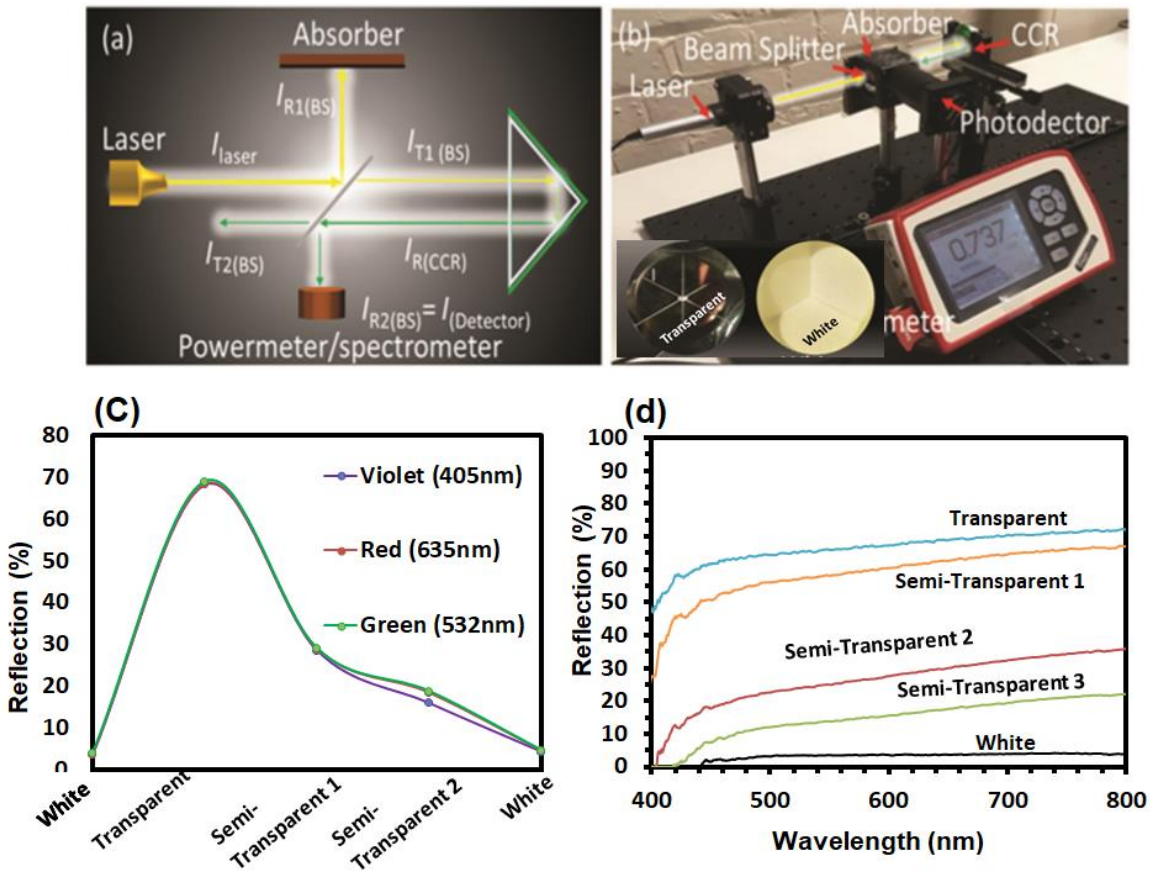

Figure 5. 6: Experimental results from hydrochromic paint analysis. (a-b) Experimental setup used to optically characterise the designed system (CCR optics). (c) Reflection (%) against given moister level during red (635 nm), green (532 nm) and violet (405 nm) normal illumination, respectively. (d) Reflection (%) during broadband light illumination under various moister levels. It is to be noted that white represents the as received paint which is milky whereas transparent represents the fully immersion in water and then the semi-transparent levels were considered during the reverse process of transformation (i.e. drying out the paint) from fully transparent to milky white respectively.

Recorded power was highest i.e. around 70% of the total power, for hydrochromic system soon after being immersed in water because the colour of received hydrochromic paint transformed from milky white to transparent (colourless), and the incident lights include; red (635nm), green (532nm) and violet (435nm) reflected towards the source through TIR mechanism. As the system dried out, the reflected power dropped down continuously and attained

approximately the initial value i.e. around 4.5 % on average once the system was fully dried and turned into milky white. A direct relationship between reflected power and moister level is observed in the event of broadband light illumination, as shown in fig (5.6d) based on the fact that hydrochromic paint transforms into transparent with the higher moister level and allow CCR to undergo through TIR based reflection as well as direct light transmission through it.

5.3.6 Computational modelling

Optical properties of liquid crystal coated CCR surface were modelled through FEM. COMSOL multi-physics simulation tools were used to simulate retroreflection and ray-tracing properties from the two/three-dimensional (2/3D) LCCR structures. Scattering, continuity-boundary conditions were used to observe retroreflection property from the liquid-coated CCR (LCCR) surfaces. 2D computation consisted of triangular meshing elements, maximum mesh-size (one-fifth of wavelength), 12201 domain and 433 boundary elements. Complete 3D mesh consists of 369417 domain elements, 13064 boundary elements, and 503 edge elements. Maximum and minimum mesh sizes were 0.667 and 0.00667 mm. Also, mesh convergence was performed to get result accuracy. User define customised physics-controlled mesh (mesh size was one fourth of wavelength) was utilised to for modelling. Customised mesh containing more mesh elements around the spherical domain. For further reduction of element number a swept mesh is applied which considerably minimises the size of the model and complexity of simulation. Customising the meshing also helps to reduce memory requirement by controlling quality of elements by creating efficient and accurate simulation environment.

Figure 5.7a shows 2D LCCR computational geometry and simulation environment. Retroreflection property of the LCCR was simulated through monochromatic light at normal illumination. The incident and retroreflected light were parallel and produced bright interference pattern towards the source. The $\boldsymbol{E}$-field intensity distributions of the retroreflected

light were computed with monochromic light (405, 532, and 632nm) at normal illumination. Maximum retro-reflection field distribution was observed with higher wavelength (632nm). Furthermore, retroreflection property of LCCR was also 3D-modelled based on structural parameters (height-6.10mm, diameters-7.16mm, etc.) available on commercial CCR (N-BK7, Edmount optics) (Figure S5.1a-c). Retroreflection property of LCCR was simulated with refractive index (RI) variation from 1.33-1.50. Higher laser wavelength (632nm) shows five-folds retroreflection improvement compared with lower-wavelength (405nm) at 1.33 RI. As RI increased, the retroreflection values decreased exponentially. Moreover, retroreflection property was simulated with wavelength (400-800nm) and RI variation (1.33-150). As wavelength increased, the retroreflection property increased exponentially. The retroreflection angle was also plotted as a function of incident angle. Linearity of the curve (R^2=1) ensures the retroreflection property of LCCR. Furthermore, 3D ray trajectory of retroreflection from LCCR was also modeled. Each ray color indicates RI value and remain constants in the full trajectory. Incident rays and retroreflected rays from LCCR are also found parallel from the ray-trajectory observation. The phase *(v_p)*, group velocity *(v_g)* of the incident (before entering the LCCR) and retroreflected (after LCCR) light remain at a constant level *(v_p=v_p=*$1.5\times10^{10}\,m/s$) (Figure S5.1d,e). However, inside the LCCR, reduced amount of group and phase value ($v_p = v_g = 10\times10^{9}\,m/s$) was observed compared with incident/retroreflected light. Similarly, constant angular frequency was ($\omega_i = \omega_r = 2.14\times10^{17}\,rad/s$) observed for incident and retroreflected light (Figure S5.1f). Again, minimum constant angular frequency ($\omega_{LCCR} = 1.43\times10^{17}\,rad/s$) was observed at inside the LCCR.

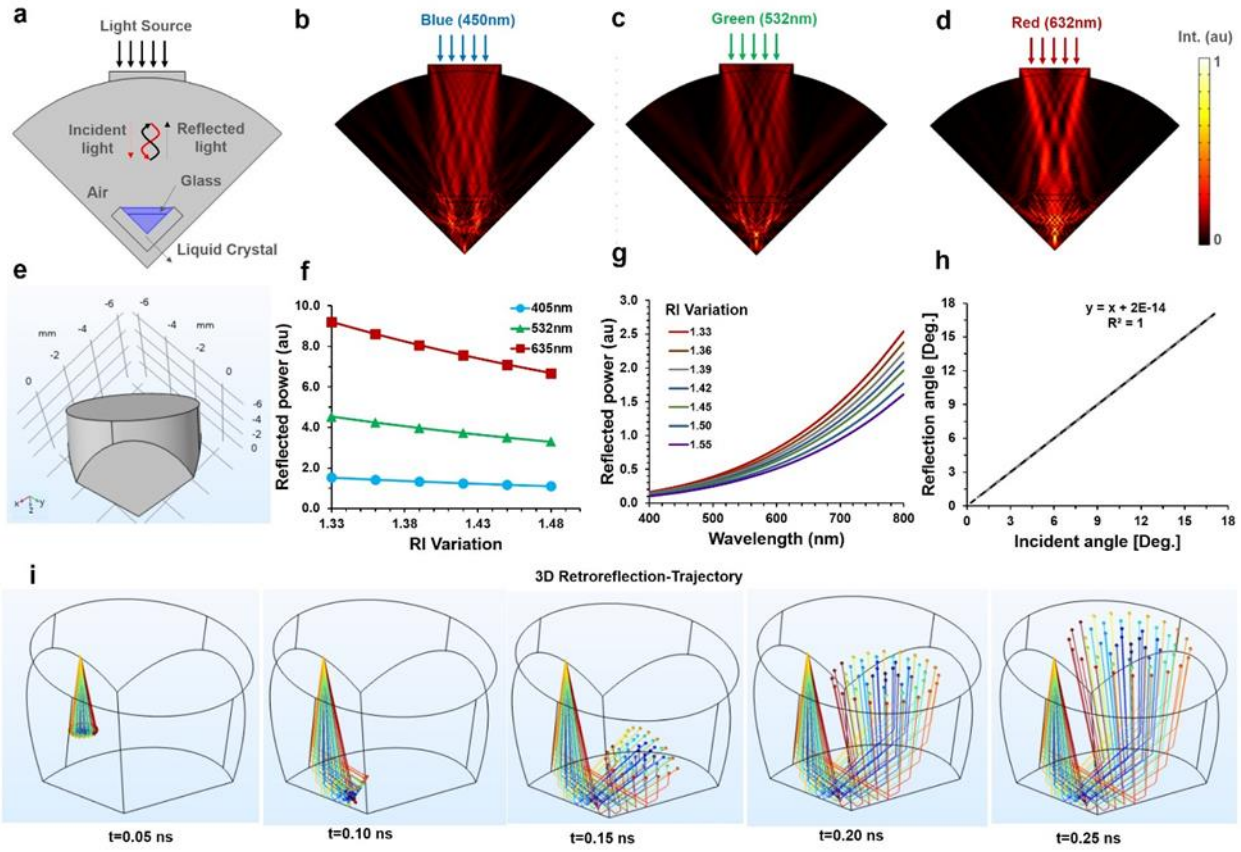

Figure 5. 7: FEM modelling of retroreflection property of the LCCR. (a) 2D computation geometry. (b-d) Electric-field distribution of the retro-reflected monochromatic light at normal illumination. (e) 3D geometry of the modelled LCCR. (f, g) Retro-reflection as a function of RI and wavelength variation. (h) Retro-reflection angle as a function of incident angle. (i) 3D retroreflected ray-trajectory as a function of computation time (t).

5.4 Discussion and summary

Liquid crystal, leuco dye and hydro-chromic paint coated on various CCRs based systems demonstrated tuneable optical properties subject to the environmental conditions. All three designed systems yielded very interesting and encouraging results with average relative errors of under 2%. The basic idea of colour visualisation was utilised to plan these simple experiments. CCR showed TIR based reflection retroreflection, where the incident light from the source was directed perpendicularly at the CCR which reflected towards the source and

showed directional reflection. Leuco dye systems are more cost-effective and robust as compared to liquid crystals. However, in terms of sensitivity liquid crystals have an edge over leuco dye, typically, a 3°C temperature change is required for a leuco dye to change colour, whereas liquid crystals based system is found to be more sensitive which require only 1°C to change its colour. Proposed applications for Leuco dyes are typically in textile industry, packaging, advertising, toys. Liquid crystals on the other hand are accurately calibrated and can be used in precision applications, such as, medical devices, thermal mapping and heat transfer studies. Presence of hysteresis loop in leuco dye systems show poor thermal conduction properties of leuco dye, however hysteresis loop was not present in liquid crystal. Tuned optical response of the coated CCR with various paints and thermochromatic materials was observed, based on external stimuli (supplied temperature). A beam splitter was accommodated between the light source and the sensor to divert reflected response towards the power meter. Although the local heating effect due to the absorbed radiation have not been studied, the phenomenon cannot be ruled out. In order to avoid such unwanted effects, low powers, as well as short operational intervals of the probing laser, can be used. The proposed study combined two commercially available components, that is, i) optical: CCRs, and ii) material: different types of dyes/liquid crystal to demonstrate a new remote sensing optical thermal sensing technique. Such combination for thermal sensing has never been reported previously, and it not available in the market. The study offers a new mode of temperature sensing via visible (monochromatic laser or broadband) light probing technique, which is capable of sensing the temperature virtually from any angle (angle independent measurement). The three reflections from mutually perpendicular planes also allow higher interaction between the probing laser beams and the thermochromic coating, hence improving the overall response. To bring the proposed sensor to the market, the performance parameters, such as accuracy, resolution, and thermal sensing range of the proposed sensor, require a detailed comparative

study with respect to the commercially available mercury or thermal imaging sensing techniques. It is believed that CCR-based remote thermal sensing can find its application in numerous fields after making appropriate selection of the sensing materials and optical components, such as in space equipment or atmospheric temperature sensing in challenging locations, in hazardous environments (posing risks like presence of toxins, corrosives, or radioactive chemicals and gases), within underground mines to provide adaptability to the ever-changing topographies, and within power generation plants where temperature is measured using an optical thermochromic system, would be immune from different interfering fields. The above study has proven that it is possible to create a remote temperature sensor by combining thermochromic material with a CCR. As temperature sensors are required to work in evermore challenging environments, development of concepts explored within this study may provide a costeffective and simple solution. There are however a number of limitations that must be overcome to ensure the success of the sensor. These include the presence of a hysteresis loop for leuco dyes, bandwidth and maximum temperature limitations for liquid crystals, and the susceptibility of the thermochromic materials to aggressive chemicals and light. Further work regarding accurate calibration of the sensor, choice of thermochromic materials for particular application, and prospective design for a commercial sensor should be carried out in future studies.

References (v)

1. Ruiz-Garcia, L., et al., *A review of wireless sensor technologies and applications in agriculture and food industry: state of the art and current trends.* sensors, 2009. **9**(6): p. 4728-4750.
2. Gungor, V.C. and G.P. Hancke, *Industrial wireless sensor networks: Challenges, design principles, and technical approaches.* IEEE Transactions on industrial electronics, 2009. **56**(10): p. 4258-4265.
3. Matese, A., et al., *A wireless sensor network for precision viticulture: The NAV system.* Computers and electronics in agriculture, 2009. **69**(1): p. 51-58.

4. Wu, H., et al., *Quartz enhanced photoacoustic H2S gas sensor based on a fiber-amplifier source and a custom tuning fork with large prong spacing.* Applied Physics Letters, 2015. 107(11): p. 111104.
5. Gungor, V.C., B. Lu, and G.P. Hancke, *Opportunities and challenges of wireless sensor networks in smart grid.* IEEE transactions on industrial electronics, 2010. **57**(10): p. 3557-3564.
6. Ahuja, D. and D. Parande, *Optical sensors and their applications.* Journal of Scientific Research and Reviews, 2012. **1**(5): p. 060-068.
7. Yoo, W.J., et al., *Fabrication and comparison of thermochromic material-based fiber-optic sensors for monitoring the temperature of water.* Optical review, 2011. **18**(1): p. 144-148.
8. Khan, M.R.R. and S.-W. Kang, *Highly sensitive temperature sensors based on fiber-optic PWM and capacitance variation using thermochromic sensing membrane.* Sensors, 2016. **16**(7): p. 1064.
9. Díaz-Herrera, N., et al., *A fibre-optic temperature sensor based on the deposition of a thermochromic material on an adiabatic taper.* Measurement Science and Technology, 2003. **15**(2): p. 353.
10. Moraleda, A., et al., *A temperature sensor based on a polymer optical fiber macro-bend.* Sensors, 2013. **13**(10): p. 13076-13089.
11. Smith, C., D. Sabatino, and T. Praisner, *Temperature sensing with thermochromic liquid crystals.* Experiments in fluids, 2001. **30**(2): p. 190-201.
12. Chen, X. and J. Yoon, *A thermally reversible temperature sensor based on polydiacetylene: Synthesis and thermochromic properties.* Dyes and Pigments, 2011. **89**(3): p. 194-198.
13. Renneberg, C.P., *Optical means for calibrating temperature*. 2013, Google Patents.
14. Kronberg, J.W., *Optical temperature indicator using thermochromic semiconductors*. 1996, Google Patents.
15. Potyrailo, R., et al., *Method of authenticating articles, authenticatable polymers, and authenticatable articles*. 2005, Google Patents.
16. Moore, D.M. and R.C. Reynolds, *X-ray Diffraction and the Identification and Analysis of Clay Minerals*. Vol. 332. 1989: Oxford university press New York.
17. Handbook of Thermochromic Liquid Crystal Technology available at: https://www.hallcrest.com/DesktopModules/Bring2mind/DMX/Download.aspx?Command=Core_Download&EntryId=280&language=en-US&PortalId=0&TabId=163 (Accessed: 09/10/17), L.H.H.o.T.L.C.T.A.a.
18. Tropea, C. and A.L. Yarin, *Springer handbook of experimental fluid mechanics*. Vol. 1. 2007: Springer Science & Business Media.
19. Scholl, M.S., *Ray trace through a corner-cube retroreflector with complex reflection coefficients.* JOSA A, 1995. **12**(7): p. 1589-1592.
20. Baumeister, P.O.C.T.W.S.P.
21. Liu, J. and R. Azzam, *Polarization properties of corner-cube retroreflectors: theory and experiment.* Applied optics, 1997. **36**(7): p. 1553-1559.
22. *Cornercube Measured Polarisation, https://www.thorlabs.com/NewGroupPage9.cfm?ObjectGroup_ID=4265, on 15/04/2018.*
23. http://www.chegg.com/homework-help/questions-and-answers/shown-figure-white-light-enters-45-90-45-crown-glass-prism-vertical-face-part-light-refrac-q5652715 (Accessed: 10/01/18), C.S.I.o.r.i.c.g.A.a.
24. Nave, R.R.o.l.A.a.h.h.p.-a.g.e.h.g.r.h.A.
25. Wollaston, W.H., *XII. A method of examining refractive and dispersive powers, by prismatic reflection.* Philosophical Transactions of the Royal Society of London, 1802(92): p. 365-380.

Chapter 6 Nanofabrication on Rigid and Flexible Substrates via Nd:YAG Laser Ablation for Remote Sensing Applications

6.1 Overview

This chapter demonstrates the single pulsed Nd:YAG laser ablation, in Denisyuk reflection mode to record 1D/2D holographic structures on various substrates with different optical properties, including rigid glass, soft polymers and gelatine coated with single as well as with multilayer of conductive and non-conductive materials. Surface morphology of polydimethylsiloxane (PDMS) based nanostructures was changed by applying mechanical force which in turn tuned their optical response at far fields depending upon the amount of force applied, yielding into a low cost and robust force sensor. This chapter introduces diffractive gratings, methodology and theory in section 6.2, while section 6.3 along with its subsections describes briefly the experimental results and analysis. Section 6.4 pivots around the discussion and summary of combined experiments.

6.2 Introduction

Holographic recording in the form of diffractive gratings are often called super prisim as they split polychromatic light into its constituents. Conventional glass prisms have limited use in advance optical devices due to their sizes and brittle nature. Planner miniature diffractive gratings have their potential use in data storage devices such as CDs/DVDs, biosensing (optical biosensor based on a porous silicon composite structure), security holograms on bank/business cards and currency notes to make forgery difficult [1-5]. Holograms made on edible materials are highly welcomed in the food industry for food decoration purposes. The personalised used of holography is limited due to the time consuming, high cost and expertise dependent

fabrication methods as well as due to the suitable materials availability. Historically, permanent images were recorded in photosensitive media based on multi-beam interference and wet chemistry involving silver halides or photoresists to create volumetric or surface gratings [6-10]. To create holograms with flexible dimensions, many recording materials have been proposed such as photorefractive, bacteriorhodopsin, thermoplastics and liquid crystals [11-16]. Amongst these various materials, photorefractive polymers have been the most promising media for rewritable holographic display. Such polymer composites are often doped with nonlinear chromophores, which can be poled by an external voltage. On the other hand, holograms are conventionally recorded by coherent laser beams, femtosecond direct laser writing [17, 18] where achieved resolution is limited due to the spot size, and other complex methods including E-beam lithography (EBL) [19] along with focussed ion beam (FIB) milling [20] which have still low-throughput, are labour-intensive and costly. Hence, the rapid fabrication of low-cost, flexible holograms at large scale production remains a big challenge.

Here, we utilised a single step, flexible, low-cost and simple method to record holograms on various different materials soft polymers, conductive/nonconductive multilayer films and on edible materials to demonstrate their application as food decoration and force sensing device. A nanosecond pulse laser and reflective object in Denisyuk reflection mode is used to record holograms in the form of periodic gratings by means of laser ablation on various light absorbing materials (Figure 6.1 a, b). Light absorbing materials coated on a surface can be selectively ablated by directing the intensity distribution of interference pattern to it. Peak intensity regions corresponding to constructive interference pattern ablate the material; however, the material in the destructive interference regions stays intact. Hence, a periodicity depending on the intensity distribution of an interference pattern can be recorded in a light-absorbing material. The collimated laser ablation is a physical process, where high peak power, determined by the ablation threshold of the coated material, is capable of selectively removing layers of material.

This is dissimilar to the photochemical patterning process. The recording of the interference pattern depends upon optical properties of recording media (*i.e.* absorption), working distance (between object to be copied and recording media), pulse duration, caption angle of the recording media, and the localised energy distribution of the laser beam, which is determined by the optical properties of the object to be copied.

Under monochromatic light illumination, uniform periodic gratings diffract light based on the periodicity as well as the wavelength of the illuminated light through them. Diffraction angles/distance of diffracted orders to the central-spot/non-diffracted zero order could be changed by somehow varying the periodicity of periodic gratings through the application of mechanical stress or due to thermal expansion/compression, as stated by Bragg's law [21, 22]. The transmitted monochromatic light through the periodic gratings is diffracted based on the periodicity of the target fringes, provided that there is a well-defined diffraction pattern at a far field. The diffraction pattern is composed of a more intense central spot due to non-diffracted light and n diffracted orders due to diffracted light intensity. If the distance of periodic gratings to the image screen and separation between the non-diffracted central spot and diffracted orders is known, then the relevant diffraction angle can be calculated by using Pythagorean theorem to figure 6.2c, from equation (6.1) [23-26],

$$sin\theta = \frac{l_1}{\sqrt{{l_1}^2+{l_2}^2}} \qquad (6.1)$$

Where θ is the diffraction angle, $l_1 = h$ is the 1st order inter space and $l_2 = d$ represents the distance between the grating sample and the image screen. The relationship between the periodicity of the gratings and diffraction distance/angle can be defined by the following equation,

$$d_1 = \frac{n \times \lambda}{sin\theta} \qquad (6.2)$$

For the 1st diffracted order, the value of n would be set as 1.

Strain created due to any applied stress (mechanical, thermal) depends upon the physical/chemical properties of the material onto which the nano-structure is engineered. On expansion, the dimension of the grating sample changes, i.e. the periodicity between the uniform periodic gratings widens. Using the extension ratio in macro-perspective, gratings period can be calculated as follows [27, 28],

$$d_2 = d_0 \times (1 + ή) \tag{6.3}$$

Here d_0 is the initial grating's period without any applied stress and ή is the extension ratio, which can be calculated by measuring the 1st order interspace. Next, changes in the optical response can be monitored to quantify the strain produced by specific values of applied stress on physical grating's structure.

6.3 Experiments and results

6.3.1 Materials and methods

Biocompatible gelatine: Gelatine is commonly used as; a food item, for smoked lenses, colour filters, photographic film emulsions, sizing, adhesives, inks and encapsulations. It is a mixture of proteins prepared by hydrolysing, via boiling, and collagen obtained from skin, ligaments, and tendons. Gelatine is composed of amino acids in the proportions; alanine, glutamic acid, hydroxyproline, proline, glycine along with small amounts of arginine, leucine, and aspartic acid [29-31]. Gelatine is approved as a food product and is easily digestible. Gelatine is strongly hydrophilic [32]. In cold water, dried gelatine can absorb up to ten times its weight of water, forming a viscous mass [33]. Adding alum to gelatine produces a harder gel [34]. Potassium chrome alum and formaldehyde (formogelatine) also harden gelatine and make it insoluble. The refractive index of gelatine is around 1.51-1.53; the melting temperature is 32 ∘c and density is 1.27 kg/m^3 [35-37].

Polydimethylsiloxane PDMD: Polydimethylsiloxane (PDMS) is non-toxic and inert silicon-based organic polymer capable of replicating 3D structures in nanometeric scales [38, 39]. PDMS has been a popular choice for soft lithography due to its robust nature, low cost and ease of fabrication to replicate nano/micro scale structures [38, 39]. Compared to traditional etching and bonding approaches, PDMS micro-modelling process is rapid and simple [40]. The optical properties of PDMS involve it having a refractive index of ~ 1.4. It is transparent in the visible range (240 nm – 1100 nm) with an extinction coefficient of < 10-10, 25 and has negligible birefringence[41], and inert properties which makes it suitable for prototyping and testing [42].

Ink characterisations: Black permanent ink (Staedtler, Germany) diluted with ethanol solution on glass, gelatine, PDMS substrates was used as a reflection holography recording medium. The Nd:YAG laser operated at 1064 nm and 300 mJ of energy was used during holographic recording. Spectrophotometer (resolution 0.1 nm) and a broadband light source (400–1100 nm) were purchased from Ocean Optics for optical measurements.

6.3.2 Holographic laser writing

Nanostructure fabrication was based on a single pulsed Nd:YAG laser and reflecting object in-line Denisyuk reflection holography mode (Figure 6.1a). The laser beam normal to the horizontal passed through the sample kept at 2D stage and reflected from the object. Reflected laser beam carrying information in the wave-front about the object from which it was reflected, propagated in an opposite direction to the incident beam. Both incident and reflected beams interfered and created standing wave effect, which showed constructive and destructive interference regions. The resulting standing wave (interference pattern) exposed the substrate with a high enough intensity to ablate the light absorbing film(s) to record the information it carried from the object in the form of periodic gratings.

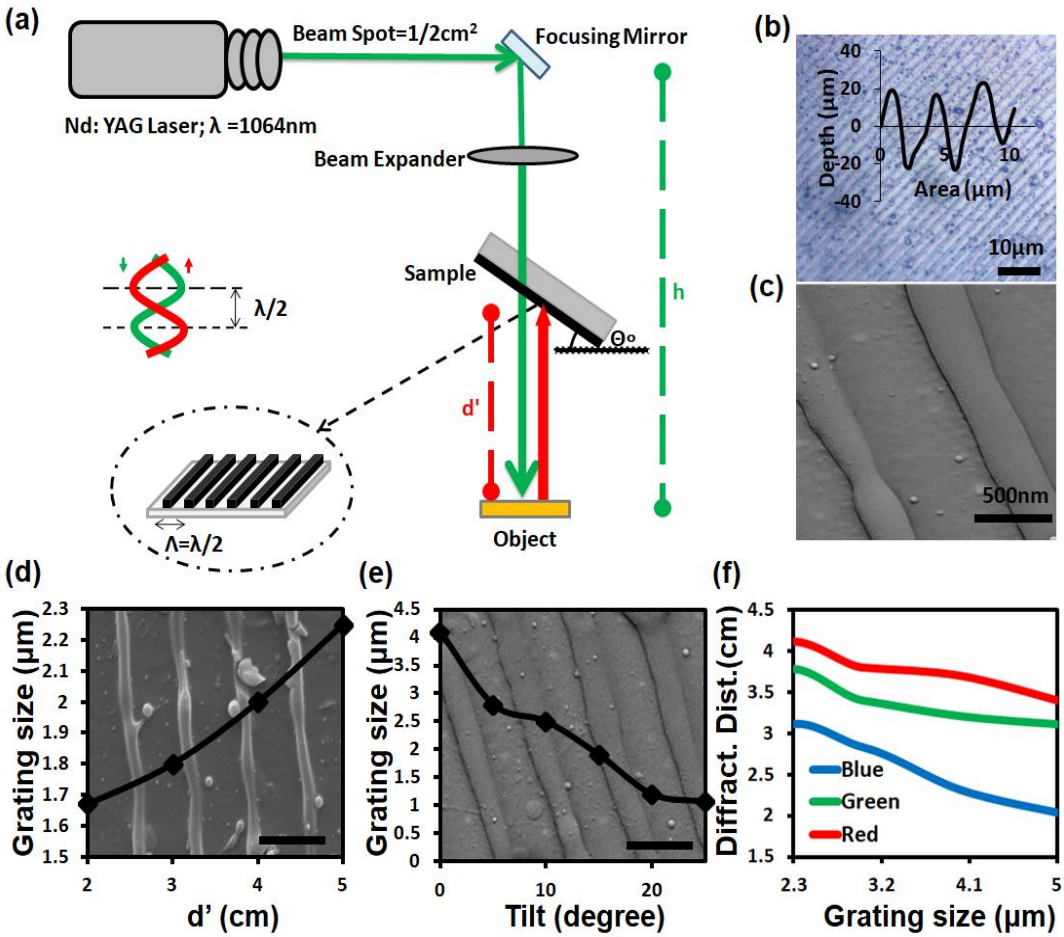

Figure 6. 1: Schematic of the laser setup (a) showing an Nd:YAG laser (1064nm) with beam spot size 1/2cm^2 directed from the top at the object to be copied. Sample is kept on a 3D stage above the object. (b) Optical microscopic images of fabricated samples showing the surface morphology of fabricated holograms; scale bar10µm (c) SEM image with scale bar 500nm. (d) SEM images with scale bars 2µm with the plot showing grating spacing as function of d variation. (e) With scale bar 2µm SEM image with plot depicting a relationship between grating spacing to the tilt angle of recording media. (f) Optical response captured during various d values and plotted d as a function of diffraction distance.

Nanostructures were recorded in the form of periodic gratings, as shown in figure 6.1(b, c), which were uniform to produce diffraction patterns at image screen during reading beam illumination. The characteristics of nanostructures made in light absorbing materials depends on the laser wavelength and geometrical parameters. The Sample (substrate coated with light

absorbing material) was adjusted in a flexible sample holder (adjustable along x, y and z axes) above the object to observe the effects of parameters i.e. d and θ variation on characteristics of recorded nanostructures. Object distance to the recording media, d was varied from 2 cm to 5 cm and the tilt angle of the substrate was gradually increased from 0° to 25° (θ=0°, 5°,10°, 15°, 20°, 25°) with respect to the object, during the recording of the nanostructures. Only one parameter was changed at a time while other parameters were kept constant. Figures 6.1(d-e), depict the grating size influenced by d and θ variation respectively. Figure 6.1(d) shows the trend observed in the increase of grating spacing from 1.7μm to 2.5μm with increasing value of d from 2cm to 5cm respectively. This is because the interference pattern spreads as it travels along a path. Similar spreading effects were also observed during optical characterisation, when the distance of the image screen to the illuminated holographic structures was deliberately increased. A decreasing trend in the grating size with increasing tilt angle is observed from figure 6.1(e); for 0◦ tilt angle, grating spacing is found to be 4.1μm, whereas for a tilt angle of 25◦, the grating spacing decreased to 0.9μm. Equation (2.33) suggests that the resultant wave oscillates in time but has spatial dependence. Also, the constructive interfering peak occurs at intervals of half wavelengths. However, other factors include, tilt angle of the sample and the distance of the object to the recording media, which can influence the periodicity, as stated by Bragg's law which states that the periodicity must be comparable to the wavelength of the standing wave created by incident and reflected waves (sticks to half of the wavelength limit). Figure 6.1(f) shows the spatial resolution, i.e. the separation between diffracted orders caused from the structured gratings, during red (650nm), green (532nm) and blue (450nm) normal light illuminations against grating spacing varied from 2.3μm to 5μm. Upon diversion from narrow grating spacing to broad grating spacing, the separation between the diffracted orders (diffraction distance) is observed to decrease, as stated by the Bragg's law.

6.3.3 Nanostructures recorded in multi-layered coatings

Optical response was predicted through computational modelling for various wavelengths of transmitted light as well as for various grating spacing, as shown in figure 6.2(a, b).

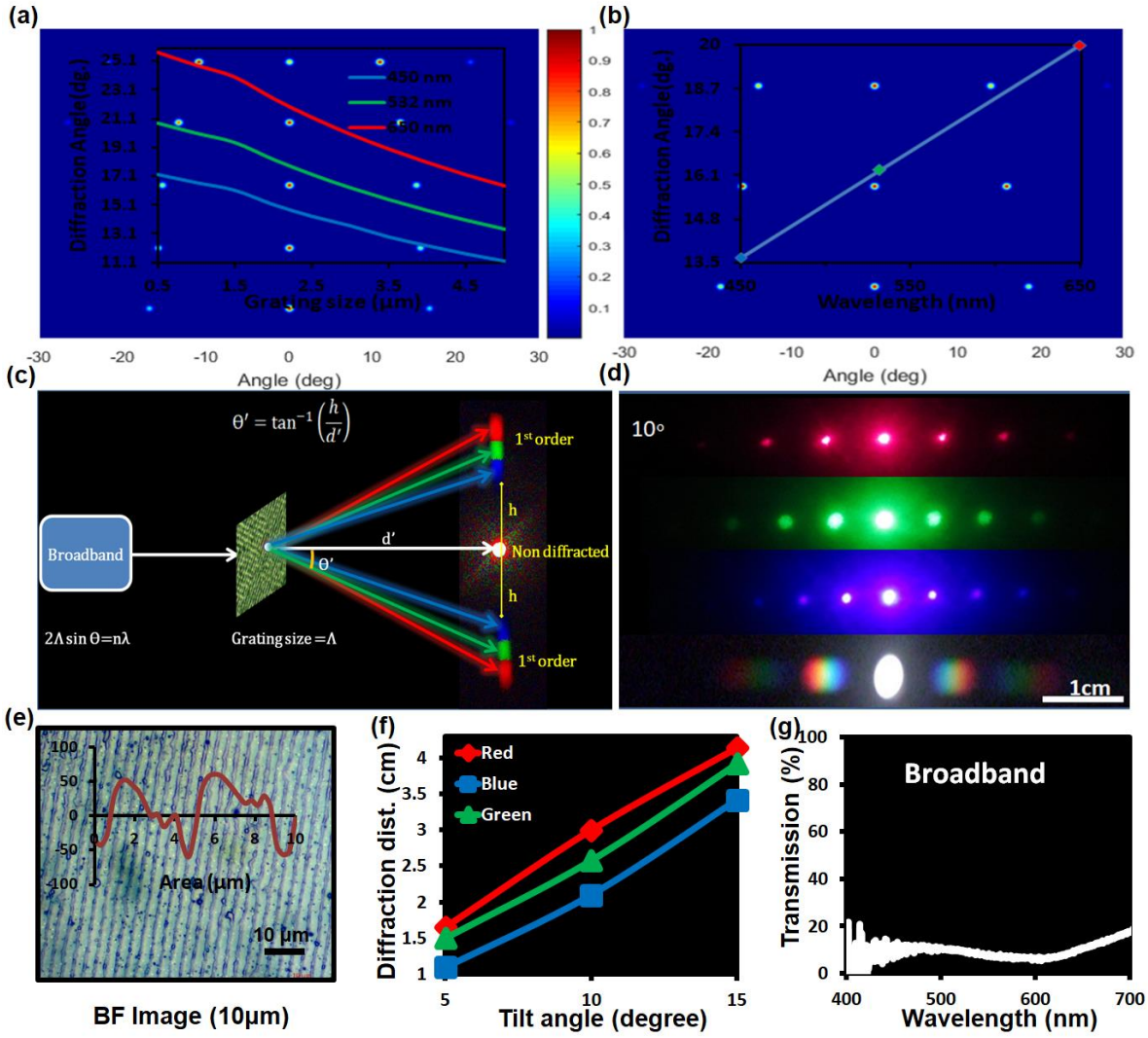

Figure 6. 2: Simulated and Experimental optical characterisation of the fabricated samples. (a) Diffraction angle (degree) with respect to grating spacing (b) Diffraction angle (degree) against the wavelength of transmitted light (c) Diffraction of broadband light at image screen. (d) Optical response under red, green, blue and white light normal illumination with scale bar 1cm. (e) Optical microscopic image providing information about the surface morphology of as fabricated gratings in multi-layered (ink/gold) coatings. (f) Optical response of the engineered structures as a function of tilt angle. (g) Transmission (%) measurements with broadband light through corresponding gratings.

Nanostructures were fabricated in a multi-layered coating, comprising of a conductive gold film on the top and a nonconductive ink film underneath deposited on a glass slide, through nanosecond pulsed laser ablation and optically characterised, using the setup shown in figure 6.2(c). Nanostructures were recorded in the form of periodic gratings shown in figure 6.2(e), which were uniform to produce diffraction patterns at the image screen during reading beam illumination; as depicted by figure 6.2(d). Monochromatic red (650nm), green (532nm), blue (450nm) and broadband light were transmitted, turn by turn, through the periodic structures fabricated within multi-layered coating. The optical response was recorded at the image screen, kept in front while the digital camera captured the response. The optical characteristics of nanostructure made in multi-layered coating were dependent on the wavelength of the transmitted light (reading beam), the distance of image screen to the sample and illumination angles. For the sake of simplicity, all other parameters were kept constant throughout the optical characterisation experiment except for the transmitted wavelength of light sources. Figure 6.2(d) shows the optical response of gratings, structured in multi-layered coating; where red (650 nm) was the highest wave length across the visible spectrum, which diffracted at the highest angle, hence indicating that the distance between diffracted orders is highest as compared to green (532 nm) and blue (450 nm), which have intermediate and lowest wavelengths, respectively. Rainbow patterns were obtained at each diffraction orders during white light illumination. Surface morphology of the fabricated structures can be seen by the BF image labelled as Figure 6.2(e). Tilt angle variation as discussed earlier by figure 6.1(d), is an important parameter used in changing the characteristics of the fabricated structures and is applied during the fabrication stage in multi-layered coating. Figure 6.2(f) shows the distance between the diffracted orders to the central spot (non-diffracted light) as a function of tilt angle, for all light wavelengths i.e. red, green and blue. It is observed that this distance increases with an increase in the tilt angle, which in turn means that the size of grating spacing engineered

within the multi-layered coating decreases with increased tilt angle. Figure 6.2(g) represents the broadband light transmission (%) through the multi-layered gratings at 10° tilt angle.

6.3.4 Edible gratings

Gelatine substrate coated with light absorbing material was used to demonstrate nanostructures fabrication on edible materials through the proposed fabrication set up (in-line Denisyuk reflection holography). Various edible nanostructures were fabricated and optically characterised by altering geometric parameters. Figure 6.3(a-c) shows the diffraction patterns obtained at the image screen by transmitting blue (450nm), green (532nm) and red (650nm) monochromatic light beams through periodic gratings fabricated on edible substrate respectively, at various tilt angles i.e. θ =0°, 5°, 10°, 15°, 20° and 25°.

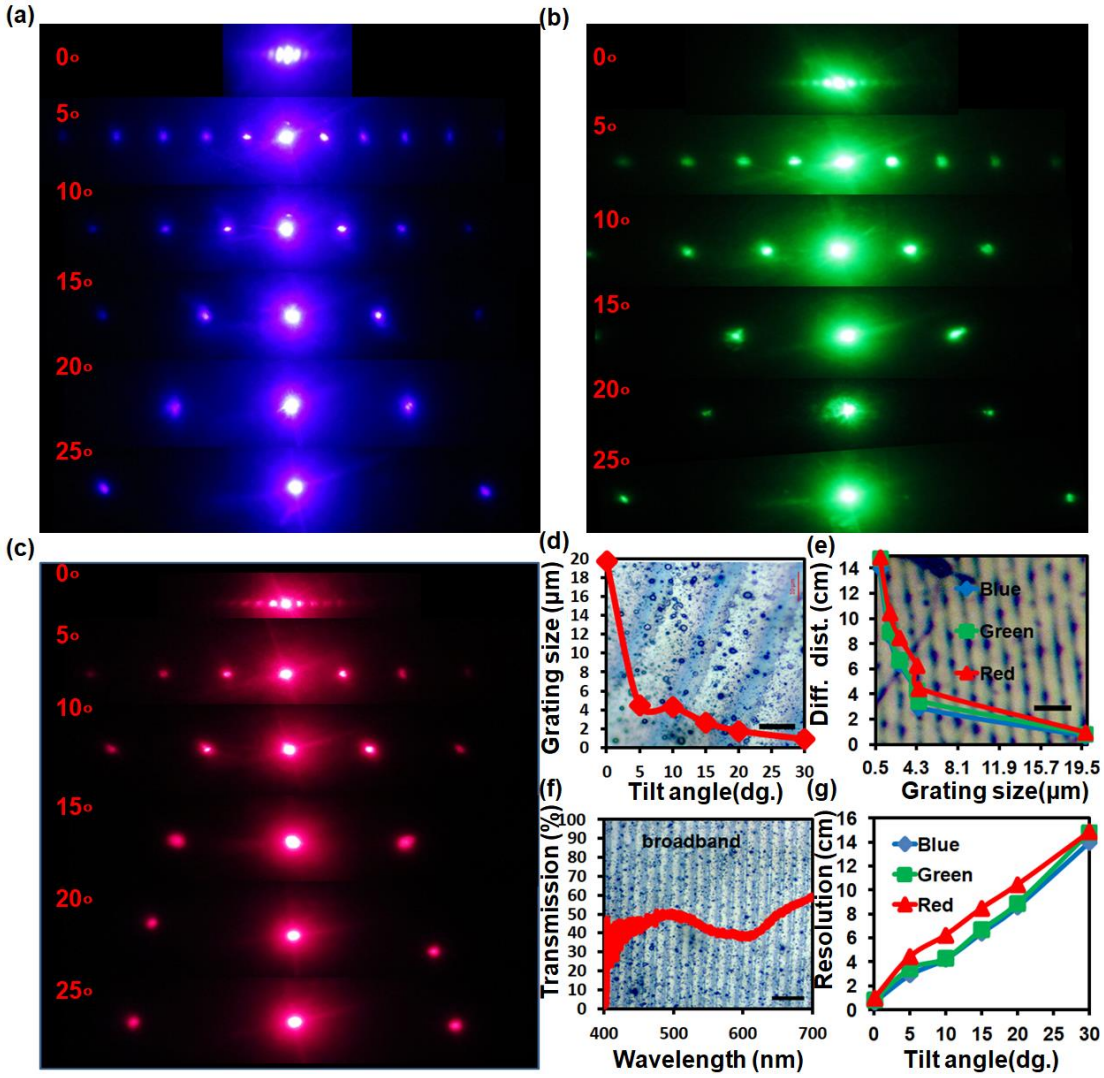

Figure 6. 3: Gratings manufactured on edible substrate (gelatine). (a-c) Diffraction patterns obtained by shining blue, green and red light through the gratings fabricated during various tilt angles (0-25°), respectively. (d) Optical microscopic image with scale bar 10μm showing topography of the edible gratings made at 0° tilt angle (θ°=0), whereas the plot showing influence of tilt angle onto the grating size. (e) BF image of surface gratings fabricated at 20° tilt angle; scale bar 5μm and the graphs showing diffraction distance with respect to grating size. Grating engineered at 10° tilt angle with the plot showing broadband light transmission (%) through them; scale bar 10μm. (f) Diffraction distance with respect to the response of the gratings made at 0-25° tilt angles with 5° increment each time under blue, green and red lights' normal illumination.

It is obvious from the diffraction patterns that each increment in the value of the tilt angle increases the diffracted order's separation. Figure 6.3(d) shows BF image of gratings made at 0° tilt angle with scale bar =10μm, the plot depicts grating size (from the end of one spacing to the end of next mutual spacing) decreased from 20μm to 0.9μm, when the exposure angle was increased from 0° to 30°, respectively. It is observed that the grating size decreases sharply from 0° to 5° of tilt angle, however beyond the 5° tilt, the decline in the grating size tends to become gradual and attains a constant value for higher tilt angles, around 30°. Equation (2.33) and figure 6.1e depict that, each constructive interfering peak occurs at a regular interval of half of the wavelength of the standing wave. However, other factors include, tilt angle of the sample and the distance of the object to the recording media can influence the periodicity of the grating and hence the overall size of the grating structure, as stated by Bragg's law. This trend is seen due to the λ/2 limit which strict the periodicity comparable to the wavelength of standing wave. Optical microscopic images taken in BF mode of the nanostructures made on edible substrate at a tilt angle of 25° are presented in figure 6.2(e). The figure shows that the very fine grating size are around 1.8μm, which is two-fold of the grating spacing, i.e.0.9μm at 25° fabrication, as shown by figure 6.1(e), which means ablated region is of the same size as non-ablated region. Spatial resolution/diffraction distance is much higher at higher tilt angles i.e. 15.6 cm against θ =30° as compared to the lower tilt angles i.e. 2cm at 5° tilt angle, as can be seen by figure 6.3(g). Plots in figure 6.3(e) are obtained by analysing blue, green and red laser beams' transmissions through the gratings made at various tilt angles. Highest wave length of 650nm (Red), diffracted at highest angle, while 532nm (green) at intermediate and 450nm (blue) at lowest angle, as predicted. Spatial resolution i.e. separation between central spot to the first order is recorded as 0.65 cm for 0° tilt angle and 13.9 cm for 25° tilt angle.

6.3.5 Tuneable gratings

PDMS, which is stretchable under mechanical stress was coated with light absorbing material (black ink) to generate gratings in flexible form and to further demonstrate its application as a force sensor. Samples were tilted at 10° with respect to the object i.e. exposure angle was 10° during fabrication. Grating's structure was analysed under the microscope and surface profile was plotted to analyse its surface morphology. Figure 6.4(a-b) presents the microscopic images showing uniformly-made gratings with surface morphology plots along with broad band light transmission through flexible periodic gratings structured on PDMS. Well-arranged periodic gratings in flexible form may yield tuneable, well-ordered diffraction patterns at the image screen without any considerable noise, for use as an effective force sensor.

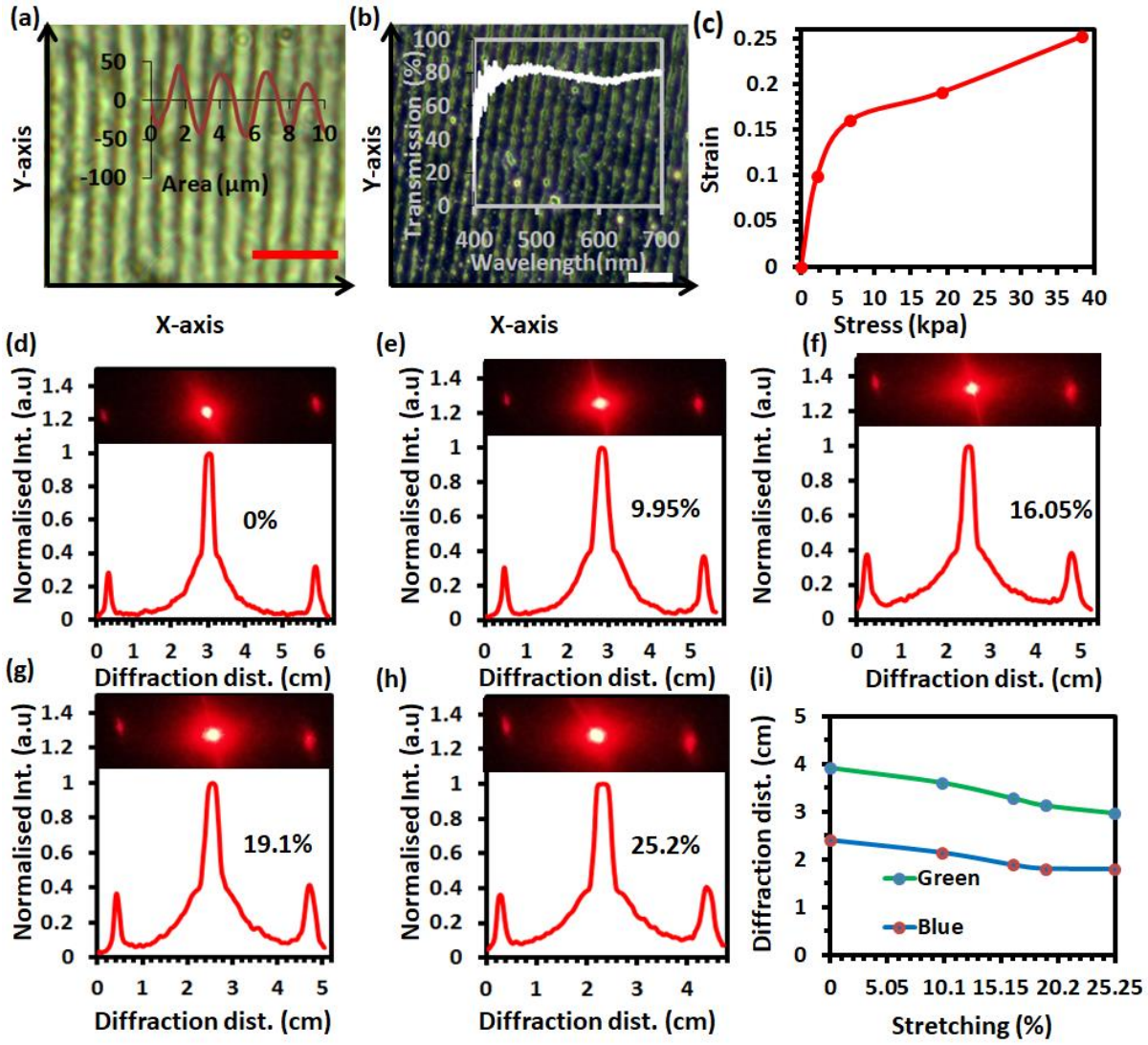

Figure 6. 4: Flexible gratings manufactured on PDMS substrate. (a, b) Optical microscopic images BF and DF modes; scale bar=10µm, plots depicting surface morphology and broadband light transmission (%) through them respectively, (c) stress against strain curve during red light normal illumination. (d-h) plots showing spatial resolution against normalised intensity during various stretching levels (0% to 25.2%). (i) Plots depicting change in spatial resolution against mechanical stretching under green and blue lights' normal illuminations in a similar manner as shown by figure 6.4 (d-h).

The sample was kept in a fixed two-dimensional stage with a weight suspension set up to be focused on any chosen point. Force, as weight suspension, was gradually applied on the stretchable periodic structures to increase the periodicity. Monochromatic light beams include red (635nm), green (532nm) and violet (435nm). These were illuminated at the normal angle

on to the sample, turn by turn, and resulting well-defined diffraction patterns were captured from the image screen for all applied stress values. The diffraction distance between the non-diffracted central spot to the diffracted first order was observed to note any changes in the optical response as result of the strain caused within the periodic structure. A linear relationship between extension ratio and periodicity of gratings was found. Expansion of grating's periodicity was found inverse to the diffraction distance of the diffracted orders, as predicted by simulations. Figure 6.4(c) represents the stress strain curve showing a linear rise from the start up to 5 kpa; whereas above that value of stress, the strain rate becomes slower i.e. due to approaching the stretching limit of the sensor. Stretching the sample means that the periodicity is increased between the adjacent grating, which in turn shifts the diffracted spots closer to the non-diffracted central spot. Reduction in the diffraction distance (tuned optical response) of the diffracted spots is then correlated to the strain caused within the PDMS based gratings by known applied force. Without stretching i.e. 0%, the diffraction distance was recorded as 6.23 cm, whereas for maximum stretching i.e. 25.2% of the original size of the sample, the diffraction distance reduced to 4.66 cm during red (650nm) light illumination. Figure 6.4 (d-h) shows the tuned optical response during red light normal illumination at the flexible gratings under various stretching, ranging from 0% to 25.2% along with their normalised intensities with respect to the diffraction distance. Figure 6.4(i) demonstrates the changes in diffraction distance during blue (450nm) and green (532nm) laser beams' normal illuminations, in similar manners as described for the red laser beam in figure 6.4(d-h). In general, there is an inverse relationship between diffraction distance to the applied stress, which is stated by the diffraction equation and is also predicted by the simulations.

6.3.6 2D nanostructures

Utilising the understandings of tilt angle variation affecting grating size, 2D gratings were constructed to demonstrate the feasibility of our fabrication setup to generate complex

nanostructures. Rectangular shaped, uniform gratings at 90° as well as at 30° were fabricated through Nd:YAG laser and in-line Denisyuk reflection holography.

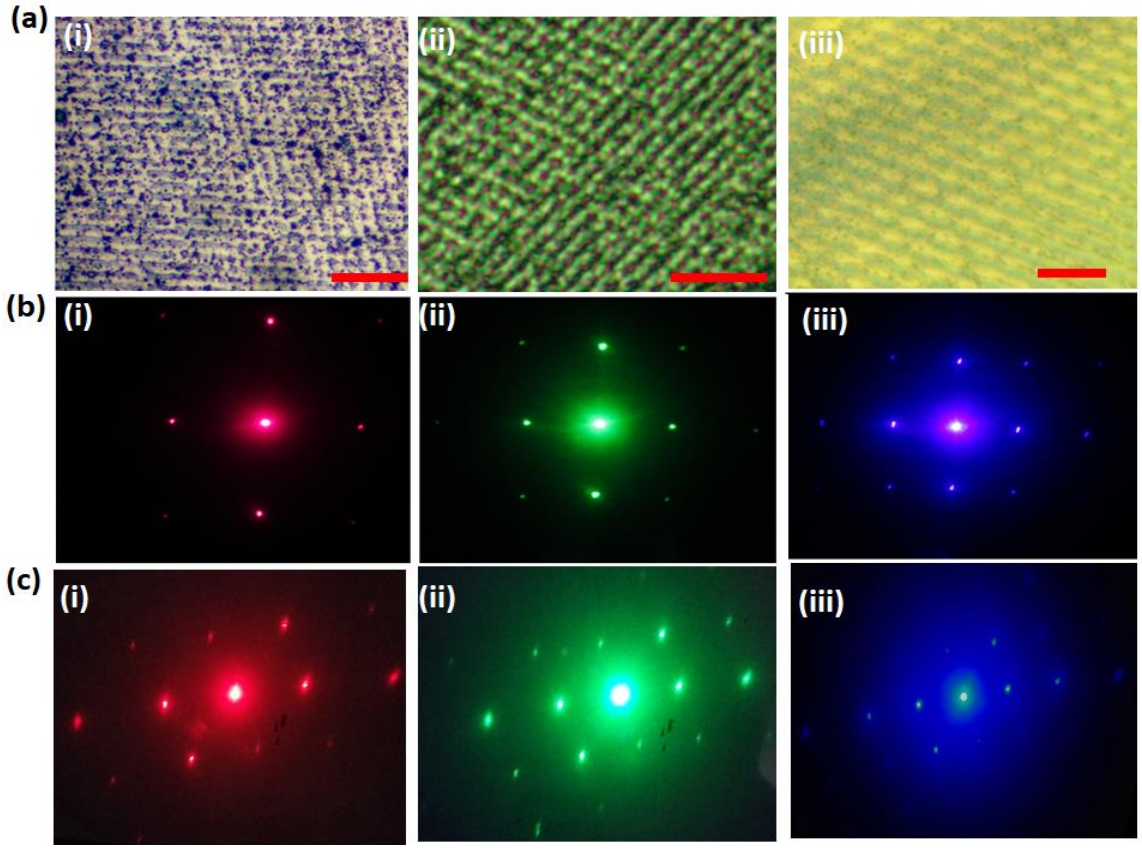

Figure 6. 5: 2D Rectangular gratings structured on ink coated glass substrate utilising the fabrication setup and direct femto second laser writing of squared shape gratings on transparent sample. (a i,ii) Microscopic images of 2D rectangular shaped gratings' structure with scale bars of 20µm and 10µm respectively. (iii) Microscopic image with scale bar of 10µm showing the 2D structures fabricated by rotating sample at 30° rotation each time (b i-iii) Optical response captured from the image screen under red, green, and blue light normal illuminations through structures shown in fig 6.5(a i, ii). figure 6.5(c i-iii) Optical response of the nano-structures recorded at 30° rotation with respect to the first laser exposure event, under red green and blue light normal illumination.

Figure 6.5a (i, ii) shows the optical microscopic images at different magnifications of the rectangular shaped structures made by twisting sample in xy plane at 90°, each time during both laser exposures. Figure 6.5a (iii) is the optical microscopic image of the structures made by

twisting sample in xy plane at 30° after first exposure. Rectangular shaped structures are obvious and uniform throughout the sample. Captured images of the optical response during red green and blue light transmission through as fabricated rectangular gratings can be viewed in Figure 6.5b (i-iii). It is observed that the horizontal/vertical spatial resolution of diffraction patterns depends upon the wavelength of transmitted beam, i.e. 650nm wavelength (red) diffracted at higher angles, and then diffraction angles gradually decreased as the transmitted wavelength decreased. Figure 6.5c (i-iii) shows the diffraction patterns obtained by transmitting same wavelengths of monochromatic lights (as from rectangular gratings) through the gratings' fabrication at 30°. It is worth mentioning that over here, the diffracted orders are not much distinguishable. It is anticipated that with few simple and fast steps, (i.e. variations in parameters) nanostructures with desired shapes and higher resolution can be fabricated if the demonstrated set up is followed.

6.3.7 Diffraction efficiencies with respect to transmission

To utilise holograms for various applications, spatial resolution is the key factor. Here, diffraction efficiency, i.e. the ratio of diffracted to non-diffracted light by grating's structure is demonstrated. Broadband light was transmitted through as coated samples with various compositions to compare diffraction efficiencies with respect to the transparencies of the samples. These measurements also optimise the flexibility of the set up used in this work to fabricate nanostructures on transparent as well as opaque samples via nanosecond laser ablation. Figure 6.6(a-d) shows the transmission (%) of broadband light through as coated; i.e. ink coated on PDMS block with 80% highest and 78% lowest transmission, ink coated glass substrate with 39.6 % highest and 10% lowest transmission, ink on gelatine leaf with 32% highest and 8% lowest transmission and ink plus gold coated on glass with highest 6.5% and 0.5% lowest transmission, respectively.

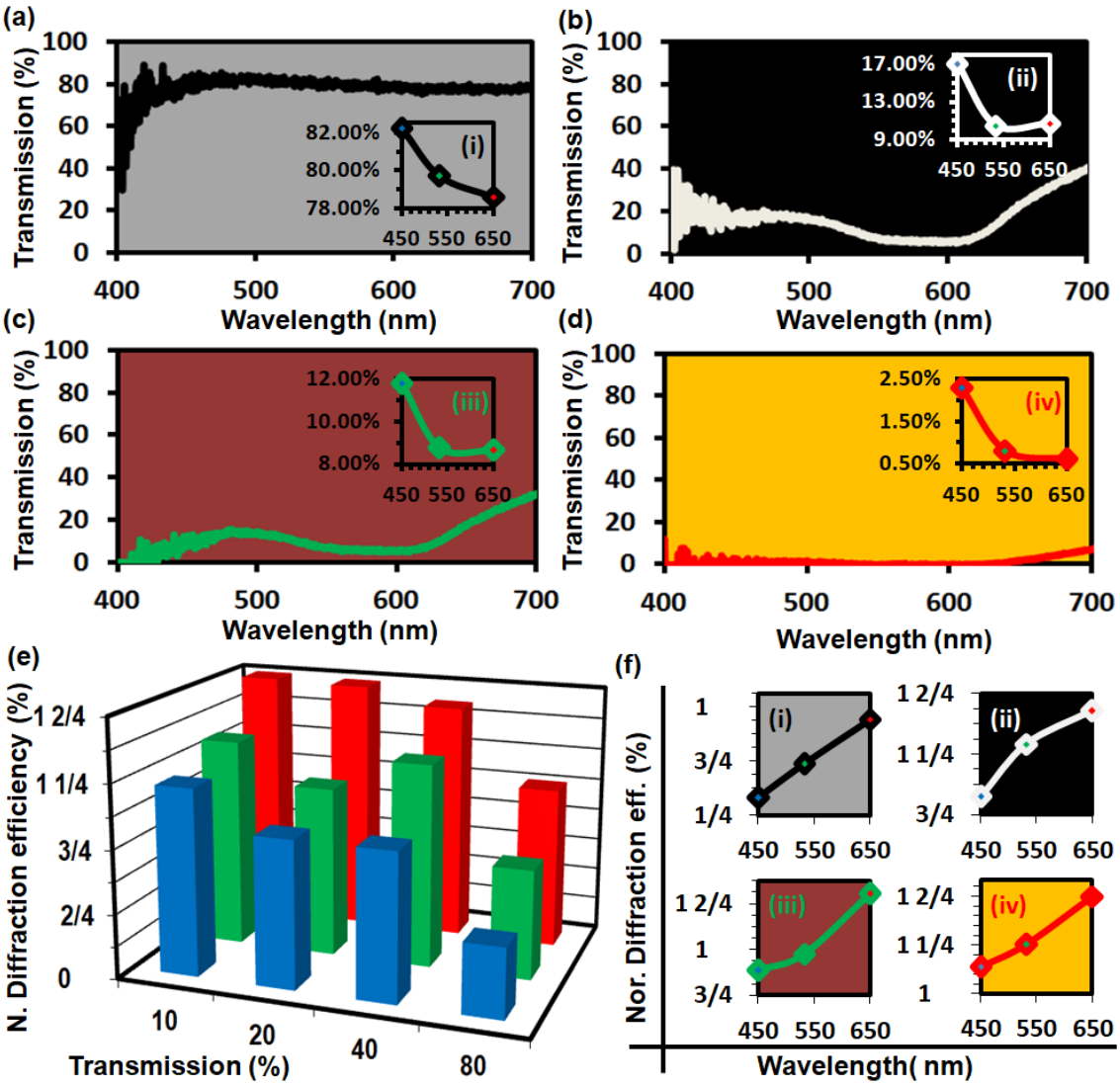

Figure 6. 6: Broadband light transmissions (%) through as coated samples. (a) Ink coated PDMS substrate (b) ink coated glass substrate (c) ink coated gelatine substrate (d) combination of ink and gold coatings on glass substrate i.e. ink coated on glass slide and gold layer was deposited on top of ink layer. (e) Normalised diffraction efficiencies (%) of the diffracted light at first order with respect to nondiffracted light at central spot as a function of broadband light transmissions (%), shown in figure 6.6(a-d). 6.6(f i-iv) Diffraction distance (cm) during blue, green and red-light transmission through fabricated gratings on the corresponding samples.

Figure 6.6(i-iv) consists of plots depicting the transmission (%) of monochromatic red (650nm), green (532nm) and blue (450nm) through samples mentioned in figure 6.6(a-d); it

was revealed that the lowest wavelength used i.e. 450 nm across the visible spectrum transmitted the most as compared to higher wavelengths, which include 532 nm and 650nm. All four substrates with various transmissions (%) ranging from 0.5% to 82% were exposed to Nd:YAG laser to record holograms successfully in the form of periodic gratings, which were then optically characterised in terms of diffraction efficiencies with respect to transmissions by illuminating monochromatic lights of 450nm, 532 nm and 650 nm wavelengths. Absolute diffraction efficiencies i.e. diffracted light intensities at the first orders to the non-diffracted light intensity at central spot for each diffraction pattern is compared and plotted in figure 6.6(e). During red (650 nm) light normal illumination at multi-layered gratings (<10% transmission), diffraction efficiency is recorded as 116%, whereas for 20%, 40% and 80% transmissions diffraction, efficiencies were recorded as 91%, 91% and 43%, respectively. Green (532nm) and blue (450nm) light transmissions also followed a similar trend, i.e. diffraction efficiency of the fabricated nanostructures is inversely proportional to the transmission (%) through the as coated samples to be structured by means of ablation. In general, red (650nm) the highest wavelength has highest diffraction efficiency as compared to green (532nm) and blue (450nm) light, respectively because the nanostructures are recorded with near infrared laser (1064nm) and have much comparable periodicity to the red light wavelength as depicted by Bragg's law. It is observed for lower transmission (%) of the material, diffraction efficiencies are higher and vice versa. For red (650nm) with 2.50%, green (532nm) 0.8% and blue (450nm) 0.6% transmissions the diffraction efficiencies are 160%, 130% and 116% respectively; obtained from multi-layered gratings, as shown in figures 6.6d (iv) and 6.6f(iv). Comparison of figure 6.6(ai, bii, ciii) and 6(fi-iii) indicates that highly transmitted wavelength through recording media, will be diffracted less through the fabricated holograms to replay the recorded event.

6.3.7 Rainbow patterns

Uniform nanostructures diffract light based on the wavelength of the light transmitted through them. Broadband light composed of seven colours was shined on various nanostructures fabricated through the setup used in this work, as shown in figure 6.7(a-d).

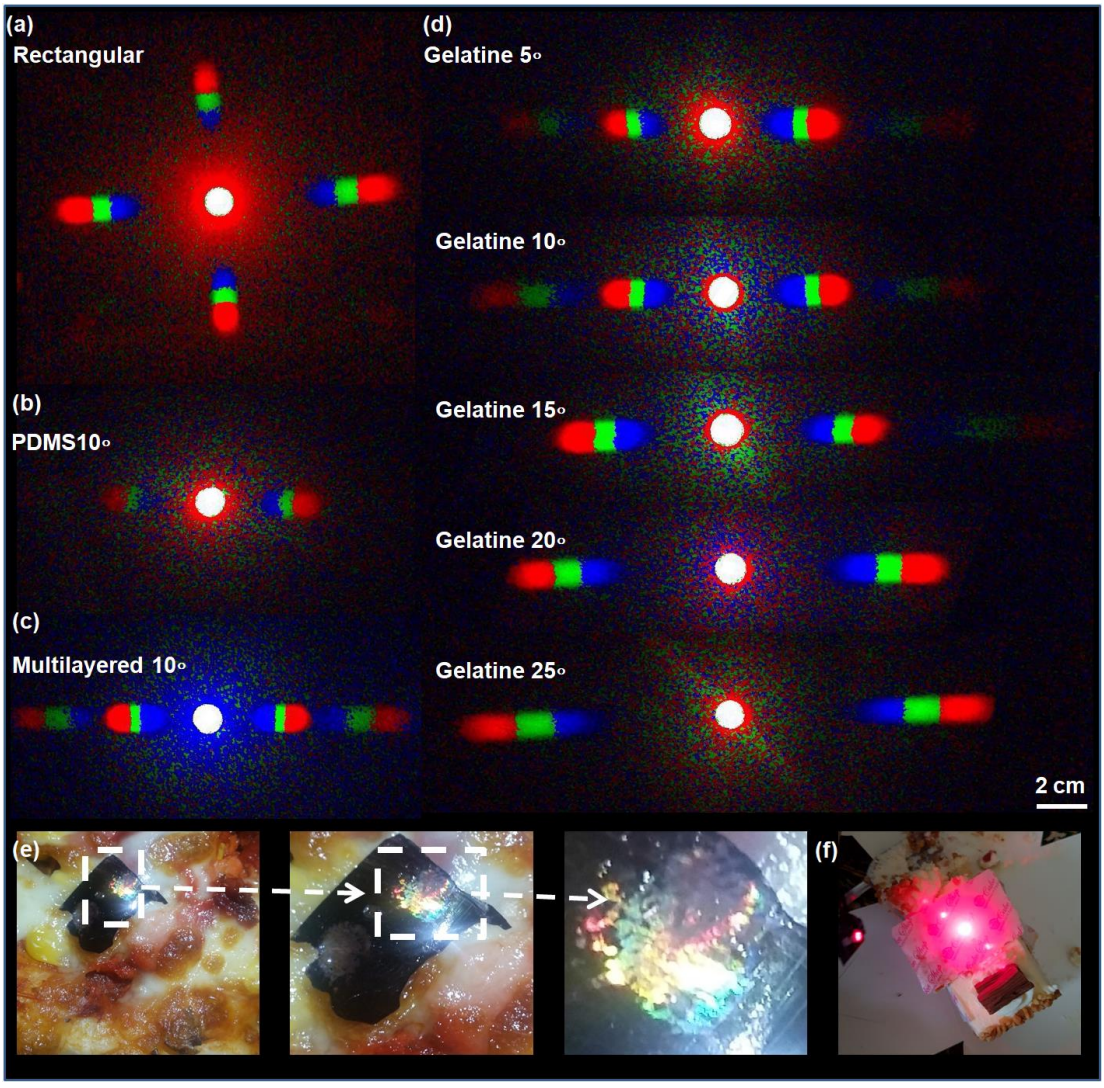

Figure 6. 7: Captured images of rainbow pattern obtained at the image screen during broadband light normal illumination through fabricated holograms via laser ablation. (a) Rectangular gratings (b) PDMS gratings fabricated at 10°. (c) Multilayer gratings engineered at 10° (d) gelatine gratings made at 5-25° tilt angles. (e-f) Broadband light illumination in reflection mode at edible gratings decorated at a Pizza and red-light transmission through them on cake.

Broadband light split into its constituent colours depending upon their wavelengths along with non-diffracted central spot (middle of the spectrum) i.e. white spot. Lowest wavelength violet diffracted at lowest angle and occupied nearest space closer to the central spot at first order, while red highest wavelength of visible spectrum diffracted most. Influence of grating size on light diffraction can be observed by figure 6.7(d). gratings with larger periodicities were formed at 5∘ exposure angle which diffract light at smaller angles with respect to non-diffracted central spot while fabrication at exposure angle 25∘ lead to fine grating's spacing which interns giving diffraction orders at the highest distance from the central spot. Edible gratings were used to decorate vegan pizza showing rainbow pattern in reflection mode and on fruit cake in transmission mode, as depicted by figure 6.7(e,) and figure 6.7(f), respectively.

6.4 Discussion and summary

1D/2D nanostructures in the form of periodic gratings based on stretchable, edible conductive and nonconductive materials have been produced *via* nanosecond pulsed laser and light reflecting object in-line Denisyuk reflection holography mode, keeping all parameters i.e. h (distance between laser tip and object), d (distance of object to the recording media), E(energy of the laser) and S (spot size) constant, except the exposure angles (i.e. tilt angles of the sample). The sample fabrication process was completed in few minutes. Black Ink was used for coating on the samples as light absorbing materials, however, to demonstrate the efficiency of the setup to fabricate nanostructures on various light absorbing materials, multi-layered films were also successfully structured. Multi-layered light absorbing coatings composed of nonconductive (ink) bottom layer deposited on a glass slide and conductive (gold) film on top of the ink layer. Potential of various materials to be structured for various optics' applications with simple, fast and flexible techniques are also discussed. Increasing d means that the standing wave (resulting from incident and reflected beams interference) travels a greater

distance before exposing the recording media, thus each increment in d resulted in the larger grating size due to beam spreading. Further, above optimum value of d (0.5-3.5 cm in this setup) the intensity of standing wave focussed on larger areas at the compensation of focused threshold intensity, which is required to ablate the target material.

To get a better spatial resolution of the optical response from physical nanostructures, gratings' spacing must be as fine as possible. The results showed that finer grating spacing yielded a higher spatial resolution. Tilt angle (i.e. the exposure angle of the standing wave to the recording media) variation of the recording media is found to be an important tool in controlling the grating size. Tuneable optical response was also demonstrated using flexible gratings structured on soft polymer substrate. Tuneable periodic gratings were stretched, i.e. grating size was increased and the changes in optical response were recorded. For each degree of stress, the grating spacing increased and the distance between the central spot to the first diffracted spot increased (higher spatial resolution). Broadband light connected with optical microscope was transmitted at normal through the surfaces of as coated samples as well as after structuring to assess the transmission (%) of various wavelengths, especially in the visible region influencing the nanofabrication with the current setup and to correlate them with their diffraction efficiencies. Recorded holograms include edible and stretchable periodic gratings' diffracted light in a similar way to the function of the object used. 2D nano-patterns were engineered by superimposition of two standing waves in an ink medium coated on a glass substrate by changing the tilt angle of the recording media by 3∘ each time, i.e. first standing wave was exposed to the sample tilted at 10∘ (larger grating size), while the second beam exposed to the same spot at 12∘ (finer grating size), to get rectangular shaped nanostructures.

Fabrication of nanostructures using the current setup found cost-effective as it is not requited to be attached with expensive equipment like e-beam and FIB milling are required to be attached with expensive SEM etc. Moreover, the fabrication process is fast, more productive

and provides more choice in the material's selection with various optical and conduction properties as compared to e-beam and FIB milling which are expertise dependent and are limited to only certain materials. Flexible (polymeric) diffractive gratings (flexible polymneric super prism) result into tuneable diffraction field with tuneable; spatial resolution, diffraction efficiencies and transmissions (%), which may be a step forward in holography and can be utilised for numerous novel applications in data storage devices such as CDs/DVDs, biosensing (polymeric gratings for endoscopic biosensing), security holograms on bank/business cards, and holograms on plastic currency notes to make forgery difficult. Nanostructures made on edible (biocompatible) material may have applications in food industry, medical research and developments. Nanostructures made on multilayer coating of conductive and nonconductive material's combination may be utilised for constructing many electrical components within few minutes. Optical properties of the recorded 1/2D nanostructures showed multiple highly intense diffraction orders, and efficient optical adjustable properties. Light diffraction properties of the different orders from the non-diffracted zero-order were tuned to higher distances by adjusting certain parameters, i.e. exposure angles and separation between object to be copied and target material, the physical grating structures, and this showed efficient tunability of the diffraction through monochromatic and broadband light at normal illumination. Therefore, holographic nanofabrication via laser ablation has applications in printable, low-cost optical devices including tuneable and biocompatible; diffraction gratings, wavelength-selective filters, diffusers, and lenses. Moreover, a single-step laser pulse ablation is a flexible, reliable and efficient technique in terms of cost and device production along with being less time consuming for recording holographic patterns on various light absorbing materials including conductive/nonconductive, single/multi-layers, transparent/opaque polymers and dyes.

References (vi)

1. Khalid, M.W., et al., *Holographic Writing of Ink-Based Phase Conjugate Nanostructures via Laser Ablation.* Scientific reports, 2017. **7**(1): p. 10603.
2. Vasconcellos, F.d.C., et al., *Printable surface holograms via laser ablation.* ACS Photonics, 2014. **1**(6): p. 489-495.
3. Xia, D., et al., *Nanostructures and functional materials fabricated by interferometric lithography.* Advanced Materials, 2011. **23**(2): p. 147-179.
4. Butt, H., et al., *Carbon nanotube based high resolution holograms.* Advanced Materials, 2012. **24**(44).
5. Lv, C., et al., *Angle-resolved diffraction grating biosensor based on porous silicon.* Journal of Applied Physics, 2016. **119**(9): p. 094502.
6. Yamaji, M., et al., *Three dimensional micromachining inside a transparent material by single pulse femtosecond laser through a hologram.* Applied Physics Letters, 2008. **93**(4): p. 041116.
7. Kondo, T., et al., *Multiphoton fabrication of periodic structures by multibeam interference of femtosecond pulses.* Applied Physics Letters, 2003. **82**(17): p. 2758-2760.
8. Chen, W., et al., *Plasmonic lens made of multiple concentric metallic rings under radially polarized illumination.* Nano letters, 2009. **9**(12): p. 4320-4325.
9. Liu, Z.-W., Q.-H. Wei, and X. Zhang, *Surface plasmon interference nanolithography.* Nano letters, 2005. **5**(5): p. 957-961.
10. Huang, M., et al., *Origin of laser-induced near-subwavelength ripples: interference between surface plasmons and incident laser.* ACS nano, 2009. **3**(12): p. 4062-4070.
11. Huang, Y.-H., J.-T. Wu, and S.-Y. Yang, *Direct fabricating patterns using stamping transfer process with PDMS mold of hydrophobic nanostructures on surface of micro-cavity.* Microelectronic Engineering, 2011. **88**(6): p. 849-854.
12. Hesselink, L., et al., *Photorefractive materials for nonvolatile volume holographic data storage.* Science, 1998. **282**(5391): p. 1089-1094.
13. Li, G. and P. Wang, *Efficient local fixing of photorefractive polymer hologram using a laser beam.* Applied physics letters, 2010. **96**(11): p. 111109.
14. Cole, M.C. and T.J. Trentler, *Thermoplastic holographic media*. 2011, Google Patents.
15. Kim, K.-H. and J.-K. Song, *Technical evolution of liquid crystal displays.* NPG Asia materials, 2009. **1**(1): p. 29.
16. Khalid, M.W., et al., *Flexible corner cube retroreflector array for temperature and strain sensing.* RSC advances, 2018. **8**(14): p. 7588-7598.
17. Watanabe, W., et al., *Fabrication of Fresnel zone plate embedded in silica glass by femtosecond laser pulses.* Optics Express, 2002. **10**(19): p. 978-983.
18. Alqurashi, T., et al., *Femtosecond laser directed fabrication of optical diffusers.* RSC Advances, 2017. **7**(29): p. 18019-18023.
19. Verheijen, M., *E-beam lithography for digital holograms.* Journal of Modern Optics, 1993. **40**(4): p. 711-721.
20. Streit-Nierobisch, S., et al., *Magnetic soft x-ray holography study of focused ion beam-patterned Co/Pt multilayers.* Journal of Applied Physics, 2009. **106**(8): p. 083909.
21. Kersey, A.D., T. Berkoff, and W. Morey, *Multiplexed fiber Bragg grating strain-sensor system with a fiber Fabry–Perot wavelength filter.* Optics letters, 1993. **18**(16): p. 1370-1372.
22. Fudouzi, H., *Optical properties caused by periodical array structure with colloidal particles and their applications.* Advanced Powder Technology, 2009. **20**(5): p. 502-508.
23. Erdogan, T., *Fiber grating spectra.* Journal of lightwave technology, 1997. **15**(8): p. 1277-1294.
24. Kim, J.H., et al., *Size-Monodisperse Metal Nanoparticles via Hydrogen-Free Spray Pyrolysis.* Advanced Materials, 2002. **14**(7): p. 518-521.
25. Berne, B.J. and R. Pecora, *Dynamic light scattering: with applications to chemistry, biology, and physics*. 2000: Courier Corporation.

26. Yetisen, A.K., et al., *Light-directed writing of chemically tunable narrow-band holographic sensors.* Advanced Optical Materials, 2014. **2**(3): p. 250-254.
27. X. Y. C. Y. Y. C. G. H. Ji Min, *"Fabrication of elastomeric tunable metallic gratings by metal transfer,".* www.paper.edu.com, 2012.
28. Yin, D., et al., *Stability improved stretchable metallic gratings with tunable grating period in submicron scale.* Journal of Lightwave Technology, 2015. **33**(15): p. 3327-3331.
29. Mills, J. and R. White, *Organic chemistry of museum objects*. 2012: Routledge.
30. Uriarte-Montoya, M.H., et al., *Giant squid skin gelatin: chemical composition and biophysical characterization.* Food Research International, 2011. **44**(10): p. 3243-3249.
31. Eastoe, J., *The amino acid composition of mammalian collagen and gelatin.* Biochemical Journal, 1955. **61**(4): p. 589.
32. Urbach, J., *Process for sterilizing hydrophilic gelatin lenses having ultraviolet stabilizers*. 1974, Google Patents.
33. Werten, M.W., et al., *Secreted production of a custom-designed, highly hydrophilic gelatin in Pichia pastoris.* Protein engineering, 2001. **14**(6): p. 447-454.
34. Van Den Bulcke, A.I., et al., *Structural and rheological properties of methacrylamide modified gelatin hydrogels.* Biomacromolecules, 2000. **1**(1): p. 31-38.
35. Gettens, R.J. and G.L. Stout, *Painting materials: a short encyclopaedia*. 1966: Courier Corporation.
36. Cygnarowicz, M.L., R.J. Maxwell, and W.D. Seider, *Equilibrium solubilities of β-carotene in supercritical carbon dioxide.* Fluid Phase Equilibria, 1990. **59**(1): p. 57-71.
37. Mozafari, M. and F. Moztarzadeh, *Controllable synthesis, characterization and optical properties of colloidal PbS/gelatin core–shell nanocrystals.* Journal of colloid and interface science, 2010. **351**(2): p. 442-448.
38. Hassanin, H., A. Mohammadkhani, and K. Jiang, *Fabrication of hybrid nanostructured arrays using a PDMS/PDMS replication process.* Lab on a Chip, 2012. **12**(20): p. 4160-4167.
39. Yuan, J., et al., *Design and fabrication of micro-cube-corner array retro-reflectors.* Optics communications, 2002. **209**(1-3): p. 75-83.
40. Karadimitriou, N., et al., *On the fabrication of PDMS micromodels by rapid prototyping, and their use in two-phase flow studies.* Water Resources Research, 2013. **49**(4): p. 2056-2067.
41. Hoshino, K. and I. Shimoyama, *Analysis of elastic micro optical components under large deformation.* Journal of Micromechanics and Microengineering, 2002. **13**(1): p. 149.
42. Jo, B.-H., et al., *Three-dimensional micro-channel fabrication in polydimethylsiloxane (PDMS) elastomer.* Journal of microelectromechanical systems, 2000. **9**(1): p. 76-81.

Chapter 7 Conclusions and Further Recommendations

7.1 Overview

Fabrication and real-life applications of various nanophotonic devices include; ink base phase conjugate nanostructures, gelatine based diffractive gratings, tuneable polymeric diffractive gratings, nanostructured multi-layered thin films, polymeric optical sensors based on CCR array and diffusing surface structures for remote sensing applications (temperature, force), CCR based leuco dye and liquid crystals based optical devices for remote temperature sensing, CCR based hydro chromic sensor for mist sensing application are demonstrated in this PhD research thesis. Ink based phase conjugate nanostructures, diffractive gratings on edible gelatine, soft polymers and coated with conductive/nonconductive substrates are generated via simple, fast and cost-effective laser interference-based ablation. Combinations of CCR with with liquid crystals, leuco dye and hydrochromic paint are utilised to develop wireless systems for remote temperature and mist sensing. Polymeric CCR array and diffusing surfaces are prepared via soft lithography in order to develop light weight, cost effective and simple systems for remote temperature and strain sensing to monitor environmental conditions within hazardous areas where personal access is not possible due to increased radioactivity, chemical hazards, or toxic gases emissions. This research demonstrates in detail the optical behaviour and dimensional changes of all fabricated optical structures under various environmental conditions through extensive optical characterisation experiments and microscopic analysis. Techniques such as theoretical analysis along with computational modelling are also employed in this research to predict and compare experimental results.

7.2 Contributions

a) Ink based phase conjugate nanostructures

Fabrication of 1D/2D phase conjugate nanostructures via laser interference-based lithography was detailed by utilising a single CCR and Nd: YAG laser in Denisyuk reflection holography mode. The fabrication technique is not expertise dependent and is not required to be attached with expensive equipment unlike e-beam lithography and FIB milling. Recorded ink-based holograms diffracted light in phase conjugation manners similar to the function of a real CCR. The only difference was that in the real CCR, 3D geometry is involved, whereas the recorded hologram in ink had a 2D geometry and showed phase conjugation properties in terms of 2D diffraction patterns under monochromatic/broadband light illumination. The resultant conjugate diffraction patterns were optically characterised, and their diffraction behaviour was predicted by numerical simulations. The intensity plots of phase-conjugated diffraction patterns showed inverse symmetry between the similar order numbers. The diffracted light intensity from the conjugated gratings was found to be two-fold than simple periodic gratings, while having unique surface morphologies with additional features, which is a step forward in holography and can be utilised to improve and develop numerous novel applications in encrypted data storage, security, remote sensing and identification.

b) Dynamic CCRs array

CCR array is replicated within PDMS via surface stamping in order to generate flexible, lightweight system for remote temperature and strain sensing. Polymeric CCR array was then optically characterised with various monochromatic light sources to assess its optical properties and was predicted through simulations. Optical response at the image screen is obtained in the form of a triangular shape, which is tuned based on the external stimuli. Manipulation in the

dimensions of CCR structures within the array by force application or thermal expansion yielded a change in the area of the optical image (triangle) at the image screen. Changes in optical response are then correlated with the applied stress and temperature values. For a desirable sensor, it is necessary to function in reflection mode, which is also demonstrated by coating the polymerised CCR array with gold. These kind of remote sensing systems are based on purely optical components, does not require power supply to function, easy to fabricate and reliable to use. Moreover, polymeric CCR array sensors may be helpful to measure temperature and strain within human restricted areas such as nuclear power plants and nuclear waste management facilities etc.

c) Thermochromatic materials and CCR based sensors

Due to retroreflection property of CCRs, they have a huge potential in developing optical sensors for measuring/supervising environmental conditions within human restricted areas (i.e. radioactive or chemically hazardous areas). The idea behind this approach involves just directing the laser beam at CCRs surface and monitoring the reflected response as they direct incident light towards the source without any angle of reflection or any illumination angles. A single CCR is coated with a thermochromatic material such as leuco dye and liquid crystals as well as with hydrochromic paint, to develop remote temperature and mist sensors. Monochromatic light sources are used to optically characterise all three systems, thermochromatic systems were monitored during heating and cooling events between their activation temperature values. Satisfactory results were obtained from both systems, with a 2% average relevant error.

d) Edible and flexible nanostructures via laser interference-based lithography in Densyuk Reflection mode

Diffractive gratings were produced within gelatine, polymers, conductive and nonconductive materials via laser interference-based lithography in Denisyuk reflection mode by optimising the fabrication setup parameters, such as h (distance between laser tip and object), d (distance of object to the recording media), E (energy of the laser), S (spot size) and exposure angles (tilt angles of the sample). Nanofabrication technique used here is found simple, cost effective and fast, fabrication process was fast completed within just few minutes and various materials with different optical properties. Black ink and gold films were used as recording media, however, to demonstrate the production flexibility of the proposed setup employed in this study to structure multi-layered light absorbing coatings composed of a nonconductive (ink) bottom layer deposited on a glass slide and a conductive (gold) film on the top were also selectively ablated. Optical properties of fabricated nanostructures in the form diffractive gratings (super prisms) was extensively studied through image projection experiments. SEM is also employed along with OM in order to characterise surface morphologies of fabricated structures. Diffractive gratings fabricated on PDMS substrate were mechanically stretched under continues light illumination. Customized optical response was tuned based on applied stress in order to show the potential of flexible gratings fabricated *via* laser interference-based lithography to be utilised as strain sensor. Diffractive grating on edible material were shown to be used as food decorating purposes.

Flexible photonic devices based on soft polymers enable environmental conditions and real-time remote sensing in various industrial applications; where conventional optical devices are based on active components i.e. they require power supply to function and might fail due to their rigidity and fabrication complexity. Polymerised diffraction gratings and diffusing

surfaces are generated through surface replication from a stencil to within the PDMS sheet. The structured sheet was mechanically extended, and the extension was remotely monitored *via* optical methods: where monochromatic light (450, 532 and 635 nm) was transmitted through the imprinted sensor under various stress levels, the optical response was recorded on an image screen and correlated with the strain created by the applied stress. The stress response was also analysed using computational modelling. The calculated Young's Modulus was found to be in a reasonable range as compared to the Young's Modulus of PDMS (360-870 kpa) Appendix D.

7.3 Conclusions

a) Holographic laser interference-based lithography can be used in combination with CCR to fabricate phase conjugate nanostructures in light absorbing media. The recording process is completed in few minutes and does not involve any expensive equipment attachments for operation unlike e-beam or FIB milling which require SEM.

b) Experiment results demonstrated that the diffracted light intensities of ink-based phase conjugate nanostructures were almost doubled as compared to the diffraction efficiencies of the simple periodic gratings. Therefore, ink-based phase conjugate diffractive gratings fabricated may have improved applications in printable, low-cost colour selective optical devices, tuneable wavelength-selective filters.

c) Optical response of ink-based phase conjugate nanostructures having unique surface morphologies with additional features, may be a step forward in holographic displays and could be utilised for numerous novel applications such as biosensing, business cards, encrypted data storage, and security.

d) Fast, flexible, cost-effective and facile laser interference lithography (in Densyuk reflection mode) can be optimised to create nanostructures in various materials for different applications such as, gelatine-based nanostructures (edible) to be used for food decoration purposes, PDMS based optical sensor for force sensing applications and multi-layered nanostructures were made with a multilayer of ink (bottom) and gold (top). Demonstration of multi-layered nanostructures where gold being conductive and ink being nonconductive material may help to create miniature and inexpensive electrical components within few seconds.

e) Ink as recording media for holographic recording of 1D/2D surface structures is cost effective, easily available, nontoxic and can yield similar image resolutions as well as diffraction efficiencies as compared to metallic coatings, such as Au and Ag. Moreover, the ink coating process is much easier and simpler than the coating procedure for other materials or metals, which require sputtering facilities.

f) Flat, thinner, flexible diffractive gratings (often called super prism) due to their compactness may be a good substitution to the rigid glass prisms, as they can effectively split polychromatic light into its constituent.

g) Optical structures engineered on soft materials with specific optical properties, on illumination, can yield tuned/varied optical response under mechanical stress. Change in customised optical responses caused by dimensional change of physical structures due to applied stress can be used to measure and quantify changes in environmental conditions.

h) Metal coated CCR has an increased acceptance angle and can be employed to reflect incident laser beam from Nd: YAG laser of high intensity to cause interference pattern, which can then be directed towards a substrate, coated with light absorbing material, to

produce well-ordered ablated and non-ablated regions on its surface. The optical properties such as phase conjugation in recorded hologram within a thin film are retained and are comparable to the optical properties of the original object (CCR).

i) Optical sensors based on purely optical elements require no power supply to function unlike electrical sensors which are based on active components, , immune to EM and thermal noise interference, no power supply needed to function and have an increased demand in most of the remote sensing devices.

j) Rigid structures with various dimensions (size, shapes, orientation) can be transferred from stencil to the target material (polymers, gelatine) by surface stamping to construct polymeric optical devices, which are flexible/stretchable, light weight, compact, cost-effective and simple in terms of fabrication and function.

k) Polymeric micro/nanostructures have the ability to be used in remote sensing applications as they can be expanded or compressed and can yield tuned optical response based on external stimuli, such as temperature variation, applied stress or other environmental factors.

l) CCRs array structures due to their retroreflection property were successfully replicated within the PDMS block to convert rigid and constant dimension structures into a flexible/stretchable CCRs array structure. Study suggests that polymeric CCR array structures can be used for remote temperature and force sensing applications.

m) Sensitivity of polymeric optical sensors could be customised by the addition of impurities in PDMS mixture during the following stages: fabrication, metallic/nonmetalic coatings, paints and polishing.

n) Difference between coated and uncoated CCRs is found only in terms of acceptance angle. Usually, available CCRs are metal coated to increase their acceptance angle. However, metal coating of CCRs can be replaced with any other desirable coating material such as thermochromatic materials, radiation sensitive material, humidity sensitive dyes, or any other materials which are sensitive to specific atmospheric factors for remote sensing purposes. The ability of CCRs to reflect incident light in the same direction to where it was first sourced, makes them a perfect choice to be employed in remote sensing devices. CCR based sensors can be used to measure environmental factors within nuclear power stations, aerospace, toxic chemical or gas facilities along with mining and in several more applications

o) Thermochromatic liquid crystal and thermochromatic leuco dye were applied for coating on uncoated glass CCRs and the surface, which were then illuminated with monochromatic light sources, while the temperature was varied within the activation temperature values of these materials. The detected optical response i.e. the reflectance percentage was dependent on the instantaneous colour of the thermochromatic material, which was in turn dependent on the temperature of the CCR surface. Both systems yielded satisfactory results with an average error of under 2%. The fabricated systems are compact, simple to fabricate and function, and operate in reflection mode, which is a more desirable factor in sensing systems. The sensor's sensitivity may be influenced by external factors such as, humidity, ambient light, dust and many more. In addition, colour visualisation of liquid crystals is strongly angular dependent, so consistency within illumination angles may help to obtain accurate results.

p) Leuco dye systems are cost effective than liquid crystals and are usually more robust. However, they are less sensitive (i.e. a 3 °C temperature change is required for a leuco dye to change its colour) than the liquid crystals (which require 1°C to change from red

to yellow). Moreover, presence of a hysteresis loop between heating and cooling events may lead to some complications in measurements, whereas, liquid crystals show consistency between both, heating and cooling temperature values and can also be accurately calibrated to get precise measurements.

q) Applied force (increasing the periodicity of adjacent gratings) is found to be inversely related to the diffraction angles (separation between the adjacent orders at image screen) during monochromatic light illumination. Whereas, diffusion fields are found directly proportional to the applied force. In both cases, optical response was tuned based on applied stress, which is the backbone of a material used for sensing.

r) Surface imprinting/embossing to replicate polymeric optical structures from the master surface is simple, productive and cost-effective but is not a fast process as a significant amount of time is required for the preparation and further treatment of the polymeric structures. In addition, the dimensions of replicated structures remain constant to that of stencil. On the other hand, laser interference lithography is a more flexible and productive technique to engineer micro/nanostructures to obtain desirable image resolution (optical response) along with being fast in terms of device production time. Moreover, it can be utilised to write holographic patterns of desirable dimensions/shapes (by simply changing certain parameters) on various light absorbing materials including transparent/opaque polymers, gelatine, metallic/non-metallic films and dyes for various everyday life applications.

7.4 Further recommendations:

Based on the key findings of this work, the following areas for further researches can be suggested:

a) Work should be carried out to modify laser interference based lithography for volumetric holographic recordings.

b) Metallic/non-metallic, conductive/nonconductive and combination of coatings instead of ink/gold could be structured to receive interesting and desirable optical properties and applications. These include structural tattoos and electrical components along with several more.

c) Chemical composition of PDMS could be changed by introducing some impurities to obtain a customised response.

d) Polymers with an increased sensitivity towards temperature could be structured via laser interference-based lithography, such as PMMA.

e) Gelatine can be structured via replication to be used for food decoration purposes.

f) Food colours should be structured via the laser based selective ablation method.

g) CCRs should be utilised for many other remote sensing applications as well by coating them with radiation, or chemical-sensitive optical materials.

h) Direct laser writing, femtosecond/picosecond laser interference methods can also be employed to fabricate nanostructures for advance optical applications.

Appendices

Appendix A

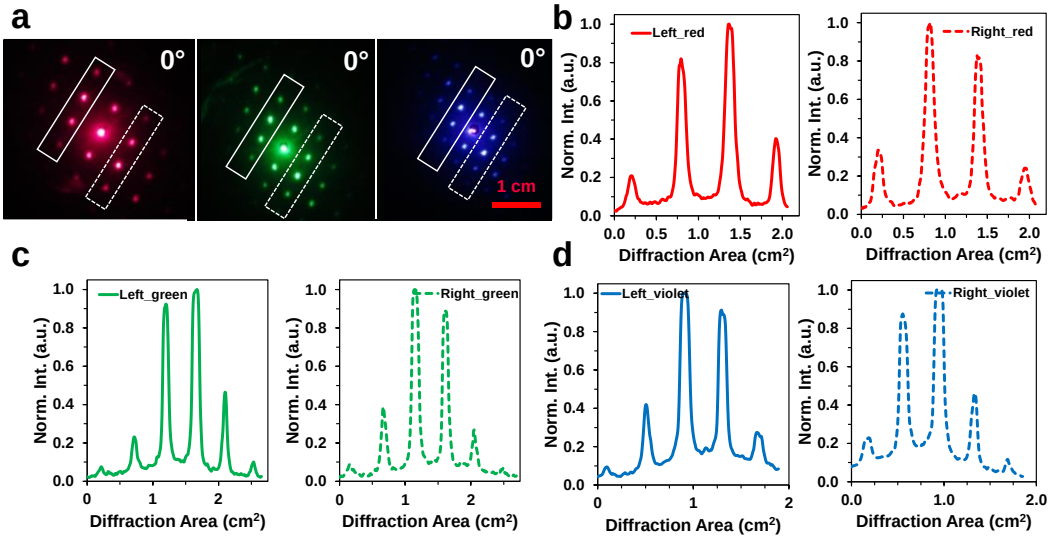

Figure S3. 1**:** (a) Conjugate diffraction patterns with 0° tilted angle. (b-d) left and right conjugation plots with red, green, and violet light through normal illumination.

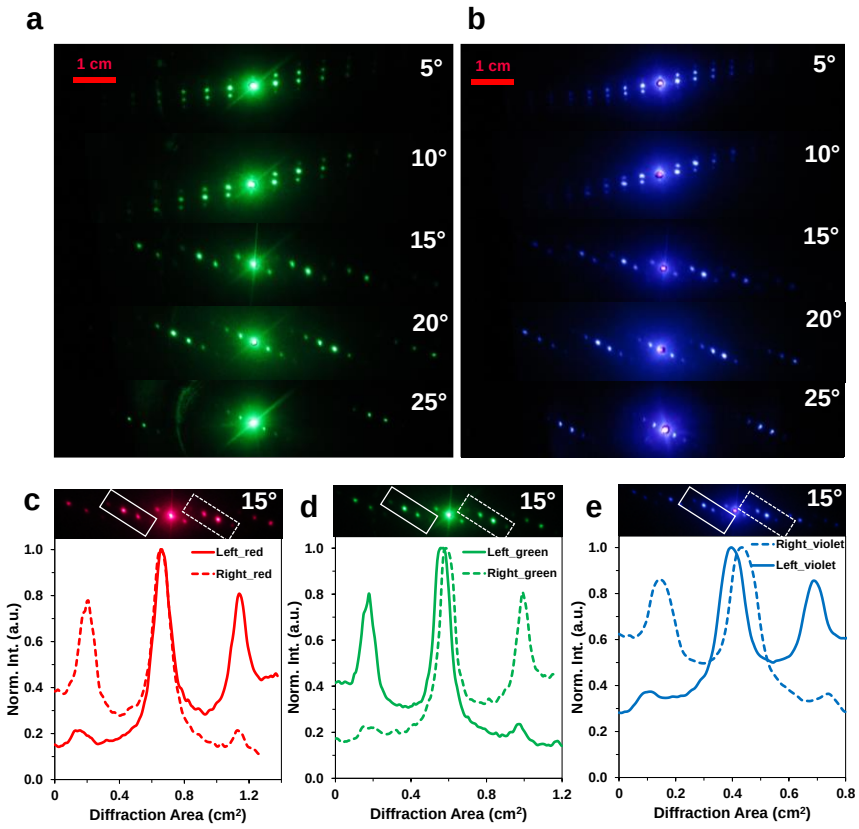

Figure S3. 2**:** (a,b) Conjugate diffraction patterns with 5-25° tilted angles. (c-e) left and right conjugation plots of 15° tilted sample with red, green, and violet light through normal illumination.

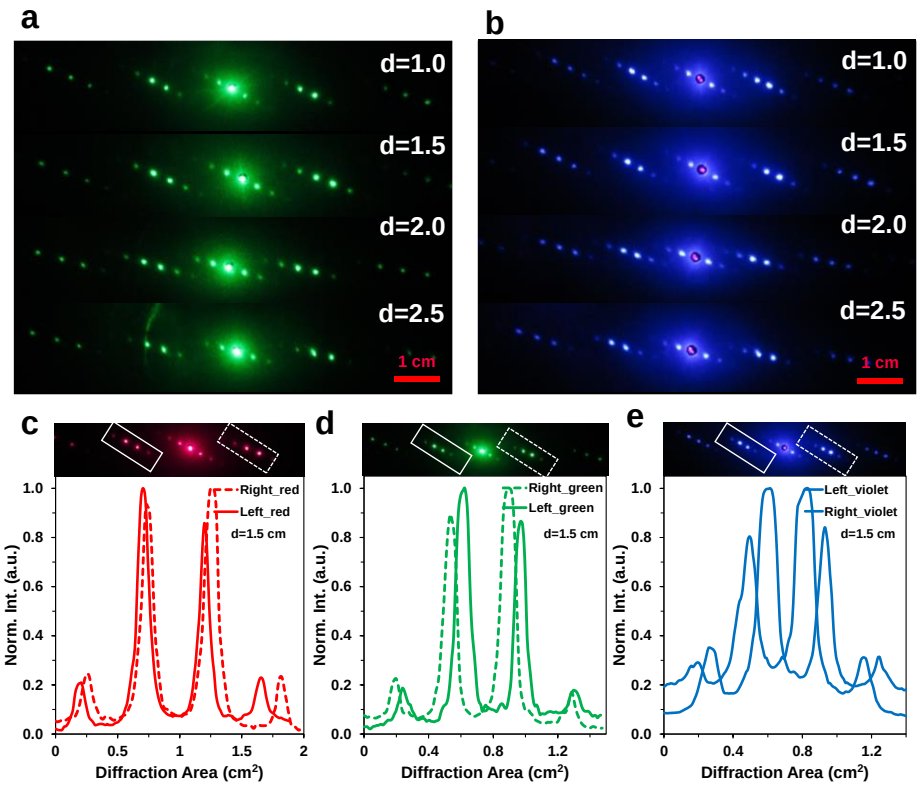

Figure S3. 3**:** (a,b) Conjugated diffraction patterns through green and violet light illumination with distance variation from 1-2.5 cm. (c-e) left and right conjugation plots of 15° tilted sample with red, green, and violet light through normal illumination.

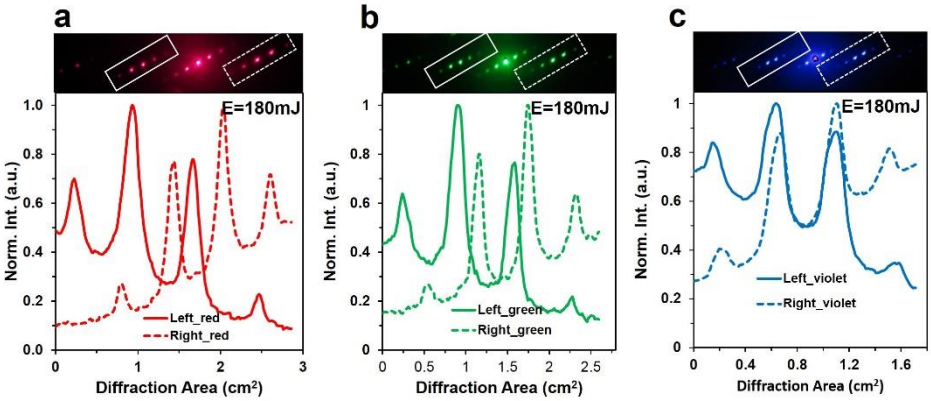

Figure S3. 4**:** (a-c) Left and right conjugation plots of the recorded sample (Energy, E=180mj) through red, green, and violet light normal illumination.

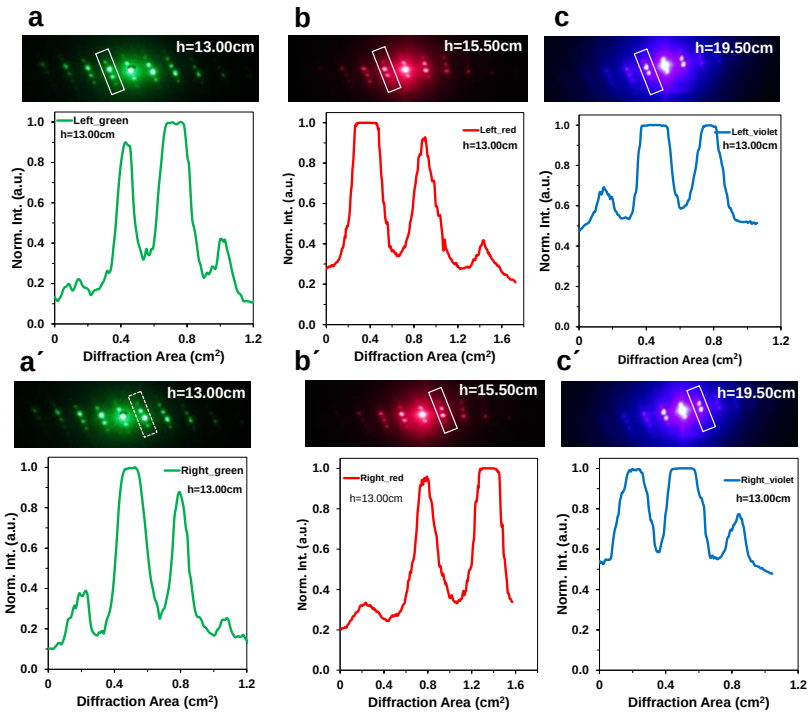

Figure S3. 5**:** (a-c) Left and right conjugation plots of the recorded sample at working height, h=13.00, 15.50, and 19.50 cm through red, green, and violet light normal illumination.

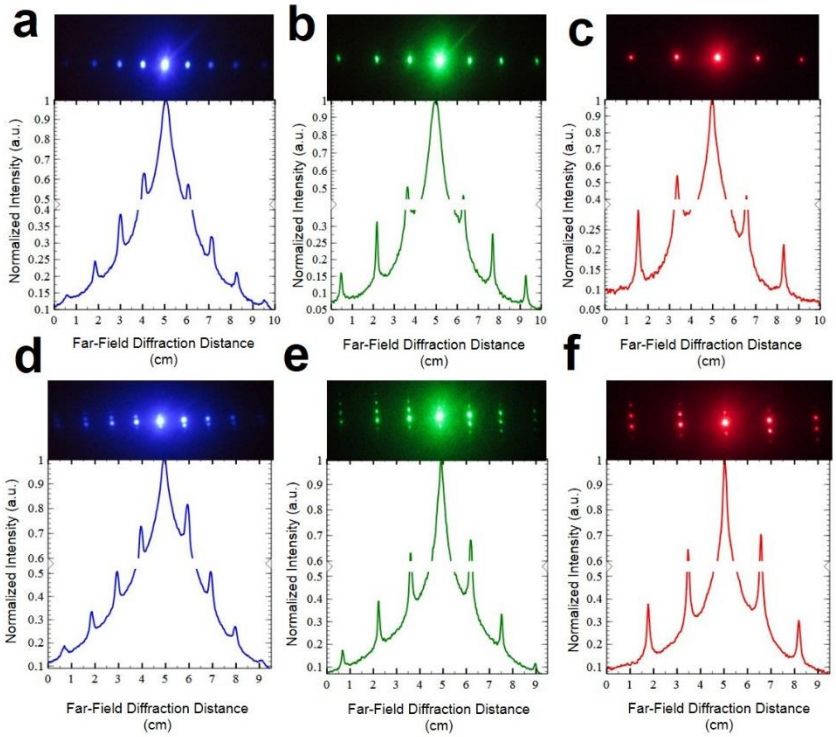

Figure S3. 6**:** (a-c) conventional, and (d-f) conjugate diffraction plots along horizontal direction through red, green, and violet light normal illumination.

Appendix-B

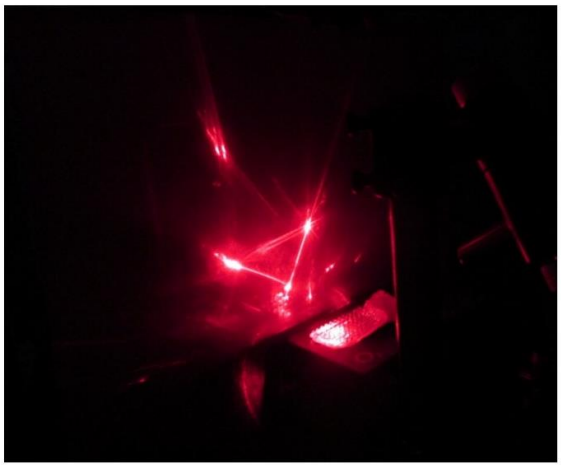

Figure S4. 1: Optical characterisation through reflection mode.

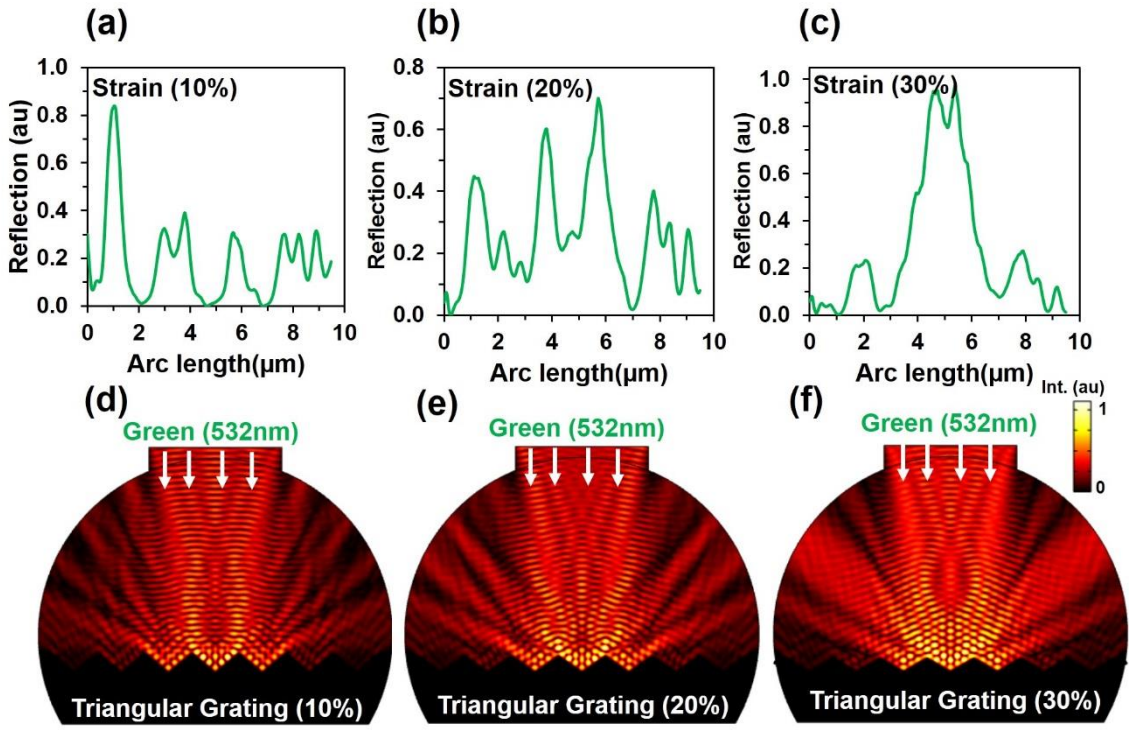

Figure S4. 2: Computational modeling of retoreflection, diffraction/scattering from triangular grating structure with strain variation (10, 20, 30%) and green light illumination.

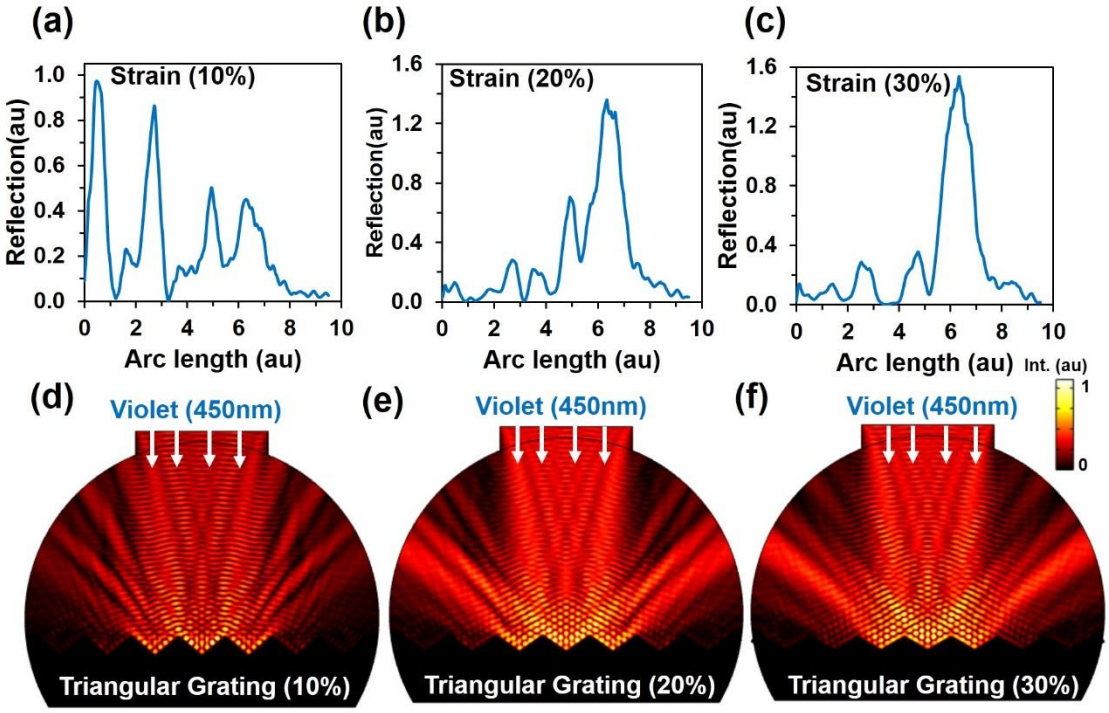

Figure S4. 3: Computational modeling of retoreflection, diffraction/scattering from triangular grating structure with strain variation (10, 20, 30%) and violet light normal illumination.

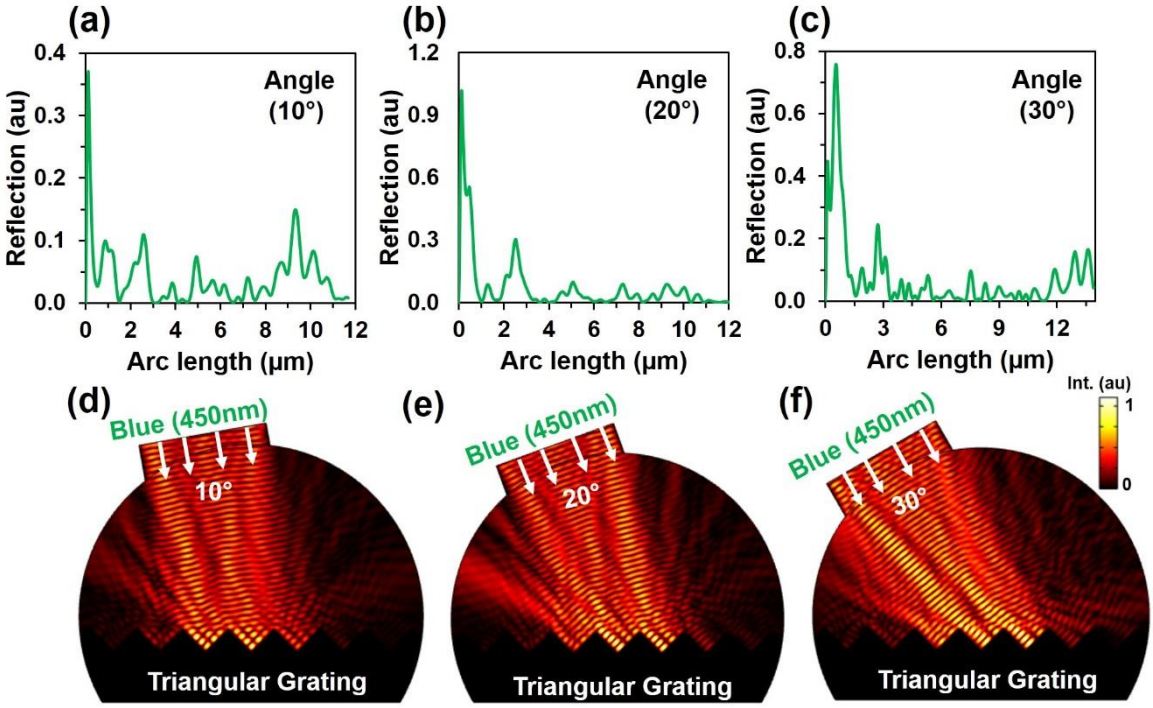

Figure S4. 4: Computational modeling of retoreflection, diffraction/scattering from triangular grating structure with green light illumination angle variation.

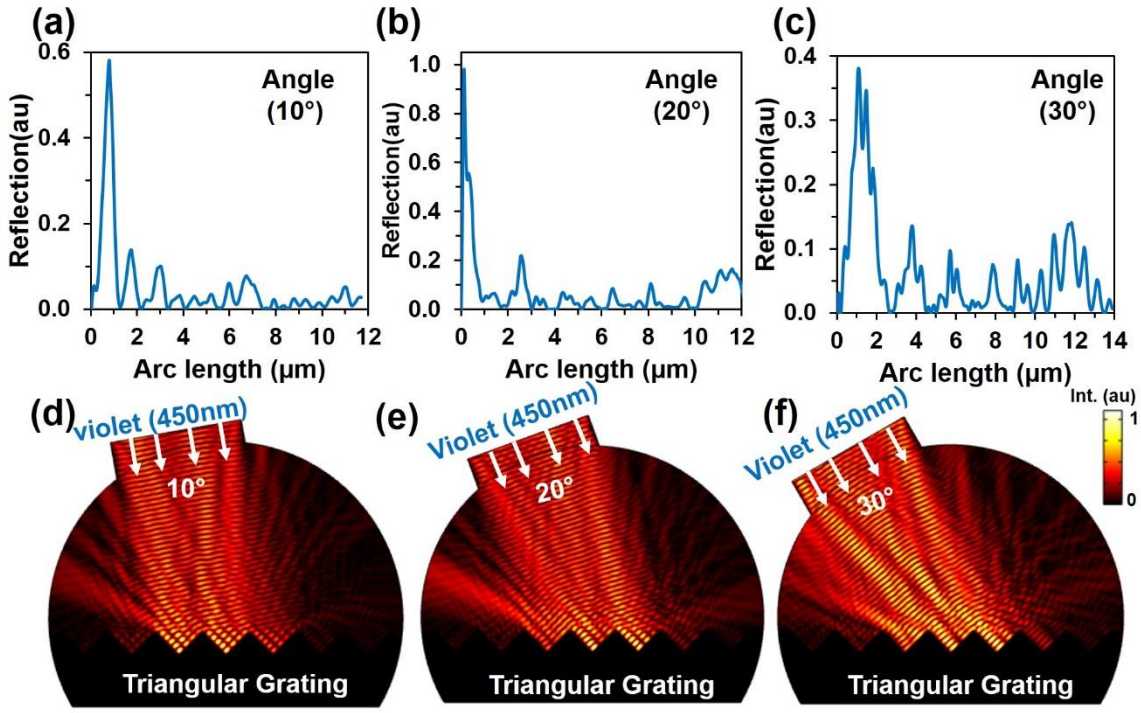

Figure S4. 5: Computational modeling of retoreflection, diffraction/scattering from triangular grating structure with violet light illumination angle variation.

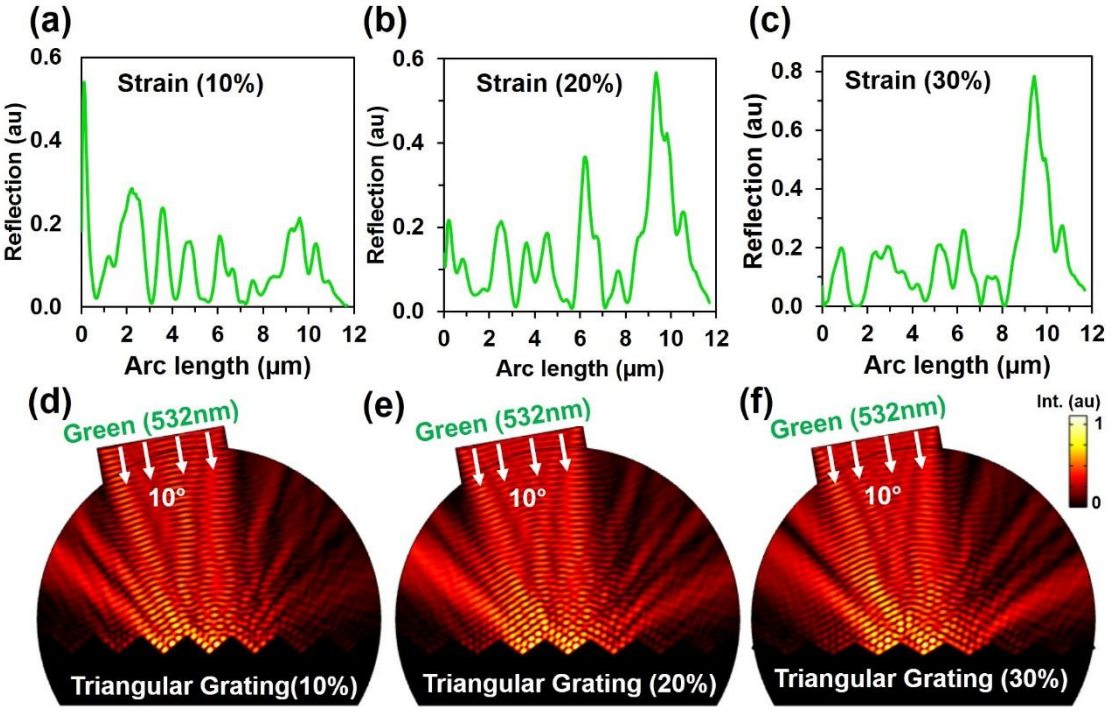

Figure S4. 6: Computational modeling of retoreflection, diffraction/scattering from triangular grating structure with strain variation (10, 20, 30%) and green light 10° illumination.

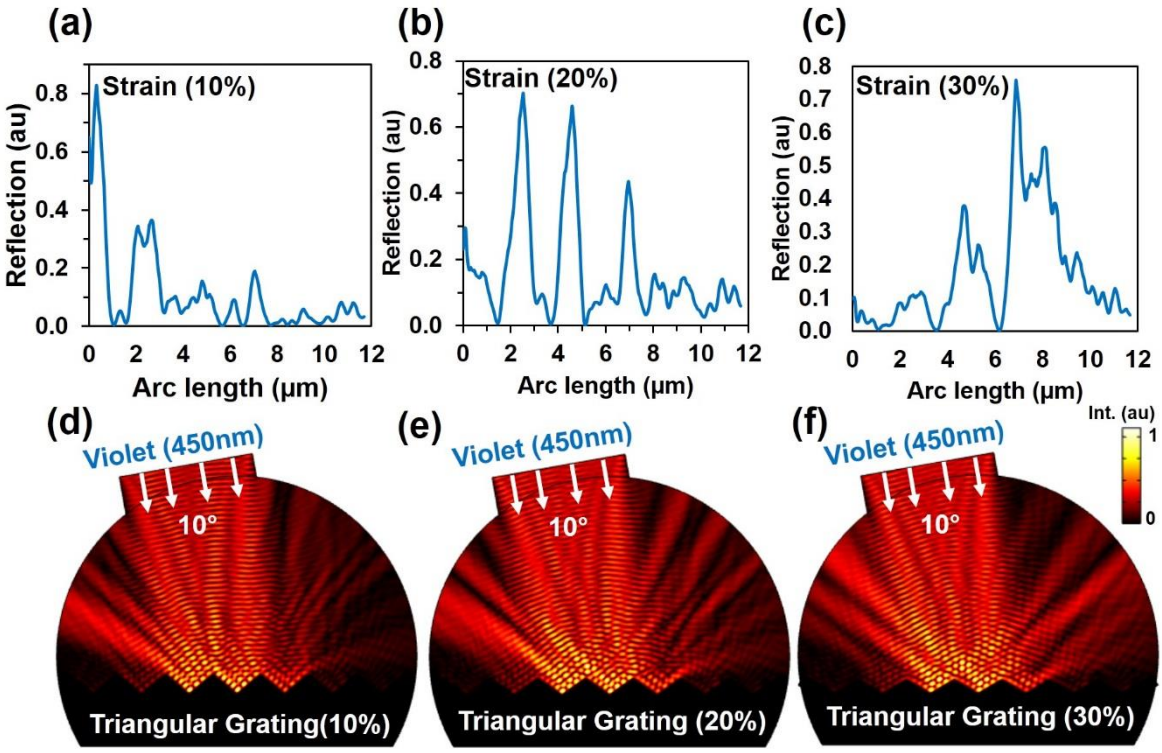

Figure S4. 7: Computational modeling of retoreflection, diffraction/scattering from triangular grating structure with strain variation (10, 20, 30%) and blue light 10° illumination.

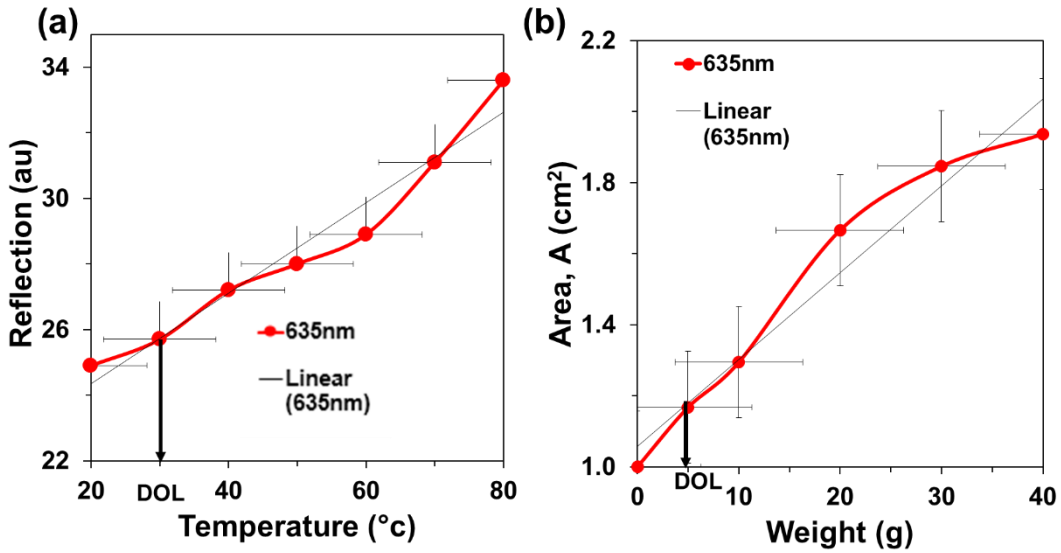

Figure S4. 8: The detection limit (DOL) calculation for (a) temperature and (b) weight variation during red (635 nm) illumination.

Appendix-C

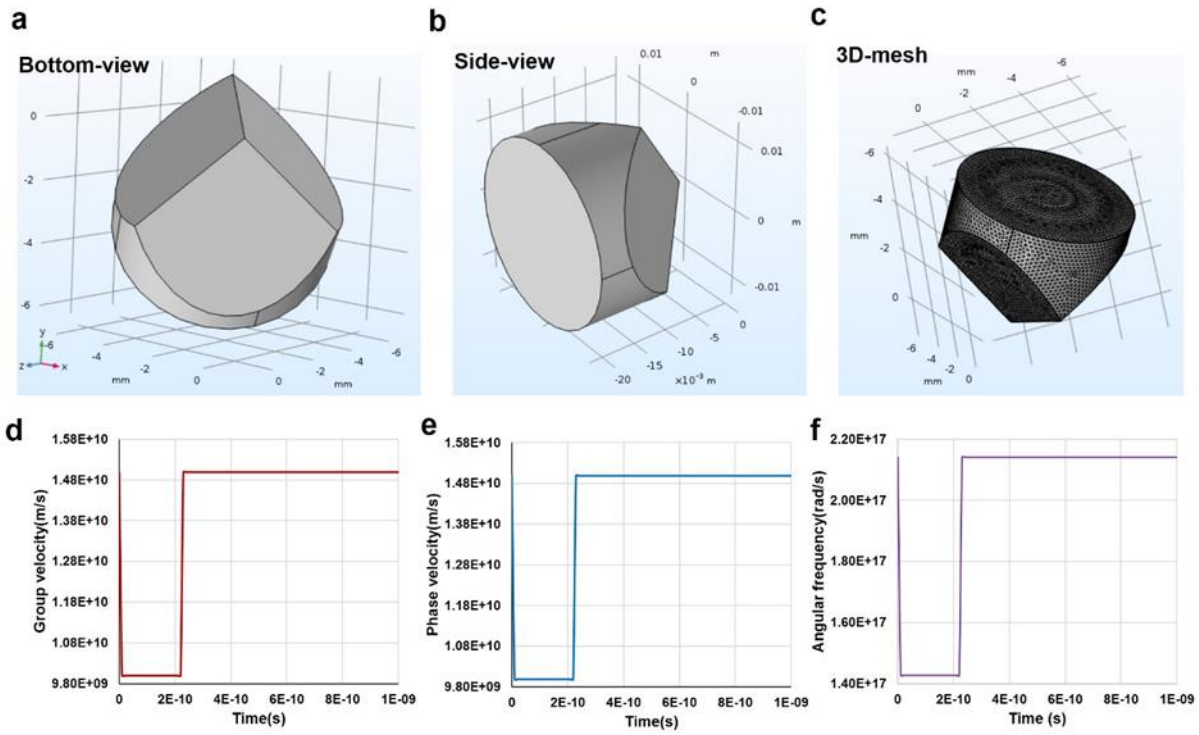

Figure S5. 1: (a-c) Bottom, Side, and 3D mesh of the LCCR, respectively. (d-f) Phase, group velocity, and angular frequency of the incident and retroreflected light as a function of computational time, respectively.

Appendix-D

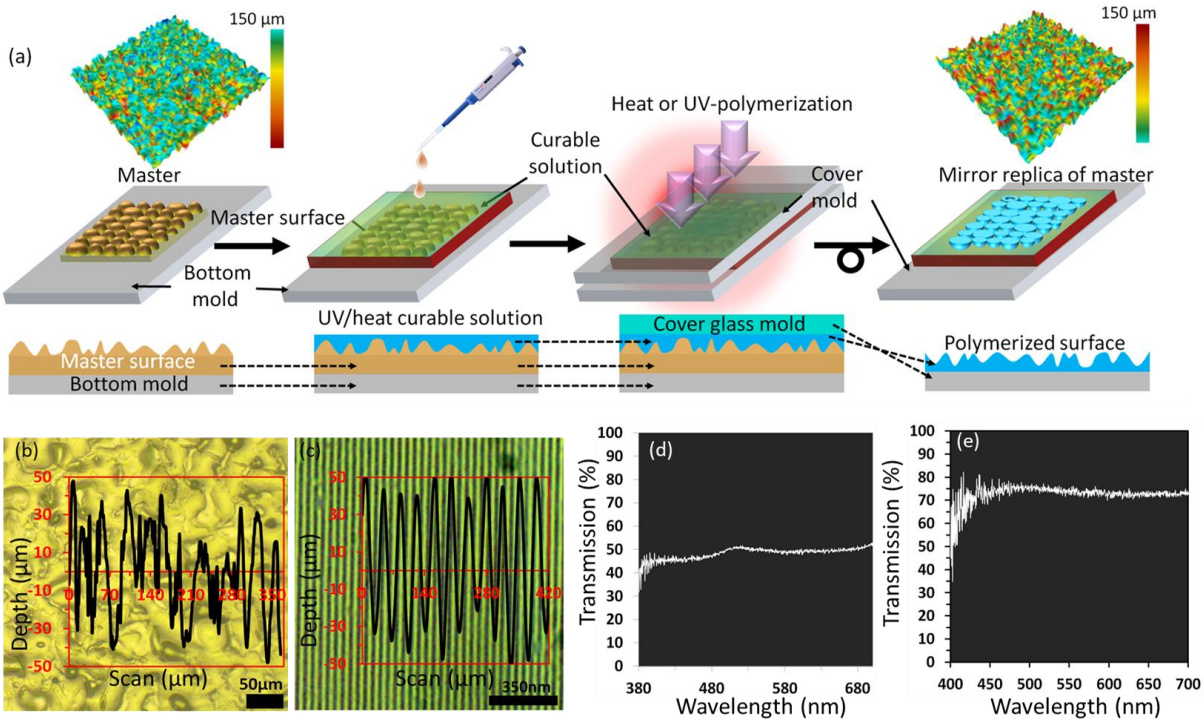

Figure S6. 1: Mirror replication of a master surface on PDMS: (**a**) schematic illustration of the replication process through which rigid nano/microstructures were transferred to a flexible form, (**b, c**) microscopic images and surface morphology analysis of the flexible polymerised optical diffuser (scale bar = 50 µm) and grating surfaces (scale bar = 350 nm), respectively , (**d, e**) broadband percentage light transmissions through the polymerised optical diffuser and periodic grating , respectively, plotted against the visible wavelength range.

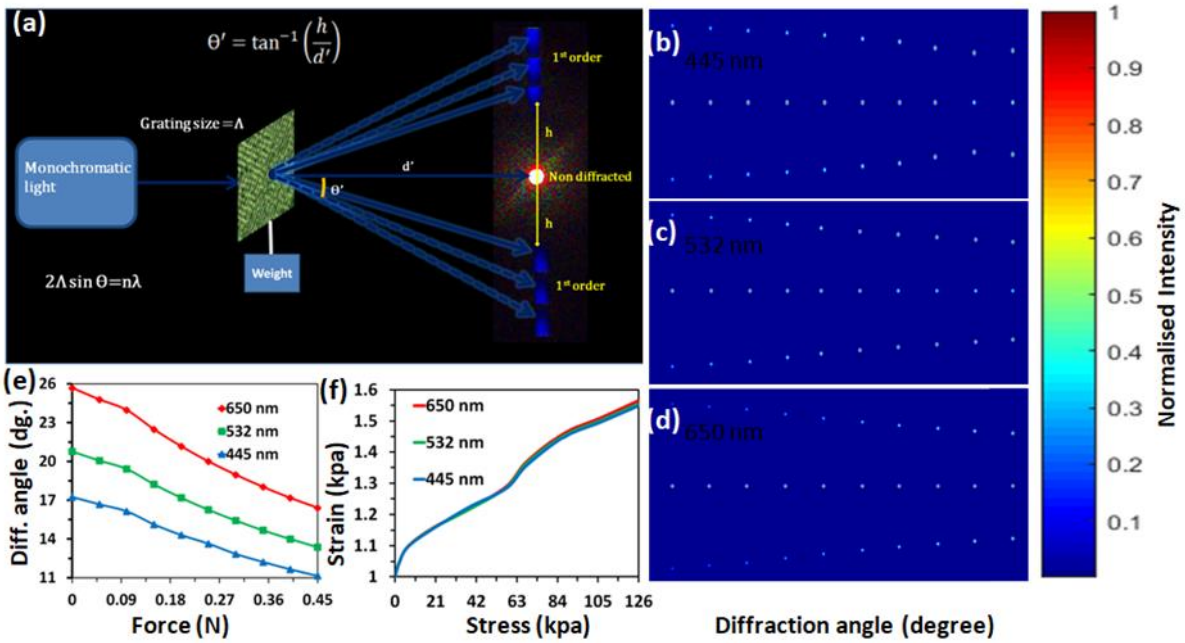

Figure S6. 2: Experimental setup for optical characterisation and simulations (a) schematic of the apparatus setup to perform optical characterisation of the polymerised samples (b-d) diffraction angles (degree) of the diffracted spots through different periodicities of the periodic gratings (i.e. left to right are for finer to gradually increasing grating spacing) under violet (445nm), green (532nm) and red (650nm) normal illuminations, respectively. (e) Plots of diffraction angles against various stress levels under various incident lights (f) stress versus strain curves for red (650nm), green (532nm) and violet (445nm) light illuminations.

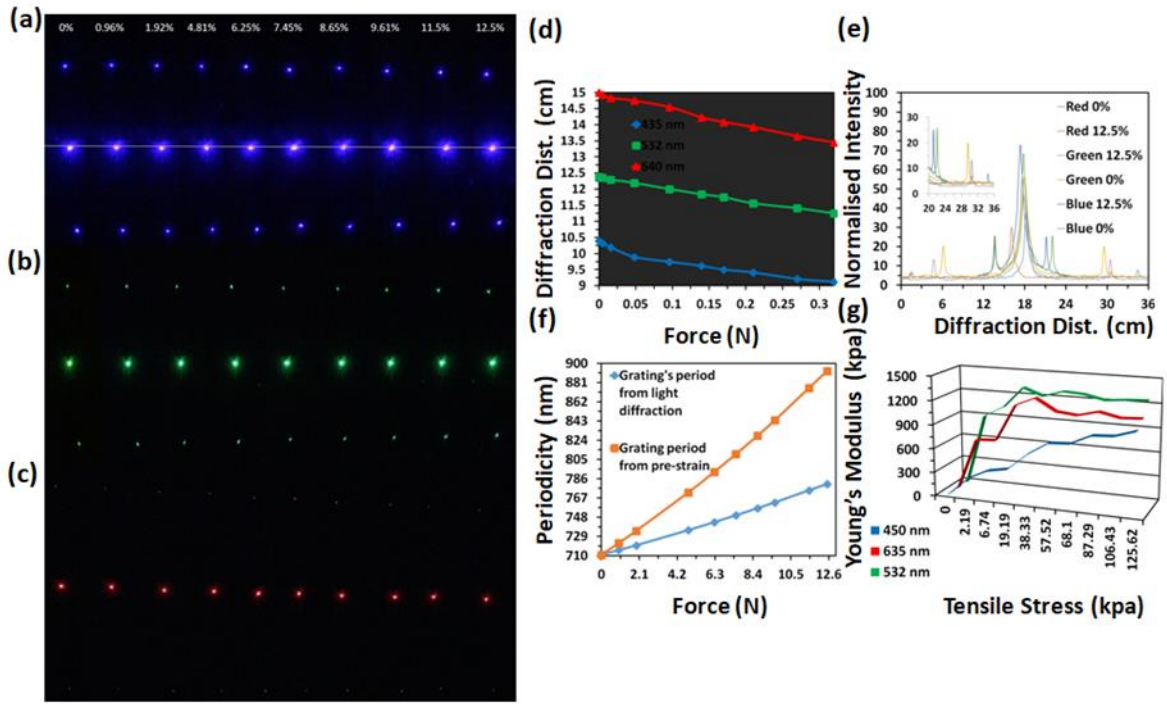

Figure S6. 3: Patterns formed from the digital camera on the image screen, obtained by illuminating red (635nm), green (532nm) and violet (445nm) monochromatic lights, respectively, through polymerised periodic gratings stretched gradually through specific weight suspensions. (d) Diffraction distance (cm) of the diffracted spots throughout relevant applied force (N) during red (640nm), green (532nm) and violet (435nm) normal illumination. (e) Normalised intensity against diffraction distance during minimum and maximum stretching of the flexible periodic gratings under various light illuminations (d) Calculated grating period (nm) with respect to applied force (N) by transmitting violet (450nm) light beam through periodic gratings and grating period calculated from pre-strain. (e) Tensile stress (kpa) versus Young's modulus (kpa) with red (635nm), green (532nm) and violet (450nm) monochromatic light sources.

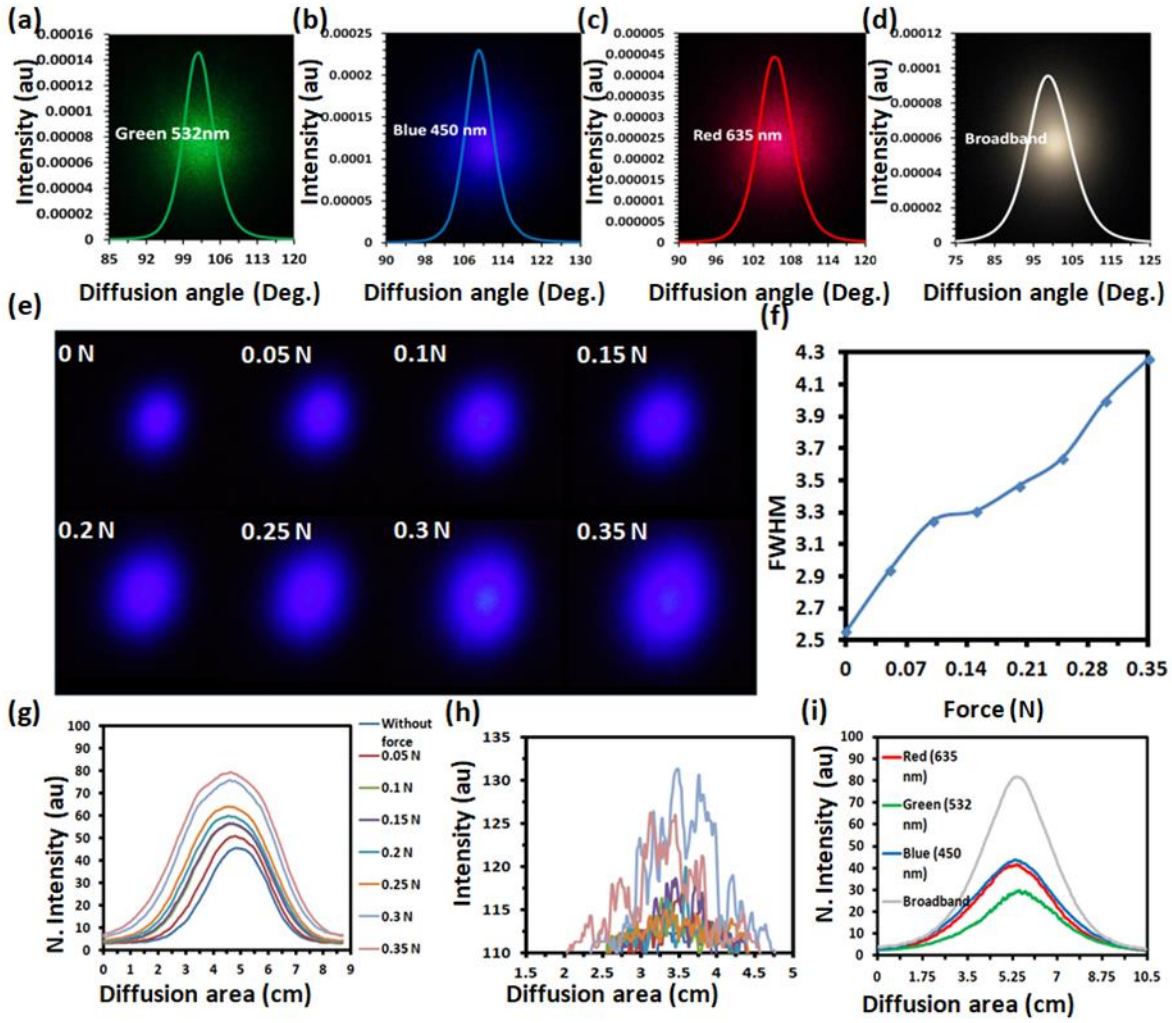

Figure S6. 4: Optical characterisation of polymerised optical diffuser (a-d) Intensity distribution with respect to diffusion angles during monochromatic green (532nm), violet (450nm), red (635nm), and broadband light normal illumination, respectively. (e) Diffusion field captured from the image screen by illuminating the sample with continuous violet (450nm) laser beam under various stress levels. (f) FWHM with respect to applied force. (g-h) change in diffusion area (cm) and transmitted violet (450nm) monochromatic light intensity through polymerised diffuser under various mechanical stresses. (i) Intensity distribution across the diffusion area at image screen during red, green, blue and broadband light illumination.

S6.1 Flexible gratings

One end of the grating sample was fixed, and the other end was loaded with known weights, so that their suspension stretched the periodic structures further on increased loading. The transmitted beam patterns from the gratings taken on the image screen contained more intense, non-diffracted central spots along with diffracted orders. The transmitted laser beams from the periodic gratings resulted in diffraction patterns on the image screen. The separation between the non-diffracted central spots to the first-order diffracted spots was taken into account to observe the changes in the optical behavior under various mechanical stress conditions.

The incident monochromatic laser beams gave diffraction patterns on the image screen following the Bragg's law, namely, $n \cdot \lambda = d \cdot \sin\theta$, where, n is an integer signifying the diffraction order, d is the groove spacing or period of the grating, and θ depicts the diffraction angle. The first-order diffraction angle can be deduced from the experimental observation by, $\theta = \sin^{-1}(l_1 /(l_1^2 + l_2^2)^{1/2})$, where l_1 and l_2 represent the first-order interspace and distance between the grating and image screen, respectively [1-4]. Consequently, the change in the grating period and therefore in the length against any load can be deduced by taking the difference between upstretched condition, namely, $d = \lambda \cdot l_1/(l_1^2 + l_2^2)^{1/2}$, and stretched condition, for which $d_i = \lambda \cdot l_i /(l_i^2 + l_2^2)^{1/2}$, where subscript i denotes the ith load suspended on the flexible grating.

A linear relationship between extension ratio of the PDMS block and periodicity of gratings was observed. The periodicities of the gratings calculated by pre-stain have the same trend to the values calculated based on the experimental data. From figure S6.3d, it can be deduced that the starting point i.e. the periodicity values without any mechanical expansion, is similar to 710.8 nm, obtained from both methods, but the growth rate is different. Some differences can be observed between the two methods. There are two reasons which could account for these differences. The first reason could be based on the fact that probably, the grating on the

substrate is not filled with the entire substrate and the grating period could not be enlarged with a homogeneous speed during the elongation of the substrate. Another reason could be due to the fact that the grating might change in the longitudinal direction during the stretching of the flexible substrate in the transverse direction.

The diffraction angle, which is the separation between diffracted to non-diffracted or mutual distance between diffracted spots, was found to be directly proportion to the applied stress, as predicted by simulations. On application of the external stress, the periodicities of the gratings were found to expand, which indicates that the distance between two slits is increasing and the transmitted light would have a wider space to pass through without any diffraction. Hence, the intensity of non-diffracted spot also increases as compared to the diffracted spots. Diffraction angles and the periodicities of the gratings were found to be inversely proportional to each other. For each increment in the value of applied force to expand the grating's period, the diffraction angle decreased independently from the wavelength of the illuminated laser i.e. all wavelengths followed the same trend. However, according to the predicted results and literature reviews, the red light diffracts at the highest angles, that is, 15° for no stress application and 13.45° for maximum stress, whereas violet, having the lowest wavelength in the visible spectrum, diffracts at the lowest angles, that is, 10.4° for without stress and 9.12° for maximum stress, as shown in **Figure S6.3e**. The diffraction angle consistently depends on the wavelength of the illuminated light, as well as, on the periodicities of the grating structure.

The Young's Modulus is calculated by tensile stress and strain. Using the area of the cross-section and net applied force, the tensile stress can be achieved. The average of measured value was taken to calculate the cross-sectional area in order to get an accurate result.

The highest Young's Modulus is created by the chromatic green laser. On the contrary, the monochromatic violet laser created the lowest Young's Modulus.

From figure S6.3g, it can be observed that green (532nm) laser and red (635nm) follow the similar trend for tensile stress against Young's Modulus. A sudden rise is noticed in the values of Young's Modulus at the beginning and at the peak stages around 40 kPa tensile stress. After achieving the peak value, the plot shows a smaller decline and maintains a relatively stable slow rise. Whereas, the values of Young's Modulus for the violet (435nm) wavelength show a rapid growth at the beginning and achieve a relatively slower growth until the tensile stress reaches up to 20 kPa. The main parameter affecting Young's Modulus is strain (change in optical response i.e. diffraction angle).

The Young's Modulus of PDMS is 360-870 kPa [5, 6] [7] which is higher than the highest value calculated in this experiment. From the obtained diffraction patterns at the image screen, it is found that the Young's Modulus values are all in a reasonable range.

As the force on the sample is increased, the level of stretched processing is improved. During this experiment, tuned diffraction is achieved based on external stimuli i.e. mechanical force.

S6.2 Flexible optical diffusers

PDMS substrate was grooved with micro/nanostructures; dimensions of these structures were comparable to the wavelength of electromagnetic radiation across visible region of the spectrum. These structures diffused visible light with high efficiency and proved wide field of view diffusers. The applied mechanical force altered the average surface morphology of these physical structures, which under continuous normal illumination with visible monochromatic and broadband light sources tuned the diffused light. Tuned diffused light based on external stimuli (mechanical stress) was captured from the image screen, kept in front of the sample and correlated with the applied stress. Mechanical stress applied to the flexible optical diffusers caused the surface structures to expand, which in turn changed the intensity of the transmitted light without interacting with the surface structures as well as altered the diffusion area across

the image screen. The surface structures were in the range of few hundred nanometers to few hundred micrometers, as shown by figure S6.1a. The optical characterisation of diffusion patterns was performed with a power meter in order to demonstrate diffusion angles with various monochromatic and broadband light sources. The sample was kept in a three dimensional stage i.e. free to move along x, y and z directions. Monochromatic red (635 nm), green (532nm) and violet (435nm) along with broadband light sources were shined at the sample normal to its plane. Photometer was fixed at a 0° and the 3D stage was moved from 0-180°. Spectrum in the form of light intensity distribution across various angles ranging from 0-180° was recorded from the computer attached to the photometer. It can be observed from figure S6.4a-c that the diffusion angle for the red (635nm) wavelength was recorded as 121°, for green (532nm) it was 114° and for violet (435nm) the diffusion angle was found to be 121°. Average diffusion angle without any stress application by transmitting broadband light source was recorded around 120°, as shown in figure S6.4d. The average transmission (%) through the flexible diffuser sample was measured to be 50% across the visible spectrum. Diffusion angle for green (532nm) was recorded as being slightly lower than that of red (635nm) and violet (435nm). This trend can be attributed to the transmission curve, shown in figure S6.2c, where a small peak is observed in the transmission of intermediate wavelengths ~500 to 560 nm across the visible spectrum, which led to narrower diffusion field of view, as more light was being transmitted without getting scattered.

In the next step, the photometer was replaced with the image screen to investigate changes in the optical properties of the sample under various stress levels. Experimental arrangements were similar to the experiments done for periodic gratings, as shown in figure S6.2a. The surface features engraved on PDMS substrate were distributed randomly causing the diffusion of light across wide angles. According to Bragg's law, the diffusion angles are defined by the size of structures, when dimensions of the structures are comparable to the wavelength of

transmitted light. Due to the random distribution of surface structures with various sizes ranging from nanometer to micrometer on the scale, the diffusion effects are also based on Rayleigh scattering, where scattered light was larger than the physical structures in the target [8]. Measured diffusion area at full width, i.e. at half of the maximum, varied from 2.56 cm^2 to 4.26 cm^2, for no force till the maximum applied force of 0.35 N, as shown in Figure S6.4g. Normalised peak intensity of scattered light was recorded as 45.7 (a.u) to 79.4 (a.u) for no force applied till the application of maximum force, i.e. 0.35 N is applied. For higher values of applied stress, several fluctuations in intensities around the centre, at 0° were observed, as shown by figure S6.4h. This is due to the reason that some light could not scatter and thus focused at the centre, when the dimensions of the structures causing diffusion became larger than that of the wavelength of the light source. Tuneable optical diffusion based on applied stress was successfully achieved with monochromatic violet (435 nm).

S6.3 Discussions

The soft polymeric flexible periodic gratings and optical diffuser changed optical properties based on external stimuli i.e. applied stress. Flexible fabricated structures were expanded by applying various loads ranging from 0-35 g with small increment in weight suspension each time. Changes in optical behaviour were continuously observed and recorded. The amount of transmitted light through PDMS based structures varied under various stress level. In general, light transmission was higher at higher stress levels. One of the reasons for this was due to the thickness (width) of the PDMS substrate, which decreased because of expansion (surface area). Another reason is that in the experimental work, the size of flexible structures under higher stress values expanded and became even larger than the wavelengths of visible spectrum, which could cause some light intensity within the beam to pass through without any interaction (diffusion/diffraction) with the larger structures. Simulations were carried out in order to

predict and successfully achieve the optical characterisations for the current polymeric devices used in this study.

An inverse relationship was found between the applied stress on flexible periodic gratings and the diffraction angle i.e. the diffraction angle decreased with applied stress, which expanded the periodicities of the gratings. Whereas, for flexible optical diffuser, a direct relationship between diffusion areas across the image screen and applied stress was observed i.e. diffusion area was largest for highest value of applied stress and vice versa. Cross-sectional area of the physical polymerised structures towards the incident light may have a high influence on the diffraction angles. Highest cross-sectional area was achieved by arranging normal illumination and keeping it consistent throughout the experiments. The periodic gratings were uniform to yield a well-ordered diffraction pattern offering flexibility in the choice of incident light position. Other parameters such as the distance between the flexible structures under normal illumination and the image screen, the spectrometer, the light source and image screen to digital camera, were kept constant during all optical characterisations. It is anticipated that external stimuli (humidity, temperature, force, and tilted illumination) may alter the optical response in a complex way and can affect the sensitivity of sensors.

S6.4 Analysis

This doctoral research has successfully demonstrated tuneable optical properties of the polymerised optical devices including periodic gratings and optical diffusers based on external stimuli (applied stress). Compared to rigid conventional nano/microstructures, selective optical diffusion as well as diffraction angles were achieved using flexible optical diffusing surface and polymerised periodic gratings, respectively. Moreover, rigid optical devices are limited due to constant dimensions, whereas, flexible optical devices change their structures' dimensions in the event of applied stress, which in turn yields the tuning of optical response,

and the devices are composed of passive components (no electronics required). PDMS based optical force sensors described in the present work are simple, low cost, easy to fabricate and feasible to operate in complex environments. The sensitivity of polymerised sensors could be customised by adding impurities in the PDMS solution during fabrication or treating with polishes, paints and coatings with selective metallic/nonmetallic components to obtain desirable optical/mechanical properties. An inverse relationship between applied force and diffraction angle of transmitted light was demonstrated during optical characterisations of flexible periodic gratings to be used as a strain sensor. Whereas, a direct relationship was observed between diffusion field and applied force during optical characterisation of polymerised optical diffusers under various stress levels. Recorded tuneable optical responses were correlated with tensile stress and were found to be in good agreement with the predicted value received from simulations and thus proved the effectiveness of the flexible devices demonstrated in this work as force sensors. Sensors based on soft, flexible nano/microstructures are reliable and may have applications in remote sensing as stress strain sensors. It is anticipated that instead of mechanical expansion/compression, similar results could be achieved under thermal expansion/compression. Also, performance of PDMS based sensors could be affected by environmental condition such as; humidity, temperature, and mechanical forces along with illumination.

References (vii)

1. Erdogan, T., *Fiber grating spectra.* Journal of lightwave technology, 1997. **15**(8): p. 1277-1294.
2. Stover, J.C., *Optical scattering: measurement and analysis*. Vol. 2. 1995: SPIE optical engineering press Bellingham.
3. Berne, B.J. and R. Pecora, *Dynamic light scattering: with applications to chemistry, biology, and physics*. 2000: Courier Corporation.
4. Yetisen, A.K., et al., *Light-directed writing of chemically tunable narrow-band holographic sensors.* Advanced Optical Materials, 2014. **2**(3): p. 250-254.

5. Park, J.Y., et al., *Increased poly (dimethylsiloxane) stiffness improves viability and morphology of mouse fibroblast cells.* BioChip Journal, 2010. **4**(3): p. 230-236.
6. Kulangara, K. and K.W. Leong, *Substrate topography shapes cell function.* Soft Matter, 2009. **5**(21): p. 4072-4076.
7. *Material: PDMS (polydimethylsiloxane)*. 2017, Material Property Database.
8. Hulst, H.C. and H.C. van de Hulst, *Light scattering by small particles*. 1957: Courier Corporation.